Structure-Property-Processing Relationships Between Polymeric Solutions and Additive Manufacturing for Biomedical Applications

Emily Marie Wilts

Dissertation submitted to the faculty of the Virginia Polytechnic Institute and State University in partial fulfillment of the requirements for the degree of

Doctor of Philosophy
In
Macromolecular Science and Engineering

Timothy E. Long (Chair)
Christopher B. Williams
Michael D. Schulz
Michael J. Bortner
Robert B. Moore

September 3, 2020
Blacksburg, VA

Keywords: additive manufacturing, binder jetting, vat photopolymerization, RAFT polymerization, poly(vinyl pyrrolidone), ring-opening polymerization, photo-kinetics

Structure-Property-Processing Relationships Between Polymeric Solutions and Additive Manufacturing for Biomedical Applications

Emily Marie Wilts

Abstract

Additive manufacturing (AM) creates 3D objects out of polymers, ceramics, and metals to enable cost-efficient and rapid production of products from aerospace to biomedical applications. Personalized products manufactured using AM, such as personalized dosage pharmaceuticals, tissue scaffolds, and medical devices, require specific material properties such as biocompatibility and biodegradability, etc. Polymers possess many of these qualities and tuning molecular structure enables a functional material to successfully deliver the intended application. For example, water-soluble polymers such as poly(vinyl pyrrolidone) and poly(ethylene glycol) both function as drug delivery materials because of their inherit water-solubility and biocompatibility. Other polymers such as polylactide and polyglycolide possess hydrolytically cleavable functionalities, which enables degradation in the body. Non-covalent bonds, such as hydrogen bonding and electrostatic interactions, enable strong connections capable of holding materials together, but disconnect with heat or solvation. Taking into consideration some of these polymer functionalities, this dissertation investigates how to utilize them to create functional biomedical products using AM.

The investigation of structure-property-processing relationships of polymer molecular structures, physical properties, and processing behaviors is transforming the field of new materials for AM. Even though novel, functional materials for AM continue to be developed, requirements that render a polymeric material printable remain unknown or vague for most AM processes. Materials and printers are usually developed separately,

which creates a disconnect between the material printing requirements and fundamental physical properties that enable successful printing. Through the interface of chemistry, biology, chemical engineering, and mechanical engineering, this dissertation aims to relate printability of polymeric materials with three types of AM processes, namely vat photopolymerization, binder jetting, and powder bed fusion.

Binder jetting, vat photopolymerization, and powder bed fusion require different viscosity and powder requirements depending on the printer capabilities, and if the material is neat or in solution. Developing scaling relationships between solution viscosity and concentration determined critical overlap (C^*) and entanglement (C_e) concentrations, which are related to the printability of the materials. For example, this dissertation discusses and investigates the maximum printable concentration in binder jetting of multiple polymer architectures in solution as a function of C^* values of the polymer. For thermal-type printheads, C^* appeared to be the highest jettable concentration, which asserted an additional method of material screening for binder jetting. Another investigation of the photokinetics as a function of concentration of photo-active polymers in solution revealed increased viscosity leads to decreased acrylate/acrylamide conversion. Lastly, investigating particle size and shape of poly(stearyl acrylate) particles synthesized through suspension polymerization revealed a combination of crosslinked and linear polymers produced high resolution parts for phase change materials. These analytical screening methods will help the progression of AM and provide future scientists and engineers a better guideline for material screenings.

Structure-Property-Processing Relationships Between Polymeric Solutions and Additive Manufacturing for Biomedical Applications

Emily Marie Wilts

General Audience Abstract

Additive manufacturing (AM), also known as 3D printing, enables the creation of 3D objects in a rapid and cost-efficient manner for applications from aerospace to biomedical sectors. AM particularly benefits the field of personalized biomedical products, such as personalized dosage pharmaceuticals, hearing aids, and prosthetic limbs. In the future, advanced detection and prevention medical screenings will provide doctors, pharmacists, and engineers very precise data to enable personalized healthcare. For example, a patient can take three different medications in one pill with the exact dosage to prevent side-effects and drug-drug interactions. AM enables the delivery and manufacturing of these personalized systems and will improve healthcare in every sector.

Investigations of the most effective materials is needed for personalized medicine to become a reality. Polymers, or macromolecules, provide a highly tunable material to become printable with slight chemical modifications. Investigation of how chemical structure affects properties, such as strength, stretchability, or viscosity, will dictate how they perform in a manufacturing setting. This process of investigation is called “structure-property-processing” relationships, which connects scientists and engineers through all disciplines. This method is used to discover which polymers will not only 3D print, but also carry medication to a patient or deliver therapeutics within the body.

Acknowledgements

I would like to first thank my advisor, Prof. Timothy Long for a life-changing four years of being in his group. Before I arrived at Virginia Tech, I asked Prof. Long if I could join his research group knowing this would be some of the most challenging years of my life and it has paid off in the fullest. Prof. Long holds his group members to an extremely high standard, which prepares us for anything we want to do after our degrees. He taught me how to give a thought-provoking and engaging presentations, how to write a research paper, and how to communicate science effectively to anyone. I will always admire how excellent he balances his job from supporting his graduate students, giving external presentations, and securing funding for our group. He has also been extremely supportive in other activities I chose to participate in such as the MACR Student Council and a Chair of the National Graduate Research Polymer Conference. His help and guidance through all of my endeavors has made me a better person. Best of luck to Dr. Long at Arizona State and I am looking forward to visiting! I would also like to thank my committee members, Prof. Christopher Williams, Prof. Robert Moore, Prof. Michael Bortner, and Prof. Michael Schulz for their continuing support throughout my degree. I am thankful to have a committee with a broad range of expertise's from Chemistry to Mechanical Engineering and Chemical Engineering. My committee's provoking questions and willingness to meet and discuss my research greatly aided to my success.

Next, I would like to thank all of the members of the Long group who I worked with during my time at Virginia Tech, and especially my mentors. My first mentor, Dr. Allison Pekkanen, is a biomedical engineer and taught me everything from synthesis to

cell culture. I always admired her work ethic—in her last semester she had an incredible amount of responsibilities and still reached all of her goals with ease. I appreciate the time she took to teach me the basics in lab to help me start one of my main funded projects with Zoetis. Dr. Jana Herzberger also had an incredible impact on me during my first and second year of graduate school. She would help me come up with project ideas and spent countless hours helping me write my first literature review. She is one of my role models and I aspire to grow into a skilled research and amazing friend and mentor. Kevin Drummey also greatly helped in my research during my second year with constant discussion of my current research and exploring ideas about poly(2-oxazoline)s. I admired his creativeness and hope to be as effective as a scientists as he is eventually. Lastly, I would also like to thank everyone in the Long group who has helped me along the way, Tyler White, Josh Wolfgang, Clay Arrington, Xi Chen, Mark Cashman, Dr. Nicholas Moon, Dr. Justin Sirrine, Dr. Ryan Mondschein, Dr. Mingtao Chen, Dr. Philip Scott, Dr. Chixia Tian, Johanna Vandenbrande, Cody Weyhrich, James Brown, Boer Liu, Chris Kasprzak, and Dr. Katherine Heiffron, for engaging conversions, working through problems, and making graduate school easier and more fun.

Throughout my four years, I mentored many undergrads and first-year graduate students who taught me valuable skills, motivated me, and contributed tremendously to my research. Corey Davis was my first REU student who was curious and full of energy. He taught me patience and how to teach students who learn differently than myself. Aleena Gula worked with me for six months with an impeccable attention to detail. She drove my research forward and was always great company. Alexandra Thorsted and Fiona Carter-Todd were only with me for a few months but taught me patience and both had a passion

for science and research. I worked with Jose Sintas, a first-year student in the Long group, my last year at Virginia Tech. He is curious, intelligent, and will be extremely successful in the Long group. I would like to thank you all for your help motivating me to teach and continue learning.

I founded and became president of the MACR Student Council and became a Chair of the National Graduate Research Polymer Conference (NGRPC) during my four years at Virginia Tech. I would like to thank the other founding members of the council, Dr. Priya Venkatraman, Dr. Camden Chatham, and Bradly Sutliff, for embarking on this journey together in hopes of improving MACR students' experiences. We organized social events for MACR students, communicated to staff and directors about improvements for the MACR program, and helped with orientation and recruitment for new students. We hope this tradition will continue and MACR students will continue feeling at home at Virginia Tech. I would also like to thank the chairs of NGRPC, Dr. Priya Venkatraman, Dr. Philip Scott, and Bradley Sutliff, and the rest of the organizing committee for working together to win the bid for NGRPC, and put on an unforgettable conference.

I would like to thank my external funding sources, Zoetis and Honeywell, for supporting me financially and scientifically throughout my degree. Working with industry enabled a deeper understanding of important aspects industry is interested in versus academia.

Last but not least, I would like to thank my loving family, friends, and partner. My Mom, Dad, and sister Erica, have been with me every step of my degree, from encouraging me to keep going and listening to my problems. Whenever I had good news or bad news, they would love to hear about my experiences at Virginia Tech. I love you all more than I

can exclaim and am so thankful for your presence in my life. Thank you to my best friend, Dr. Priya Venkatraman, for being by my side throughout all of graduate school. From starting the MACR Student Council to NGRPC, we have always worked so well together and made a real difference at Virginia Tech. She was also a huge emotional support whenever we had problems with research and our environment. I definitely could not have finished this degree without her and can't wait to see how high she sores in life. Last but not least I would like to thank my partner who has been a major support system for my final two years of graduate school. We have so much fun together and he is always willing to listen and work through my frustrations. I love you to the moon and back and am thoroughly looking forward to our future.

Attributions

Prof. Timothy E. Long is the author's advisor and a Professor of Chemistry and the previous Director of Macromolecules Innovation Institutes (MII) at Virginia Tech.

Prof. Christopher B. Williams is a Professor of Mechanical Engineering, the Associate Director of MII, and a collaborator on chapter 4, 5, 7, 8, 9, 10, and 12.

Dr. Jana Herzberger was a postdoctoral student in Prof. Long's research group and a collaborator on chapter 2.

Dr. Allison M. Pekkanen was a doctoral student in Prof. Long's research group and a collaborator on chapter 4.

B. Tyler White is a doctoral student in Prof. Long's research group and a collaborator on chapter 4.

Viswanath Meenakshisundaram is a doctoral student in Prof. Williams' research group and a collaborator on chapter 4.

Dr. Donald C. Aduba was a postdoctoral student in Prof. Williams' research group and a collaborator on chapter 4.

Aleena Gula was an undergraduate student in Prof. Long's research group and a collaborator on chapter 5.

Corey Davis was a REU student in Prof. Long's research group and a collaborator on chapter 5.

Dr. Nicholas Chartrain was a doctoral student in Prof. Williams' research group and a collaborator on chapter 5.

Fiona Carter-Todd was an undergraduate student in Prof. Long's research group and a collaborator on chapter 6.

Jose Sintas is a doctoral student in Prof. Long's research group and a collaborator on chapter 6 and 10.

Da Ma is a doctoral student in Prof. Williams' research group and a collaborator on chapters 7 and 9.

Dr. Yun Bai was a doctoral student in Prof. Williams' research group and a collaborator on chapter 7.

Julia Pimentel was an undergraduate student in Prof. Williams' research group and a collaborator on chapter 10.

Daniel Rau was a doctoral student in Prof. Williams' research group and a collaborator on chapter 12.

Table of Contents

List of Figures

a function of mol % TPO, **(C)** depicts conversion (%) as a function of UV exposure time, and **(D)** depicts conversion as a function of SH equivalents.

Figure 8.4. Using poly(2-(3-butenyl)-2-oxazoline, 100 mol % grafting sites, to explore steric hindrance effects on vinyl conversion where **(A)** depicts conversion as a function of PVP graft M_n and **(B)** summarizes all of the grafting results depicting conversion as a function of mol % grafting sites.

Figure 8.5. DSC reveals glass transition temperatures (T_g) of each graft copolymer system compared to Fox T_g estimations. **(A)** depicts T_g and Fox T_g estimation as a function of graft copolymer composition and **(B)** shows heat flow as a function of temperature for two example graft copolymers and their corresponding precursors.

Figure 8.6. (A) Zero-shear viscosity as a function of mol % grafting sites in DI water and **(B)** elucidates solution viscosity as a function of shear rate depicting 10%, 2.5 and a linear PVP analog at the same M_n.

Figure 8.7. Image of a binder jetted tablet printed ring with 10%:2.5 at 10 wt % in deionized water and 80:20 lactose:powdered sugar by weight.

Figure S8.1. ^{1}H NMR spectroscopy of 2-(3-butenyl)-2-oxazoline in $CDCl_3$.

Figure S8.2. ^{1}H NMR spectroscopy of *O*-ethyl-*S*-(1-ethylphenyl) dithiocarbonate in $DMSO_{d6}$.

Figure S8.3. ^{1}H NMR spectroscopy of 5k PVP in $CDCl_3$.

Figure S8.4. ^{1}H NMR spectroscopy of 90:10 PMeOx-*co*-PEneOx (PMeEneOx) in $CDCl_3$.

Figure S8.5. ^{1}H NMR spectroscopy of PMeEneOx 90:10 and 2.5 kg mol^{-1} depicts the elimination of the vinyl peaks at 5.8 to 4.8 ppm indicating full conversion of grafting sites.

Figure 9.1. (A) Solution viscosity as a function of PMeOx-*g*-PVP composition and **(B)** Z parameter as a function of PMeOx-*g*-PVP composition.

Figure 9.2. Specific viscosity (η_{sp}) as a function of concentration of 10%, 2.5 and 25%, 5 where the inflection point denotes *C**.

Figure 9.3. (A) Compressive strength as a function of PMeOx-*g*-PVP composition and **(B)** compressive strength comparison of linear, 4-arm star, and graft PVP at similar molecular weights. (Data reproduced with permission from Wilts et. al.[16])

List of Tables

List of Schemes

Chapter 1: Dissertation Overview and Background

1.1 New materials for vat photopolymerization

Vat photopolymerization (VP), also known as stereolithography (SLA), selectively solidifies a liquid, photo-active precursor through UV light-assisted crosslinking or polymerization layer-by-layer into a 3D shape. Photoactive monomers, oligomers or polymers, photo-initiators, and additives commonly comprise the vat mixture.[1–3] Rate of reaction, photoactive precursor viscosity, and strength of each layer all contribute to printability of the material. The precursor must react fast enough to solidify in reasonable timeframes (~0-15 s) to enable quick printing. Viscosity of the precursor defines the vat photopolymerization method used. Some systems rely on low viscosity (1-10 Pa·s) coalescence to refill the build platform while higher viscosities require a recoating blade.[4] Strength of each layer ensures the layer will remain in place as the next layer is spread across the build platform. These main factors determine how a new material for vat photopolymerization are designed.[5,6]

Two main types of vat photopolymerization include bottom-up (constrained surface) and top-down (free surface) approaches.[2,7] The bottom-up approach involves curing on a build stage that moves up and out of the vat. This requires the material to adhere to the build stage and remain in place throughout the print.[8,9] The top-down approach contains a stage that moves down, where the printed part is submerged into the vat. This requires the material to not only adhere to the build stage, but also not dissolve in the vat while printing occurs.[10] Digital light processing (DLP) SLA and laser-SLA represent the two methods of light deliverance to the precursor. DLP provides a broad range wavelength and is either delivered through mask projection or scanning techniques. Laser-based

systems deliver one wavelength of light and continuously draw each layer over the build stage. While laser-based systems provide higher resolution (5-10 μm), more considerations of exposure time and speed might be considered to control cure depth.[11]

1.1.1. Incorporation of supramolecular interactions in new materials for VP

Supramolecular interactions encompass types of non-covalent bonds with relatively less strength compared to covalent bonds. Some examples include ionic and hydrogen bonding interactions, which are abundant in nature.[12] Although these bonds are not as strong as covalent bonds, the reversibility and stimuli-responsivity provide unique advantages. Specifically, polyelectrolytes and polymers containing hydrogen bonding provide increased melt viscosity and mechanical strength. However, the labile bonds allow for dissociation when exposed to heat or solvents.[13,14]

Additive manufacturing utilizes supramolecular interactions in novel material design to take advantage of the labile and reversible bonds, especially for biomedical applications.[15] Natural polymers such as chondroitin sulfate (CS), dextran, chitosan, sodium alginate, and hyaluronic acid not only possess supramolecular functionalities, but also easily switchable moieties to enable additive manufacturing. For example, functionalizing polysaccharide backbones with acrylate, methacrylate and thiol moieties induce photoactive for SLA-type printing.[12] The natural polymer backbone and the supramolecular interactions increase cell adhesion and proliferation, while also maintaining strength. Some examples of synthetic polymers containing supramolecular functionalities include sulfonated-PEG, sulfonated-PCL, and nucleo-based monomers integrated into polyester backbones.[16,17] Aside from the biological activity of supramolecular interactions, they also sometimes enable dissolution and degradable after

printing. For example, instead of chemically crosslinking for SLA-type printing, polyelectrolytes provide a non-covalently crosslinked system that is also dissolvable, which is discussed in Chapter 4.

Chapter 4 investigates photopolymerizing aqueous, electrolyte-containing monomers into solids for VP. Usually in VP, photoactive, liquid precursors are crosslinked into solids, but forfeit the ability to dissolve after printing. Using electrolyte-containing monomers to create polyelectrolytes creates a network of covalently and non-covalently bonded polymers. The labile, non-covalent electrostatic interactions dissociate in water and render the printed part soluble in water. The main copolymer combination in Chapter 4, TMAEA and *N*-vinyl pyrrolidone, provide a range of mechanical properties and photokinetics after and during photopolymerization. The resulting parts dissolve and swell in water, rendering the systems ideal for sacrificial scaffolds for VP.

1.1.2. Bulk and solution viscosity effects on photokinetics and printability

One of the most influential properties of new materials for VP is the photoactive precursor viscosity. Viscosity affects whether the precursor will flow onto the build-stage to evenly deposit subsequent layers and will affect photokinetics and conversion of the active moieties.[2] **Figure 1.1** depicts a top-down-SLA printer where the print is submerged into the vat during printing. After curing a layer, the elevator lowers and the precursor flows onto the build stage or a recoating blade deposits the material.[18] The viscosity of the precursor will determine the time-scale of printing each layer and if the layer is evenly distributed. Viscosity affects photokinetics through the mobility of the precursor, which could help or hinder the ability for reactive group to react, and the speed at which the liquid precursor forms a solid. Conversion will also vary with changes in viscosity, which could

greatly affect the strength and cytotoxicity of the final part. As these theories have not been reported, Chapter 5 and 6 aim to elucidate the relationship between viscosity and photokinetics.

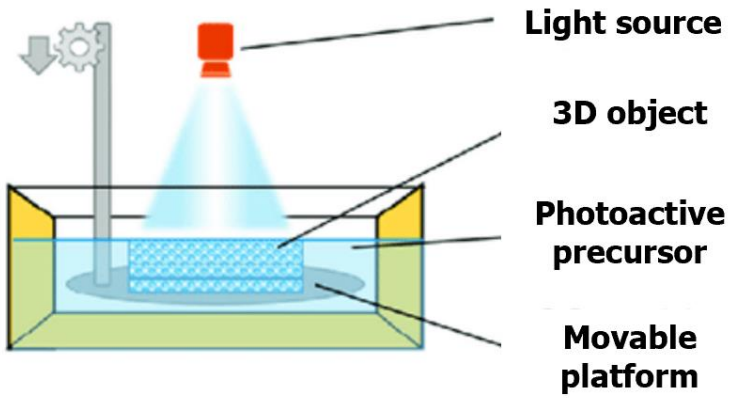

Figure 1.1. Depiction of a top-down-SLA printer adapted from Mao *et al.*[18]

Chapter 5 and 6 describe relationships between viscosity and photokinetics. Chapter 5 describes the development of PLGA-based photoactive precursors. The varying lactide to glycolide ratios created a range of precursor viscosities, which led to differences in photokinetics. Photocalorimetry revealed the higher the viscosity, the lower the conversion, which imparted cytotoxicity in the crosslinked parts. As a continuation of this study, Chapter 6 reports poly(ethylene glycol)-diacrylate and hydrogen-bonding poly(ethylene glycol)-diacrylamide at 2, 8, and 35 kg mol^{-1} in nine different concentrations. Photorheology and photocalorimetry revealed increasing viscosity led to decreased conversion and fast solidification times. These studies present the opposite behavior of the Trommsdorff effect, which states localized viscosity increases in free radical polymerizations results in a slowing of termination events, thus higher conversions.[19] When crosslinking polymers in solution, this study revealed an increase in reaction time with increased concentration and higher viscosity, but decreased conversion.

1.2 New materials for binder jetting additive manufacturing

Binder jetting additive manufacturing (BJ AM) is a powder-based printer that utilizes a binder to selectively solidify powder layer-by-layer into a 3D shape.[20] **Figure 1.2** depicts a typical BJ AM set-up beginning with a liquid adhesion supply (binder) leading to a printhead.[21] The printhead ejects the binder onto the powder surface and solidifies around the powder, sometimes with the assistance of heat or light to cure the binder. After one layer is printed, the roller pushes another even layer of powder over the print area to prepare for the next ejection. As this process continues, a series of elevators ascends the powder supply section and descends the build platform to enable a continuous printing environment. Common powder bed materials include polymers, ceramics, and metals. Complex combinations of thermal-curing materials, solvents, polymers, and surfactants comprise the binder formulation depending on the end function of the part.[22–24]

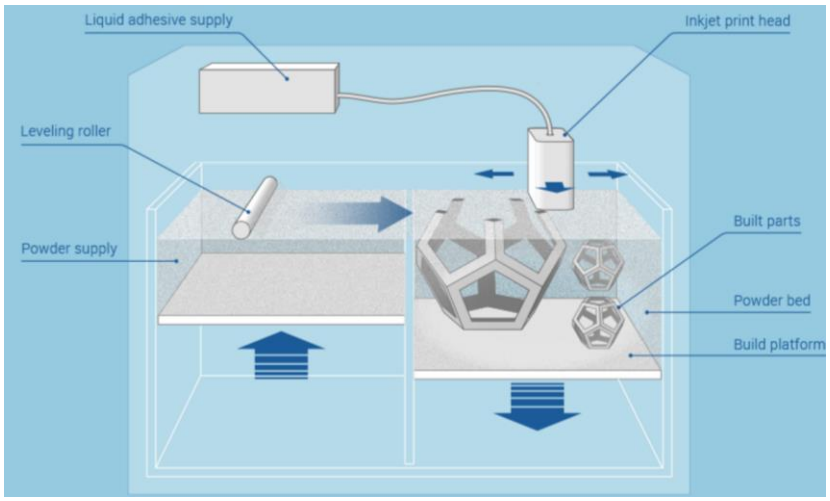

Figure 1.2. Depiction of binder jetting additive manufacturing. (Reproduced from Additively.com[21])

Jettability of formulated binder is a complex process that depends on type of printhead and contents of the binder. To determine if the binder will jet out of the printhead

nozzle, researchers often use the Ohnesorge (*Oh*) number (**Eqn. 1**) and the Z parameter (**Eqn. 2**) where η, σ, ρ, and α represent viscosity, surface tension, density, and nozzle radius.

$$Oh\ \# = \frac{\eta}{(\sigma\rho\alpha)^{0.5}} \qquad \textbf{Eqn. 1}$$

$$\frac{1}{Oh} = Z \qquad \textbf{Eqn. 2}$$

Reis and Derby *et al.* used computational fluid dynamics of drop formation with a parallel experimental study to determine the jettable range falls between Z = 1-10. This experiment used particle-filled binders with a piezoelectric printhead.[22,24] However, multiple following reports elucidated the types of materials in the binder, i.e. particles, small molecules, or polymers, and the type of printhead used, piezoelectric or thermal, greatly influence the jettability range. Moon *et al.* used combinations ethylene glycol and water on a piezoelectric system and determined a jettable range of Z = 4-14 through observing single drop formation, position accuracy, and maximum jettable frequency.[25] Other studies investigated the differences in jettablility comparing piezoelectric and thermal printheads, which elucidated more variation of the jettable range.[26] Polymeric solutions also produce varying jettability ranges depending on the polymer relaxation time, extensibility, and complex rheology.[27] The differences in binder content, solvent, and printhead all produce variability in the Z parameter jettable range, which could suggest other factors must be considered to predict jettability for new materials.

1.2.1. Relationships between polymeric solution properties and successful jetting

Jetting of polymeric solutions requires consideration of viscoelastic properties and relaxation times. A polymer relaxes, or returns to its equilibrium state, after a stress has been applied or the system is deformed. The elastic behavior of a polymer fluid is governed by its equilibrium microstructure state. When a polymeric fluid is deformed, thermodynamic forces in the form of elastic energy return the system into its equilibrium state.[28] This elastic energy is stored during the deformation process, but because polymer fluids are not ideal systems, they also experience a viscous dissipative response. The timescale at which a polymer in solution relaxes depends on the concentration in solution, classification of solvent, and intra and intermolecular interactions. All of these factors are important when determining if a polymeric solution is jettable because the relaxation time will affect the viscoelastic properties of the ink, thus rendering it jettable or not.[28,29]

If the relaxation times of the polymers are longer than the jetting process, they may not be able to jet out of the nozzle. A typical timescale for an actuation pulse is 20 μs, where many concentrated polymeric solutions have relaxation times of ~0.1 s.[27,30] As an example, Hutchings *et al.* investigated jetting of dilute polymeric solutions and developed a quantitative model which predicts jettability of said solutions based on the system's *Wi* number and the polymer extensibility (*L*). Others have investigated the effect of the *Wi* number on jettability in dilute solutions ($Wi < ½$), but this report aimed to investigate viscoelastic solutions exhibiting higher *Wi* numbers.[31] The experiments assumed a constant drop velocity of 6 m s^{-1} and the relaxation times were determined from a Zimm model.

Chapters 7 and 9 describe the relationships between predicting printability using the *Oh* number and the critical overlap concentration (C^*) of linear, 4-arm star, and graft poly(vinyl pyrrolidone) (PVP) solutions using a thermal printhead. Previous reports

discussed above proved the *Oh* number does not take into consideration the viscoelastic properties of polymeric solutions, did not study varying polymeric architectures, and few studies were conducted on thermal printheads. These studies found the polymeric solution in each architecture did not jet above their respective *C** values, indicating the thermal printhead process could not overcome the viscosity increase related to polymer chain overlap. This study also revealed a jettability *Oh* number ranged from 2 to above 15, which is consistent with other literature that the range of 1-10 does not hold for all binder compositions.

1.3 Water-soluble polymers for personalized dosage pharmaceuticals

Additive manufacturing (AM) of pharmaceuticals has the potential to provide patients with personalized dosage pharmaceuticals with tunable release profiles.[32,33] An estimated 75-85% of side-effects are a direct result of inaccurate dosing and pharmaceutical combinations because of varying weights and metabolic rates of patients.[34] To ameliorate this problem, researchers strive to use fuse filament fabrication, binder jetting, and selective laser sintering AM technologies to produce personalized dosage tablets, while also transforming the tablet and implant making process into a more time- and cost-efficient process.[35,36] In 2015, Aprecia Pharmaceuticals achieved FDA approval for additively manufactured tablets, called Spritam, using binder jetting AM.[37] The availability of commercially available printers and the opportunity to use existing excipients from compression molding tablet processes deem this AM method as advantageous for personalized dosage pharmaceuticals.

The three main AM technologies used to produce personalized dosage pharmaceuticals include fuse filament fabrication (FFF) , binder jetting (BJ), and selective

laser sintering (SLS) AM.[36] FFF uses heat to partially melt a polymer filament and extrude the material out of a nozzle to form 3D parts.[38] BJ is a powder bed-based system where an adhesive binder is jetted onto a powder surface to make layers. The adhesive used to bind the powder layers usually contains a polymeric binder, solvent, additives to tune solution properties, and often the active pharmaceutical ingredient (API) in certain applications.[36] SLS is also a powder bed-bed system where a laser heats layers on a build stage to form cohesive layers. Both FFF and SLS both use heat to form parts, which could prove problematic for API in the system. BJ suffers from low strength, which could prevent the achievable of different release rates. Because of these potential setbacks, researchers have been attempting to improve these systems to enable them viable for potential production of personalized dosage pharmaceuticals.[20,36]

AM of tablets has the potential to provide patients with personalized dosage pharmaceuticals with tunable release profiles. The main advantages of using AM to produce pharmaceuticals are control of API dosages, complex geometries enabling various release rates, the ability to deliver very small amount of API, and the reduction of waste.[32,39] Conventional tablet processing systems do not have the tunability capabilities of AM and thus could not provide patients with personalized dosage pharmaceuticals. Having AM machines in pharmacy offices will provide patients with personalized medicine that will reduce side-effects.[36]

Figure 1.3 depicts the futuristic system and medical processes that could enable personalized dosage pharmaceuticals produced using AM a reality. The process begins with the patient where futuristic data collection technology will track a patient's health. This data will then be transferred to the universal healthcare network, which can be

accessed by a team of healthcare professionals. The professionals can then write a prescription based on the results and send it directly to the pharmacy. Pharmacies with 3D printers will print the personalized dosage oral medications. These tablets will contain the exact amount of API to ensure no interactions with other APIs, which in turn will reduce side effects. This plan is ultimately futuristic and many policies would have to be put in place to enable this system, but the potential to make huge improvements to our current healthcare systems remains.[38]

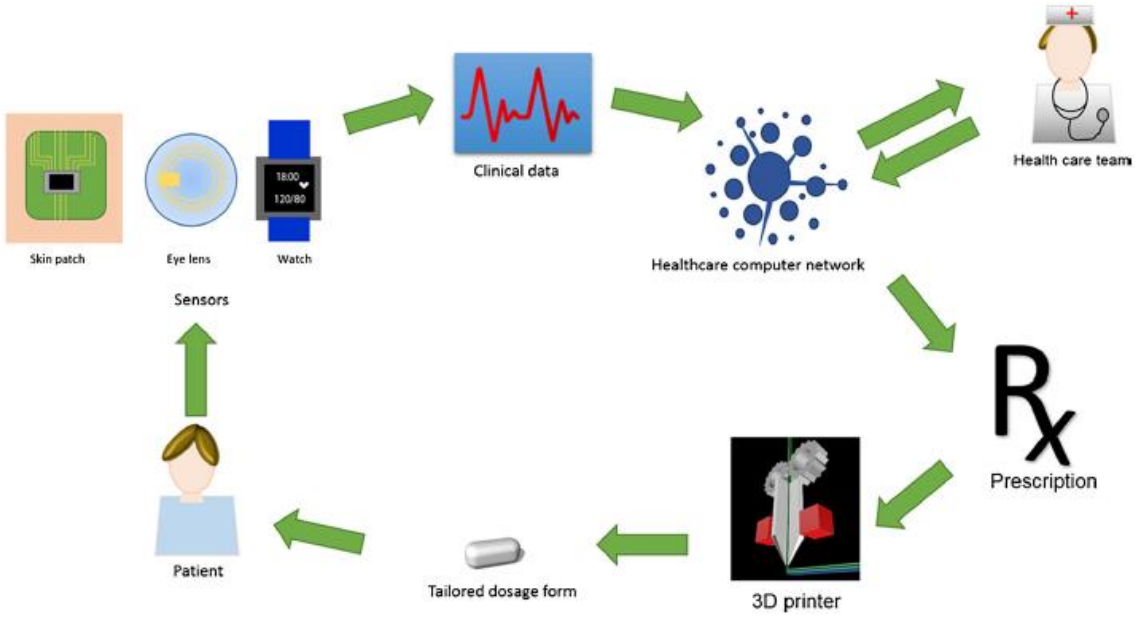

Figure 1.3. Futuristic medical and production process of personalized dosage pharmaceuticals. (Image reproduced from Alhnan *et al.*[38])

Delivering API in the form of implants is one of the major research areas in AM of personalized dosage pharmaceuticals. Tarcha *et al.* demonstrated API can be deposited in low doses onto stents using binder jetting printheads. They proved this method improved consistency of API and offered improved coating efficiency compared to conventional methods.[40] In another example, Sandler *et al.* coated catheters using inkjet printheads with nitrofurantoin, an antimicrobial. They used FFF to first fabrication PLA filaments and

structures, and the additional printhead to provide the coating.[41] Other examples include creating complex geometries with varied release rates based on shape and degradation speed and selective porous morphology through printing to tune dissolution or degradation.[36]

The other major research area in AM of personalized dosage pharmaceuticals research area is fabricating oral tablets to deliver API. Katstra *et al.* used binder jetting AM to demonstrate the production of low dose tablets, measuring about 0.34 ng of API per drop of binder. They also characterized physical properties to prove similar hardness and friability compared to compression modelled tablets.[39] Yu *et al.* fabricated one of the first zero-order release tablets using a combination of complex geometries and different binders to tune dissolution and release of the API.[33] Other applications include transdermal delivery systems, which are beginning to become popular in the literature.[36]

Two major unexplored areas in 3D printable personalized dosage pharmaceuticals are studying structure-property relationships between polymer structure and 3D part properties and the use of vat photopolymerization to print tablets. Polymers used for AM of this technologies are usually commercially available. Because of the limited exploration into novel polymer structures or novel architectures, the literature lacks in how these structural changes affect the printing process and the final 3D part properties.[12,16,17]

Another area that is lacking in the literature includes using vat photopolymerization for 3D printable personalized dosage pharmaceuticals. Vat photopolymerization is an AM technology that utilizes photo-active precursors in the form of a liquid and UV light is used to cure each layer. Using this method for medical applications can be problematic considering the UV light stability of APIs, toxicity of photo-active precursors, and toxicity

of photo-initiators. These problems are slowly being overcome in the literature with other medical applications such as tissue scaffolds.[12,42] This type of AM can greatly aid in increasing the speed of production as the new Carbon printer can print in seconds to minutes, in contract to the other AM technologies mentioned that print in minutes to hours. To make this technology a reality, the speed of production is one large hurdle that must be overcome.[43]

One area that 3D printable pharmaceuticals will not be advantageous is in the mass production of tablets and oral medication. Conventional tablet processing is completed using either wet or dry granulation of powders, and subsequent compression on a series of dies. This is a very economical system as companies have conveyor belts that compress pills within 500-50 ms per tablet.[44] In terms of mass production, binder jetting AM does not compare economically to the conventional process and at this stage would be very expensive. The binder jetting AM process takes about 20 minutes to print 10 tablets, 60 min of heating in the chamber, followed by an optimal vacuum dying step for 24 hours. In this amount of time, the conventional process could have produced hundreds of thousands of pills.[33]

Chapters 4, 7, 8, and 9 focus on employing VP and binder jetting AM platforms to produce personalized tissues scaffolds and personalized dosage pharmaceuticals. Chapter 5 focuses on PLGA-based photoactive precursors to produce degradable tissue scaffolds for exact sizes and shapes to suit patients' needs. Chapters 7, 8, and 9 use binder jetting to create personalized dosage pharmaceuticals. The tablets produced contained 5, 10, 25, and 50 wt % active pharmaceutical ingredient (API) in the powder bed. ^{1}H NMR spectroscopy

determined the API was evenly distributed around the tablet. Developing novel materials for all types of AM will eventually lead to personalized medicine for all.

1.4 New materials for powder bed fusion: particle formation through suspension polymerization

Powder bed fusion is a type of additive manufacturing where a laser selectively sinters or melts materials in a powder bed layer-by-layer. Once the laser irradiates the first layer, a roller spreads an even layer of powder over the build stage to prepare for the subsequent layer.[45,46] Using polymeric powders requires the consideration of three printability parameters, called the printability triad. Powder recoating, energy input, and cooling/coalescence function in concert to produce additively manufactured parts with high resolution and fidelity.[46,47]

Powder recoating depends on particle shape, size, flow, and the Hauser ratio. Ideally, powders with a spherical shape and average size ranging from 45 to 90 μm enable optimal flowability.[48] The Hauser ratio, the ratio between the tap and apparent density, determines the flowability where below 1.25 is considered ideal.[49] After determination of successful flowability, the bed temperature and energy input must be determined to induce effect interlayer adhesion and prevent curling on the edges. The "supercooling window" or the first derivative method determine the bed temperature, where both calculations choose a temperature slightly below the melting temperature. In crystalline polymers, this prevents the melted polymer layer from cooling quickly and producing curling. The energy input is then determined based on the polymer melting temperature and the degradation temperature, which are both determined using differential scanning calorimetry (DSC) and thermogravimetric analysis (TGA).[47,50] Cooling and coalescence depend on the zero-shear

viscosity and the cooling kinetics of the crystalline polymer at its melting temperature. The zero-shear viscosity must be low enough for the particles to coalesce, and the cooling process must be slow enough for interlayer adhesion to occur. **Figure 1.4** from Chatham *et al*. outlines the specific factors and optimal ranges for the printability triad.[46]

Summary of theoretical material properties for successful LS printing. * denotes values for nylon-12 for use as "known good," but should not be regarded as physical limit.

Powder Recoating	
Average particle diameter (d50)	45–90 μm
Percentage of fine (< 10 μm) particles	<5 %
alternatively, nano-roughness surface treatment	
Hausner Ratio	<1.25
Sphericity	>0.6
Avalanche Angle	5.25° *
Energy Input	
Heat of fusion	90 J/g *
Molecular motion resonance near laser wavelength	10.6 μm
Small temperature range for flow transition:	
Peak width at half max	5 °C *
Difference between onset and endset of melting	10 °C *
Stable molecular weight	EMRdeg » 1 Limited side reactions
Coalescence and Cooling	
Characteristic relaxation time	»1
Zero-shear viscosity to surface tension ratio	<1
Zero-shear viscosity	60 Pa·s *
Surface energy	35-40 mN/m *
Maximum out of plane curl	50 μm *

Figure 1.4. Theoretical printing parameters for powder bed fusion reproduced with permission from Chatham *et al.*[46]

Few polymers meet the powder standards for powder bed fusion because of the difficulty in processing spherical particles with a narrow size distribution. Some popular examples include Nylon-6[51], poly(phenylene sulfide)[47], and ultra-high molecular weight polyethylene[52]. Methods of developing spherical particles include grinding, solvent precipitation, and melt emulsification. Grinding polymeric powders produces undesired particle shape and size control, but can be useful if selective sieving is performed.[53] Solvent precipitation involves using a large volume of organic solvents and the solvent/polymer relationship must be thoroughly investigated before particle size is controlled.[54] Melt

emulsification produce spherical particles through melting a polymer in an incompatible solvent in the presence of an emulsifier to stabilize spherical particles.[55] This method is successful at controlled particle size and shape, but also can only be applied to few polymer systems. An alternative method of producing powders with narrow size distributions and spherical particles is discussed in Chapter 10.

Chapter 10 describes using suspension polymerization to produce spherical particles of poly(stearyl acrylate) for powder bed fusion. Suspension polymerization methods polymerizes non-dissolved monomer particles in water in the presence of a stabilizer. Stearyl acrylate and poly(vinyl alcohol) as a stabilizer was stirred at 400 rpm in water where a radical initiator polymerizes the particles. After the reaction is complete, lyophilization isolated the particles. The average particle sizes ranged from 10 to 180 μm with gel fractions around 60%. Because of the high gel fraction, neat poly(stearyl acrylate) exhibited a zero-shear viscosity of 2000 Pa·s. To lower this parameter, poly(stearyl acrylate) produced through free radical polymerization was added at the system at 50 wt %, which produced a zero-shear viscosity of 150.8 Pa·s. The ideal combination, 50:50 wt:wt, was printed using a Prodways ProMaker 2000HT machine printer to produce reproducible parts with high resolution.

1.5 References

(1) Herzberger, J.; Meenakshisundaram, V.; Williams, C. B.; Long, T. E. 3D Printing All-Aromatic Polyimides Using Stereolithographic 3D Printing of Polyamic Acid Salts. *ACS Macro Lett.* **2018**, *7* (4), 493–497. https://doi.org/10.1021/acsmacrolett.8b00126.

(2) Herzberger, J.; Sirrine, J. M.; Williams, C. B.; Long, T. E. Polymer Design for 3D Printing Elastomers: Recent Advances in Structure, Properties, and Printing. *Prog. Polym. Sci.* **2019**, *97*, 101144. https://doi.org/10.1016/j.progpolymsci.2019.101144.

(3) Sirrine, J. M.; Meenakshisundaram, V.; Moon, N. G.; Scott, P. J.; Mondschein, R. J.; Weiseman, T. F.; Williams, C. B.; Long, T. E. Functional Siloxanes with Photo-

Activated, Simultaneous Chain Extension and Crosslinking for Lithography-Based 3D Printing. *Polymer (Guildf).* **2018**, *152*, 25–34. https://doi.org/10.1016/j.polymer.2018.02.056.

(4) Appuhamillage, G. A.; Chartrain, N.; Meenakshisundaram, V.; Feller, K. D.; Williams, C. B.; Long, T. E. 10th Anniversary: Vat Photopolymerization-Based Additive Manufacturing: Current Trends and Future Directions in Materials Design. **2019**. https://doi.org/10.1021/acs.iecr.9b02679.

(5) Gibson, I.; Rosen, D.; Stucker, B.; Gibson, I.; Rosen, D.; Stucker, B. Vat Photopolymerization Processes. In *Additive Manufacturing Technologies*; Springer New York, 2015; pp 63–106. https://doi.org/10.1007/978-1-4939-2113-3_4.

(6) Huang, Y.; Leu, M. C.; Mazumder, J.; Donmez, A. Additive Manufacturing: Current State, Future Potential, Gaps and Needs, and Recommendations. *J. Manuf. Sci. Eng. Trans. ASME* **2015**, *137* (1). https://doi.org/10.1115/1.4028725.

(7) Lee, J.-Y.; An, J.; Chua, C. K. Fundamentals and Applications of 3D Printing for Novel Materials. *Appl. Mater. Today* **2017**, *7*, 120–133. https://doi.org/10.1016/J.APMT.2017.02.004.

(8) Pan, Y.; Zhou, C.; Chen, Y. A Fast Mask Projection Stereolithography Process for Fabricating Digital Models in Minutes. *J. Manuf. Sci. Eng. Trans. ASME* **2012**, *134* (5). https://doi.org/10.1115/1.4007465.

(9) Huang, Y. M.; Kuriyama, S.; Jiang, C. P. Fundamental Study and Theoretical Analysis in a Constrained-Surface Stereolithography System. *Int. J. Adv. Manuf. Technol.* **2004**, *24* (5–6), 361–369. https://doi.org/10.1007/s00170-003-1627-9.

(10) Sun, A. X.; Lin, H.; Beck, A. M.; Kilroy, E. J.; Tuan, R. S. Projection Stereolithographic Fabrication of Human Adipose Stem Cell-Incorporated Biodegradable Scaffolds for Cartilage Tissue Engineering. *Front. Bioeng. Biotechnol.* **2015**, *3*, 115. https://doi.org/10.3389/fbioe.2015.00115.

(11) Schmidleithner, C.; Kalaskar, D. M. Stereolithography. In *3D Printing*; InTech, 2018. https://doi.org/10.5772/intechopen.78147.

(12) Pekkanen, A. M.; Mondschein, R. J.; Williams, C. B.; Long, T. E. 3D Printing Polymers with Supramolecular Functionality for Biological Applications. **2017**. https://doi.org/10.1021/acs.biomac.7b00671.

(13) Sirrine, J. M.; Schexnayder, S. A.; Dennis, J. M.; Long, T. E. Urea as a Monomer for Isocyanate-Free Synthesis of Segmented Poly(Dimethyl Siloxane) Polyureas. *Polymer (Guildf).* **2018**, *154*, 225–232. https://doi.org/10.1016/J.POLYMER.2018.09.003.

(14) Wilts, E. M.; Herzberger, J.; Long, T. E. Addressing Water Scarcity: Cationic Polyelectrolytes in Water Treatment and Purification. *Polym. Int.* **2018**, *67* (7). https://doi.org/10.1002/pi.5569.

(15) Radhakrishnan, J.; Subramanian, A.; Krishnan, U. M.; Sethuraman, S. Injectable and 3D Bioprinted Polysaccharide Hydrogels: From Cartilage to Osteochondral Tissue Engineering. *Biomacromolecules* **2017**, *18* (1), 1–26. https://doi.org/10.1021/acs.biomac.6b01619.

(16) Pekkanen, A. M.; Zawaski, C.; Stevenson, A. T.; Dickerman, R.; Whittington, A. R.; Williams, C. B.; Long, T. E. Poly(Ether Ester) Ionomers as Water-Soluble Polymers for Material Extrusion Additive Manufacturing Processes. *ACS Appl. Mater. Interfaces* **2017**, *9* (14), 12324–12331. https://doi.org/10.1021/acsami.7b01777.

(17) Sirrine, J. M.; Pekkanen, A. M.; Nelson, A. M.; Chartrain, N. A.; Williams, C. B.; Long, T. E. 3D-Printable Biodegradable Polyester Tissue Scaffolds for Cell Adhesion. *Aust. J. Chem.* **2015**, *68* (9), 1409. https://doi.org/10.1071/CH15327.

(18) Mao, Y.; Miyazaki, T.; Sakai, K.; Gong, J.; Zhu, M.; Ito, H. A 3D Printable Thermal Energy Storage Crystalline Gel Using Mask-Projection Stereolithography. *Polymers (Basel).* **2018**, *10* (10), 1117. https://doi.org/10.3390/polym10101117.

(19) Tulig, T. J.; Tirrell, M. Toward a Molecular Theory of the Trommsdorff Effect. *Macromolecules* **1981**, *14* (5), 1501–1511. https://doi.org/10.1021/ma50006a070.

(20) Goole, J.; Amighi, K. 3D Printing in Pharmaceutics: A New Tool for Designing Customized Drug Delivery Systems. *Int. J. Pharm.* **2016**, *499* (1–2), 376–394. https://doi.org/10.1016/J.IJPHARM.2015.12.071.

(21) Binder Jetting - Additively https://www.additively.com/en/learn-about/binder-jetting (accessed Nov 14, 2019).

(22) Reis, N.; Ainsley, C.; Derby, B. Ink-Jet Delivery of Particle Suspensions by Piezoelectric Droplet Ejectors. *J. Appl. Phys.* **2005**, *97* (9), 094903. https://doi.org/10.1063/1.1888026.

(23) Friederich, A.; Binder, J. R.; Bauer, W. Rheological Control of the Coffee Stain Effect for Inkjet Printing of Ceramics. *J. Am. Ceram. Soc.* **2013**, *96* (7), 2093–2099. https://doi.org/10.1111/jace.12385.

(24) Derby, B. Inkjet Printing Ceramics: From Drops to Solid. *J. Eur. Ceram. Soc.* **2011**, *31* (14), 2543–2550. https://doi.org/10.1016/J.JEURCERAMSOC.2011.01.016.

(25) Jang, D.; Kim, D.; Moon, J. Influence of Fluid Physical Properties on Ink-Jet Printability. *Langmuir* **2009**, *25* (5), 2629–2635. https://doi.org/10.1021/la900059m.

(26) Özkol, E.; Ebert, J.; Telle, R. An Experimental Analysis of the Influence of the Ink Properties on the Drop Formation for Direct Thermal Inkjet Printing of High Solid Content Aqueous 3Y-TZP Suspensions. *J. Eur. Ceram. Soc.* **2010**, *30* (7), 1669–1678. https://doi.org/10.1016/J.JEURCERAMSOC.2010.01.004.

(27) Hoath, S. D.; Hutchings, I. M.; Martin, G. D.; Tuladhar, T. R.; Mackley, M. R.;

Vadillo, D. Links Between Ink Rheology, Drop-on-Demand Jet Formation, and Printability. *J. Imaging Sci. Technol.* **2009**, *53* (4), 041208. https://doi.org/10.2352/J.ImagingSci.Technol.2009.53.4.041208.

(28) Sunthar, P. Polymer Rheology. In *Rheology of Complex Fluids*; Springer New York, 2010; pp 171–191. https://doi.org/10.1007/978-1-4419-6494-6_8.

(29) Chhabra, R. P. Non-Newtonian Fluids: An Introduction BT - Rheology of Complex Fluids; Krishnan, J. M., Deshpande, A. P., Kumar, P. B. S., Eds.; Springer New York, 2010; pp 3–34. https://doi.org/10.1007/978-1-4419-6494-6_1.

(30) Vadillo, D. C.; Tuladhar, T. R.; Mulji, A. C.; Jung, S.; Hoath, S. D.; Mackley, M. R. Evaluation of the Inkjet Fluid's Performance Using the "Cambridge Trimaster" Filament Stretch and Break-up Device. *J. Rheol. (N. Y. N. Y).* **2010**, *54* (2), 261–282. https://doi.org/10.1122/1.3302451.

(31) Clasen, C.; Plog, J. P.; Kulicke, W.-M.; Owens, M.; Macosko, C.; Scriven, L. E.; Verani, M.; McKinley, G. H. How Dilute Are Dilute Solutions in Extensional Flows? *J. Rheol. (N. Y. N. Y).* **2006**, *50* (6), 849–881. https://doi.org/10.1122/1.2357595.

(32) Moulton, S. E.; Wallace, G. G. 3-Dimensional (3D) Fabricated Polymer Based Drug Delivery Systems. *J. Control. Release* **2014**, *193*, 27–34. https://doi.org/10.1016/J.JCONREL.2014.07.005.

(33) Yu, D. G.; Zhu, L.-M.; Branford-White, C. J.; Yang, X. L. Three-Dimensional Printing in Pharmaceutics: Promises and Problems. *J. Pharm. Sci.* **2008**, *97* (9), 3666–3690. https://doi.org/10.1002/jps.21284.

(34) Cohen, J. S. Ways to Minimize Adverse Drug Reactions. *Postgrad. Med.* **1999**, *106* (3), 163–172. https://doi.org/10.3810/pgm.1999.09.688.

(35) Raijada, D.; Genina, N.; Fors, D.; Wisaeus, E.; Peltonen, J.; Rantanen, J.; Sandler, N. A Step Toward Development of Printable Dosage Forms for Poorly Soluble Drugs. *J. Pharm. Sci.* **2013**, *102* (10), 3694–3704. https://doi.org/10.1002/JPS.23678.

(36) Prasad, L. K.; Smyth, H. 3D Printing Technologies for Drug Delivery: A Review. *Drug Dev. Ind. Pharm.* **2016**, *42* (7), 1019–1031. https://doi.org/10.3109/03639045.2015.1120743.

(37) rebuffs Monsanto, S. First 3D-Printed Pill. *Nature* **2015**, *33*, 1014.

(38) Alhnan, M. A.; Okwuosa, T. C.; Sadia, M.; Wan, K.-W.; Ahmed, W.; Arafat, B. Emergence of 3D Printed Dosage Forms: Opportunities and Challenges. *Pharm. Res.* **2016**, *33* (8), 1817–1832. https://doi.org/10.1007/s11095-016-1933-1.

(39) Katstra, W. .; Palazzolo, R. .; Rowe, C. .; Giritlioglu, B.; Teung, P.; Cima, M. . Oral Dosage Forms Fabricated by Three Dimensional Printing™. *J. Control. Release* **2000**, *66* (1), 1–9. https://doi.org/10.1016/S0168-3659(99)00225-4.

(40) Tarcha, P. J.; Verlee, D.; Hui, H. W.; Setesak, J.; Antohe, B.; Radulescu, D.; Wallace, D. The Application of Ink-Jet Technology for the Coating and Loading of Drug-Eluting Stents. *Ann. Biomed. Eng.* **2007**, *35* (10), 1791–1799. https://doi.org/10.1007/s10439-007-9354-2.

(41) Sandler, N.; Salmela, I.; Fallarero, A.; Rosling, A.; Khajeheian, M.; Kolakovic, R.; Genina, N.; Nyman, J.; Vuorela, P. Towards Fabrication of 3D Printed Medical Devices to Prevent Biofilm Formation. *Int. J. Pharm.* **2014**, *459* (1–2), 62–64. https://doi.org/10.1016/j.ijpharm.2013.11.001.

(42) Mondschein, R. J.; Kanitkar, A.; Williams, C. B.; Verbridge, S. S.; Long, T. E. Polymer Structure-Property Requirements for Stereolithographic 3D Printing of Soft Tissue Engineering Scaffolds. *Biomaterials* **2017**, *140*, 170–188. https://doi.org/10.1016/J.BIOMATERIALS.2017.06.005.

(43) Wang, J.; Goyanes, A.; Gaisford, S.; Basit, A. W. Stereolithographic (SLA) 3D Printing of Oral Modified-Release Dosage Forms. *Int. J. Pharm.* **2016**, *503* (1–2), 207–212. https://doi.org/10.1016/j.ijpharm.2016.03.016.

(44) The Colorful History of Pills Can Fill Many a Tablet - Los Angeles Times https://www.latimes.com/archives/la-xpm-2002-mar-25-he-booster25-story.html (accessed Nov 16, 2019).

(45) Bhavar, V.; Kattire, P.; Patil, V.; Khot, S.; Gujar, K.; Singh, R. A Review on Powder Bed Fusion Technology of Metal Additive Manufacturing. In *Additive Manufacturing Handbook*; CRC Press, 2017; pp 251–253. https://doi.org/10.1201/9781315119106-15.

(46) Chatham, C. A.; Long, T. E.; Williams, C. B. A Review of the Process Physics and Material Screening Methods for Polymer Powder Bed Fusion Additive Manufacturing. *Progress in Polymer Science*. Elsevier Ltd June 1, 2019, pp 68–95. https://doi.org/10.1016/j.progpolymsci.2019.03.003.

(47) Chatham, C. A.; Long, T. E.; Williams, C. B. Powder Bed Fusion of Poly(Phenylene Sulfide)at Bed Temperatures Significantly below Melting. *Addit. Manuf.* **2019**, *28*, 506–516. https://doi.org/10.1016/j.addma.2019.05.025.

(48) Rapid Prototyping: Laser-based and Other Technologies - Patri K. Venuvinod, Weiyin Ma - Google Books https://books.google.com/books?hl=en&lr=&id=HM3eBwAAQBAJ&oi=fnd&pg=PR11&ots=TUu5G_E_5z&sig=PWWHgjjO-q1TkeV5g2DaiqsZ1tM#v=onepage&q&f=false (accessed Nov 9, 2019).

(49) Zou, R. P.; Yu, A. B. Evaluation of the Packing Characteristics of Mono-Sized Non-Spherical Particles. *Powder Technol.* **1996**, *88* (1), 71–79. https://doi.org/10.1016/0032-5910(96)03106-3.

(50) Hopmann, C.; Kreimeier, S. Modelling the Heating Process in Simultaneous Laser

Transmission Welding of Semicrystalline Polymers. *J. Polym.* **2016**, *2016*, 1–10. https://doi.org/10.1155/2016/3824065.

(51) Telenko, C.; Seepersad, C. C. A Comparison of the Energy Efficiency of Selective Laser Sintering and Injection Molding of Nylon Parts. *Rapid Prototyp. J.* **2012**, *18* (6), 472–481. https://doi.org/10.1108/13552541211272018.

(52) Khalil, Y.; Hopkinson, N.; Kowalski, A.; Fairclough, J. P. A. Characterisation of UHMWPE Polymer Powder for Laser Sintering. *Materials (Basel).* **2019**, *12* (21), 3496. https://doi.org/10.3390/ma12213496.

(53) Schmid, M.; Amado, A.; Wegener, K. Polymer Powders for Selective Laser Sintering (SLS). In *AIP Conference Proceedings*; American Institute of Physics Inc., 2015; Vol. 1664. https://doi.org/10.1063/1.4918516.

(54) *686 B2 1. PROCESS FOR THE MANUFACTURE OF POLYAMIDE-12 POWDER WITH A HIGH MELTING POINT*.

(55) Schmidt, J.; Sachs, M.; Fanselow, S.; Wirth, K.-E.; Peukert, W. *NOVEL APPROACHES FOR THE PRODUCTION OF POLYMER POWDERS FOR SELECTIVE LASER BEAM MELTING OF POLYMERS*.

Chapter 2: Addressing Water Scarcity: Cationic Polyelectrolytes in Water Treatment and Purification

Emily M. Wilts, Jana Herzberger, and Timothy E. Long*

(Published in *Polymer International* **2018**, 67 (7), 799-814)

Department of Chemistry, Macromolecules Innovation Institute, Virginia Tech, Blacksburg, VA 24061

Keywords: wastewater treatment, water purification, cationic polyelectrolytes, flocculation, coagulation

2.1 Abstract

Synthetic cationic polyelectrolytes (CPE) serve as coagulation and flocculation agents in wastewater treatment due to a synergy of inherent electrostatic interactions and hydrophilic properties. In wastewater treatment, CPEs act as coagulation and flocculation agents to aggregate impurities and enable water purification. New health and environmental-related regulations provide motivation for government agencies and industrial companies to reuse wastewater. Chemical structure, molecular weight, charge density, and functionality of CPEs provide tailorability for specific purification needs. Cationic polyacrylamides, ammonium-based polymers, poly(allyldimethyl-ammonium chloride), and epichlorohydrin/dimethylamine-based polymers are the most common CPEs used as coagulation and flocculation agents because they are economical and water-soluble with tunable charge densities at high molecular weights. Free radical polymerization, step-growth polymerization, and post-polymerization modification methods afford each polymer system. This review highlights recent advancements in synthetic methods to yield CPEs, structure-property relationships as related to flocculation efficiency, and a summary of their toxicity and environmental impact.

2.2 Introduction

In this review, we elaborate recent advances in CPE synthetic methods used for several types of water treatment and characterization techniques of both CPEs and aggregated impurities. CPEs effectively coagulate and flocculate impurities in wastewater from human usage and mining, papermill, textile, and farming industries. They also exhibit anti-fouling and anti-bacterial properties, which prevent biological growth throughout the purification process. While reviews on synthetic methods of CPEs used for flocculation are sparse, several recently published reviews discuss polymer flocculation of natural organic material, soluble dyes, contaminants in oil sands tailings ponds, and contaminants in papermill wastewater.[1-5] Additional reviews elaborate the physics and dynamics of polymer flocculation mechanisms, natural cationic polymers, and anionic polymers for flocculation in water treatment.[6-9] In the concluding section, we discuss future directions of the field and potential novel polymers for water treatment from a polymer chemistry perspective.

CPEs are polymers with positively charged moieties and anionic counterions present on each repeating unit or a large portion of units.[10-12] Common groups of CPEs include polymers with ammonium, phosphonium, and imidazolium groups.[13-14] CPE systems exhibit physical crosslinks through electrostatic interactions, often called supramolecular interactions. Electrostatic interactions are not as strong as covalent bonds, yet they enable higher thermal transitions and better mechanical properties compared to non-ionic polymers. The tailorability of CPEs is well-documented; tuning molecular weight, positively charged moiety, anionic counterion or charge density afford CPEs for various applications.[15-16] For example, CPEs are used for water treatment, anti-microbial

materials, and non-viral gene delivery. Our group previously synthesized and studied ammonium, phosphonium, imidazolium, and zwitterion-containing polymers for non-viral gene-delivery and to uncover structure-property relationships. We demonstrated multiple post-polymerization methods to modify amines, phosphines, and imidazoles with alkyl-halides to achieve cationic groups with tailored charge density and other properties.[13, 17-18] These same synthetic methods tailor CPE flocculation and coagulation efficiency and are thus used for water treatment purposes.

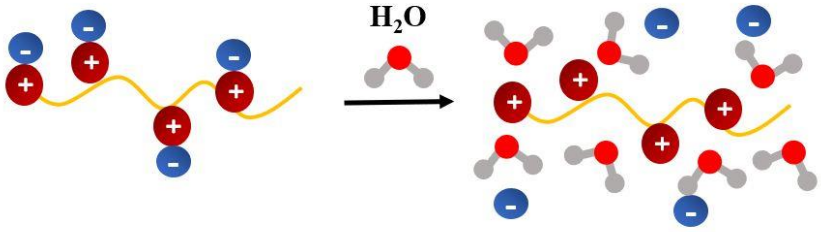

Scheme 2.1. CPE in its pure state (left) and in water where dissociation of the counterion occurs. (right).

Polymers for flocculation and coagulation in water treatment are water-soluble to allow interactions with impurities. Depending on solvent and pH, the positively charged moiety and anionic counterions dissociate, thus enabling the polymer backbone to repel itself, adopting a ridged-rod conformation, and allowing interactions with other negatively charges materials. **Scheme 2.1** depicts the dissociation of counterions from a CPE backbone in the presence of water. The electropositive hydrogens in water attract the anionic counterions and the electronegative oxygen attracts the positively charged backbone, which promotes dissociation. The degree of the dissociation depends on the pH of the water. CPEs have an optimal pH when the salt most strongly dissociates, leaving the

strongest electrolyte possible. The addition of salts to a CPE-containing solution allows screening of the cationic charges and the polymer will adopt a random coil conformation, which is typical for non-ionic polymers.[19-20]

Synthetic CPEs function as primary flocculants and secondary coagulation aids and perform better compared to inorganic salts and natural cationic polyelectrolytes, which also serve as primary flocculants. CPEs offer stable and filterable aggregated impurities, which improves water quality and reduces production costs. Compared to inorganic salt coagulation, CPE systems result in less dissolved solids in the final product and require an average of 90 wt% less polymer dosage to achieve the same flocculation efficiencies. Natural CPEs offer biodegradable properties, but require higher dosages compared to synthetic CPEs. Some disadvantages of synthetic CPE flocculation agents include a narrow optimal dosage range, potential toxic monomer contamination, and non-biodegradability. In general, the advantages of synthetic CPE flocculation agents outweigh natural CPEs, therefore the majority of impurity flocculation in wastewater utilizes synthetic CPE flocculants.[21-22]

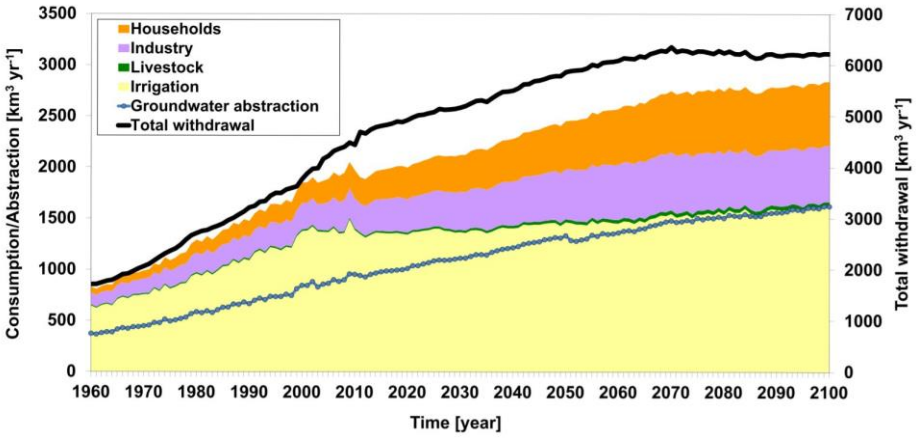

Figure 2.1. Nonrenewable water consumption/abstraction (left-axis) and total withdrawal (right-axis) from 1960 to 2100. (Adapted from Wada *et. al.*[23])

Fresh and saline-water are essential in industry, farming, and everyday life. In 2010, the United States withdrew 355 billion gallons of water constituting 14 % saline-water and 86 % fresh-water. Thermoelectric power, irrigation, and public supply are among the largest consumers of water comprising 45 %, 33 %, and 12 % usage, respectively.[24] The use of fresh- or saline-water in industrial processes leads to contamination through the industrial process itself or through contaminates in nature after it is discarded. Due to new regulations, cost efficiency, and environmental impacts, industry and government are moving towards purifying their wastewater for reuse.[25] Recently, Wada, Bierkens *et. al.* developed a new model to predict water reserves around the world until 2100 called the blue water sustainability index (B1WSI), which accounts for nonrenewable groundwater and non-sustainable water use. Depicted in **Figure 2.1**, total water withdraws will continue to increase ~20 % from now until 2100 to meet the increasing demands of our expanding population. Relying on nonrenewable water sources will lead to hindered crop production around the world.[23] Wastewater reuse is one method currently employed to help preserve water sources around the world.

2.3 Contaminated wastewater types

An average American in the United States produces an estimated 50-60 gallons of wastewater per day through domestic use and wastewater produced from food, fuel, and consumer products.[24] Depending on the type of water, e.g. fresh or saline, and how the water was used, wastewater contaminates vary between natural material and biological

growth to heavy metals and synthetic pollutants. Consequently, each wastewater type requires tailored purification steps.

The most abundant contaminant in wastewater and drinking water supplies is natural organic material (NOM). NOMs are present in water reservoirs and wells, which are the most common storage methods for drinking water. NOMs are either aquagenic, originating from water, or pedogenic, originating from soil. Geological and ecological systems combined with weather patterns, such as floods and droughts, govern the types of NOMs present in water sources. Typical sources of NOM include decaying plants, plant trimmings, and animal manure, which leach organic materials such as biopolymers, carbohydrates, and proteins.[26-27] Removal of NOMs prevent unfavorable water properties, such as odor and color, presence of heavy metals that travel with NOM, and increased probability of biological growth.[1, 28] The most effective method of purification depends on the quantity and quality of NOMs in contaminated water. Flocculation, sedimentation, and sand filtration of contaminated water offer an economically conscience method of NOM and other impurity removal.

Treated blackwater/sludge water or raw sewage provides another reusable water source used for irrigation, industrial cooling towers, and toilet water. Sewage wastewater is separated into two groups; greywater contains water from sinks, showers, kitchen, and laundry applications where blackwater refers to flushed toilet water containing feces, urine, and toilet paper.[29] People around the world produce billions of gallons of sewage wastewater daily and most towns and cities have multiple sewage treatment facilities. Blackwater comprises less volume in sewage wastewater but poses the highest health risk, and therefore requires more complex and stringent purification methods such as anaerobic

treatment systems and UV light sterilization to eliminate pathogens. Greywater constitutes 70 % of sewage water and is the most promising for purification and reuse. Constructed wetlands store and decontaminate greywater providing high capacity and method simplicity while producing water for industrial processes. Local sewage treatment plants commonly resupply lakes and rivers with decontaminated water from nearby wetlands and sell or donate solid organic material to farmers for fertilizers.[30-31]

Wastewater from textile industries represents one of the most difficult types of water to purify. The complexity of compounds in the latter, such as dyes, heavy metals, dispersing agents, and surfactants complicates treatment methodology and requires a multi-step purification process. Soluble dyes contain carcinogenic material and heavy metals, which are problematic for the environmental, human, animal, and aquatic life health. Dyes also add color to surface water, which disrupts the biosphere by preventing light from entering underlying soil.[6, 32] Currently, nanofiltration is predominately used to remove soluble dyes but this method lacks anti-fouling capabilities. To reduce the risk of biological growth during the purification process, additives such as cationic, anionic, or natural polymers are required in the flocculation process.[2] Due to the complicated processes associated with treating this specific wastewater, textile industries treat wastewater in-house for other industrial processes.

The paper-making process produces an estimated 20-60 k gallons of wastewater per ton of final product with pollutants ranging from biomolecules to organic solvents.[33] The process begins with the removal of dirt and debris from wood pulp, which is subsequently boiled and washed for bleaching. After the pulp bleaching and a series of treatments using inorganic dyes and organic compounds, manipulation of the processed

pulp through molds and wires creates the final paper product.[4] Wastewater pollutants from this process cause water discoloration, promote slime growth, and have toxic effects on local aquatic life. Due to government regulations, wastewater from pulp and paper-making processes must meet certain standards before releasing water into the environment. CPEs do not function as primary flocculation agents, but serve as secondary or tertiary coagulants to remove organic materials and inorganic dyes in papermill wastewater.[34]

Wastewater from mining represents another challenge for water purification. Specifically, kaolin clay is a major contaminate in mining wastewater, and bitumen extraction produces wastewater called oil sands tailings. Kaolin clay originates from the mineral kaolinite, which is abundant near mining sites. Kaolin clay suspensions have turbidities of 360 Nephelometric Turbidity Units (NTU), a pH of 5 in solution on average, and contains mostly negatively charged particles. These properties enable CPEs to effectively flocculate kaolin clay particles and remove them from the treated water system.[35] Canada has 141,000 square kilometers of bitumen reserves, which is equivalent to 177 billion barrels of crude oil after harvesting. Hot water, 2.5 m^3 per barrel of bitumen, separates the bitumen from sand and other oils present in the reserves. After 90 % of bitumen extraction, millions of gallons of wastewater containing fine clay suspensions remain. Polyacrylamide (PAM) and cationic polyacrylamide (CPAM) flocculate the fine clay suspensions to recover and reuse wastewater from oil sands tailings.[3]

While the four described types of contaminated waters are flocculated and subsequently discarded or repurposed, CPEs are also used for harvesting microalgae, an important source for biodiesel, oils, and other biological materials.[36] Biodiesel is a renewable energy source that serves as a replacement for fossil fuels, but the current

harvesting process is expensive and commercially impractical. Ferric, magnesium, and calcium salts provide flocculation of microalgae as an alternative chemical flocculation process, but only when used in significant bulk. CPEs flocculate microalgae cultured in freshwater with a lower dosage and create more stable aggregated cells. Salts present in marine microalgae harvesting inhibit CPE flocculation due to charge screening and thus do not successfully aggregate the microalgae cells. CPEs flocculate microalgae effectively because the algae have negative surface charges. After screening CPEs to ensure they are not toxic to the microalgae, harvesting with CPE flocculation currently uses little energy and is time efficient compared to conventional methods. [37-38]

2.4 Flocculation and coagulation mechanisms

Flocculation and coagulation are similar processes, but differ in the aggregation mechanisms.[39] Flocculation occurs when a polymer absorbs to multiple particle surfaces and therefore aggregates the material.[40] The resulting aggregates are commonly called flocs. A change in temperature, pH, or charge enables coagulation where particles aggregate together.[41-43] A review by Bolto *et. al.*[6] provides an in-depth explanation of the polymer physics and dynamics of polymer flocculation mechanisms.

Polymer bridging is a well-established mechanism for CPE flocculation of impurities.[41] Bridging occurs when high molecular weight ($> 10^7$ g mol^{-1}) CPEs absorb to the surface of several particles, which binds the particles together through electrostatic forces and leads to the formation of a floc.[42] **Figure 2.2A** depicts an example of polymer bridging where two CPE chains interact with three particles and cause aggregation. This type of flocculation requires an optimal dose of CPE within a certain charge density range to achieve the highest flocculation efficiency (FE). For example, Figure **2.2B** depicts an

effect called restabilization, which occurs when there is an excess of positively charged species (e.g. CPEs) in the system than negatively charged sites on the particles preventing the CPE from binding multiple particles. Successful CPE flocculation through polymer bridging depends strongly on molecular weight and dosage.[6, 44]

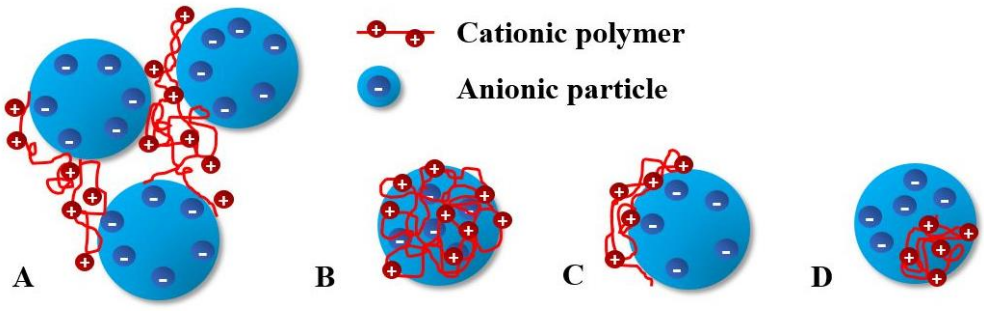

Figure 2.2. Different types of coagulation and flocculation mechanisms of cationic polyelectrolytes; (A) polymer bridging, (B) restabilization, (C) charge neutralization, (D) electrostatic patch.[6]

An alternative coagulation mechanism is charge neutralization, the primary mechanism of low molecular weight and high charge density CPEs. **Figure 2.2C** depicts charge neutralization where CPEs bind with negatively charged particles thus neutralizing the total charge of the system. This mechanism limits the repulsion between negatively charged particles allowing coagulation. **Figure 2.2D** depicts an electrostatic patch, a type of charge neutralization in which the CPE acts as a patch on the particle surface, limiting repulsion between particles. An electrostatic patch differs from general charge neutralization because it applies an overall charge neutralization of the particle, but negatively charged sites remain due to the small surface area coverage of the CPE. This enables other particles to absorb to the patches, thus increasing flocculation efficiency (FE).

Zeta potential of the wastewater and flocculation agent solution confirms if charge neutralization is occurring. A zeta potential of around 0 ± 0.1 mv implies a neutral solution charge, which indicates the cationic groups neutralized the anionic particles thus enabling them to coagulate.[6, 45-46]

Molecular weight and charge density are essential factors in polymer bridging and charge neutralization flocculation mechanisms.[47] Forming stable flocs from polymer bridging require molecular weights over one million g mol^{-1}.[48] This molecular weight range allows the polymer chains to bind to multiple particles. Researchers studied polymers with different architectures, e.g. linear vs. graft polymers to compare effects on particle flocculation. Another determining factor is the charge density of the CPE where a range of 10-30 % charge density enables binding while preventing particle restabilization. Charge densities above 30 % not only cause restabilization, but also have potential to start repelling particles. This range is also important because of the complex composition of wastewater where particles are neutral, positively, and negatively charged.[6, 49] Many other factors affect floc formation such as pH of the wastewater and hydrophobicity/hydrophilicity of the CPE. As discussed previously, CPEs dissociate depending on the pH of the system thus enabling a stronger or weaker electrolyte. Stronger electrolytes contain more potential to bind particles thus creating denser and more stable flocs. Other factors include order and speed of addition of CPE into the wastewater and particle size of impurities.[50]

Flocculation and coagulation agents play a role in the typical water purification process, depicted in **Figure 2.3**. The process begins at step A where a coagulation or flocculation agent enters the contaminated water system. The contaminated water and coagulation agent rapidly mix until coagulation occurs. Step B involves slow mixing where

the aggregated particles form flocs. This mixture moves to a sedimentation tank, step C, where the flocs settle to the bottom of the tank and the water is syphoned off the top. At step D a filtering system separates the purified water from flocs or other unwanted particles. The process ends at step E, where the purified water is disinfected and stored for later use.[25] This process provides the optimal conditions to remove as much undesired material as possible.[51] For different types of contaminated waters, industries may add additional steps, not included in the figure below, to remove specialized impurities.[49, 52]

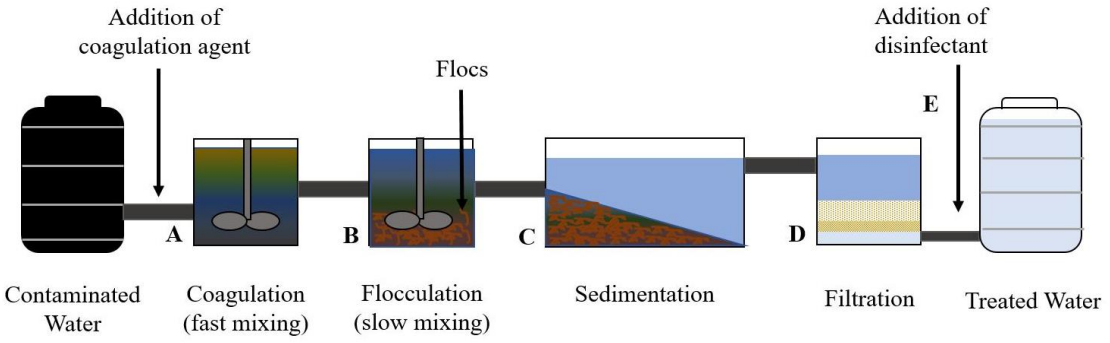

Figure 2.3. Typical purification process of contaminated water; (A) coagulation, (B) flocculation, (C) sedimentation, (D) filtration, (E) disinfection and storage.

2.5 Characterization

Molecular weight and charge density are the most important properties of CPEs for flocculation in wastewater treatment, as discussed previously. Determining molecular weight of CPEs remains challenging due to the ionic interactions. Scientists measured relative molecular weight using intrinsic viscosity and light scattering. Alternatively, size exclusion chromatography (SEC) measures relative molecular weights where aqueous SEC is the most popular; however, SEC is challenging because of electrostatic interactions the affects hydrodynamic radius of the polyelectrolyte.[53] Because SEC uses hydrodynamic

radius to determine molecular weight, SEC cannot determine absolute molecular weight alone.[54] In a study of ultra-high molecular weight cationic polyacrylamide ($10^8 – 10^9$ g mol^{-1}), Woo, Moon *et. al.* employed field-flow fractionation, multi-angle laser light scattering (MALLS) and differential refractive index to determine molecular weight. In this case, SEC was not used because of the lack of columns with the appropriate pore sizes to measure ultra-high molecular weight polymers.[55] Our group previously used a combination of aqueous SEC and MALLS to determine absolute molecular weight of 12,12- and 6,12-ammonium-based polyelectrolytes. The development of an aqueous SEC mobile phase avoided electrostatic interactions and aggregation. A combination of water/methanol/acetic acid, 54/23/23, v/v/v at 0.54 M sodium acetate and a pH of 4.0 served as a SEC solvent which not only prevented aggregates, but also delivered reproducible molecular weight data.[56]

Charge density of CPEs is an important property for flocculation and coagulation[57] where different post-polymerization modification methods or the choice of monomer controls charge density.[58] For example, synthesizing copolymers with one charged and one neutral monomer controls charge density depending on monomer ratio. Post-polymerization modification also affords controlled charge density. For example, Allen et. al polymerized poly(1-vinylimidizole) and subsequently quaternized the imidazole units with 2-bromoethanol to control charge density and its effect on DNA binding for non-viral gene delivery.[59]

A technique called colloid titration is the most accepted method to determine charge density of CPEs.[6] This technique is based on the stoichiometric interactions between CPEs and oppositely charged materials. Kam, Gregory *et. al.* established this method and used

an anionic polyelectrolyte, potassium polyvinyl sulfate, and three types of end-point detectors to perform a colloid titration. Two methods involve the visual and spectrophotometric determination of the color change induced by a cationic dye, *o*-toluidine blue. The third method used a streaming current detector to monitor electrokinetic detection of charge neutralization. At lower charge density (below 10 %), visual indication of color changed was deemed unreliable, but the other two methods were in agreement for charge density determination across all ranges.[60]

Before testing FE, a standard mixing, floc forming apparatus and procedure called a jar test ensures reproducible stirring conditions. A jar test contains several beakers and mixes the wastewater and flocculation agent together at two different speeds, e.g. 120 and 40 rpm, respectively, which closely resembles flocculation procedures in treatment plants.[61] To evaluate FE after this process, researchers employ multiple methods such as dewatering, turbidity, and remaining solids depending on the contaminate.

2.6 Synthesis and characterization of types of polymers used for wastewater treatment

2.6.1 Polyacrylamides and copolymers

Cationic polyacrylamides (CPAM) and polyacrylamide (PAM) copolymers serve as effective flocculation agents and coagulant aids owing to their water-solubility, low-cost, and high molecular weight.[62-66] CPAM consists of neutral PAM segments and segments containing charged ammonium moieties.[67] PAM is also a common polymer used for flocculation because it is non-toxic to humans, animals, and plant; however, residual monomer in PAM and CPAM may raise environmental concerns. PAM acts as a

flocculation agent alone and interacts with wastewater impurities via hydrogen-bonding and undergoes thermal, mechanical, and chemical degradation through the reactive amide moiety. These intermolecular forces also enable interactions with iron, calcium, aluminum, and titanium salts, which when combined form effective flocculation composites.[68-70] Huang, Yue *et. al.* demonstrated that the addition of polyacrylamide to polytitianium sulfate improved both floc strength and recovery ability in humic acid-kaolin water treatment.[71] Lee, Hong *et. al.* studied the effect of a PAM-$CaCl_2$ hybrid polymer on flocculating kaolin clay where the system achieved > 98% turbidity removal.[35]

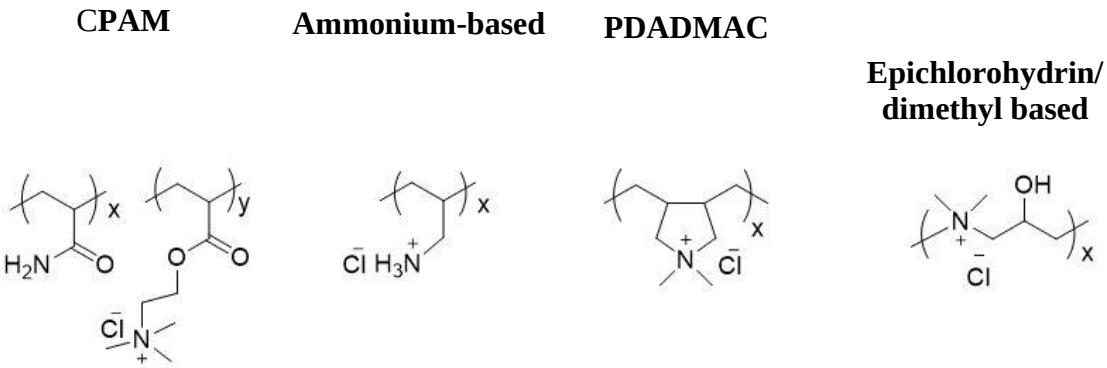

Figure 2.4. Common polymers used for flocculation and coagulation in water treatment; from left to right CPAM, ammonium-based, PDADMAC, and epichlorohydrin/dimethylamine- based.

Free radical polymerization of acrylamide yields high molecular weight PAM. Industrially, nitrile hydratase hydrolyzes nitriles to afford acrylamide. Radical polymerization of acrylamide and a positively charged vinyl monomer yields CPAM. Common co-monomers include acryloyloxy ethyltrimethyl ammonium chloride (PDAC) and methacryloxy ethyltrimethyl ammonium chloride (PDMC). **Scheme 2.2** depicts the

synthesis of PDAC or PDMC type monomers where trans-esterification of a short-chain alkyl acrylate and a tertiary amine-containing alcohol produces dialkylaminoacrylate. A quaternization reaction between an alkyl halide and dialkylaminoacrylate affords a cationically charged vinyl-type monomer.[72] Order of addition and monomer concentration yields polymers with different sequence distributions and different charge densities. This section focuses on the synthesis of PAMs and CPAMs used and tested for flocculation and coagulation aids, any polymer or copolymer of PAM.[8]

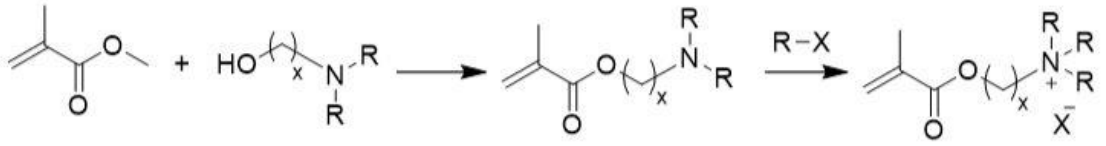

R = CH_2, CH_2CH_2, $CH_2CH_2CH_2$
X = Cl, Br, I

Scheme 2.2. Synthetic pathway to common ammonium-containing vinyl monomers. (Adapted from Williams *et. al.*[72])

Lee, Tong *et. al.* demonstrated another method of synthesizing cationic ammonium-containing monomers with tunable R groups. Depicted in **Scheme 2.3**, the nucleophilic primary amine in acrylamide attacks the sterically hindered epoxy ring in epichlorohydrin to produce 3-arcylamido-isoproanol chloride. Next, the alkyl tertiary amine, either hexyl, octyl, or dodecyl in this study, undergoes nucleophilic substitution to create a vinyl ammonium-containing monomer. Free-radical polymerization yields high molecular weight CPAM with varying hydrophobic nature depending on the ammonium alkyl chains.[73] In this study, PAM-*co*-poly(3-acrylamido-2-hydroxypropyltrihexylammonium) chloride (PAHPTAHC) with 1 mol% PAHPTAHC

removed 99 % turbidity of a kaolin clay suspension and performed better than the octyl and dodecyl analogs. As the molar percent of hydrophobic monomer increases in the polymerization, molecular weight decreased because of decreased solubility in the aqueous polymerization medium. PAHPTAHC contained the least hydrophobic character and therefore achieved the highest molecular weight. The authors hypothesize the higher molecular weight achieved higher flocculation because of greater potential to bridge particles together.[74]

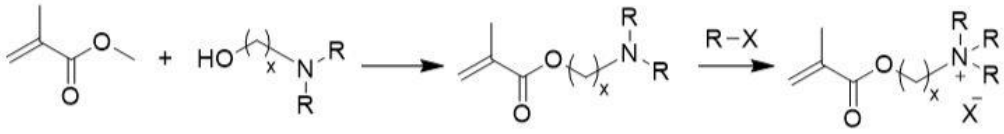

R = hexyl, octyl, dodecyl

Scheme 2.3. Synthetic pathway to 3-acrylamido-2-hydroxypropyltrialkylammonium chloride. (Adapted from Lee *et. al*.[73])

Recently, researchers discovered an increase in FE through grafting PAM and CPAM to natural polymers such as starch, carboxymethyl guar gum, hydroxypropyl methyl cellulose, and dextrin.[75-83] Banerjee, Bandopadhyay *et. al.* grafted PAM to starch using microwave irradiation and cerium ammonium nitrate (CAN) to selectively initiate the C_5 primary alcohol on starch, depicted in **Scheme 2.4**. Using CAN without microwave irradiation results in free radical formation at the C_2 and C_3 diol because of the increased localized electron density. When exposed to a high energy state from a microwave radiation, the exothermic route, initiation at the C_2 and C_3 diol is not preferred. The strongly electrophilic Ce(IV) ion selectively creates a free radical on the primary alcohol leading to

a potential initiation cite for vinyl monomers. This study examines microalgae recovery in a pH range from 4-10.5. They determined higher degrees of grafting and a pH of 10.5 resulted in the highest microalgae recovery of 86 %.[75] Pal, Panda *et. al.* synthesized PAM grafted to dextrin also using microwave irradiation and potassium persulfate to generate free radicals. They reported that polar groups, e.g. hydroxy moieties on the dextrin backbone, absorbed the microwaves which consequently severed the bonds and created free radicals. They also confirmed varying molecular weight and grafting percentages lead

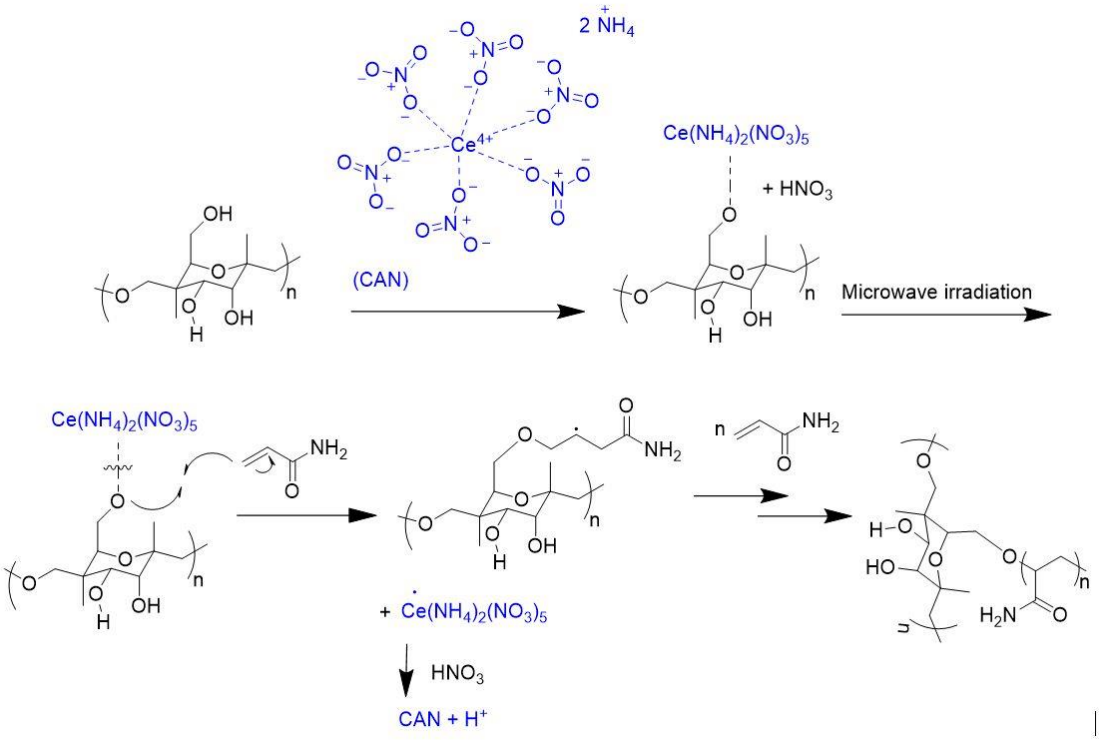

to increased floc settling velocity than commercially available systems.[76]

Scheme 2.4. CAN catalyzed, microwave irradiation-assisted mechanism of starch-graft-PAM. (Adapted from Banerjee *et. al.*[75])

Ternary polymer systems with PAM also function as effective flocculation agents.[84] Sakohara, Iizawa *et. al.* studied thermosensitive ternary CPEs with *N*-

isopropylacrylamide, *N*,*N*-dimethylaminopropyl acrylamide, and *N*-tert-butylacrylamide as a hydrophobic component to control lower critical solution temperature and study its effect on flocculating kaolin clay particles.[85-86] In another ternary system Yang, Liu *et. al.* discovered the copolymer of PAM, PDADMAC, and poly(butyl acrylate) (PBA) achieved a 93.4 % FE at 50 mg L^{-1} of oil wastewater.[87] Ma, Fu *et. al.* added a hydrophobic monomer to PAM-*co*-PDADMAC to study the effects on flocculation of high turbidity kaolin suspension. UV light initiation polymerized the triblock copolymer of PAM, PDADMAC, and coconut diethanolamide (CDEA), depicted in **Scheme 2.5**. FT-IR spectroscopy, ^{1}H NMR spectroscopy, and SEM confirmed the polymer structure and an amorphous morphology of the formed flocs. The three different ratios of PAM:PDADMAC:CDEA all performed better than the control, CPAM. The best performer, 1:1:0.05 PAM:PDADMAC:CDEA, yielded a transmittance of 82.12 - 86.64% at a dosage of 1.5 mg L^{-1} across a pH range of 2-10.[88] Zhu, Tshukudu *et. al.* studied a ternary copolymer system of PAM, poly (methacryloxyethyltrimethyl ammonium) chloride (PDMC), and poly(acryloxyethyltrimethyl ammonium) chloride (PDAC) and its effect on sludge dewatering. This system achieved 63.5 % dewatering at a pH of 7.0.[89] PAM and PDADMAC are also used as co-flocculants, which increases FE in pulp and papermill wastewater.[90]

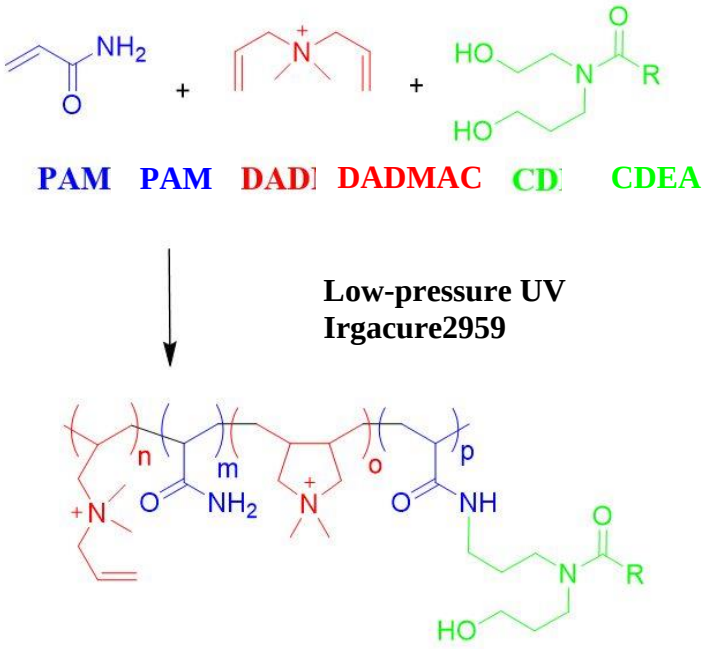

Scheme 2.5. Low-pressure UV initiated PAM-*co*-PDADMAC-*graft*-CDEA synthetic scheme. (Adapted from Ma *et. al.*[88])

Sequence distribution of CPAM and co-monomers influence FE. Chen et. al synthesized blocky copolymers of acrylamide and PDAC for flocculants for sludge water treatment. The authors used UV-light irradiation to synthesize blocky copolymers and utilized sodium polyacrylate as a template to tailor the reactivity ratios of the two monomers. The motivation to obtain a blocky structure stems from the idea that a more concentrated charge density flocculates particles better compared to other copolymer distributions.[91] Others also studied microblock structures for flocculants using a copolymer of PAM and poly(methacrylamido propyltrimethyl) ammonium chloride and reported similar dewatering effects.[92-93] To evaluate FE, Chen et. al used the filter cake moisture content to characterize sludge state and specific resistance of filtration to evaluate sludge filtration performance. Compared to random copolymers, the microblock, cationic

structures improved dewatering properties because of their increased charge neutralization and bridging properties.[94-95] Li, Xu *et. al.* also studied microblock CPAM structures in flocculating sludge water. **Figure 2.5** depicts sludge water before and after treatment with the CPAM.[93]

Figure 2.5. Sludge wastewater (before) and the formation of flocs after CPE treatment (after) using a microblock PAM and PDMC copolymer. (Reproduced from Li *et. al.*[93])

2.6.2 Ammonium-based polymers

Ammonium-based polymers contain a quaternized nitrogen atom, called an ammonium moiety, in a side-chain or main-chain of a polymer. Quaternization of a tertiary amine by an alkyl halide creates ammonium moieties, which have the basic structure of NR_4^+, where R is usually an alkyl group. Depending on the alkyl halide chosen to quaternize the system, the polymer will have different properties. For example, ammonium-based polymers bearing alkyl chains are used as disinfectants or anti-microbial materials and are more hydrophobic. Ammonium moieties are stable when in contact with acids, oxidants, electrophiles, and most nucleophiles. Ammonium-based polymers and PAM also form successful flocs with sludge wastewater and NOM, as discussed in the previous section.

Isik, Mecerreyes *et. al.* performed anion exchanges to afford poly(ionic liquid) nanoparticles for potential flocculants. The authors investigated three polymer systems, poly(1-vinyl-3-ethyl imidazolium bromide), poly(diallyldimethylammonium chloride) and poly(allylamine hydrochloride) partially exchanged with 1-10 mol % lithium bis(trifluoromethanesulphonyl)imide (LiTFSI) over different molecular weights. As incorporation of LiTFSI increases, the relative size of the self-assembled nanoparticles increases.[27] Calculation of total suspended solids removed determined FE of the partially exchanged polymers mixed at 9 rpm with waterborne silica dispersions. The cationic polymers with partial anion exchange create physical crosslinks because of the $TFSI^-$ aggregates. The cationic portion of the polymer extends outward into the water because of its inherit hydrophilicity, which disrupts colloidal silica dispersions. This process also involves charge neutralization of the polymer, which further aids to the system FE. The system with the highest total suspended solid removed was poly(allylamine hydrochloride) with 5 % LiTFSI exchanged and a molecular weight of 120k g mol^{-1}.[27]

In another example of ammonium-based flocculants, Dharani, Balasubramanian *et. al.* demonstrated the effectiveness of flocculating microalgae with a PDMC and poly(4-methacryloyl 1-cyclopentyl) piperazinium chloride (PMACPPC) grafted to acryloyl chitosan. The synthesis of 4-methacryloyl 1-cyclopentyl piperazinium chloride begins with the quantization and functionalization of *N*-cyclopentyl piperazine with methacroyloyl chloride. The synthesis of functionalized chitosan starts with mixing chitosan powder and methane sulfonic acid and subsequent stirring with acryloyl chloride. Free radical polymerization enables a random copolymer of PDMC and PMACPPC to graft onto the functionalized chitosan.[28] To determine FE of acryloyl chitosan-*graft*-(PDMC-*co*-

PMACPPC), the author harvested C. vulgaris microalgae and combined the graft and homopolymers in concentrations from 20-100 ppm. The best performing combination had a FE of 70 % and 71 % with 20 ppm and 100 ppm of acryloyl chitosan-*graft*-(PDMC-*co*-PMACPPC), respectively. The authors hypothesize the high molecular weight of the graft polymers play an important role in its FE.[28]

Zhang, Huang *et. al.* synthesized PDMC grafted to colloidal silica particles using a grafting-from method, depicted in **Scheme 2.6**. The synthesis begins with an azo initiator, 4,4-azobis (4-cyanopentanoic acid-(3-hydridodiethylsilyl), which attaches to the surface of the silica particles. Next, PDAC is grafted from the particle *in-situ*. Colloidal titration and aqueous SEC determined charge density and molecular weight of the system while TEM captured the size and shape of the brush polymer. Zeta potential, relative turbidity, dynamic drainage jar, focused beam reflectance measurement (FBRM), and field emission scanning electron microscopy collectively determined FE of eucalyptus kraft pulp and kaolin particles. The graft polymer sustained a high FE than the control, a homo-polymer of PDMC and flocculated according the polymer bridging mechanism.[96]

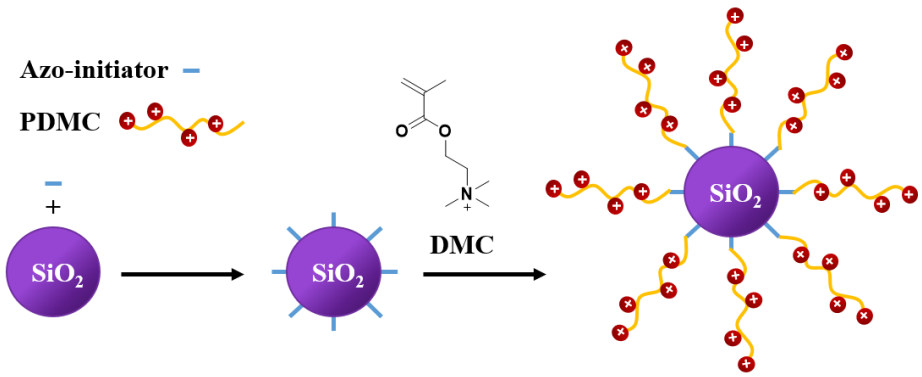

Scheme 2.6. Synthetic depiction of PDMC grafted from colloidal silica particles. (Adapted from Zhang *et. al.*[96])

Table 2.1. Summary of CPEs and properties used for water treatment: CPAM, PAM, and ammonium-based.

Category	Name	Mole % charge	Molecular weight (g mol^{-1})	Sequence Distribution/ Architecture	Contaminate Type	Dosage (mg L^{-1})	pH	Flocculation efficiency	Reference
CPAM	PAM-*co*-PDADMAC-*co*-CDEA	40	[a]	Random, linear	Kaolin suspension	1.5	2-10	84.5 %[d]	88
CPAM	PAM-*co*-PDMC-*co*-PDAC	30.7	$1.28 \cdot 10^7$	Random, linear	Sludge	0.5 g kg^{-1} g	7.0	63.5 %[b]	89
CPAM	PAM-*co*-PDADMAC-*co*-PBA	[a]	[a]	Random, linear	Oil	50	7.0	93.4 %	87
CPAM	PAM-*co*-PDAC-*co*-PBA	32.2	$1.1 \cdot 10^7$	Random, linear	Sludge	40	7.0	5.5 NTU[d]	84
CPAM	PAM-*co*-PMAPTAC	25	[a]	Blocky, linear	Sludge	40	6.0	68.01 %[d]	92
CPAM	Aluminum chloride and starch-*g*-(PAM-*co*-PDMC)	[a]	[a]	Graft	Papermill	871, 22.3	8.4	95.7 %[d]	81
CPAM	PAM-*co*-PAHPTAHC	1	$2.13 \cdot 10^6$	Random, linear	Kaolin suspension	0.3	2.0	99 %[d]	74
CPAM	Chitosan-*g*-(CTA-*co*-PAM)	45	[a]	Graft	Kaolin suspension	0.1	7.0	97.5 %[d]	82
PAM	Starch-*g*-PAM	n/a	$>10^6$	Graft	Microalgae	0.8	10.5	86 %[e]	75
PAM	Dextran-*g*-PAM	n/a	$5.39 \cdot 10^6$	Graft	Kaolin suspension	[a]	7.0	[a]	76
PAM	Carboxymethyl guar gum-*g*-PAM	n/a	$7.4 \cdot 10^6$	Graft	Sludge	0.1	7.0	90 %[d]	77
PAM	Hydroxypropyl methyl cellulose-*g*-PAM	n/a	$2.7 \cdot 10^4$	Graft	Kaolin suspension	2.5	7.0	25.3 NTU[d]	80
Ammonium-based	Poly(allylamine hydrochloride) 5 % LiTFSI exchanged	[a]	$1.2 \cdot 10^5$	Homopolymer	Silica dispersions	9	7.0	90 %[d]	27
Ammonium-based	Acryloyl chitosan-*graft*-(DMC-*co*-MACPPC)	[a]	$>10^4$	Random, graft	Microalgae	20	7.0	73 %[e]	28
Ammonium-based	PDMC-*graft*-colloidal silica particles	[a]	[a]	Graft	Kaolin suspension/ bleached eucalyptus kraft pulp	5 mg g^{-1} g	[a]	0.4 relative turbidity[d]	96

[a]Data not available
Flocculation efficiency experiment: [b]Dewatering, [c]Percent solids, [d]Turbidity, [e]microalgae recovery, [f]dye removal
[g]Weight of polymer per weight or volume of contaminant

2.6.3 Poly(allyldimethyl-ammonium chloride)

Poly(allyldimethyl-ammonium chloride) (PDADMAC) acts as an effective flocculation agent because of its water-solubility, high charge density, and high molecular weight. PDADMAC is also considered non-toxic and does not produce harmful byproducts in the presence of chlorine, which enables its use in drinking water purification.[97-99] PDADMAC effectively flocculates particles such as clay, microalgae and bacteria.[100-102] Aside from homo and copolymers of PDADMAC, which are discussed in this section, it is important to mention flocculation agents made from PDADMAC composites.[103-104] For example Li, Fu *et. al.* combined poly(aluminum chloride) and PDADMAC to flocculate sludge wastewater impurities. **Figure 2.6** depicts the photomicrographs at 200x magnification revealing dense flocs after treatment with the PDADMAC composite.[105]

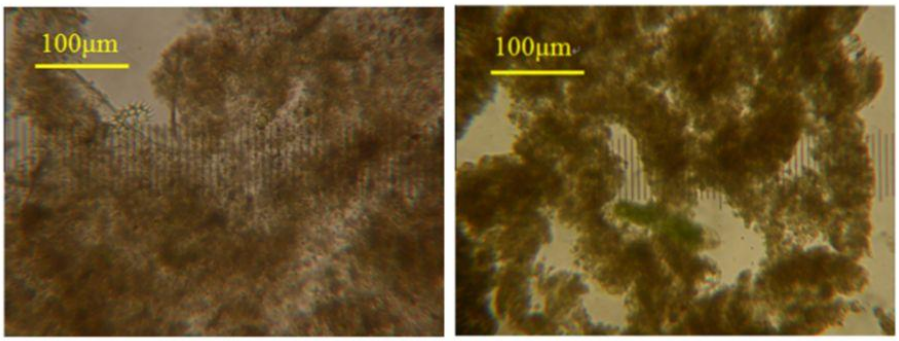

Figure 2.6. Photomicrographs at 200x magnification of aggregated sludge water with poly(aluminum chloride) (left) and flocs formed from poly(aluminum chloride) and PDADMAC.(Reproduced from Li *et. al.*[105])

Free radical polymerization of DADMAC and a substituted peroxide or persulfate as an initiator yields cis and trans isomers of PDADMAC at medium molecular weight ranges (10^5 to 10^6 g mol^{-1}). Polymerization of DADMAC affords *N*-substituted piperidine

and *N*-substituted pyrrolidone, depicted in **Scheme 2.7**, where the *N*-substituted pyrrolidone is sterically favored. The polymerization begins when the initiator produces a free radical on either C_2 allyl carbon. Next, cyclization occurs between the free radical and the opposing C_1 or C_2 allyl carbons, resulting in a 6-membered or 5-membered ring, respectively. Carefully controlled temperature, pressure, and monomer concentration produce linear PDADMAC chains while avoiding crosslinking, which results in an insoluble product. Wilson, Sanderson *et. al.* describes a custom reaction vessel with four inlets consisting of initiator funnel, water funnel, condenser with a vacuum attachment, and thermometer to control the vessel conditions of the exothermic reaction.[21, 106]

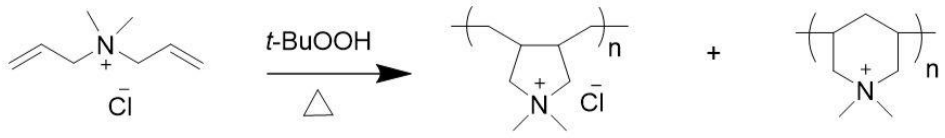

DADMAC | ***N*-substituted pyrrolidone (major)** | ***N*-substituted piperidine (minor)**

Scheme 2.7. Synthesis of PDADMAC depicting major and minor products. (Adapted from Wilson *et. al.*[21])

Grafting PDADMAC to natural polymers is a popular trend because of the increased molecular weight of the system and potential biodegradability, which helps FE and produces less waste. Anthony, Sims *et. al.* synthesized chitosan-*graft*-PDADMAC to improve flocculation and harvesting efficiency of microalgae. The synthesis begins with two separate vessels, one containing natural chitosan and the other containing PDADMAC. The addition of ceric ammonium nitrate to both vessels initiates the formation of free

radicals, which will later enable the attachment of the PDADMAC. When these two systems are combined, the radicals form a bond thus creating chitosan-*graft*-PDADMAC using the grafting-to method. To measure FE, the authors used wastewater from Logan city facultative lagoons. A concentration of 10-20% graft polymer relative to weight of microalgae removed 50-60% solids. Increased polymer dosage resulted in the overall charge of the system becoming positive, which destabilized the flocculated particles. The authors compared this value to homopolymers of PDADMAC and chitosan, which both removed less microalgae at higher concentrations than the chitosan-*graft*-PDADMAC.[107]

Lv, Ding *et. al.* demonstrated another example of PDADMAC grafted to a natural polymer where PDADMAC is grafted to starch using horseradish peroxidase and H_2O_2 initiation. The authors first used enzymes to degrade starch to yield a water-soluble backbone for the graft copolymer, which also controlled the flocculation mechanism of the final system. Higher molecular weight starches, over 10^5 g mol^{-1}, resulted in polymer bridging while lower molecular weight resulted in charge neutralization. This type of initiation creates a radical on either the primary or secondary alcohol moieties on the starch backbone, which subsequently polymerizes DADMAC from the free radical sites. The authors used FTIR, ^1H and ^{13}C NMR spectroscopy, SEC, graft percent, and graft efficiency to characterize the polymer. **Figure 2.7** shows an SEM of flocs formed from the graft copolymer system and sludge water and a depiction of the flocculation process on the molecular level. Turbidity removal ratio measurements compared the FE of each system while surface tension and zeta potential elucidated flocculation mechanisms. Copolymers containing varying amounts of PDADMAC provided a decrease in sludge water content from 50.6 % to 97.9 %.[108]

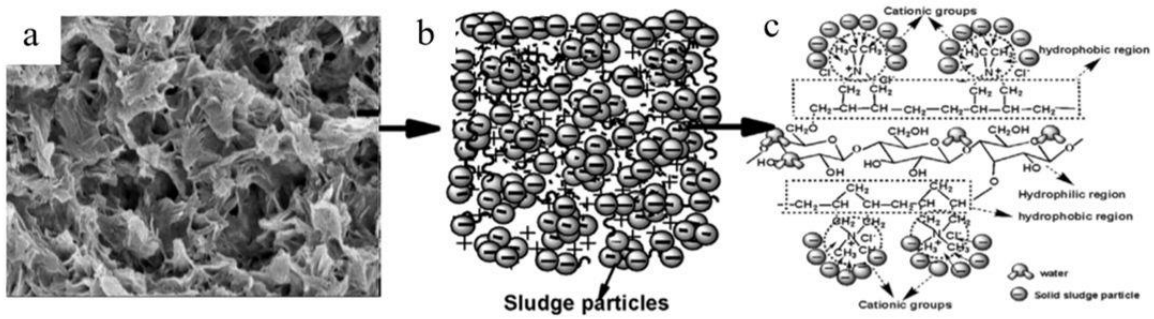

Figure 2.7. (a) SEM image of sludge and starch-*g*-PDADMAC floc; (b) flocculation mechanism; (c) depiction of hydrophilic and hydrophobic sections of the polymer system. (Reproduced from Lv *et. al.*[108])

Copolymers of PDADMAC and non-ionic comonomers demonstrate effective flocculation of impurities in sludge and bentonite contaminated water, which contain a broad particle size distribution. Abdiyev, Nuraje *et. al.* synthesized copolymers of PDADMAC and *N,N*-dimethylacrylamide in varying concentrations and measured the effect on intrinsic viscosity, FE, and zeta potential. The authors reported an improvement of zeta potential, closer to zero, compared to the PDADMAC homopolymer and achieved these flocculation efficiencies at a lower polymer dosage. Because of the low zeta potential reading of the water, the main mechanism of flocculation is charge neutralization. The authors also hypothesize the slightly hydrophobic *N,N*-dimethylacrylamide monomer plays an important role in the ability of the system to flocculate a wide size and chemical composition range of particles.[109]

PDADMAC

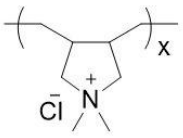

***N,N*-dimethyl acrylamide**

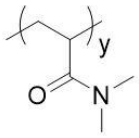

Figure 2.8. PDADMAC-*co*-*N*,*N*-dimethylacrylmide. (Adapted from Abdiyev *et. al.*[109])

2.6.4 Epichlorohydrin-dimethylamine based CPEs

Polycondensation with epichlorohydrin and a secondary or primary amine affords epichlorohydrin-dimethylamine based (EPI-DMA) polymers. Polycondensation reactions occur between telechelic monomers, which produces a condensate. Depicted in **Scheme 2.8**, in this process the nucleophilic amine attacks the least sterically hindered and electrophilic α-carbon in the epoxy ring. The epoxy ring then closes with Cl^- as a leaving group. The amine attacks the epoxy ring again, which grows the polymer chain while creating ammonium groups in the backbone. Typically, polycondensation does not yield high molecular weight polymers compared to polymers synthesized from free radical polymerization. This reaction creates low molecular weight polymers with quaternary ammonium moieties in the polymer backbone.[6, 110] Structural changes of the diamine monomer or copolymerizing with different diamine monomers enables charge density tunability. Flocculation agents made with EPI-DMA-based polymers usually use an amine crosslinker to increase FE and isolate impurities, commonly soluble or reactive dyes from textile industies.[111] Because these systems are commonly crosslinked, convention chemical structure confirmation techniques, such as ^1H and ^{13}C NMR spectroscopy, are not used. Intrinsic viscosity and FTIR spectroscopy often confirm chemical structures of these crosslinked systems. Other common flocculation agents for removing dyes from wastewater include inorganic salts such as ferric, aluminum, and magnesium salts. Low cost and reduced sludge production deem synthetic polymers the ideal choice for purification of dye-contaminated wastewater.

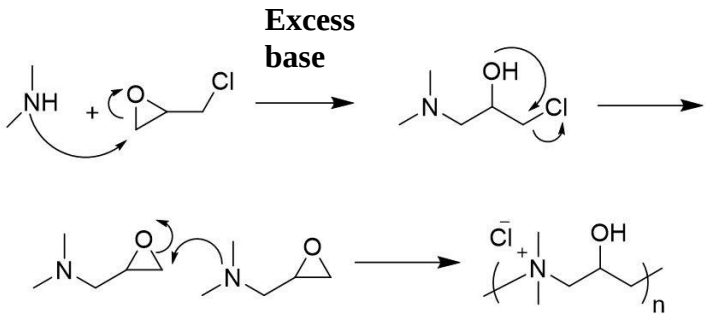

Scheme 2.8. EPI-DMA polymerization mechanism.

Grafting ammonium-containing side groups to natural polymers provide effective flocculation properties.[83] Ghimici, Nichifor *et. al.* synthesized *N*-alkyl-*N*,*N*-dimethyl-*N*-(2-hydroxypropyl) ammonium chloride grafted to dextrin and evaluated the FE with respect to varying alkyl chain length, molecular weight and charge density. The synthesis begins with a condensation reaction between epichlorohydrin, *N*, *N*-dimethyl-*N*-alkylamine and dextrin where the reaction conditions afforded ammonium moieties, depicted in **Scheme 2.9**. The systematic investigation of the length of alkyl chain dependence on FE revealed an increase in FE from the ethyl to butyl chain but a decrease from octyl to docdecyl. The authors hypothesize electrostatic and hydrophobic interactions both contribute to the flocculation of the clay suspensions. They also observed an increase in efficiency with increased charge density but molecular weight did not employ a difference. [112] In another example of grafting ammonium-containing side chains to natural polymers, Song, Zhang *et. al.* synthesized 3-chloro-2-hydroxypropyl-trimethylammonium chloride (CHPTAC) grafted to cellulose. CHPTAC undergoes an epoxy-forming reaction in the presence of H_2O and NaOH, which is then subsequently reacted with cellulose under basic conditions to form cellulose-*graft*-2-hydroxypropyl-trimethylammonium chloride at degrees of substitution of 0.38, 0.50, and 0.74. The graft polymers achieved a 93 % color removal of

reactive dyes. The authors also examined antimicrobial properties against *Escherichia coli* and *Staphylococcus aureus* and discovered the polymer prevent growth of both bacteria species.[113]

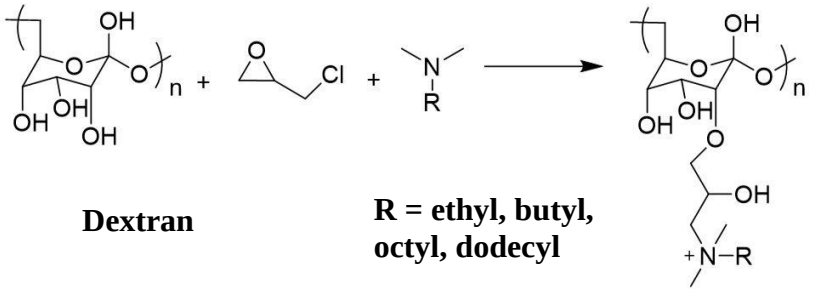

Scheme 2.9. Synthesis of dextrin-*graft*-*N*-alkyl-*N,N*-dimethyl-*N*-(2-hydroxypropyl) ammonium chloride. (Adapted from Ghimici *et. al.*[112])

Wang, Li *et. al.* studied the removal of disperse and reactive dyes from wastewater with a modified EPI-DMA copolymer. The polycondensation reaction occurred with epichlorohydrin, dimethylamine and diaminoethane to yield a CPE copolymer with varying intrinsic viscosity, crosslinking, and charge density. To measure FE, the authors compared turbidity and dye removal paired with zeta potential and compared the results with polyaluminum chloride and polyaluminum chloride/EPI-DMA controls. The authors also monitored dye and turbidity removal with addition of 0-3000 mg L^{-1} NaCl to observe the effects of increased ionic strength of the wastewater. They noticed a negligible effect on the FE of the disperse dye and a negative effect on the reactive dye. The best performing EPI-DMA system with intrinsic viscosity of 3200 mPa·s removed 96 % dye and 96 % turbidity over a pH range of 2-10, which proved more effective than both controls EPI-DMA or polyaluminum chloride alone.[61]

Figure 2.9. EPI-DMA-DIPA and Congo red floc observed using light microscopy (A) and SEM (B). (Adapted from Gupta et. al.[114])

Gupta, Bux *et. al.* studied the removal of azo dyes from wastewater using a EPI-DMA copolymer. Epichlorohydrin, dimethylamine and *N*,*N*-diisopropylamine (EPI-DMA-DIPA) formed a crosslinked copolymer via polycondensation. FTIR, TGA, and XRD confirmed the structure of the charged copolymer. The copolymer was combined with an azo dye at different pHs and mixed rapidly. After the flocs formed and settled, the authors used SEM and light microscopy, depicted in **Figure 2.9**, to observe the morphological changes between the dye by itself and the floc formation. The optimum pH range for this system is 4-10 and the optimal dosage is 80 mg L^{-1}. The authors also determined these ranges enable the polymer system to flocculation via polymer bridging and charge neutralization.[114]

EPI-DMA polymers are also commonly paired with polyferric chloride to create a composite flocculation system.[115-117] Yang, Chen *et. al.* examined a EPI-DMA and polyferric chloride composite on its FE of a reactive dye suspension. They concluded this composite exhibited an increase in flocculation from zeta potential experiments. The authors also monitored the amorphous floc structure, which depicted connected sheet-like structures.[116]

2.6.5 Other

Other CPEs used for flocculation and coagulation of contaminates in wastewater include zwitterionic, amphoteric, degradable, imidazole-containing, and pyridinium-containing polymer systems. Zwitterionic polymers contain positive and negative charges, which provide the opportunity to interact with positively and negatively charged contaminants. Amphoteric polymers become positively or negatively charged, or neutral depending on pH and hydrolytically degradable polymer flocculants provide high flocculation efficiencies paired with biodegradability found in natural polymer flocculants. Imidazole-containing and pyridinium-containing CPEs offer alternative cationically charged groups with potentially different flocculation properties.

Although zwitterions are unconventional CPEs, some systems prove successful in flocculation of contaminates in wastewater. Xu, Li *et. al.* synthesized a copolymer of PAM, PDCM, and sodium acrylate to create a PAM-zwitterionic species for flocculation. A viscometer measured the intrinsic viscosity and a spectrophotometer determined the FE of mining wastewater. This polymer structure and sequence takes into account the presence of cationic and anionic charged particles in the wastewater and therefore can flocculate each species. The results proved that the novel polymer has flocculating efficiencies comparable to CPAM at a pH of 6.5.[118]

Amphoteric polymers provide successful flocculation capabilities and experience anionic or cationic charges depending on the pH of the system. Yang, Yang *et. al.* investigated modified chitosan on flocculation of kaolin suspensions. The two-step synthesis began with nucleophilic substitution of 3-chloro-2-hydroxypropyl trimethyl ammonium chloride onto a chitosan backbone followed by the addition of

monochloroacetic acid to produce 3-chloro-2-hydroxypropyl trimethylammonium chloride modified carboxymethyl chitosan (CMC-CTA). Depicted in **Figure 2.10**, as the pH shifts from 2 to 10, the polymer transitions from cationically charged to neutral to anionically charged. At a pH of 4 and 0.1 mg L^{-1} of polymer dosage, CMC-CTA achieved 99 % transmittance through the supernatant fluid. At a pH of 4, the polymer is mostly cationic, which enables electrostatic interactions with negatively charged kaolin suspension particles.[119] In another example, Jiang, Tian *et. al.* synthesized a modified β-cyclodextrin (β-CD) and PDAC copolymer and measured FE of soluble dyes. Esterification of maleic anhydride and β-CD yielded polymerizable vinyl carboxylic acid groups, which were subsequently polymerized with PDAC. **Figure 2.10** depicts a SEM image of β-CD-MAH-PDAC surface. β-CD-MAH-PDAC at a pH of 4 and 10 mg L^{-1} removed 90 % of soluble dyes.[120]

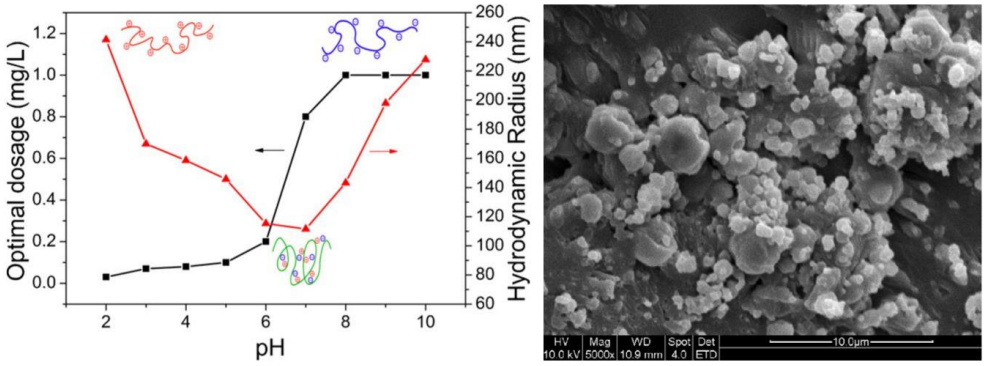

Figure 2.10. Cationic and anionic transitions of CMC-CTA from a pH range of 2 to 10 (left) (Reproduced from Yang *et. al.*[119]) A SEM of the surface of solid β-CD-MAH-PDAC (right) (Reproduced from Jiang *et. al.*[120])

Degradable synthetic CPEs offer the benefits of natural CPEs along with increased FE of tailorable synthetic CPEs. Gumfekar, Hutchinson *et. al.* investigated FE of oil sands

tailings with cationic hydrolytically cleavable polycaprolactone-based CPEs. The polycaprolactone choline iodide ester methacrylate (poly(PCL_2ChMA)) synthesis begins with the ring-opening polymerization of ε-caprolactone initiated with 2-(dimethylamine)-ethanol and subsequently functionalized with methacryloyl chloride. Methyl iodine quaternized the tertiary amine and radical polymerization of the macromer and PDMC and PAM yielded CPE copolymers greater than $5 \cdot 10^5$ g mol^{-1}.[121] Poly(PCL_2ChMA) performed the best at 5000 ppm, 6.6 NTU of supernatant liquid and increased dewatering properties after degradation.[122]

Pyridine-containing and pH responsive CPE flocculants deliver high harvesting efficiencies of microalgae. Kan, Cranston *et. al.* synthesized poly(4-vinylpyridine) grafted to cellulose nanocrystals (CNC) (P4VP-g-CNC) through CAN and HNO_3 initiation. They proved the pyridine moiety is positively charged below a pH of 5 and neutral and hydrophobic above a pH 5, which functions as a pH responsive flocculant.[123] Vandamme, Thielemans *et. al.* grafted pyridinium-containing side groups onto CNCs, depicted in **Figure 2.11**, which they harvested from cotton wool through hydrolysis with sulfuric acid.[124] In a one pot reaction, *p*-toluenesulfonyl chloride activated the esterification of bromoalkyl benzoic acid with the primary and secondary hydroxyls on the CNC backbone. In the same reaction vessel, the alkyl-bromide moiety nucleophilically attacked pyridine to afford a pyridinium cation.[125] Pyridinium-containing 4-(bromomethyl)benzoic acid-graft-CNCs ((Br)(PyBnOO)-g-CNCs) and pyridinium-containing 4-(bromoethyl)benzoic acid-graft-CNCs ((Br)(PyMeBnOO)-g-CNCs) flocculated microalgae at 89 % and 97 % respectively. The authors hypothesize the a higher molar percent of cation groups increased the flocculation efficiency of (Br)(PyMeBnOO)-*g*-CNCs.[124] In another structurally similar

example, Eyley, Thielemans *et. al.* synthesized pH responsive, imidazole-containing side groups on cellulose nanocrystals (CNCs) for microalgae flocculation depicted in **Figure 2.11**. The authors synthesized the graft polymer using the same route as Vandamme, Thielemans *et. al.* but supplemented the pyridine with imidazole to produce a neutral, pH responsive polymer. At a pH of 4.0, the polymer became positively charged and flocculated 90 % of microalgae at 200 mg L^{-1}.[126]

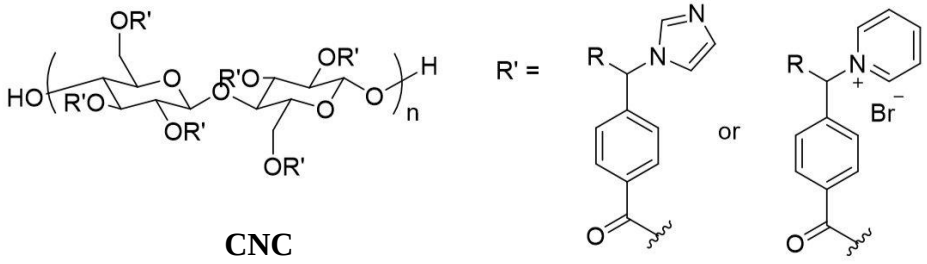

CNC

R = H, CH_3

Figure 2.11. CNC grafted polymers with imidazole-containing 4-(bromoethyl)benzoic acid (left) (Adapted from Eyley *et. al.*[126]) and pyridinium-containing 4-(bromoethyl)benzoic acid (right). (Adapted from Vandamme *et. al.*[124])

Table 2.2. Summary of CPEs and properties used for water treatment: PDADMAC, EPI-DMA, and Other.

Category	Name	Mole % charge	Molecular weight (g mol^{-1})	Sequence Distribution/ Architecture	Contaminate Type	Dosage (mg L^{-1})	pH	Flocculation efficiency	Reference
PDADMAC	PDADMAC-*co*-*N, N*-dimethylacrylamide	70	[a]	Random	Sludge	90	[a]	90-95 %[d]	109
PDADMAC	Chitosan-*g*-PDADMAC	[a]	[a]	Graft	Microalgae	1:1wt % algae: CPE	7.0	70 %[c]	107
PDADMAC	Starch-*g*-PDADMAC	46	$6.5 \cdot 10^4$	Graft	Sludge	0.6 wt% of contaminant	7.0	95.8 %[c]	108
EPI/DMA	Dextran containing N-ethyl-*N, N*-dimethyl-*N*-(2-hydroxypropyl) ammonium chloride	30	$4 \cdot 10^4$	Random, pendant	Kaolin suspension	11	4.5	99 %[d]	112
EPI/DMA	Dextran containing *N*-dodecyl-*N, N*-dimethyl-*N*-(2-hydroxypropyl) ammonium chloride	30	$4 \cdot 10^4$	Random, pendant	Kaolin suspension	15	4.5	98.8 %[d]	112
EPI/DMA	EPI-DMA	5.36 mmol g^{-1}	[a]	Random	Disperse and Soluble Dyes	50	2-10	96 %[f]	61
EPI/DMA	EPI-DMA-DIPA	[a]	[a]	Random	Soluble Dyes	80	4-10	98 %[f]	114
EPI/DMA	cellulose-*g*-2-hydroxypropyl-trimethylammonium chloride	38	$>10^5$	Graft	Reactive Dyes	120	9.0	93 %	113
EPI/DMA	konjac glucomannan-*g*-2-hydroxypropyl-trimethylammonium chloride	42	[a]	Graft	Kaolin suspension	4 mg kg^{-1} [g]	5.0	96 %[d]	83
Other	[Br][PyMeBnOO]-*g*-CNC	1.31 mmol g^{-1}	[a]	Graft	Microalgae	40	10.8	97 %[e]	124
Other	[Br][PyBnOO]-*g*-CNC	0.95 mmol g^{-1}	[a]	Graft	Microalgae	70	10.8	89 %[e]	124
Other	Poly(PCL_2ChMA)	1.9 mmol g^{-1}	$4.3 \cdot 10^5$	Random	Oil Sand Tailings	5000	8.0	[a]	121, 122
Other	ImBnOO-*g*-CNC	0.32 mmol g^{-1}	[a]	Graft	Microalgae	200 g L^{-1} [g]	4.0	90 %[e]	126
Other	CMC-CTA	[a]	$>10^5$	Graft	Kaolin suspension	0.1	4.0	99 %[d]	119
Other	β-CD-MAH-*co*-TMAEMC	[a]	[a]	Graft	Soluble Dyes	10	4.0	90 %[f]	120

[a]Data not available

Flocculation efficiency experiment: [b]Dewatering, [c]Percent solids removal, [d]Turbidity, [e]microalgae recovery, [f]dye removal

[g]Weight of polymer per weight or volume of contaminant

2.7 Toxicity and effect on the environment

Cationic polyelectrolytes are acutely toxic to humans, animals and aquatic fauna and flora where toxic levels range from 0.1-1 mg L^{-1}.[127-130] Fortunately, the level of contamination in sewage, sludge and surface water ranges from ng L^{-1} to μg L^{-1} but considering CPEs are popular in the water treatment process it is still important to understand their toxicity and impact on the environment.[131-132] During the water treatment process, it is possible that small amounts of CPEs are present in the final product, which enables exposure to the environment. Previously, studies showed an average of 90% CPE removal from treated wastewater through sorption or anaerobic biodegradgation.[133-134] Some effective methods of detecting CPEs in the environment include high-performance liquid chromatography (HPLC), gas chromatography, mass spectrometry, and HPLC paired with tandem mass spectrometers.[134]

It is well known that CPEs are acutely toxic but studies exploring chemical modifications such as charge density, molecular weight, architecture and functionality and their effect on toxicity are lacking.[135] Costa, Rasteiro *et. al.* compared the ecotoxicity of two CPAM systems with different degrees of branching. This study concluded the more highly branched CPAM was significantly less toxic because of its hydrodynamic volume. Because the branched CPAM had a smaller hydrodynamic volume and aggregated more, it had less contact with biological surfaces thus decreasing its toxicity. The author concludes it is possible to use intrinsic viscosity to determine relative hydrodynamic volume to estimate toxicity.[136] Fischer, Kissel *et. al.* investigated CPE cytotoxicity comparing molecular weight and charge density and found cell death occurred when the polyelectrolytes had the most opportunity to interact with the cell membrane. The specific

molecular weights and charge density to reach a toxic level depended on the polymer system and how it was orientated.[137]

2.8 Conclusions and Future Directions

This review discusses recent advances in CPE synthesis with respect to their role in flocculation and coagulation for water treatment. It highlighted CPEs including PAM, CPAM, ammonium-based polymers, PDADMAC and EPI/DMA for the treatment of blackwater/sludge water, textile and mining industry wastewater and harvesting microalgae for biodiesel. The most critical factors affecting flocculation efficiencies of CPEs are molecular weight and charge density. However, different polymeric architectures and variations in charge distributions, e.g. block-like vs. random polymers also affect flocculation efficiencies. With increasing population and demand for water, wastewater reuse will provide an effective method of water preservation. The design of tailored CPEs to improve water purification will help to tackle this challenge of the future.

Few studies report the synthesis of non-commercially available monomers and polymers with some exceptions.[73, 124, 126] Vandamme *et. al.* and Eyley *et. al.* synthesized novel pyridinium-containing and imidazole-containing side-groups grafted to CNC, which yielded a biodegradable flocculation agent for harvesting microalgae. Lee *et. al.* described novel synthetic methods of CPAM with varying ammonium alkyl chain lengths. While commercially available monomers and polymers provide a cost efficient and convenient solution, potentially better CPE systems for flocculation and coagulation may exist. For example, poly(2-oxazoline)s are water-soluble polymers with tailorable structures and anti-fouling properties. This class of polymers provide materials for drug delivery and

biomedical applications because of their low toxicity and antimicrobial properties. The tailorability of the side-chain groups provides the opportunity for ammonium-based, pyridinium-based, imidazolium-based side-groups, and other charged moieties. Other new monomers with phosphonium, imidazolium or ammonium moieties could also function as effective flocculation agents because of their charge density tailorability and high molecular weight potential.

To date, a systematic investigation on how differences in molecular weight and polymeric architecture influence FE of CPEs is lacking. Pal *et. al.* discussed the effect of PAM chain length when grafted to dextrin, and found FE is dependent on this variable.[76] Razali *et. al.* examined molecular weight and dosage dependence on flocculation of PDADMAC.[99] The effect of molecular weight on FE of polymers known for flocculation of impurities along with new materials needs to be investigated. As discussed in this review, researchers frequently use graft polymers as flocculation agents for the increase in molecular weight.[75, 78] Exploring architectures such as stars, graft, branched, and hyperbranched and how the molecular weight of each arm or branch affects FE would elucidate beneficial structure-property relationships. For example, the mobility of star polymers may have higher polymer bridging potential than linear analogs and an optimal molecular weight of each arm or graft also may have an effect on FE. Flocculation and coagulation of wastewater impurities using CPEs provides unrivaled flocculation capabilities of contaminants from mining, papermill, textile, and farming industries. With continuing exploration of synthetic CPEs for wastewater treatment, reuse of water will become an important strategy to save water reserves on Earth.

2.9 Acknowledgments

The authors would like to thank Jana Herzberger and Kristie Caddick for editing and support and Christiansburg Wastewater for perspective.

2.10 References

(1) Matilainen, A.; Vepsäläinen, M.; Sillanpää, M., Natural organic matter removal by coagulation during drinking water treatment: a review. *Adv. Colloid Interface Sci.* **2010,** *159* (2), 189-197.

(2) Zahrim, A.; Tizaoui, C.; Hilal, N., Coagulation with polymers for nanofiltration pre-treatment of highly concentrated dyes: a review. *Desalination* **2011,** *266* (1), 1-16.

(3) Vedoy, D. R.; Soares, J. B., Water-soluble polymers for oil sands tailing treatment: A Review. *The Canadian Journal of Chemical Engineering* **2015,** *93* (5), 888-904.

(4) Kamali, M.; Khodaparast, Z., Review on recent developments on pulp and paper mill wastewater treatment. *Ecotoxicology and environmental safety* **2015,** *114*, 326-342.

(5) Verma, A. K.; Dash, R. R.; Bhunia, P., A review on chemical coagulation/flocculation technologies for removal of colour from textile wastewaters. *Journal of environmental management* **2012,** *93* (1), 154-168.

(6) Bolto, B.; Gregory, J., Organic polyelectrolytes in water treatment. *Water Res.* **2007,** *41* (11), 2301-2324.

(7) Bolto, B. A., Soluble polymers in water purification. *Prog. Polym. Sci.* **1995,** *20* (6), 987-1041.

(8) Jiang, Z.; Zhu, J., Cationic Polyacrylamide: Synthesis and Application in Sludge Dewatering Treatment: A Review. *Asian J. Chem.* **2014,** *26* (3), 629.

(9) Goldblatt, M. E.; Leitz, C. R., Chemistry and Application of Coagulants and Flocculants in Industrial Wastewater Treatment Systems. *Proceedings of the Water Environment Federation* **2015,** *2015* (16), 2007-2028.

(10) Hunley, M. T.; England, J. P.; Long, T. E., Influence of Counteranion on the Thermal and Solution Behavior of Poly (2-(dimethylamino) ethyl methacrylate)-Based Polyelectrolytes. *Macromolecules* **2010,** *43* (23), 9998-10005.

(11) Hemp, S. T.; Allen Jr, M. H.; Smith, A. E.; Long, T. E., Synthesis and properties of sulfonium polyelectrolytes for biological applications. *ACS Macro Letters* **2013,** *2* (8), 731-735.

(12) Mortimer, D. A., Synthetic polyelectrolytes—a review. *Polym. Int.* **1991,** *25* (1), 29-41.

(13) Anderson, E. B.; Long, T. E., Imidazole-and imidazolium-containing polymers for biology and material science applications. *Polymer* **2010,** *51* (12), 2447-2454.

(14) Hemp, S. T.; Allen Jr, M. H.; Green, M. D.; Long, T. E., Phosphonium-containing polyelectrolytes for nonviral gene delivery. *Biomacromolecules* **2011,** *13* (1), 231-238.

(15) Hara, M., *Polyelectrolytes: science and technology*. CRC Press: 1992.

(16) Pergushov, D. V.; Babin, I. A.; Zezin, A. B.; Müller, A. H., Water-soluble macromolecular co-assemblies of star-shaped polyelectrolytes. *Polym. Int.* **2013,** *62* (1), 13-21.

(17) Hemp, S. T.; Zhang, M.; Allen, M. H.; Cheng, S.; Moore, R. B.; Long, T. E., Comparing ammonium and phosphonium polymerized ionic liquids: thermal analysis, conductivity, and morphology. *Macromol. Chem. Phys.* **2013,** *214* (18), 2099-2107.

(18) Schultz, A. R.; Lambert, P. M.; Chartrain, N. A.; Ruohoniemi, D. M.; Zhang, Z.; Jangu, C.; Zhang, M.; Williams, C. B.; Long, T. E., 3D Printing Phosphonium Ionic Liquid Networks with Mask Projection Microstereolithography. *ACS Macro Letters* **2014,** *3* (11), 1205-1209.

(19) McKee, M. G.; Hunley, M. T.; Layman, J. M.; Long, T. E., Solution rheological behavior and electrospinning of cationic polyelectrolytes. *Macromolecules* **2006,** *39* (2), 575-583.

(20) Zhou, J.; Shangguan, Y.; Wu, Q.; Zheng, Q., Solution properties of hydrophobically modified polyelectrolytes synthesized via solution and micellar copolymerization. *Polym. Int.* **2011,** *60* (3), 353-361.

(21) John, W. Synthesis, properties and analysis of polydadmac for water purification. Stellenbosch: Stellenbosch University, 2008.

(22) Nozaic, D.; Freese, S.; Thompson, P., Longterm experience in the use of polymeric coagulants at Umgeni Water. *Water Science and technology: Water supply* **2001,** *1* (1), 43-50.

(23) Wada, Y.; Bierkens, M. F., Sustainability of global water use: past reconstruction and future projections. *Environmental Research Letters* **2014,** *9* (10), 104003.

(24) Maupin, M. A.; Kenny, J. F.; Hutson, S. S.; Lovelace, J. K.; Barber, N. L.; Linsey, K. S. *Estimated use of water in the United States in 2010*; 2330-5703; US Geological Survey: 2014.

(25) Teh, C. Y.; Budiman, P. M.; Shak, K. P. Y.; Wu, T. Y., Recent advancement of coagulation–flocculation and its application in wastewater treatment. *Industrial & Engineering Chemistry Research* **2016,** *55* (16), 4363-4389.

(26) Sillanpää, M., *Natural organic matter in water: Characterization and treatment methods*. Butterworth-Heinemann: 2014.

(27) Isik, M.; Fernandes, A. M.; Vijayakrishna, K.; Paulis, M.; Mecerreyes, D., Preparation of poly (ionic liquid) nanoparticles and their novel application as flocculants for water purification. *Polymer Chemistry* **2016,** *7* (8), 1668-1674.

(28) Dharani, M.; Balasubramanian, S., Synthesis, characterization and application of acryloyl chitosan anchored copolymer towards algae flocculation. *Carbohydr. Polym.* **2016,** *152*, 459-467.

(29) Morel, A., *Greywater management in low and middle-income countries*. Dubenforf, CH: Swiss Federal Institute of Aquatic Science and Technology: 2006.

(30) Paulo, P. L.; Azevedo, C.; Begosso, L.; Galbiati, A. F.; Boncz, M. A., Natural systems treating greywater and blackwater on-site: Integrating treatment, reuse and landscaping. *Ecol. Eng.* **2013,** *50*, 95-100.

(31) Luostarinen, S.; Sanders, W.; Kujawa-Roeleveld, K.; Zeeman, G., Effect of temperature on anaerobic treatment of black water in UASB-septic tank systems. *Bioresour. Technol.* **2007,** *98* (5), 980-986.

(32) Anjaneyulu, Y.; Chary, N. S.; Raj, D. S. S., Decolourization of industrial effluents–available methods and emerging technologies–a review. *Reviews in Environmental Science and Bio/Technology* **2005,** *4* (4), 245-273.

(33) Nemerow, N. L.; Dasgupta, A., Industrial and hazardous waste treatment. **1991**.

(34) Pokhrel, D.; Viraraghavan, T., Treatment of pulp and paper mill wastewater—a review. *Sci. Total Environ.* **2004,** *333* (1), 37-58.

(35) Lee, K. E.; Teng, T. T.; Morad, N.; Poh, B. T.; Hong, Y. F., Flocculation of kaolin in water using novel calcium chloride-polyacrylamide (CaCl 2-PAM) hybrid polymer. *Sep. Purif. Technol.* **2010,** *75* (3), 346-351.

(36) Chen, C.-Y.; Yeh, K.-L.; Aisyah, R.; Lee, D.-J.; Chang, J.-S., Cultivation, photobioreactor design and harvesting of microalgae for biodiesel production: a critical review. *Bioresour. Technol.* **2011,** *102* (1), 71-81.

(37) Barros, A. I.; Gonçalves, A. L.; Simões, M.; Pires, J. C., Harvesting techniques applied to microalgae: a review. *Renewable and Sustainable Energy Reviews* **2015,** *41*, 1489-1500.

(38) Milledge, J. J.; Heaven, S., A review of the harvesting of micro-algae for biofuel production. *Reviews in Environmental Science and Bio/Technology* **2013,** *12* (2), 165-178.

(39) Kawamura, S., Considerations on improving flocculation. *Journal-American Water Works Association* **1976,** *68* (6), 328-336.

(40) Shaikh, S. M.; Nasser, M. S.; Hussein, I.; Benamor, A.; Onaizi, S. A.; Qiblawey, H., Influence of polyelectrolytes and other polymer complexes on the flocculation and rheological behaviors of clay minerals: A comprehensive review. *Sep. Purif. Technol.* **2017,** *187*, 137-161.

(41) Ruehrwein, R.; Ward, D., Mechanism of clay aggregation by polyelectrolytes. *Soil science* **1952,** *73* (6), 485-492.

(42) Stechemesser, H.; Dobiáš, B., *Coagulation and flocculation*. Taylor & Francis: 2005.

(43) Bratby, J., *Coagulation and flocculation in water and wastewater treatment*. IWA publishing: 2016.

(44) Aguilar, M.; Saez, J.; Lloréns, M.; Soler, A.; Ortuno, J.; Meseguer, V.; Fuentes, A., Improvement of coagulation–flocculation process using anionic polyacrylamide as coagulant aid. *Chemosphere* **2005,** *58* (1), 47-56.

(45) Kasper, D. R. Theoretical and experimental investigations of the flocculation of charged particles in aqueous solutions by polyelectrolytes of opposite charge. California Institute of Technology, 1971.

(46) Gregory, J., Rates of flocculation of latex particles by cationic polymers. *J. Colloid Interface Sci.* **1973,** *42* (2), 448-456.

(47) Rasteiro, M.; Garcia, F.; Ferreira, P.; Antunes, E.; Hunkeler, D.; Wandrey, C., Flocculation by cationic polyelectrolytes: relating efficiency with polyelectrolyte characteristics. *J. Appl. Polym. Sci.* **2010,** *116* (6), 3603-3612.

(48) Caskey, J.; Primus, R., The effect of anionic polyacrylamide molecular conformation and configuration on flocculation effectiveness. *Environmental Progress & Sustainable Energy* **1986,** *5* (2), 98-103.

(49) Yoon, S.-Y.; Deng, Y., Flocculation and reflocculation of clay suspension by different polymer systems under turbulent conditions. *J. Colloid Interface Sci.* **2004,** *278* (1), 139-145.

(50) Petzold, G.; Schwarz, S., Polyelectrolyte complexes in flocculation applications. In *Polyelectrolyte complexes in the dispersed and solid state II*, Springer: 2013; pp 25-65.

(51) Leu, R.-J.; Ghosh, M. M., Polyelectrolyte characteristics and flocculation. *Journal (American Water Works Association)* **1988**, 159-167.

(52) Al-Asheh, S.; Aidan, A., Operating Conditions of Coagulation-Flocculation Process for High Turbidity Ceramic Wastewater. *Journal of Water and Environmental Nanotechnology* **2017,** *2* (2), 80-87.

(53) Dobrynin, A. V.; Colby, R. H.; Rubinstein, M., Scaling theory of polyelectrolyte solutions. *Macromolecules* **1995,** *28* (6), 1859-1871.

(54) Williams, S. R.; Long, T. E., Recent advances in the synthesis and structure–property relationships of ammonium ionenes. *Prog. Polym. Sci.* **2009,** *34* (8), 762-782.

(55) Woo, S.; Lee, J. Y.; Choi, W.; Moon, M. H., Characterization of ultrahigh-molecular weight cationic polyacrylamide using frit-inlet asymmetrical flow field-flow fractionation and multi-angle light scattering. *J. Chromatogr. A* **2016,** *1429*, 304-310.

(56) Layman, J. M.; Borgerding, E. M.; Williams, S. R.; Heath, W. H.; Long, T. E., Synthesis and characterization of aliphatic ammonium ionenes: Aqueous size exclusion chromatography for absolute molecular weight characterization. *Macromolecules* **2008,** *41* (13), 4635-4641.

(57) Ajjan, F. N.; Ambrogi, M.; Tiruye, G. A.; Cordella, D.; Fernandes, A. M.; Grygiel, K.; Isik, M.; Patil, N.; Porcarelli, L.; Rocasalbas, G., Innovative Polyelectrolytes/Poly (ionic liquid) s for Energy and Environment. *Polym. Int.* **2017**.

(58) Hemp, S. T.; Zhang, M.; Tamami, M.; Long, T. E., Phosphonium ionenes from well-defined step-growth polymerization: thermal and melt rheological properties. *Polymer Chemistry* **2013,** *4* (12), 3582-3590.

(59) Allen Jr, M. H.; Green, M. D.; Getaneh, H. K.; Miller, K. M.; Long, T. E., Tailoring charge density and hydrogen bonding of imidazolium copolymers for efficient gene delivery. *Biomacromolecules* **2011,** *12* (6), 2243-2250.

(60) Kam, S.-k.; Gregory, J., Charge determination of synthetic cationic polyelectrolytes by colloid titration. *Colloids and Surfaces A: Physicochemical and Engineering Aspects* **1999,** *159* (1), 165-179.

(61) Wang, Y.; Gao, B.; Yue, Q.; Zhan, X.; Si, X.; Li, C., Flocculation performance of epichlorohydrin-dimethylamine polyamine in treating dyeing wastewater. *Journal of environmental management* **2009,** *91* (2), 423-431.

(62) Hoover, M. F., Cationic quaternary polyelectrolytes—a literature review. *Journal of Macromolecular Science—Chemistry* **1970,** *4* (6), 1327-1418.

(63) Baade, W.; Hunkeler, D.; Hamielec, A., Copolymerization of acrylamide with cationic monomers in solution and inverse‐microsuspension. *J. Appl. Polym. Sci.* **1989,** *38* (1), 185-201.

(64) Aksberg, R.; Wågberg, L., Hydrolysis of cationic polyacrylamides. *J. Appl. Polym. Sci.* **1989,** *38* (2), 297-304.

(65) Vajihinejad, V.; Guillermo, R.; Soares, J. B., Dewatering Oil Sands Mature Fine Tailings (MFTs) with Poly (acrylamide-co-diallyldimethylammonium chloride): Effect of Average Molecular Weight and Copolymer Composition. *Industrial & Engineering Chemistry Research* **2017,** *56* (5), 1256-1266.

(66) O'Shea, J.-P.; Qiao, G. G.; Franks, G. V., Temperature responsive flocculation and solid–liquid separations with charged random copolymers of poly (N-isopropyl acrylamide). *J. Colloid Interface Sci.* **2011,** *360* (1), 61-70.

(67) Ma, J.; Fu, K.; Jiang, L.; Ding, L.; Guan, Q.; Zhang, S.; Zhang, H.; Shi, J.; Fu, X., Flocculation performance of cationic polyacrylamide with high cationic degree in humic acid synthetic water treatment and effect of kaolin particles. *Sep. Purif. Technol.* **2017,** *181*, 201-212.

(68) Yu, W.-z.; Liu, H.-j.; Xu, L.; Qu, J.-h.; Graham, N., The pre-treatment of submerged ultrafiltration membrane by coagulation—Effect of polyacrylamide as a coagulant aid. *Journal of membrane science* **2013,** *446*, 50-58.

(69) Zhao, Y.; Gao, B.; Qi, Q.; Wang, Y.; Phuntsho, S.; Kim, J.-H.; Yue, Q.; Li, Q.; Shon, H., Cationic polyacrylamide as coagulant aid with titanium tetrachloride for low molecule organic matter removal. *J. Hazard. Mater.* **2013,** *258*, 84-92.

(70) Manafi, M.; Manafi, P.; Agarwal, S.; Bharti, A. K.; Asif, M.; Gupta, V. K., Synthesis of nanocomposites from polyacrylamide and graphene oxide: Application as flocculants for water purification. *J. Colloid Interface Sci.* **2017,** *490*, 505-510.

(71) Huang, X.; Zhao, Y.; Gao, B.; Sun, S.; Wang, Y.; Li, Q.; Yue, Q., Polyacrylamide as coagulant aid with polytitanium sulfate in humic acid-kaolin water treatment: Effect of dosage and dose method. *Journal of the Taiwan Institute of Chemical Engineers* **2016,** *64*, 173-179.

(72) Williams, P. A., *Handbook of industrial water soluble polymers*. John Wiley & Sons: 2008.

(73) Lee, K. E.; Poh, B. T.; Morad, N.; Teng, T. T., Synthesis and characterization of hydrophobically modified cationic polyacrylamide with low concentration of cationic monomer. *Journal of Macromolecular Science®, Part A: Pure and Applied Chemistry* **2009,** *46* (3), 240-249.

(74) Lee, K. E.; Morad, N.; Poh, B. T.; Teng, T. T., Comparative study on the effectiveness of hydrophobically modified cationic polyacrylamide groups in the flocculation of kaolin. *Desalination* **2011,** *270* (1), 206-213.

(75) Banerjee, C.; Gupta, P.; Mishra, S.; Sen, G.; Shukla, P.; Bandopadhyay, R., Study of polyacrylamide grafted starch based algal flocculation towards applications in algal biomass harvesting. *Int. J. Biol. Macromol.* **2012,** *51* (4), 456-461.

(76) Pal, S.; Nasim, T.; Patra, A.; Ghosh, S.; Panda, A., Microwave assisted synthesis of polyacrylamide grafted dextrin (Dxt-g-PAM): Development and application of a novel polymeric flocculant. *Int. J. Biol. Macromol.* **2010,** *47* (5), 623-631.

(77) Pal, S.; Ghorai, S.; Dash, M.; Ghosh, S.; Udayabhanu, G., Flocculation properties of polyacrylamide grafted carboxymethyl guar gum (CMG-g-PAM) synthesised by conventional and microwave assisted method. *J. Hazard. Mater.* **2011,** *192* (3), 1580-1588.

(78) Zhang, C.; Yang, J.; Li, J.; Fang, Z.; He, Y., Poly-(acryl amine–co-dimethyldiallyl ammonium chloride) graft starch flocculant for cleaning-up of wastewater. *Water Sci. Technol.* **2016,** *73* (10), 2394-2401.

(79) Song, H., Synthesis and application of cationic starch graft polymer by using the complex initiation system. *Carbohydr. Polym.* **2010,** *82* (3), 768-771.

(80) Das, R.; Ghorai, S.; Pal, S., Flocculation characteristics of polyacrylamide grafted hydroxypropyl methyl cellulose: An efficient biodegradable flocculant. *Chem. Eng. J.* **2013,** *229*, 144-152.

(81) Wang, J.-P.; Chen, Y.-Z.; Wang, Y.; Yuan, S.-J.; Yu, H.-Q., Optimization of the coagulation-flocculation process for pulp mill wastewater treatment using a combination of uniform design and response surface methodology. *Water Res.* **2011,** *45* (17), 5633-5640.

(82) Lu, Y.; Shang, Y.; Huang, X.; Chen, A.; Yang, Z.; Jiang, Y.; Cai, J.; Gu, W.; Qian, X.; Yang, H., Preparation of strong cationic chitosan-graft-polyacrylamide

flocculants and their flocculating properties. *Industrial & Engineering Chemistry Research* **2011,** *50* (12), 7141-7149.

(83) Tian, D.; Wu, X.; Liu, C.; Xie, H. Q., Synthesis and flocculation behavior of cationic konjac glucomannan containing quaternary ammonium substituents. *J. Appl. Polym. Sci.* **2010,** *115* (4), 2368-2374.

(84) Zheng, H.; Sun, Y.; Guo, J.; Li, F.; Fan, W.; Liao, Y.; Guan, Q., Characterization and evaluation of dewatering properties of PADB, a highly efficient cationic flocculant. *Industrial & Engineering Chemistry Research* **2014,** *53* (7), 2572-2582.

(85) Sakohara, S.; Yagi, S.; Iizawa, T., Dewatering of inorganic sludge using dual ionic thermosensitive polymers. *Sep. Purif. Technol.* **2011,** *80* (1), 148-154.

(86) Sakohara, S.; Kawachi, T.; Gotoh, T.; Iizawa, T., Consolidation of suspended particles by using dual ionic thermosensitive polymers with incorporated a hydrophobic component. *Sep. Purif. Technol.* **2013,** *106*, 90-96.

(87) Yang, Z. L.; Gao, B. Y.; Li, C. X.; Yue, Q. Y.; Liu, B., Synthesis and characterization of hydrophobically associating cationic polyacrylamide. *Chem. Eng. J.* **2010,** *161* (1), 27-33.

(88) Ma, J.; Shi, J.; Ding, H.; Zhu, G.; Fu, K.; Fu, X., Synthesis of cationic polyacrylamide by low-pressure UV initiation for turbidity water flocculation. *Chem. Eng. J.* **2017,** *312*, 20-29.

(89) Zhu, J.; Zheng, H.; Jiang, Z.; Zhang, Z.; Liu, L.; Sun, Y.; Tshukudu, T., Synthesis and characterization of a dewatering reagent: cationic polyacrylamide (P (AM–DMC–DAC)) for activated sludge dewatering treatment. *Desalination and Water Treatment* **2013,** *51* (13-15), 2791-2801.

(90) Ariffin, A.; Razali, M.; Ahmad, Z., PolyDADMAC and polyacrylamide as a hybrid flocculation system in the treatment of pulp and paper mills waste water. *Chem. Eng. J.* **2012,** *179*, 107-111.

(91) Guan, Q.; Zheng, H.; Zhai, J.; Zhao, C.; Zheng, X.; Tang, X.; Chen, W.; Sun, Y., Effect of template on structure and properties of cationic polyacrylamide: characterization and mechanism. *Industrial & Engineering Chemistry Research* **2014,** *53* (14), 5624-5635.

(92) Li, X.; Zheng, H.; Gao, B.; Sun, Y.; Liu, B.; Zhao, C., UV-initiated template copolymerization of AM and MAPTAC: Microblock structure, copolymerization mechanism, and flocculation performance. *Chemosphere* **2017,** *167*, 71-81.

(93) Li, X.; Zheng, H.; Gao, B.; Sun, Y.; Tang, X.; Xu, B., Optimized preparation of micro-block CPAM by response surface methodology and evaluation of dewatering performance. *RSC Advances* **2017,** *7* (1), 208-217.

(94) Chen, W.; Zheng, H.; Guan, Q.; Teng, H.; Zhao, C.; Zhao, C., Fabricating a flocculant with controllable cationic microblock structure: characterization and sludge conditioning behavior evaluation. *Industrial & Engineering Chemistry Research* **2016,** *55* (10), 2892-2902.

(95) Guan, Q.; Tang, M.; Zheng, H.; Teng, H.; Tang, X.; Liao, Y., Investigation of sludge conditioning performance and mechanism by examining the effect of charge density on cationic polyacrylamide microstructure. *Desalination and Water Treatment* **2016,** *57* (28), 12988-12997.

(96) Zhang, X.; Huang, Y.; Fu, K.; Yuan, S.; Huang, C.; Li, H., Preparation and performance of cationic flocculant for papermaking based on the graft polymerization of cationic chains from colloidal silica particles. *Colloids and Surfaces A: Physicochemical and Engineering Aspects* **2016,** *491*, 29-36.

(97) Wandrey, C.; Jaeger, W., Copolymerization of dimethyl diallyl ammonium chloride and acryl amide. *Acta Polym.* **1985,** *36* (2), 100-102.

(98) Bolto, B., Reaction of chlorine with organic polyelectrolytes in water treatment: a review. *Journal of Water Supply: Research and Technology-Aqua* **2005,** *54* (8), 531-544.

(99) Razali, M.; Ahmad, Z.; Ahmad, M.; Ariffin, A., Treatment of pulp and paper mill wastewater with various molecular weight of polyDADMAC induced flocculation. *Chem. Eng. J.* **2011,** *166* (2), 529-535.

(100) Edzwald, J. K., *Water Quality and Treatment A Handbook on Drinking Water*. McGrawHill: 2010.

(101) Yu, J.; Wang, D.; Ge, X.; Yan, M.; Yang, M., Flocculation of kaolin particles by two typical polyelectrolytes: A comparative study on the kinetics and floc structures. *Colloids and Surfaces A: Physicochemical and Engineering Aspects* **2006,** *290* (1), 288-294.

(102) Bauer, D.; Killmann, E.; Jaeger, W., Flocculation and stabilization of colloidal silica by the adsorption of poly-diallyl-dimethyl-ammoniumchloride (PDADMAC) and of copolymers of DADMAC with N-methyl-N-vinyl-acetamide (NMVA). *Colloid. Polym. Sci.* **1998,** *276* (8), 698-708.

(103) Moussas, P.; Zouboulis, A., Synthesis, characterization and coagulation behavior of a composite coagulation reagent by the combination of polyferric sulfate (PFS) and cationic polyelectrolyte. *Sep. Purif. Technol.* **2012,** *96*, 263-273.

(104) Zheng, H.; Tshukudu, T.; Yang, J., Optimization of the coagulation-flocculation process for wastewater treatment using polymeric ferric sulfate (PFS)-Poly-diallyl dimethyl ammonium chloride (PDADMAC) composite coagulant. *Hydrol Curr Res* **2012,** *3*, 4.

(105) Li, X.; Zhang, Y.; Zhao, X.; Gao, N.; Fu, T., The characteristics of sludge from enhanced coagulation processes using PAC/PDMDAAC composite coagulants in treatment of micro-polluted raw water. *Sep. Purif. Technol.* **2015,** *147*, 125-131.

(106) John, W.; Buckley, C.; Jacobs, E.; Sanderson, R. In *Synthesis and use of PolyDADMAC for water purification*, Biennial Conference of the Water Institute of Southern Africa, Durban, South Africa, 2002.

(107) Anthony, R. J.; Sims, R. C., Chitosan-graft-polydiallyldimethyl ammonium chloride for microalgae harvesting from wastewater. *Desalination and Water Treatment* **2016,** *57* (2), 881-887.

(108) Lv, S.; Sun, T.; Zhou, Q.; Liu, J.; Ding, H., Synthesis of starch-g-p (DMDAAC) using HRP initiation and the correlation of its structure and sludge dewaterability. *Carbohydr. Polym.* **2014,** *103*, 285-293.

(109) Abdiyev, K. Z.; Toktarbay, Z.; Zhenissova, A. Z.; Zhursumbaeva, M. B.; Kainazarova, R. N.; Nuraje, N., The new effective flocculants–Copolymers of N, N-dimethyl-N, N-diallyl-ammonium chloride and N, N-dimethylacrylamide. *Colloids and Surfaces A: Physicochemical and Engineering Aspects* **2015,** *480*, 228-235.

(110) Vorchheimer, N., Polyelectrolytes for Water and Wastewater Treatment. *CRC Press, Boca Raton* **1981**.

(111) Wang, Y.-F.; Gao, B.-Y.; Yue, Q.-Y.; Wang, Y.; Yang, Z.-L., Removal of acid and direct dye by epichlorohydrin–dimethylamine: flocculation performance and floc aggregation properties. *Bioresour. Technol.* **2012,** *113*, 265-271.

(112) Ghimici, L.; Nichifor, M., Novel biodegradable flocculanting agents based on cationic amphiphilic polysaccharides. *Bioresour. Technol.* **2010,** *101* (22), 8549-8554.

(113) Song, Y.; Zhang, J.; Gan, W.; Zhou, J.; Zhang, L., Flocculation properties and antimicrobial activities of quaternized celluloses synthesized in NaOH/urea aqueous solution. *Industrial & Engineering Chemistry Research* **2009,** *49* (3), 1242-1246.

(114) Gupta, S.; Nayunigari, M.; Misra, R.; Ansari, F.; Dionysiou, D.; Maity, A.; Bux, F., Synthesis and performance evaluation of a new polymeric composite for the treatment of textile wastewater. *Industrial & Engineering Chemistry Research* **2015,** *55* (1), 13-20.

(115) Yang, Z.; Liu, X.; Gao, B.; Zhao, S.; Wang, Y.; Yue, Q.; Li, Q., Flocculation kinetics and floc characteristics of dye wastewater by polyferric chloride–poly-epichlorohydrin–dimethylamine composite flocculant. *Sep. Purif. Technol.* **2013,** *118*, 583-590.

(116) Yang, Z.; Lu, X.; Gao, B.; Wang, Y.; Yue, Q.; Chen, T., Fabrication and characterization of poly (ferric chloride)-polyamine flocculant and its application to the decolorization of reactive dyes. *Journal of materials science* **2014,** *49* (14), 4962-4972.

(117) Sun, S.; Gao, B.; Yue, Q.; Li, R.; Song, W.; Bu, F.; Zhao, S.; Jia, R.; Song, W., Comparison of epichlorohydrin–dimethylamine with other cationic organic polymers as coagulation aids of polyferric chloride in coagulation–ultrafiltration process. *J. Hazard. Mater.* **2016,** *307*, 108-118.

(118) Xu, C.; Wang, Y.; Nie, R.; Li, M.; Li, B., Photo-Initiated Fabrication of Zwitterionic Polyacrylamide with Enhanced Flocculation Activity. *Asian J. Chem.* **2014,** *26* (5), 1352.

(119) Yang, Z.; Shang, Y.; Lu, Y.; Chen, Y.; Huang, X.; Chen, A.; Jiang, Y.; Gu, W.; Qian, X.; Yang, H., Flocculation properties of biodegradable amphoteric chitosan-based flocculants. *Chem. Eng. J.* **2011,** *172* (1), 287-295.

(120) Jiang, X.; Qi, Y.; Wang, S.; Tian, X., New amphoteric flocculant containing beta-cyclodextrin, synthesis, charaterization and decolorization properties. *J. Hazard. Mater.* **2010,** *173* (1), 298-304.

(121) Rooney, T. R.; Gumfekar, S. P.; Soares, J. B.; Hutchinson, R. A., Cationic Hydrolytically Degradable Flocculants with Enhanced Water Recovery for Oil Sands Tailings Remediation. *Macromolecular Materials and Engineering* **2016,** *301* (10), 1248-1254.

(122) Gumfekar, S. P.; Rooney, T. R.; Hutchinson, R. A.; Soares, J. B., Dewatering Oils Sands Tailings with Degradable Polymer Flocculants. *ACS Applied Materials & Interfaces* **2017**.

(123) Kan, K. H.; Li, J.; Wijesekera, K.; Cranston, E. D., Polymer-grafted cellulose nanocrystals as pH-responsive reversible flocculants. *Biomacromolecules* **2013,** *14* (9), 3130-3139.

(124) Vandamme, D.; Eyley, S.; Van den Mooter, G.; Muylaert, K.; Thielemans, W., Highly charged cellulose-based nanocrystals as flocculants for harvesting Chlorella vulgaris. *Bioresour. Technol.* **2015,** *194*, 270-275.

(125) Jasmani, L.; Eyley, S.; Wallbridge, R.; Thielemans, W., A facile one-pot route to cationic cellulose nanocrystals. *Nanoscale* **2013,** *5* (21), 10207-10211.

(126) Eyley, S.; Vandamme, D.; Lama, S.; Van den Mooter, G.; Muylaert, K.; Thielemans, W., CO 2 controlled flocculation of microalgae using pH responsive cellulose nanocrystals. *Nanoscale* **2015,** *7* (34), 14413-14421.

(127) Chen, Y.; Geurts, M.; Sjollema, S. B.; Kramer, N. I.; Hermens, J. L.; Droge, S. T., Acute toxicity of the cationic surfactant C12‐benzalkonium in different bioassays: How test design affects bioavailability and effect concentrations. *Environ. Toxicol. Chem.* **2014,** *33* (3), 606-615.

(128) Jing, G.; Zhou, Z.; Zhuo, J., Quantitative structure–activity relationship (QSAR) study of toxicity of quaternary ammonium compounds on Chlorella pyrenoidosa and Scenedesmus quadricauda. *Chemosphere* **2012,** *86* (1), 76-82.

(129) Sánchez-Fortún, S.; Marvá, F.; D'ors, A.; Costas, E., Inhibition of growth and photosynthesis of selected green microalgae as tools to evaluate toxicity of dodecylethyldimethyl-ammonium bromide. *Ecotoxicology* **2008,** *17* (4), 229-234.

(130) Cooper, J. C., Review of the environmental toxicity of quaternary ammonium halides. *Ecotoxicology and environmental safety* **1988,** *16* (1), 65-71.

(131) Martínez-Carballo, E.; González-Barreiro, C.; Sitka, A.; Kreuzinger, N.; Scharf, S.; Gans, O., Determination of selected quaternary ammonium compounds by liquid chromatography with mass spectrometry. Part II. Application to sediment and sludge samples in Austria. *Environ. Pollut.* **2007,** *146* (2), 543-547.

(132) Martínez-Carballo, E.; Sitka, A.; González-Barreiro, C.; Kreuzinger, N.; Fürhacker, M.; Scharf, S.; Gans, O., Determination of selected quaternary ammonium compounds by liquid chromatography with mass spectrometry. Part I. Application to surface, waste and indirect discharge water samples in Austria. *Environ. Pollut.* **2007,** *145* (2), 489-496.

(133) Boethling, R. S., Environmental fate and toxicity in wastewater treatment of quaternary ammonium surfactants. *Water Res.* **1984,** *18* (9), 1061-1076.

(134) Zhang, C.; Cui, F.; Zeng, G.-m.; Jiang, M.; Yang, Z.-z.; Yu, Z.-g.; Zhu, M.-y.; Shen, L.-q., Quaternary ammonium compounds (QACs): a review on occurrence, fate and toxicity in the environment. *Sci. Total Environ.* **2015,** *518*, 352-362.

(135) Harford, A. J.; Hogan, A. C.; Jones, D. R.; van Dam, R. A., Ecotoxicological assessment of a polyelectrolyte flocculant. *Water Res.* **2011,** *45* (19), 6393-6402.

(136) Costa, R.; Pereira, J.; Gomes, J.; Gonçalves, F.; Hunkeler, D.; Rasteiro, M., The effects of acrylamide polyelectrolytes on aquatic organisms: relating toxicity to chain architecture. *Chemosphere* **2014,** *112*, 177-184.

(137) Fischer, D.; Li, Y.; Ahlemeyer, B.; Krieglstein, J.; Kissel, T., In vitro cytotoxicity testing of polycations: influence of polymer structure on cell viability and hemolysis. *Biomaterials* **2003,** *24* (7), 1121-1131.

Chapter 3: Sustainable Additive Manufacturing: Predicting Binder Jettability of Water-Soluble, Biodegradable, and Recyclable Polymers

(Published in Polymer International, **2020,** *accepted*)

Emily M. Wilts[1] and Timothy E. Long[1*]

[1]*Department of Chemistry, Macromolecules Innovation Institute, Virginia Tech, Blacksburg, VA 24061*

[2]*Department of Mechanical Engineering, Macromolecules Innovation Institute, Virginia Tech, Blacksburg, VA 24061*

3.1 Abstract

Additive manufacturing generates custom, rapidly produced products while reducing waste through often utilizing water-soluble, biodegradable, and recyclable polymers for a more sustainable future. Binder jetting additive manufacturing (BJ AM) creates 3D objects upon depositing liquid adhesive onto a powder bed, while a roller spreads powder over a build stage to form subsequent layers. Many factors affect jettability and printability including printhead design, binder material, binder solvent, and powder characteristics. Material design for higher strength BJ AM parts using metals, ceramics, or polymers exploits binders or particles that transform into thermosets or permanently shaped matrices through thermal or UV curing and sintering. While many BJ AM examples utilize biodegradable, water-soluble, and recyclable polymers for biomedical and industrial applications, a wider array of opportunities exist to degrade, dissolve, and reuse printed materials. Systematically shifting to these polymers will facilitate reuse and recycling of both binders and powders, but more studies to improve part strength are required. This review describes an overview of polymer jettability and a perspective into opportunities currently underutilized in transitioning BJ AM into a more sustainable AM platform.

3.2 Introduction

Binder jetting additive manufacturing (BJ AM) is a powder-based 3D printing method used to produce parts for applications ranging from biomedical to aerospace industries.[1] In 1993, a group from MIT invented BJ AM, and Z Corporation obtained the license in 1995.[2] BJ AM exhibits a higher build rate compared to other extrusion and vat photopolymerization AM processes because of the smaller amounts of material deposited for printing large objects and no need for support material. Current systems print at 200 cm^3 min^{-1} with build volumes up to 780 mm x 400 mm x 400 mm.[3,4] Depicted in **Figure 3.1**, a powder bed equipped with a roller to spread powder layers acts as the printer build stage. Elevators below the build stage move lower to allow space for the next powder layer while auxiliary elevators move the powder reservoir upward to help deliver the powder. Printability depends on three main parameters: (1) piezoelectric vs. thermal printhead mechanism, (2) binder composition and solvent, and (3) powder penetration. After initial printing, the 3D object is bound together through adhered particles, termed a "green body". Post-processing is common for metal and ceramic parts where high temperatures thermally degrades and vaporizes the binder and sinters particles. Other post-processing techniques include moderate heating (> 60 ^oC) to evaporate solvent without binder removal and sintering.[5] Our research group has extensively reviewed the AM literature with a focus on the correlation of polymer structure on printability for diverse printing modalities.[6–9]

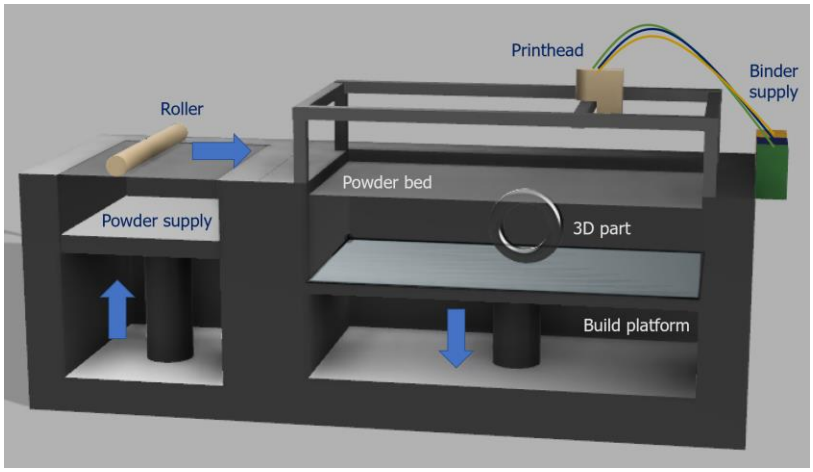

Figure 3.1. Schematic of BJ AM.

Manufacturing accounts for 31% of greenhouse gases in the world and 19% of total energy use in the United States.[10] Compared to subtractive manufacturing, additive manufacturing generates less waste and accelerates manufacturing of custom parts. Many studies examining energy use, material use and recovery, and developing cross-process assessment models of other powder bed AM platforms are established, but because of inferior mechanical performance of BJ AM parts, few studies exist.[11–14] As an example, Tang *et. al.* examined the energy use and CO_2 production of a binder-jetted aircraft engine bracket compared to fabrication through traditional computer numerical control (CNC) milling processes. These researchers found the former case consumed 23% less energy and produced 53% less CO_2.[15] While BJ AM already provides more sustainable manufacturing methods compared to traditional processes, there are still opportunities remaining through using degradable or thermoplastic binders, which enables isolation and reuse of binders.

3.3 Printhead Mechanism

Figure 3.2 depicts BJ AM processing considerations when choosing a printhead, binder, and powder. While application ultimately directs decisions on binder type and

powder, compatibility within all three parameters generally dictates successful printing. Piezoelectric and thermal printheads facilitate ejection of binder from the nozzle. Piezoelectric systems contain a piezoelectric element adjacent to the nozzle and applied electric pulses mechanically move the element, forcing a drop out of the nozzle.[16,17] This mechanism is more controlled compared to thermal printheads because different applied waveforms provide varying ejection shear rates and more precise volume of binder. Thermal printheads utilize explosive evaporation to create a vapor bubble within the nozzle that forces drop ejection.[18] Electrical pulses heat a resistor element in the nozzle, which locally and rapidly heats the solvent to the superheat limit temperature (T_{SL}), which is 90% of the critical fluid temperature. This rapid liquid-vapor phase change is known as explosive evaporation and occurs at 312 ^{o}C for water.[19,20] While thermal printheads are less expensive, piezoelectric systems provide more precise placement of binder, more control over ejection, and in some cases, ejection of higher viscosities.

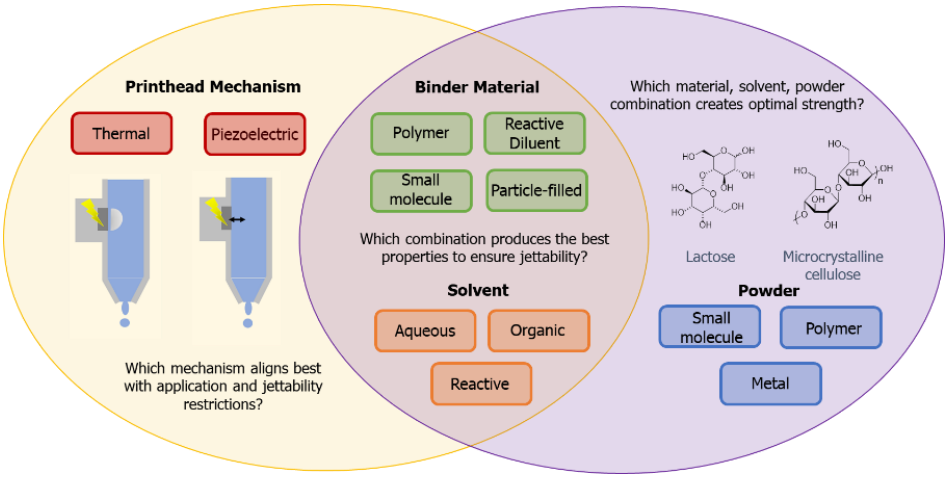

Figure 3.2. Choosing binder materials for BJ AM depends on solution property restrictions of printhead mechanisms and compatibility with powders.

3.4 Binder and Solvent

The Ohnesorge number (*Oh*) (**Eqn. 3**) predicts jettability in drop-on-demand BJ systems based on viscosity, surface tension, and density. *Oh* manifests from two other dimensionless numbers called the Reynolds (*Re*) number (**Eqn. 1**) and Weber (*We*) number (**Eqn. 2**), which represent optimal energy for drop ejection and stable drop formation. υ, ρ, α, σ, and η represent drop velocity, density, capillary nozzle radius, surface tension, and viscosity, respectively.[17,21,22] **Eqn. 4** is the inverse of the *Oh* number called the *Z* parameter and also predicts jettability. Fromm *et. al.* first established this grouping of dimensionless numbers as predictive of stable drop formation at Z > 2.[22]

$$Re = \frac{\upsilon \rho \alpha}{\eta} \quad \textbf{Eqn. 1}$$

$$We = \frac{\upsilon^2 \rho \alpha}{\sigma} \quad \textbf{Eqn. 2}$$

$$\frac{We^{0.5}}{Re} = Oh\,\# = \frac{\eta}{(\sigma \rho \alpha)^{0.5}} \quad \textbf{Eqn. 3}$$

$$\frac{1}{Oh} = Z \quad \textbf{Eqn. 4}$$

Expanding on this theory and using a piezoelectric printhead and particle-filled binders, Reis and Derby *et. al.* established a Z parameter jettable range of 1-10.[16] Ranges of jettable solution viscosity and surface tensions are 1 to 20 mPa·s and 20 to 40 mN m^{-1}, respectively, where these properties have a largest effect on jettability.[23,24] Z < 1 corresponds to binders exhibiting high viscosities where viscous dissipation prevents ejections of drops. Binders with Z > 10 create undesirable satellite drops upon ejection, which creates inconsistent binder deposit and thus inconsistent layers.[25] This range remains as a benchmark, but varies greatly depending on printhead mechanism and type of binders. Example binders include small molecules, polymers, particles and oligomers, which lead to different rheological properties in solution.[16,19,21,26,27]

Depending on printhead mechanism and binder material, recent literature suggests varying Z parameter ranges to predict printability. Reis *et. al.* established the range of Z =

1-10 using computational fluid dynamics models and a parallel study using ceramic-filled binders and a piezoelectric printhead.[21,25] Jang *et. al.* investigated binders containing water, ethylene glycol, and water and found jettable ranges of Z = 4-14. They examined fluids ranging from Z = 1-17 using in situ droplet formation and considering ejection accuracy and single drop formation, while using the maximum jetting frequencies on a piezoelectric printhead.[26] These two experiments are in some agreement, but varying binder materials may cause the differences in jettable ranges. Ozkol *et. al.* conducted a study using a thermal printhead on ceramic-filled binders and found the previously established jettability upper range did not apply to thermal printheads. They cited the considerably high ejection pressure of thermal printheads compared to piezoelectric printheads as a possible explanation for jetting high surface tensions binders (> 50 mN m^{-1}).[19]

Binder selection depends on the targeted application, selected powder, and post-processing methods. Printing with metal or ceramic powders requires post-print sintering to increase part density and strength.[28] This frequently results in binders thermally degrading and vaporizing, which maintains high density and strength. Common binders for metal adherence include organic crosslinkers, polyacrylic acids, and polysiloxanes.[29–31] Other powders that do not need sintering for certain applications, i.e., lactose for oral tablets require consideration of binders remaining in the final part. Therefore, biocompatibility and water-solubility of binders become increasingly important for biomedical applications, where poly(vinyl pyrrolidone) and poly(L-lactide) represent common binders.[5,32]

Binders adhere particles together through two common methods named In-Liquid or In-Bed. In-Liquid requires the liquid binder to contain all of the adhesive materials while In-Bed also incorporates binder coatings around particles that when solvated, glues powders together.[33,34] In-Liquid methods occasionally clog nozzles, but In-Bed methods also decrease final part density if sintering is necessary.[35–37] Some researchers developed more porous structures using In-Bed techniques with starch and dextran and aqueous solutions, which solidified and increased inter-particle binder upon solvation.[34]

3.4.1 Polymer-containing binders

Polymeric solutions exhibit viscoelastic properties, which impacts jettability on piezoelectric and thermal printheads. Relaxation times dictate the ability of the polymers to shear thin and extend thus affecting jettability. Jetting processes actuation pulses are estimated at 20 μs, which raises concern for concentrated polymer solutions with relaxations times of 0.1 s.[38,39] Hutchings *et. al.* investigated this relationship through developing a quantitative model and jetting dilute polymeric solutions to establish jettability parameters based on the Weissenberg (*Wi*) and polymer extensibility (*L*) on piezoelectric printheads. and developed a quantitative model which predicts jettability of said solutions based on the system's *Wi* number and *L*.[40] Regime I represented Newtonian fluids where polymer chains are relaxed ($Wi < 1/2$) and as concentration increases, in Regime II the solution becomes viscoelastic, but the chains are not at the greatest extensibility ($1/2 < Wi < L$). In Regime III, the polymer chains are fully extended in the ligament ($Wi > L$). In general, as molecular weight increases, the *Wi* number increases, which decreases the concentrations where the polymeric solution is jettable. They

confirmed their results using low dispersity, linear polystyrene samples in diethyl phthalate from 24 to 488 kDa.[39,41]

Other studies investigated using the critical overlap concentration (C^*) as a maximum polymer concentration of linear, star, and graft polymers on thermal printheads.[5,42] As the concentration of polymers in solution increases, the solution exhibits transitions from dilute to semi-dilute unentangled regimes. Dilute solutions behave as Newtonian fluids, and the viscosity of the solution solely depends on the contribution from single-coil polymer chains.[43–45] The critical overlap concentration (C^*) denotes the transition from the dilute to the semi-dilute unentangled regime, where the solution acts as a viscoelastic fluid and the viscosity depends on the interaction between polymer chains. Wilts and Long *et. al.* showed linear, 4-arm star, and graft poly(vinyl pyrrolidone) jet at varying molecular weights below C^* where it also acted as an upper jettable bound.[5]

Many polymers used in BJ AM are biodegradable, water-soluble, or recyclable, which may deem this AM platform suitable for more sustainable manufacturing in the future. Most biodegradable polymers used in BJ AM not only create products for biomedical applications such as oral tablets, implantable devices, and tissue regeneration, but also have potential for other applications requiring high strength parts.[46–48] Poly L-lactide (PLLA), ethyl cellulose, microcrystalline cellulose, polycaprolactone (PCL), hydroxyapatite (HA), and maltodexdrin represent popular powder materials enabling biocompatibility and strength.[32,49–54] Others used these materials as binders, for example, Wu *et al.* utilized PLLA as a binder and powder for implantable devices with slow drug release. *In vitro* studies revealed an initial burst of active ingredient and a steady decrease

in release rate over 30 days.[55] Ethyl cellulose and PCL also served as effective binders for zero-order release and delayed release tablets, respectively.[49,50] A combination of maltodextrin and poly(vinyl alcohol) as binders for bone replacement materials reached compression strengths of 375 MPa, indicating biodegradable polymers may offer potential for other high strength applications.[48]

BJ AM utilizes water-soluble polymers primarily as binders, but water-soluble polymers also serve as powders for biomedical applications. Poly(vinyl pyrrolidone) (PVP), also called Povidone®, represents one of the most popular polymeric binders owing to its biocompatibility, water-solubility, high glass transition temperatures, and binding properties.[5,56] PVP in BJ AM functions for oral tablet, implantable devices, resorbable devices, and 2D printing applications.[57–59] The inherent solubility of PVP renders this binder optimal for immediate release tablets and devices, which help patients who have problems swallowing pills.[42,60] Poly(vinyl alcohol) and poly(ethylene oxide) also function as successful binders and powders for bone replacement and oral tablets.[61–63]

3.5 Powder penetration and recycling

Interactions and compatibility of the powder and binder govern the ability for binder to penetrate and wet the surfaces of particles. Metals, small molecules, and polymers all act as powders for BJ AM depending on the application.[4,5,48,64] Miyanaji *et. al.* developed a physics-based model that built a relationship between capillary pressure and binder saturation, where binder saturation is the ratio of volume of binder jetted to total pore volume.[65] While this system aided in characterizing the static relationships in the binder-powder penetration process, Bai *et. al.* recognized a need for a system that

investigated dynamic interactions between powder and binder. Measuring the binder penetration depth and time enabled calculation of the dynamic contact angle.[66]

The first two material considerations in terms of successful penetration of the binder droplet into the powder bed are the porosity between particles and the viscosity and surface tension relationship in the binder. As the porosity of the powder particles increases, the faster the binder will penetrate the substrate because of increased capillary forces. Higher viscosity and lower surface tension binders will penetrate the substrate slower because of the decreased capillary forces.[66] Suwanprateeb *et. al.* demonstrated that a binder with more than 40 wt % maltodextrin did not penetrate the surface of PMMA particles because the viscosity of the binder was too high.[48]

The wettability and compatibility of the powder and binder is also essential when considering material design for binder jetting.[67–69] Bai *et. al.* developed a method of calculating the dynamic contact angle of binder and powder interactions based on penetration time. Contact angles of below 90^{o} represent fast penetration of the binder into the powder bed, which are optimal conditions for printing. In this specific example, the higher the solid content, the slower the binder penetration into the powder bed.[66] When designing new materials for binder jetting, hydrophobic and hydrophilic interactions between binder and powder govern this relationship. For example, a combination such as lactose as the powder and a water-based binder would most likely have a dynamic contact angle of below 90^{o} because they are both hydrophilic materials. If the binder was mostly made of hexanes, the particles and binder would not be compatible thus resulting in poor binder penetration into the substrate.[17,70]

Extensive research into life cycle analyses of metal-based additive manufacturing (including BJ AM) explores energy use, material recycling and reuse, and process optimization.[71] Recycled free powder after a print may maintain defects from bed temperature and sintering outside of the print area. One of the challenges is a lack of standardization in metal/binder combinations, processes, and post-processing, which is very important for powder recycling and reuse.[72,73] Recycled powder should exhibit the same properties as the original, but recent experiments reported a slightly higher PDI in particle size in recycled powders, probably due to mild chemical or physical changes during the printing and post-processing steps. Suggested processes for recovering powders only from the printing beds include sieving and water vacuums, which also may affect physical characteristics of recycled powders. Manufacturers reported a 74-80% powder recovery rate where irregularly shaped particles were removed.[71] Studies also suggest the potential of reusing materials from damaged parts through reserve engineering, laser additive repairs, and free-form surface reconstruction.[74] Few studies investigated recycling and reusing BJ AM parts made from polymers, but potential solubility and thermal reprocessing could render this technology optimal for a circular economy.[75]

Applications of BJ AM encompass multiple disciplines and function as aerospace parts to bone replacement materials. **Figure 3.3** depicts three common BJ AM produced objects ranging across manufacturing sectors. **Figure 3.3A** depicts oral pills made through BJ AM of a lactose and poly(vinyl pyrrolidone)-based binder. A fundamental study elucidated pill strength dependency on molecular weight and architecture.[5] **Figure 3.3B** represents an example of bone replacement where the authors investigated strength and porosity of printed parts increasing maltodextrin concentrations in the binder from 10 to

60%.[48] Lastly, Figure 3.**3C** depicts an engine bracket used in a case study to determine energy and CO_2 savings through manufacturing through AM or computer numerical control (CNC) milling processes.[15]

Figure 3.3. BJ AM **(A)** oral tablets, **(B)** skull implant for bone replacement, and **(C)** an engine bracket. (Reproduced with the permission of Wilts *et. al.*[5] Copyright (2019), American Chemical Society, Patirupanusara *et. al.*[48], and Tang *et. al*.[15])

3.6 Perspective

BJ AM is an extremely industrially relevant manufacturing process, however, to expand the variety of novel binder materials, more consensus and clarity of jettability parameters must be established. The Z parameter is a simple metric based deeply on fluid mechanics but falls short in dictating suitability across different printhead mechanisms and binder material type. Studies show varying jettable ranges depending on piezoelectric or thermal actuation for drop ejection of 1-10 and 4-14, respectively. The established range also greatly varies based on binder type i.e. small molecules, oligomers, polymer, or particle-filled solutions. Polymeric viscoelasticity is also not taken into account and as a result, quantitative modeling of jetting polymer solutions soon replaced the Z parameter as

the jettability predictor. The unique rheological properties of each listed binder type matched with more accurate shear rate estimates of jetting may also help mold jettability parameters. Moving forward, developing more accurate predictive jettability parameters for each printhead mechanism and type of binder will provide clarity into how to develop new binders for BJ AM.

Based on current literature, potential in sustainable and circular economy manufacturing using BJ AM lies in discovering methods to recycle printed parts using thermoplastic binders, thermoplastic powders, and reversible crosslinks. Thermoplastic binders not only allow for thermal degradation post-printing when using metal or ceramic powders, but also possess the potential to form recyclable, strong BJ AM parts. For example, poly(methyl methacrylate) (PMMA) powder, poly(vinyl alcohol) and maltodextrin binders formed BJ AM parts with 375 MPa compressive strength.[48] To recycle and reuse the binder, an aqueous wash could isolate the binder without dissolving the PMMA. PMMA could also selectively dissolve and used in subsequent prints as an effort to "unzip" the BJ AM process. Unfortunately, non-crosslinked polymers may not provide sufficient strength for BJ AM parts, however degradable or reversible bonds have not been widely utilized. Crosslinked polymers provide strength in BJ AM but unfortunately do not dissolve and cannot be recycled. Utilizing hydrolytically cleavable bonds, thermally reversible bonds, or dynamic covalent networks will provide part strength, and the opportunity to degrade printed parts.

3.7 Acknowledgements

The authors would like to thank Prof. Christopher Williams, Yun Bai, Susan Ma, and Ashwash Kumar for extensive discussions about BJ AM. Thank you to the

Macromolecules Innovation Institute and MACR program for stipend support and access to advanced characterization tools.

3.8 References

(1) Ziaee, M.; Crane, N. B. Binder Jetting: A Review of Process, Materials, and Methods. *Additive Manufacturing*. Elsevier B.V. August 1, 2019, pp 781–801. https://doi.org/10.1016/j.addma.2019.05.031.

(2) Sachs, E.; Cima, M.; Williams, P.; Brancazio, D.; Cornie, J. Three Dimensional Printing: Rapid Tooling and Prototypes Directly from a CAD Model. *J. Manuf. Sci. Eng. Trans. ASME* **1992**, *114* (4), 481–488. https://doi.org/10.1115/1.2900701.

(3) Nied, H. F.; Taylor, C. A.; Delorenzi, H. G. Three-dimensional Finite Element Simulation of Thermoforming. *Polym. Eng. Sci.* **1990**, *30* (20), 1314–1322. https://doi.org/10.1002/pen.760302009.

(4) Bai, Y.; Williams, C. B. An Exploration of Binder Jetting of Copper. *Rapid Prototyp. J.* **2015**, *21* (2), 177–185. https://doi.org/10.1108/RPJ-12-2014-0180.

(5) Wilts, E.; Ma, D.; Bai, Y.; Williams, C. B.; Long, T. E. Comparison of Linear and 4-Arm Star Poly(Vinyl Pyrrolidone) for Aqueous Binder Jetting Additive Manufacturing of Personalized Dosage Tablets. *ACS Appl. Mater. Interfaces* **2019**, *11* (27), 23938–23947. https://doi.org/10.1021/acsami.9b08116.

(6) Herzberger, J.; Sirrine, J. M.; Williams, C. B.; Long, T. E. Polymer Design for 3D Printing Elastomers: Recent Advances in Structure, Properties, and Printing. *Prog. Polym. Sci.* **2019**, *97*, 101144. https://doi.org/10.1016/j.progpolymsci.2019.101144.

(7) Mondschein, R. J.; Kanitkar, A.; Williams, C. B.; Verbridge, S. S.; Long, T. E. Polymer Structure-Property Requirements for Stereolithographic 3D Printing of Soft Tissue Engineering Scaffolds. *Biomaterials* **2017**, *140*, 170–188. https://doi.org/10.1016/J.BIOMATERIALS.2017.06.005.

(8) Pekkanen, A. M.; Mondschein, R. J.; Williams, C. B.; Long, T. E. 3D Printing Polymers with Supramolecular Functionality for Biological Applications. *Biomaterials* **2017**, *18* (9), 2669–2687. https://doi.org/10.1021/acs.biomac.7b00671.

(9) Scott, P. J.; Meenakshisundaram, V.; Hegde, M.; Kasprzak, C.; Winkler, C.; Feller, K.; Williams, C. B.; Long, T. E. 3D Printing Latex: A Route to Complex Geometries of High Molecular Weight Polymers. *ACS Appl. Mater. Interfaces* **2020**, *12* (9), 10918–10928. https://doi.org/10.1021/acsami.9b19986.

(10) Nancy Diaz, Moneer Helu, Stephen Jayananthan, Yifen Chen, Arpad Horvath, D. D. Environmental Analysis of Milling Machine Tool Use in Various Manufacturing Environments. In *IEEE Xplore*; Arlington, VA, 2010; p 11416445. https://doi.org/10.1109/ISSST.2010.5507763.

(11) Min, W.; Yang, S.; Zhang, Y.; Yapyao, Z. A Comparative Study of Metal Additive Manufacturing Processes for Elevated Sustainability. In *ASME 2019 International*

Design Engineering Technical Conferences and Computers and Information in Engineering Conference; Anaheim, CA, 2019. https://doi.org/https://doi.org/10.1115/DETC2019-97436.

(12) Yang, S.; Talekar, T.; Sulthan, M.; Zhao, Y. A Generic Sustainability Assessment Model towards Consolidated Parts Fabricated by Additive Manufacturing Process. *Procedia Manuf.* **2017**, *10*, 831–844. https://doi.org/https://doi.org/10.1016/j.promfg.2017.07.086.

(13) Xu, X.; Meteyer, S.; Perry, N.; Zhao, Y. F. Energy Consumption Model of Binder-Jetting Additive Manufacturing Processes. *Int. J. Prod. Res.* **2015**, *53* (23), 7005–7015. https://doi.org/10.1080/00207543.2014.937013.

(14) Tang, Y.; Mak, K.; Zhao, Y. A Framework to Reduce Product Environmental Impact through Design Optimization for Additive Manufacturing. *J. Clean. Prod.* **2016**, *137* (20), 1560–1572. https://doi.org/https://doi.org/10.1016/j.jclepro.2016.06.037.

(15) Tang, Y.; Mak, K.; Zhao, Y. F. A Framework to Reduce Product Environmental Impact through Design Optimization for Additive Manufacturing. *J. Clean. Prod.* **2016**, *137*, 1560–1572. https://doi.org/10.1016/j.jclepro.2016.06.037.

(16) Reis, N.; Ainsley, C.; Derby, B. Ink-Jet Delivery of Particle Suspensions by Piezoelectric Droplet Ejectors. *J. Appl. Phys.* **2005**, *97* (9), 094903. https://doi.org/10.1063/1.1888026.

(17) Prasad, L. K.; Smyth, H. 3D Printing Technologies for Drug Delivery: A Review. *Drug Dev. Ind. Pharm.* **2016**, *42* (7), 1019–1031. https://doi.org/10.3109/03639045.2015.1120743.

(18) Chen, P. H.; Chen, W. C.; Chang, S. H. Bubble Growth and Ink Ejection Process of a Thermal Ink Jet Printhead. *Int. J. Mech. Sci.* **1997**, *39* (6), 683–689. https://doi.org/10.1016/s0020-7403(96)00067-7.

(19) Özkol, E.; Ebert, J.; Telle, R. An Experimental Analysis of the Influence of the Ink Properties on the Drop Formation for Direct Thermal Inkjet Printing of High Solid Content Aqueous 3Y-TZP Suspensions. *J. Eur. Ceram. Soc.* **2010**, *30* (7), 1669–1678. https://doi.org/10.1016/J.JEURCERAMSOC.2010.01.004.

(20) Rembe, C.; Aus Der Wiesche, S.; Hofer, E. P. Thermal Ink Jet Dynamics: Modeling, Simulation, and Testing. *Microelectron. Reliab.* **2000**, *40* (3), 525–532. https://doi.org/10.1016/s0026-2714(99)00233-4.

(21) Derby, B. Inkjet Printing Ceramics: From Drops to Solid. *J. Eur. Ceram. Soc.* **2011**, *31* (14), 2543–2550. https://doi.org/10.1016/J.JEURCERAMSOC.2011.01.016.

(22) Fromm, J. E. Numerical Calculation of the Fluid Dynamics of Drop-on-Demand Jets. *IBM J. Res. Dev.* **1984**, *28* (3), 322–333. https://doi.org/10.1147/rd.283.0322.

(23) Hon, K. K. B.; Li, L.; Hutchings, I. M. Direct Writing Technology—Advances and Developments. *CIRP Ann.* **2008**, *57* (2), 601–620. https://doi.org/10.1016/J.CIRP.2008.09.006.

(24) Friederich, A.; Binder, J. R.; Bauer, W. Rheological Control of the Coffee Stain Effect for Inkjet Printing of Ceramics. *J. Am. Ceram. Soc.* **2013**, *96* (7), 2093–2099. https://doi.org/10.1111/jace.12385.

(25) Reis, N.; Derby, B. Ink Jet Deposition of Ceramic Suspensions: Modelling and Experiments of Droplet Formation. In *Materials Research Society Symposium - Proceedings*; Cambridge University Press, 2000; Vol. 624, pp 65–70. https://doi.org/10.1557/proc-625-117.

(26) Jang, D.; Kim, D.; Moon, J. Influence of Fluid Physical Properties on Ink-Jet Printability. *Langmuir* **2009**, *25* (5), 2629–2635. https://doi.org/10.1021/la900059m.

(27) Mckinley, G. H. *Dimensionless Groups For Understanding Free Surface Flows of Complex Fluids*; 2005.

(28) Snelling, D.; Li, Q.; Meisel, N. A.; Williams, C. B.; Batra, R.; Druschitz, A. Lightweight Metal Cellular Structures via Indirect 3D Printing and Casting. *Adv. Eng. Mater.* **2015**, *17* (7), 923–932. https://doi.org/https://doi.org/10.1002/adem.201400524.

(29) Reis, N.; Ainsley, C.; Derby, B. Viscosity and Acoustic Behavior of Ceramic Suspensions Optimized for Phase-Change Ink-Jet Printing. *J. Am. Ceram. Soc.* **2005**, *88* (4), 802–808. https://doi.org/10.1111/j.1551-2916.2005.00138.x.

(30) Moon, J.; Grau, J. E.; Knezevic, V.; Cima, M. J.; Sachs, E. M. Ink-Jet Printing of Binders for Ceramic Components. *J. Am. Ceram. Soc.* **2004**, *85* (4), 755–762. https://doi.org/10.1111/j.1151-2916.2002.tb00168.x.

(31) Patterson, R.; Hollenberg, D.; Alderfer, Robert C. Desjarlais, G. E. Ink Jet Printable Coatings. US4732786A, 1988.

(32) Park, A.; Wu, B.; Griffith, L. G. Integration of Surface Modification and 3D Fabrication Techniques to Prepare Patterned Poly(L-Lactide) Substrates Allowing Regionally Selective Cell Adhesion. *J. Biomater. Sci. Polym. Ed.* **1998**, *9* (2), 89–110. https://doi.org/10.1163/156856298X00451.

(33) Kani, E. N.; Allahverdi, A. Effects of Curing Time and Temperature on Strength Development of Inorganic Polymeric Binder Based on Natural Pozzolan. *J. Mater. Sci.* **2009**, *44* (12), 3088–3097. https://doi.org/10.1007/s10853-009-3411-1.

(34) Lam, C. X. F.; Mo, X. M.; Teoh, S. H.; Hutmacher, D. W. Scaffold Development Using 3D Printing with a Starch-Based Polymer. *Mater. Sci. Eng. C* **2002**, *20* (1–2), 49–56. https://doi.org/10.1016/S0928-4931(02)00012-7.

(35) Lee, K.; Lim, S.; Tron, A.; Mun, J.; Kim, Y. J.; Yim, T.; Kim, T. H. Polymeric Binder Based on PAA and Conductive PANI for High Performance Silicon-Based Anodes. *RSC Adv.* **2016**, *6* (103), 101622–101625. https://doi.org/10.1039/c6ra23805j.

(36) Karimian, H.; Babaluo, A. A. Effect of Polymeric Binder and Dispersant on the Stability of Colloidal Alumina Suspensions. *Iran. Polym. J. (English Ed.* **2006**, *15* (11), 879–889.

(37) Utela, B.; Storti, D.; Anderson, R.; Ganter, M. A Review of Process Development Steps for New Material Systems in Three Dimensional Printing (3DP). *Journal of Manufacturing Processes*. Elsevier BV July 1, 2008, pp 96–104. https://doi.org/10.1016/j.jmapro.2009.03.002.

(38) Vadillo, D. C.; Tuladhar, T. R.; Mulji, A. C.; Jung, S.; Hoath, S. D.; Mackley, M. R. Evaluation of the Inkjet Fluid's Performance Using the "Cambridge Trimaster" Filament Stretch and Break-up Device. *J. Rheol. (N. Y. N. Y).* **2010**, *54* (2), 261–282. https://doi.org/10.1122/1.3302451.

(39) Hoath, S. D.; Harlen, O. G.; Hutchings, I. M. Jetting Behavior of Polymer Solutions in Drop-on-Demand Inkjet Printing. *J. Rheol. (N. Y. N. Y).* **2012**, *56* (5), 1109–1127. https://doi.org/10.1122/1.4724331.

(40) Hoath, S. D.; Hutchings, I. M.; Martin, G. D.; Tuladhar, T. R.; Mackley, M. R.; Vadillo, D. Links Between Ink Rheology, Drop-on-Demand Jet Formation, and Printability. *J. Imaging Sci. Technol.* **2009**, *53* (4), 041208. https://doi.org/10.2352/J.ImagingSci.Technol.2009.53.4.041208.

(41) Hoath, S. D.; Hutchings, I. M.; Martin, G. D.; Tuladhar, T. R.; Mackley, M. R.; Vadillo, D. Links Between Ink Rheology, Drop-on-Demand Jet Formation, and Printability. *J. Imaging Sci. Technol.* **2009**, *53* (4), 041208. https://doi.org/10.2352/J.ImagingSci.Technol.2009.53.4.041208.

(42) Wilts, E.M.; Long, T. E. Thiol-Ene Addition Enables Tailored Synthesis of Poly(2-Oxazoline)-Graft- Poly(Vinyl Pyrrolidone) Copolymers for Binder Jetting 3D Printing. *Polym. Int.* **2020**, *accepted*.

(43) Gupta, P.; Elkins, C.; Long, T. E.; Wilkes, G. L. Electrospinning of Linear Homopolymers of Poly(Methyl Methacrylate): Exploring Relationships between Fiber Formation, Viscosity, Molecular Weight and Concentration in a Good Solvent. *Polymer (Guildf).* **2005**, *46* (13), 4799–4810. https://doi.org/10.1016/J.POLYMER.2005.04.021.

(44) Matthew G. McKee, †; Garth L. Wilkes, ‡; Ralph. H. Colby, § and; Timothy E. Long*, †. Correlations of Solution Rheology with Electrospun Fiber Formation of Linear and Branched Polyesters. *Macromolecules* **2004**, *37* (5), 1760–1767. https://doi.org/10.1021/MA035689H.

(45) Matthew G. McKee; Matthew T. Hunley; John M. Layman, A.; Long*, T. E. Solution Rheological Behavior and Electrospinning of Cationic Polyelectrolytes. *Macromolecules* **2005**, *39* (2), 575–583. https://doi.org/10.1021/MA051786U.

(46) Rahman, Z.; Charoo, N. A.; Kuttolamadom, M.; Asadi, A.; Khan, M. A. Printing of Personalized Medication Using Binder Jetting 3D Printer. In *Precision Medicine for Investigators, Practitioners and Providers*; Elsevier, 2020; pp 473–481. https://doi.org/10.1016/b978-0-12-819178-1.00046-0.

(47) Norman, J.; Madurawe, R. D.; Moore, C. M. V.; Khan, M. A.; Khairuzzaman, A. A New Chapter in Pharmaceutical Manufacturing: 3D-Printed Drug Products. *Adv. Drug Deliv. Rev.* **2017**, *108*, 39–50. https://doi.org/10.1016/j.addr.2016.03.001.

(48) Patirupanusara, P.; Suwanpreuk, W.; Rubkumintara, T.; Suwanprateeb, J. Effect of Binder Content on the Material Properties of Polymethyl Methacrylate Fabricated by Three Dimensional Printing Technique. *J. Mater. Process. Technol.* **2008**, *207* (1–3), 40–45. https://doi.org/10.1016/J.JMATPROTEC.2007.12.058.

(49) Deng, G. Y.; Xiang, L. Y.; Wei, D. H.; Liu, J.; Yun, G. W.; Xu, H. Tablets with Material Gradients Fabricated by Three-Dimensional Printing. *J. Pharm. Sci.* **2007**, *96* (9), 2446–2456. https://doi.org/10.1002/jps.20864.

(50) Wu, B.; Borland, S.; Giordano, R.; Cima, L. Solid Free-Form Fabrication of Drug Delivery Devices. *J. Control. Release* **1996**, *40* (1–2), 77–87. https://doi.org/https://doi.org/10.1016/0168-3659(95)00173-5.

(51) Zhou, Z.; Buchanan, F.; Mitchell, C.; Dunne, N. Printability of Calcium Phosphate: Calcium Sulfate Powders for the Application of Tissue Engineered Bone Scaffolds Using the 3D Printing Technique. *Mater. Sci. Eng. C* **2014**, *38* (1), 1–10. https://doi.org/10.1016/j.msec.2014.01.027.

(52) Huang, W.; Zheng, Q.; Sun, W.; Xu, H.; Yang, X. Levofloxacin Implants with Predefined Microstructure Fabricated by Three-Dimensional Printing Technique. *Int. J. Pharm.* **2007**, *339* (1–2), 33–38. https://doi.org/https://doi.org/10.1016/j.ijpharm.2007.02.021.

(53) Lee, B.; Yun, Y.; Choi, J.; Choi, Y.; Kim, J. Fabrication of Drug-Loaded Polymer Microparticles with Arbitrary Geometries Using a Piezoelectric Inkjet Printing System. *Int. J. Pharm.* **2012**, *427* (2), 305–310. https://doi.org/https://doi.org/10.1016/j.ijpharm.2012.02.011.

(54) Lee, W.; Yu, P.; Hong, M.; Widjaja, E.; Loo, S. Designing Multilayered Particulate Systems for Tunable Drug Release Profiles. *Acta Biomater.* **2012**, *8* (6), 2271–2278. https://doi.org/https://doi.org/10.1016/j.actbio.2012.02.007.

(55) Wu, G.; Wu, W.; Zheng, Q.; Li, J.; Zhou, J.; Hu, Z. Experimental Study of PLLA/INH Slow Release Implant Fabricated by Three Dimensional Printing Technique and Drug Release Characteristics in Vitro. *Biomed. Eng. Online* **2014**, *13* (1), 97. https://doi.org/10.1186/1475-925X-13-97.

(56) Katstra, W. .; Palazzolo, R. .; Rowe, C. .; Giritlioglu, B.; Teung, P.; Cima, M. . Oral Dosage Forms Fabricated by Three Dimensional Printing^{TM}. *J. Control. Release* **2000**, *66* (1), 1–9. https://doi.org/10.1016/S0168-3659(99)00225-4.

(57) Lee, K. J.; Kang, A.; Delfino, J. J.; West, T. G.; Chetty, D.; Monkhouse, D. C.; Yoo, J. Evaluation of Critical Formulation Factors in the Development of a Rapidly Dispersing Captopril Oral Dosage Form. *Drug Dev. Ind. Pharm.* **2003**, *29* (9), 967–979. https://doi.org/10.1081/DDC-120025454.

(58) Wang, C. C.; Tejwani, M. R.; Roach, W. J.; Kay, J. L.; Yoo, J.; Surprenant, H. L.; Monkhouse, D. C.; Pryor, T. J. Development of near Zero-Order Release Dosage Forms Using Three-Dimensional Printing (3-DP^{TM}) Technology. *Drug Dev. Ind. Pharm.* **2006**, *32* (3), 367–376. https://doi.org/10.1080/03639040500519300.

(59) Yu, D.; Branford-White, C.; Ma, Z.; Zhu, L.; Li, X. Novel Drug Delivery Devices

for Providing Linear Release Profiles Fabricated by 3DP. *Int. J. Pharm.* **2009**, *370* (1–2), 160–166. https://doi.org/https://doi.org/10.1016/j.ijpharm.2008.12.008.

(60) Wilts, E. M.; Pekkanen, A. M.; White, B. T.; Meenakshisundaram, V.; Aduba, D. C.; Williams, C. B.; Long, T. E. Vat Photopolymerization of Charged Monomers: 3D Printing with Supramolecular Interactions. *Polym. Chem.* **2019**, *10* (12). https://doi.org/10.1039/c8py01792a.

(61) Yan, X.; Carr, W. W.; Dong, H. Drop-on-Demand Drop Formation of Polyethylene Oxide Solutions. *Phys. Fluids* **2011**, *23* (10). https://doi.org/10.1063/1.3643269.

(62) Alhnan, M. A.; Okwuosa, T. C.; Sadia, M.; Wan, K.-W.; Ahmed, W.; Arafat, B. Emergence of 3D Printed Dosage Forms: Opportunities and Challenges. *Pharm. Res.* **2016**, *33* (8), 1817–1832. https://doi.org/10.1007/s11095-016-1933-1.

(63) Goole, J.; Amighi, K. 3D Printing in Pharmaceutics: A New Tool for Designing Customized Drug Delivery Systems. *Int. J. Pharm.* **2016**, *499* (1–2), 376–394. https://doi.org/10.1016/J.IJPHARM.2015.12.071.

(64) Bai, Y.; Williams, C. The Effect of Inkjetted Nanoparticles on Metal Part Properties in Binder Jetting Additive Manufacturing. *Nanotechnology* **2018**, *29* (39).

(65) Miyanaji, H.; Zhang, S.; Yang, L. A New Physics-Based Model for Equilibrium Saturation Determination in Binder Jetting Additive Manufacturing Process. *Int. J. Mach. Tools Manuf.* **2018**, *124*, 1–11. https://doi.org/https://doi.org/10.1016/j.ijmachtools.2017.09.001.

(66) Bai, Y.; Wall, C.; Pham, H.; Esker, A.; Williams, C. Characterizing Binder–Powder Interaction in Binder Jetting Additive Manufacturing Via Sessile Drop Goniometry. *J. Manuf. Sci. Eng.* **2019**, *141* (1), 011005. https://doi.org/https://doi.org/10.1115/1.4041624.

(67) Markicevic, B.; D'Onofrio, T. G.; Navaz, H. K. On Spread Extent of Sessile Droplet into Porous Medium: Numerical Solution and Comparisons with Experiments. *Phys. Fluids* **2010**, *22* (1), 012103. https://doi.org/10.1063/1.3284782.

(68) Holman, R.; Cima, M.; Uhland, S.; Sachs, E. Spreading and Infiltration of Inkjet-Printed Polymer Solution Droplets on a Porous Substrate. *J. Colloid Interface Sci.* **2002**, *249*, 432–440. https://doi.org/doi:10.1006/jcis.2002.8225.

(69) Alghunaim, A.; Kirdponpattara, S.; Newby, B. Techniques for Determining Contact Angle and Wettability of Powders. *Powder Technol.* **2016**, *287*, 201–215. https://doi.org/https://doi.org/10.1016/j.powtec.2015.10.002.

(70) Rowe, C. .; Katstra, W. .; Palazzolo, R. .; Giritlioglu, B.; Teung, P.; Cima, M. . Multimechanism Oral Dosage Forms Fabricated by Three Dimensional Printing™. *J. Control. Release* **2000**, *66* (1), 11–17. https://doi.org/10.1016/S0168-3659(99)00224-2.

(71) Oros Daraban, A. E.; Negrea, C. S.; Artimon, F. G. P.; Angelescu, D.; Popan, G.; Gheorghe, S. I.; Gheorghe, M. A Deep Look at Metal Additive Manufacturing Recycling and Use Tools for Sustainability Performance. *Sustainability* **2019**, *11* (19), 5494. https://doi.org/10.3390/su11195494.

(72) Paris, H.; Mokhtarian, H.; Coatanéa, E.; Museau, M. Comparative Environmental Impacts of Additive and Subtractive Manufacturing Technologies. *CIRP Ann.* **2016**, *65* (1), 29–32. https://doi.org/https://doi.org/10.1016/j.cirp.2016.04.036.

(73) Mani, M.; Lyons, K.; Gupta, S. Sustainability Characterization for Additive Manufacturing. *J. Res. NIST* **2014**, *119*, 419–428.

(74) Matthey, J.; Dawes, J.; Bowerman, R.; Trepleton, R. Introduction to the Additive Manufacturing Powder Metallurgy Supply Chain Exploring the Production and Supply of Metal Powders for AM Processes. *Technol. Rev* **2015**, No. 3, 243–256. https://doi.org/10.1595/205651315X688686.

(75) World Economic Forum. *The New Plastics Economy: Rethinking the Future of Plastics*; 2016.

Chapter 4: Vat Photopolymerization of Charged Monomers: 3D Printing with Supramolecular Interactions

Emily M. Wilts[1], Allison M. Pekkanen[2], B. Tyler White[1], Viswanath Meenakshisundaram[3], Donald C. Aduba Jr.[3], Christopher B. Williams[3], and Timothy E. Long[1*]

(Published in *Polymer Chemistry*, **2019**, *10*, 1442-1451)

[1]*Department of Chemistry, Macromolecules Innovation Institute, Virginia Tech, Blacksburg, VA 24061*

[2]*School of Biomedical Engineering and Sciences, Virginia Tech, Blacksburg, VA 24061*

[3]*Department of Mechanical Engineering, Virginia Tech, Blacksburg, VA 24061*

4.1 Abstract

Additive manufacturing enables the creation of novel structures and geometries previously unattainable through traditional processing techniques. In particular, vat photopolymerization provides unprecedented resolution through the tailored delivery of light with photo-crosslinkable or photo-polymerizable materials. Traditionally, chemical crosslinks generate a permanent network, which exhibits swelling but not dissolution. In this work, photopolymerization of photo-reactive monomers with acrylate, acrylamide, and vinyl polymerizable sites enabled the formation of water-soluble 3D printed parts using vat photopolymerization. A library of monomers with varied ionic and hydrogen bonding sites provided photopolymerized films with tensile properties approaching 1200 % elongation at break and 0.47 MPa stress at 100 % elongation. The rate of polymerization and the subsequent mechanical properties revealed a dependence on the type of supramolecular interactions and functionality on the resulting hydrogel. The diverse functionality of the monomers enabled aqueous dissolution times ranging from 27 to 41 min. Vat photopolymerization of a trimethylammonium ethyl acrylate chloride solution and with 30

wt% *N*-vinyl pyrrolidone provided 3D parts with fine structural resolution. This method of creating soluble, water-swollen structures through vat photopolymerization provides future research with a larger library of monomers for diverse applications including soluble support scaffolds.

4.2 Introduction

Additive manufacturing (AM) provides a unique method for the creation of complex geometries, which enables the design of features that enable enhanced functionality.[1-2] Many AM processes currently exist, including material extrusion, powder-bed fusion, and vat photopolymerization.[3-4] These methods enable the control of geometry and porosity throughout the resulting part, reduction of waste compared to traditional manufacturing, and design of previously unattainable geometries.[5] Vat photopolymerization, also referred to as stereolithography, operates through the selective patterning of UV light with vats of photopolymer precursors containing photoinitiator to create chemically or physically crosslinked solids.[4] Upon the introduction of light, chemical crosslinking occurs at the site of irradiation to form a solid network with a characteristic depth, which depends on light intensity, exposure time, photoinitiator content, and presence of photo-absorbers.[6-7] Advantages of vat photopolymerization relative to other printing technologies include fabricating micron-scale features, excellent surface finish, and accuracy of printed parts.[8-9] However, a limited material selection restricts vat photopolymerization as traditional processes typically require a low viscosity, photo-crosslinkable oligomeric precursor that leads to chemical crosslinking to successfully form 3D parts.[10]

Supramolecular interactions employ reversible, non-covalent bonding between molecules and polymers. Commonly investigated supramolecular interactions in polymers include ionic interactions, hydrogen bonding, metal-ligand coordination, and pi-pi stacking.[11] Ionic interactions and hydrogen bonding continue to play a critical role in the creation of complex structures through ionic aggregation and multiple hydrogen bonding motifs.[12-13] While typically weaker than covalent bonds, the synergistic effect of collective interactions significantly enhances the intermolecular forces between polymer chains.[12] Supramolecular interactions offer impact in adhesive and biomedical applications due to their reversibility under stimuli and the breadth of interactions found in nature.[12, 14-16] Additionally, the ability of supramolecular interactions to reduce or eliminate anisotropic strength profiles in AM parts remains a focus of recent research.[17] Liska *et. al.* detailed the examination of monofunctional monomers for vat photopolymerization, but failed to realize well-defined parts without incorporation of chemical crosslinkers.[18] The ability to probe supramolecular interactions to form well-defined 3D networks without the need for chemical crosslinking remains unexplored.

The generation of complex additively manufactured parts also often requires support scaffolds to hold over-hanging structures in place during printing. Because vat photopolymerization traditionally utilizes permanent, covalent crosslinks, dissolvable support scaffolds fail to exist. Current methods to produce sacrificial support structures rely on digital grayscale images, which produce partially crosslinked polymers and subsequent removal through partially dissolving or swelling the scaffold in organic solvents.[19] Other methods include designing easily-removeable support scaffolds that maintain limited contact with the printed part. With the development of multi-material

printing systems, incorporation of physically crosslinked and dissolvable scaffolds into a system is now possible.[20]

In this work, vat photopolymerization AM enabled the creation of dissolvable parts where supramolecular interactions dictated monomer selection and facilitated the creation of water-swollen gels. The broad selection of functionalized monomers achieved a spectrum of mechanical properties, from elastomers to thermoplastics with a range of dissolution rates. Characterization of the photopolymerization process employed both differential scanning calorimetry and rheology, each coupled with a UV light source, which revealed a dependence of monomer functionality and water content. Tensile analysis revealed high elongation of each photopolymerized gel (up to 1200%), highlighting a strong dependence on water content and ionic interactions. Hysteresis experiments further confirmed the elastomeric properties of each system. Finally, vat photopolymerization of monomer solutions yielded well-defined printed parts, which retained water solubility. This report enables future study into dissolvable parts created through vat photopolymerization for fully soluble support scaffold applications.

4.3 Materials and Methods

4.3.1 Materials

Trimethylammonium ethyl acrylate chloride solution (TMAEA, 80 wt % in water), 3-sulfopropyl acrylate potassium salt (SPAK), 2-acrylamido-2-methyl-1-propane sulfonic acid sodium salt (AASNa, 50 wt % in water), 2-acrylamido-2-methyl-1-propane sulfonic acid (AAS), *N*-vinyl pyrrolidone (NVP), and poly(ethylene glycol) methyl ether acrylate ($PEGMEA_{480}$) were purchased from Sigma-Aldrich. 2-hydroxy-4'-(2-hydroxyethoxy)-2-methylpropiophenone (Irgacure 2959) and diphenyl(2,4,6-trimethylbenzoyl) phosphine

oxide (TPO) were purchased from Sigma-Aldrich and dissolved in ethanol and acetone before use, respectively. 2,5-bis(5-*tert*-butyl-benzoxazol-2-yl)thiophene (BBOT), a UV blocker, was purchased from Sigma-Aldrich and dissolved in NVP before use. All solvents were purchased from Spectrum, Inc. and used as received.

4.3.2 Analytical Methods

Photocalorimetry (Photo-DSC) was performed on a TA Instruments Q2000 with an Omnicure S2000 photo-attachment with fiber optic cable. T-zero pans were loaded as either sample pans or reference pans and equilibrated at 25 °C. Following a 1 min isotherm, 8 mW/cm^2 of 365 nm light was introduced to the pans. Following a 5 min irradiation, the light was turned off and the background heat from the light was noted. Integrations of the peaks with background correction afforded the heat of polymerization. To calculate percent conversion, the standard values for ΔH_{rxn} for the homopolymerization of acrylates and acrylamides (86 kJ/mol)[21] and NVP (53.9 kJ/mol)[22] were employed. The ΔH_{rxn} values obtained from photo-DSC were normalized based on the weight of each monomer used in the experiment. Photorheology of polymerized monomer occurred on a TA Instruments DHR-2 Discovery Rheometer with a photo-attachment and a 20 mm quartz bottom plate with 20 mm disposable upper geometry. Samples were equilibrated at 25 °C for 30 s to provide baselines for all samples. Samples were oscillated at 1 Hz, providing sampling rates relevant for the second timescale. Following 30 s, samples were irradiated at 8 mW/cm^2 and the modulus was monitored. The crossover point was determined as the first instance that the storage modulus (G') exceeded loss modulus (G"). Tensile testing was performed on film-punched dogbones from photocured films with a crosshead motion of 500 mm/min and grip-to-grip separation of 26.25 mm on an Intron 5500R. Hysteresis

testing was performed on film-punched dogbones from photocured films with a crosshead motion of 5 mm/min, 100% strain for five cycles with a grip-to-grip separation of 26.25 mm. The area under the curve was calculated using the trapezoid method[23] and the cycles were compared at n=5 samples. Dynamic light scattering (DLS) was performed on a Malvern ZetaSizer at room temperature with a backscattering angle of 145 ° and a wavelength of 435 nm.

4.3.3 Film Preparation

$PEGMEA_{480}$, TMAEA, and AASNa were used as received (0 wt%, 20 wt%, and 50 wt% water, respectively). AAS and SPAK were dissolved at 50 wt% water prior to use and NVP was used without further modification. 2 wt% photoinitiator in ethanol was added to monomer solutions to initiate the photopolymerization. Films were prepared by irradiation from a broad-band UV source at 8.5 mW/cm^2 in an Ace Glass Incorporated photo-cabinet until they were free-standing. Typically, the film was exposed to UV light for 30 s per side to ensure full conversion. Films were used for subsequent analysis without further purification or extraction.

4.3.4 Dissolution Testing

Sections of gel were placed in RO water at 1 mg mL^{-1} at 23 ^oC. The water was stirred rapidly with a magnetic stir bar and the time to full dissolution was noted. Data is presented as an average with a standard deviation of n = 3 samples.

4.3.5 3D Printing

TMAEA (20 wt% water) and combinations of TMAEA and NVP with 2 wt% TPO in acetone were added to a 50-mL vat of an Autodesk Ember® digital light processing (DLP) mask-projection stereolithography, bottom-up, 3D printer with a LED ultraviolet light

source at 405 nm with an intensity of 20 mW/cm^2. Autodesk Print Studio design software imported 3D digital models as .stl files sent to the Autodesk Ember® for printing. The first layer was irradiated for 8 s to ensure adhesion to the stainless aluminum build platform. The next four layers were irradiated for 3 s, which incorporated intermediate layers to support the remaining layers. All subsequent model layers were each irradiated for 2 s. The set later thickness was 50 μm, which was controlled by linear actuation of the build stage in the vertical z-direction. Between each layer, the build stage was raised to allow fresh monomer solution onto the PDMS optical window and to recoat the part until the build was complete. Printed parts were gently detached from the build stage before analysis. Because of material incompatibilities with the Autodesk Ember®, printing of combinations containing *N*-vinyl pyrrolidone proceeded on a custom-build 3D printer. To begin the printing process, 1, 2, 2.5 and 3 wt% of TPO was added to a solution of TMAEA with 30 wt% NVP and 0.4 wt% BBOT. The formulations were irradiated with UV light for 5 s and the thickness of the irradiated film was measured. Beyond 2 wt% TPO, the thickness of the cured film reached convergence. The resin formulation with 2 wt% TPO was added to a vat and placed in the build area of a custom top-down mask-projection vat-photopolymerization machine. A build-stage with a glass substrate was inserted into the resin. A broad-spectrum UV light source (300-500 nm) irradiated the surface of the resin with an intensity of 1.96 mW/cm^2 (measured at 365 nm). From the working curve[24], the exposure time for curing 100 μm was estimated to be 5 s. Upon loading and slicing the .stl file with 100 μm layer thickness, the first layer was projected on the build stage. The stage was lowered by 100 μm and a fresh coat of resin was deposited in the build area. This process of projection and recoating continued till the complete part was fabricated. The

parts were then removed from the build-stage, cleaned with ethanol, and patted dry with tissue. Printed parts were then irradiated in a UV post curing chamber for 10 min.

4.3.6 Shrinking Study

3D printed cubes (1 x 1 x 1 cm) were placed on a porous substrate in a vacuum oven at 5 mbar and 60 ^{o}C from 0 to 24 h. Measurements were taken in the x, y, and z directions at 2, 4, 6, 8, 16, and 24 h where data is presented as an average of n=3 samples.

4.3.7 Water-Uptake/Swelling Study

3D printed cubes (1 x 1 x 1 cm) were dried for 24 h in a vacuum oven at 60 ^{o}C and 5 mbar for 24 h. The part was weighed and placed in 100 mL of water without agitation in order to encourage swelling and not dissolution. The weight of the part was measured at 2, 4, 6, 8, 16, and 24 h where the data is presented as an average of n=3 samples. The surface of the parts were dried on the surface with tissue before weighing to prevent water accumulation on the surface from contributing to water-uptake measurements.

4.3.8 Statistical Analysis

Statistical testing was performed using JMP software. An ANOVA test followed by a Tukey's HSD provided differences between treatment groups at 95% confidence.

4.3.9 Nomenclature

When referring to the copolymer systems of TMAEA and NVP, each sample is named "TMAEA-*co*-NVP" followed by the weight percent of NVP incorporation. As an example, a copolymer system with 2.5 wt% NVP is denoted as "TMAEA-*co*-NVP2.5".

4.4 Results and Discussion

Traditional vat photopolymerization AM processes utilize chemical crosslinking to ensure part fidelity upon printing. However, this process generates a permanent chemical

network with the inability to fully dissolve for support scaffold applications.[25] This work describes the identification of ionic monomers in water to afford a range of acrylate, acrylamide, and vinyl monomers suitable for the 3D printing of physically-crosslinked objects. Equivalent structures in acrylate vs. acrylamide (3-sulfopropyl acrylate potassium salt (SPAK)) vs. (2-acrylamido-2-methyl-1-propane sulfonic acid sodium salt (AASNa)) as well as ionic vs. acid forms (AASNa vs. 2-acrylamido-2-methyl-1-propane sulfonic acid (AAS)) provided a library of promising monomers to evaluate photopolymerized hydrogel properties and to aid future rational design (**Scheme 4.1**). TMAEA ultimately demonstrated mechanical properties most promising for vat photopolymerization, but to increase part strength and provide a range of water dissolution rates, *N*-vinyl pyrrolidone (NVP) was added as a comonomer.

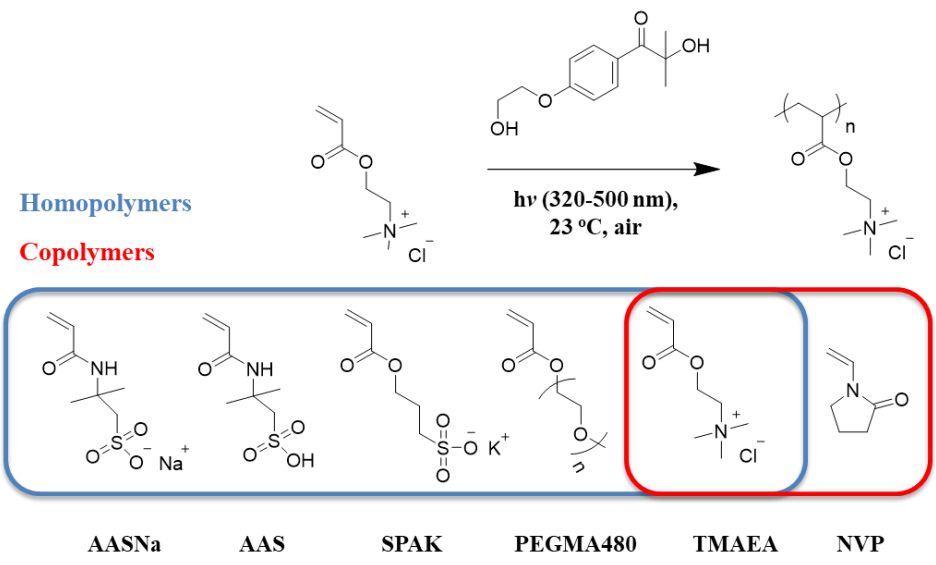

Scheme 4.1. Photopolymerization of various monomers in the presence of photoinitiator and UV irradiation to produce homopolymers and copolymers.

TMAEA and *N*-vinyl pyrrolidone (NVP) copolymers provided the opportunity to observe a systematic change in mechanical properties and water dissolution rates based on

NVP incorporation. The literature broadly describes free radical polymerization and reverse addition-fragmentation chain transfer polymerization of NVP copolymerized with acrylate and ammonium-containing monomers.[26-29] Roka *et. al.* measured reactivity ratios of NVP and 2-(dimethylamino)ethyl methacrylate suggesting the formation of pseudo-diblock copolymers. They observed multiple glass transition temperatures of the copolymers where transitions near 180 ^{o}C were associated with the poly(*N*-vinyl pyrrolidone) (PVP) blocks.[27] The addition of NVP to copolymer systems with acrylates in the presence of oxygen is also known to decrease inhibition during photopolymerization. It was hypothesized that molecular oxygen is quenched through photooxidation with the NVP amide bond or the formation of an excimer with the amide bond.[30] Thus, we propose that the copolymerization of TMAEA and NVP will provide higher strength materials and higher conversions compared to polyelectrolyte homopolymer systems. TMAEA proved the optimal candidate for vat photopolymerization based on photo-kinetics and mechanical properties from photo-polymerized films, which deemed this monomer as the most logical copolymer for the NVP-containing systems. This is a significant advantage for vat photopolymerization processes as most machines print in the presence of oxygen.

Photo-DSC and photorheology provided photo-kinetics of each system to aid in predicting specifications needed for vat photopolymerization. Photo-DSC generated heats of reaction (ΔH_{rxn}) as a function of irradiation time and allowed for estimations of polymerization rate and monomer conversion (**Figures 4.1A and 4.1B**). TMAEA proved to evolve the most heat upon irradiation, potentially due to higher conversion percentages or a lower wt% water in the system. However, $PEGMEA_{480}$, which did not contain water, exhibited a broad peak and lower evolved heat of polymerization potentially due to lack of

supramolecular interactions. Each of the acrylamide monomers (AAS and AASNa) experienced shorter times to peak heat flow compared to the equivalent acrylate (SPAK), suggesting a possible role of hydrogen bonding in the polymerization process or acrylamide vs. acrylate reactivity.[31] Aqueous size exclusion chromatography of the photopolymerized systems attempted to measure molecular weights, but ionic aggregation prevented reproducible separation. The size of each of these aggregates and their shape potentially directed both the kinetics of polymerization and the properties of the free-standing film.[32-33] Further studies of the particular mechanism and the potential use of these monomers is currently underway.

Photo-DSC of TMAEA and NVP copolymerizations revealed an increase in ΔH_{rxn} with increasing NVP incorporation. The time to reach a maximum in heat flow was longer compared to the other polyelectrolyte systems, and a trend was not observed. Photo-DSC of neat NVP with either Irgacure 2959 or TPO revealed less than 12% conversion during the 5 min experiment. This observation suggested the formation of TMAEA-*co*-NVP copolymers rather than a blend of TMAEA and NVP homopolymers. Liska *et. al.* observed a similar phenomenon where NVP reached the highest conversions with Irgacure 819 as a photoinitiator compared to multiple other photoinitiator systems. They hypothesized Irgacure 819 maintained the best solubility in NVP, which facilitated radical polymerization.[18]

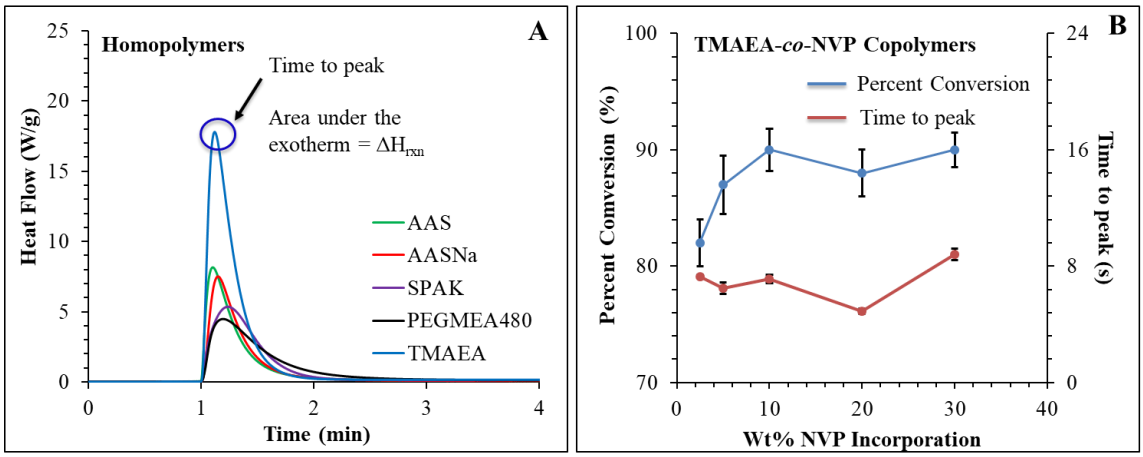

Figure 4.1. (A) Heat flow as a function of time where UV light exposure began at 1 min for each homopolymer. The time to peak is denoted as the maxima in the trace and the area under the curve represents the ΔH_{rxn}. **(B)** Time to peak and ΔH_{rxn} as a function of wt% NVP incorporation.

After normalizing the ΔH_{rxn} values to the moles of monomer and using literature standards for 100% conversion of acrylates (86 kJ/mol)[21] and NVP (53.9 kJ/mol)[22], the relative monomer percent conversions were calculated. TMAEA, AAS, AASNa, and SPAK exhibited conversions of 75, 35, 40, and 45%, respectively (**Table S4.1**). TMAEA and SPAK, i.e. acrylate-containing monomers, exhibited statistically higher conversions compared to acrylamide-containing monomers (AAS and AASNa). The calculated conversions support the longer dissolution times for TMAEA and SPAK compared to AAS and AASNa. TMAEA had the highest conversion possibly due to ordering before polymerization. To further explore this hypothesis, complex viscosities for each monomer system dissolved in varying wt% water were studied, which suggests monomer ordering (**Figure S4.2**). TMAEA exhibited the largest complex viscosity in 20 wt% water (0.062

Pa·s), which suggested an increase in ionic aggregation and ordering compared to the other samples.

TMAEA and NVP copolymer systems exhibited higher conversions (82 – 90%) compared to all homopolymers. As discussed previously, NVP is known to reduce termination in free radical polymerizations in the presence of oxygen.[30] As NVP incorporation increased, conversion increased, where statistical differences existed between TMAEA-*co*-NVP2.5 and TMAEA-*co*-NVP5, TMAEA-*co*-NVP10, TMAEA-*co*-NVP20, and TMAEA-*co*-NVP30. Most vat photopolymerization systems print in the presence of air through free radical polymerization where oxygen will terminate propagation. Adding a monomer that reduces termination provides advantages with part strength and fidelity. While unreacted monomer still exists in the discussed systems, ranging from an estimated 18-10 % in the TMAEA-*co*-NVP copolymers, future use of oxygen scavenging components will potentially mitigate this problem.

Photorheology of monomers revealed a trend in plateau storage modulus (G_N^o) as a function of monomer and water content in the homopolymer systems (**Figures 4.2A and 4.2B**). G_N^o values from photorheology provide a relative strength profile that will directly affect the vat photopolymerization process. TMAEA exhibited significantly increased G_N^o following polymerization compared to all other monomers. Both the rate of polymerization and increased conversion likely led to a fast crossover time (2 s) and enhanced G_N^o, lending itself as the prime candidate for vat photopolymerization. Despite its lower water content, $PEGMEA_{480}$ failed to reach the same G_N^o as TMAEA, suggesting that the ionic interactions in TMAEA generated a more physically crosslinked film than non-charged $PEGMEA_{480}$. Furthermore, as SPAK, AAS, and AASNa each possessed 50 wt% water, direct

comparisons between acrylate, acrylamide, and the role of ions was investigated. As confirmed from results of photo-DSC, SPAK exhibited a much slower rate of polymerization and thus a longer time to reach the G'-G" crossover point (16 s) than either AAS (6 s) or AASNa (7 s). The role of ion incorporation into monomers also afforded gels of varied modulus, as seen in the comparison between AAS and AASNa. When comparing AASNa to SPAK, the rate of polymerization potentially limits molecular weight growth after ~5 s of AASNa, while SPAK continues to polymerize over much longer time scales. The acid form of the acrylamide monomer generated moduli similar to $PEGMEA_{480}$ despite containing 50 wt% water.

Photorheology of TMAEA and NVP combinations revealed an apparent relationship between G_N^o and NVP incorporation (**Figure 4.2B**). The G_N^o steadily increased from 0.058 MPa for TMAEA-*co*-NVP2.5 to 0.470 MPa for TMAEA-*co*-NVP30, which confirmed NVP increases the modulus of the hydrogels. Combinations containing above 30 wt% NVP resulted in inconsistent and non-reproducible measurements of mechanical properties, therefore the 30 wt% NVP incorporation was the highest included. These combinations contain fewer ionic interactions compared to neat TMAEA and other monomer systems discussed above. The increase in modulus is likely due to the high glass transition temperature of poly(vinyl pyrrolidone) (PVP), which ranges from 150 – 180 ^oC in the absense of water in the formation of pseudo-diblock copolymers.[27, 29, 34]

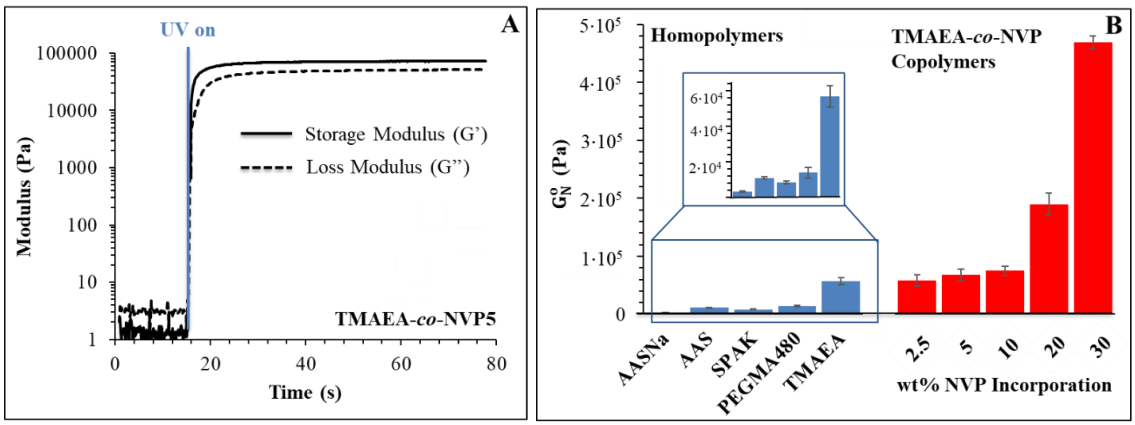

Figure 4.2. (A) A representative photo-rheology trace where the sample is exposed to UV light after 15 s and the plateau storage modulus (G_N^o) is denoted. **(B)** G_N^o as a function of homopolymer composition and wt% NVP incorporation.

To further confirm the importance of electrostatic interactions in the resulting photopolymerized parts, two non-charged controls, 2-(dimethylamino)ethyl acrylate (DMAEA) and $PEGMEA_{480}$, were also tested. DMAEA is structurally equivalent to TMAEA besides the absence of an ammonium moiety. Photo-DSC and photo-rheology (**Figure S4.1A and S4.1B**) revealed low conversion values compared to the charged monomers and the absence of a crossover point in photo-rheology. The resulting product from photo-rheology was a viscous liquid, which is consistent when no crossover point is observed. $PEGMEA_{480}$ served as the second control because this monomer was able to form solid parts after photopolymerizing, even though it does not have an equivalent structure to any of the charged monomers.

After measuring the photo-kinetics of the homopolymer and copolymers, controlled dissolution experiments determined water dissolution times of the photopolymerized films. Water dissolution studies also revealed an increase in dissolution time with increasing incorporation of NVP in TMAEA-*co*-NVP copolymers where statistical differences arose

between TMAEA-*co*-NVP2.5, TMAEA-*co*-NVP20, and TMAEA-*co*-NVP30. This compositional range provided dissolution rates ranging from 27 to 41 min, which demonstrated the potential to 3D print fully dissolvable parts using vat photopolymerization. Because vat photopolymerization usually employs covalent crosslinks that render the final part insoluble, this system has the potential to serve as a dissolvable support scaffold.

The role of physical crosslinks in the dissolution of photopolymerized parts will be an essential part of soluble support scaffold applications. Exposure to excess water resulted in the dissociation of the charges and their counterions, which facilitated the breaking up of electrostatic aggregates and full dissolution. As noted in **Figure 3**, monomer type, acrylamides vs. acrylates (SPAK, AASNa), dictated the time to full dissolution, while wt% water in the films did not influence the rates. Statistical differences arose between all acrylate- and acrylamide-containing systems, but a trend was not observed between different supramolecular interactions (ionic vs. acid forms). This suggested a higher degree of polymerization resulting from acrylate- vs. acrylamide-containing systems where increased molecular weight presumably increased dissolution time. Photo-DSC explored this hypothesis further. Interestingly, $PEGMEA_{480}$ failed to dissolve in water after more than 24 h under the described conditions.[35]

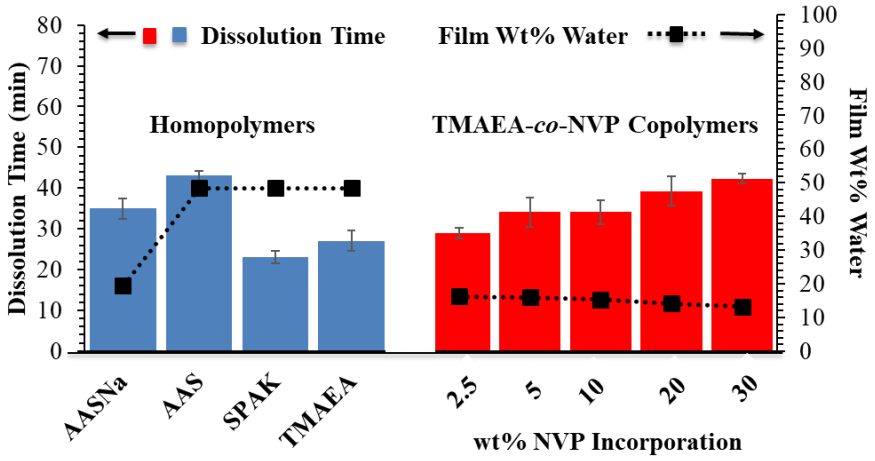

Figure 4.3. Dissolution rate as a function of homopolymer composition and NVP incorporation with a magnetic stir bar at 1 mg mL^{-1} and 23 ^{o}C.

As described in **Figure 4.3**, each film or printed object contained varying amounts of water, leading to hydrogels. The subsequent mechanical testing was performed using unextracted, water-swollen gels where the presence of water greatly aided to the elastic behavior. After elimination of water upon heating at 80 ^{o}C under high vacuum for 24 h, the films or printed parts became rigid and brittle. The parts were also very hydroscopic, and exposure to atmospheric conditions for only minutes resulted in sticky surfaces.

Tensile tests revealed strength, elongation, and hysteresis for each system. Tensile experiments of photopolymerized TMAEA-*co*-NVP films revealed a systematic increase in stress at 100% elongation and decrease of strain at break when increasing NVP content, depicted in **Figures 4.4A and 4.4B**. The photopolymerized film of neat TMAEA experienced the largest strain at break possibly due to the highest level of ionic interactions as physical crosslinks and the most water content acting as a plasticizer. As the incorporation of NVP increased from 2.5 to 30 wt%, the material transformed from a typical thermoplastic elastomer (TPE) to an engineering plastic based on the tensile

analysis. Samples containing 2.5 to 20 wt% NVP did not experience a distinct linear region at the beginning of the experiment or demonstrate a measurable yield stress, which is consistent with elastomeric materials. TMAEA-*co*-NVP30 contained a distinct linear region with a yield stress, indicating toughness owing to the large wt% of NVP incorporation. **Figure 4.4B** emphasizes the large increase in stress at 100% elongation from TMAEA-*co*-NVP20 to TMAEA-*co*-NVP30, which possibly arose from macrophase separation of the copolymers present in TMAEA-*co*-NVP30, depicted visually in **Figure 4.5**.[36] **Figure 4.5A**, **4.5B**, and **4.5C** depict photo-polymerized films of TMAEA, TMAEA-*co*-NVP10, and TMAEA-*co*-NVP30, respectively. TMAEA appeared optically clear while increasing NVP incorporation resulted in increasing opaqueness. The tensile data from samples PEGMEA480, AAS, AASNa, and SPAK is included in the supplemental section (**Table S4.3**) and follows similar trends demonstrated from photorheology.

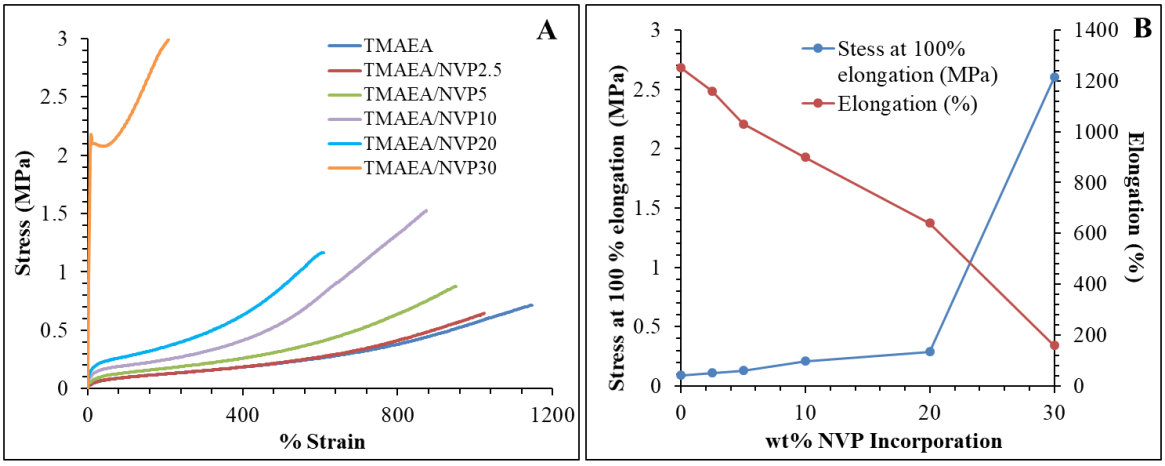

Figure 4.4. (A) Stress vs. strain curves of photopolymerized unextracted films of TMAEA with 2.5 to 30 wt% NVP. **(B)** Stress at 100% elongation and strain at break as a function of wt% NVP incorporation.

Figure 4.5. (A) Photopolymerized films of TMAEA, **(B)** TMAEA-*co*-NVP10 copolymer, and **(C)** TMAEA-*co*-NVP30 copolymer.

Hysteresis experiments at 100% elongation over five cycles confirmed the elastomeric properties of TMAEA-*co*-NVP combinations. **Figure 4.6A** depicts the hysteresis profile of TMAEA photopolymerized films. This data revealed low amounts of hysteresis after five cycles (9-14%), which suggested the physical ionic crosslinks and water plasticization resisted permanent deformation. **Figure 4.6B** depicts TMAEA-*co*-NVP10 hysteresis profile, which begins to show residual strain and permanent deformation after each cycle. The hysteresis profile of TMAEA-*co*-NVP30, depicted in **Figure 4.6C**, reveals the most hysteresis and most residual strain compared to the previous two samples. After cycle 1, TMAEA-*co*-NVP30 experiences an average of 28% residual strain and does not recover after each cycle. While physical ionic crosslinks and water-plasticization provide some elastic properties, the data suggests the PVP pseudo-blocks experience permanent deformation.[37]

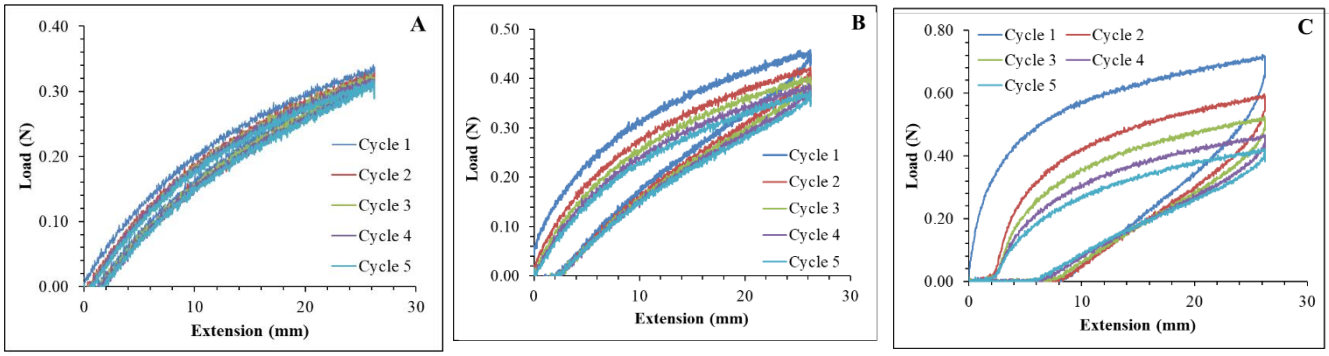

Figure 4.6. Hysteresis experiments at 100% elongation for five cycles of **(A)** TMAEA, **(B)** TMAEA-*co*-NVP10, and **(C)** TMAEA-*co*-NVP30 photopolymerized films.

Vat photopolymerization of TMAEA with 2 wt% TPO revealed the fabrication of fine features upon rapid printing. As the printing proceeded, residual TMAEA, near 25%, resided within the part interior and was trapped within the structure based on monomer conversion values measured using photo-DSC. Other observations included overcure due to the rapid polymerization of TMAEA monomer likely played a role in part fidelity. As shown in **Figure 4.7A**¸ the top crenellations in the rook design maintained fine feature resolution characteristic of vat photopolymerization. Due to the solubility of printed parts, uncured monomer remained within the printed part, despite drying steps, prior to scanning electron microscopy (SEM). When examined further using SEM (**Figure 4.7B**), the crenellations exhibited a surface roughness characteristic of the layer thickness because of light penetration within each layer. Despite this characteristic surface roughness, distinct layers did not develop, suggesting strong interlayer interactions and a blending of layers during the print process. The physical properties of printed parts rival those seen in bulk gels, suggesting a lack of anisotropy characteristic in traditional 3D printed parts.

A top-down vat-photopolymerization system enabled the fabrication of complex lattice structures with pillar widths as small as 500 μm, depicted in **Figure 4.7C**. TMAEA and NVP system exhibit high G_N^o, which facilitated the printing of self-supporting geometries. Printing with 2 wt% TPO without the addition of photo-blocker resulted in overcure and structural imperfections within the lattice. With the addition of 0.4 wt% BBOT, the polymerized area remained within the area exposed to UV light, creating a lattice structure with high accuracy compared to the programmed CAD design.

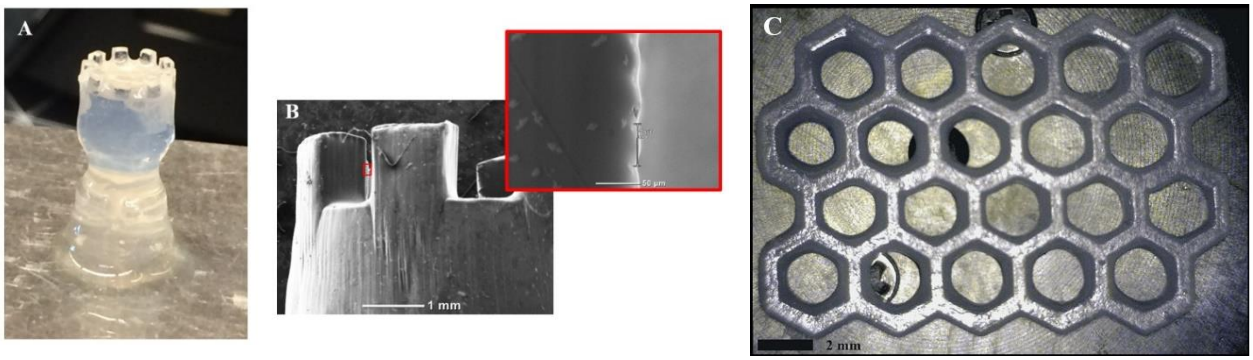

Figure 4.7. (A) Vat photopolymerization of a rook with TMAEA using an Autodesk Ember. **(B)** SEM imaging reveals distinct crenellations and characteristic surface roughness relative to layer thickness. **(C)** Top-down vat photopolymerization with TMAEA-*co*-NVP30 fabricated a complex lattice structure with pillar widths as small as 500 μm.

Vat polymerization of 1 x 1 x 1 cm cubes of each TMAEA and TMAEA-*co*-NVP30 provided well-defined 3D parts for shrinking and swelling studies. **Figure 4.8A** depicts water-uptake of TMAEA and TMAEA-*co*-NVP30 printed parts where both exceeded 5000% uptake. TMAEA reached 9000% water-uptake after 24 h owing to its higher ionic

content compared to TMAEA-*co*-NVP30.[38-39] TMAEA-*co*-NVP30 also exhibited a larger range of standard deviations because some samples did not maintain a uniform shape and partially dissolved. **Figure 4.8B** depicts % shrinkage of each sample in the x, y, and z directions revealing an average of 17 and 13% isotropic shrinkage of TMAEA and TMAEA-*co*-NVP30, respectively. The larger % shrinkage in the neat TMAEA sample arose from the larger wt% water content of the hydrogel before drying, 20 wt%, compared to TMAEA-*co*-NVP30, 13.3 wt%. The varying shrinkage rates of each sample and in each direction may have resulted from non-uniform heating in the vacuum oven or variation in the surface exposure to the vacuum, as one side was placed on a porous surface.

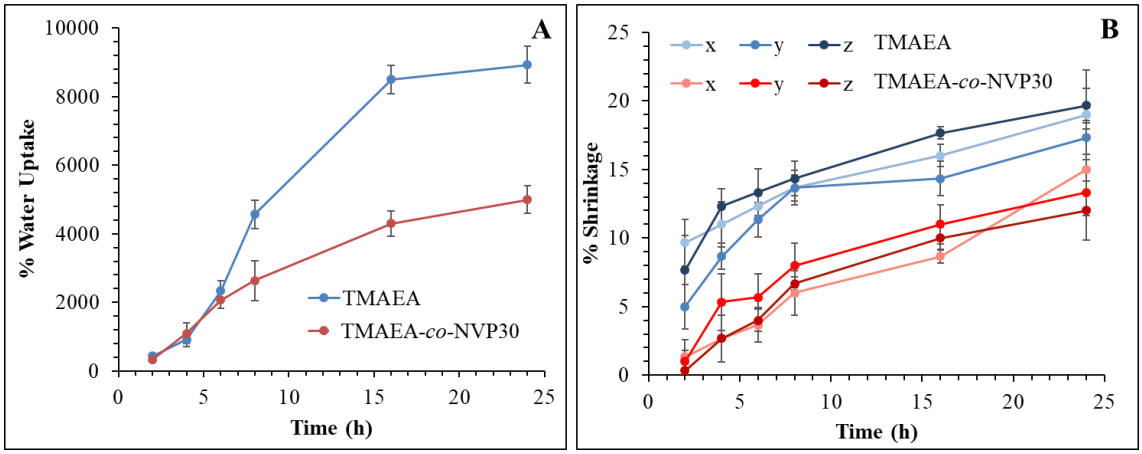

Figure 4.8. (A) Percent water uptake for TMAEA and TMAEA-*co*-NVP30 based on mass over 24 h. **(B)** Shrinking studies of TMAEA and TMAEA-*co*-NVP30 under high vacuum at 40 ^{o}C for 24 h.

4.5 Conclusion

Fully-soluble 3D printed parts employing ionic interactions resulted from vat photopolymerization additive manufacturing processes. These fully-soluble, 3D printed parts represent a new class of materials for high resolution, vat photopolymerization and this concept has the potential to enable soluble support scaffolds. This report details the

characterization of water-soluble gels created through photopolymerization. A wide range of monomers afforded the development of a broad spectrum of gel properties based on supramolecular interactions. TMAEA and NVP combinations demonstrated tunable mechanical properties from TPEs to engineering plastics. Furthermore, preliminary investigation using a vat photopolymerization additive manufacturing process produced parts with well-defined features and the absence of defined layers, paving the way for future work to examine the limits of resolution and properties afforded by this process.

4.6 Acknowledgments

The authors would like to thank Dr. Charles Carfagna for analytical support.

4.7 References

(1) Wegst, U. G.; Bai, H.; Saiz, E.; Tomsia, A. P.; Ritchie, R. O., Bioinspired structural materials. *Nature materials* **2015,** *14* (1), 23-36.

(2) Compton, B. G.; Lewis, J. A., 3D-printing of lightweight cellular composites. *Advanced materials* **2014,** *26* (34), 5930-5935.

(3) Chia, H. N.; Wu, B. M., Recent advances in 3D printing of biomaterials. *Journal of biological engineering* **2015,** *9* (1), 4.

(4) Gross, B. C.; Erkal, J. L.; Lockwood, S. Y.; Chen, C.; Spence, D. M., Evaluation of 3D printing and its potential impact on biotechnology and the chemical sciences. ACS Publications: 2014.

(5) Gao, W.; Zhang, Y.; Ramanujan, D.; Ramani, K.; Chen, Y.; Williams, C. B., . . . Zavattieri, P. D., The status, challenges, and future of additive manufacturing in engineering. *Computer-Aided Design* **2015,** *69*, 65-89.

(6) Schultz, A. R.; Lambert, P. M.; Chartrain, N. A.; Ruohoniemi, D. M.; Zhang, Z.; Jangu, C., Long, T. E., 3D Printing Phosphonium Ionic Liquid Networks with Mask Projection Microstereolithography. *ACS Macro Letters* **2014,** *3* (11), 1205-1209.

(7) Sirrine, J. M.; Pekkanen, A. M.; Nelson, A. M.; Chartrain, N. A.; Williams, C. B.; Long, T. E., 3D-printable biodegradable polyester tissue scaffolds for cell adhesion. *Australian Journal of Chemistry* **2015,** *68* (9), 1409-1414.

(8) Spadaccini, C. M.; Farquar, G.; Weisgraber, T.; Gemberling, S.; Fang, N.; Xu, J., . . . Lee, H., High resolution projection micro stereolithography system and method. Google Patents: 2016.

(9) Sirrine, J. M.; Meenakshisundaram, V.; Moon, N. G.; Scott, P. J.; Mondschein, R. J.; Weiseman, T. F., Long, T. E., Functional siloxanes with photo-activated, simultaneous chain extension and crosslinking for lithography-based 3D printing. *Polymer* **2018**.

(10) Stansbury, J. W.; Idacavage, M. J., 3D printing with polymers: Challenges among expanding options and opportunities. *Dental Materials* **2016,** *32* (1), 54-64.

(11) Lu, W.; Le, X.; Zhang, J.; Huang, Y.; Chen, T., Supramolecular shape memory hydrogels: a new bridge between stimuli-responsive polymers and supramolecular chemistry. *Chem. Soc. Rev.* **2017,** *46* (5), 1284-1294.

(12) Webber, M. J.; Appel, E. A.; Meijer, E.; Langer, R., Supramolecular biomaterials. *Nature materials* **2016,** *15* (1), 13-26.

(13) Akar, M.; Sirkecioglu, O.; Bicak, N., Synthesis of methacrylate pendant polyelectrolyte as water-soluble multifunctional cross-linker. *Eur. Polym. J.* **2017,** *97*, 418-422.

(14) Zhang, K.; Aiba, M.; Fahs, G. B.; Hudson, A. G.; Chiang, W. D.; Moore, R. B., . . . Long, T. E., Nucleobase-functionalized acrylic ABA triblock copolymers and supramolecular blends. *Polymer Chemistry* **2015,** *6* (13), 2434-2444.

(15) Zhang, K.; Chen, M.; Drummey, K. J.; Talley, S. J.; Anderson, L. J.; Moore, R. B.; Long, T. E., Ureido cytosine and cytosine-containing acrylic copolymers. *Polymer Chemistry* **2016,** *7* (43), 6671-6681.

(16) Wilts, E. M.; Herzberger, J.; Long, T. E., Addressing water scarcity: cationic polyelectrolytes in water treatment and purification. *Polym. Int.* **2018**.

(17) Highley, C. B.; Rodell, C. B.; Burdick, J. A., Direct 3D printing of shear-thinning hydrogels into self-healing hydrogels. *Advanced Materials* **2015,** *27* (34), 5075-5079.

(18) Liska, R.; Schwager, F.; Maier, C.; Cano-Vives, R.; Stampfl, J., Water-soluble photopolymers for rapid prototyping of cellular materials. *Journal of Applied Polymer Science* **2005,** *97* (6), 2286-2298.

(19) Xia, C.; Fang, N., Fully three-dimensional microfabrication with a grayscale polymeric self-sacrificial structure. *Journal of Micromechanics and Microengineering* **2009,** *19* (11), 115029.

(20) Ready, S.; Whiting, G.; Ng, T. N. In *Multi-material 3D printing*, NIP & Digital Fabrication Conference, Society for Imaging Science and Technology: 2014; pp 120-123.

(21) Andrzejewska, E.; Andrzejewski, M., Polymerization kinetics of photocurable acrylic resins. *J. Polym. Sci., Part A: Polym. Chem.* **1998,** *36* (4), 665-673.

(22) BASF Published value.

(23) RLJDF, B., *Numerical Analysis*. 7th ed.; Brooks/Cole: 2000.

(24) Jacobs, P. F., *Rapid prototyping & manufacturing: fundamentals of stereolithography*. Society of Manufacturing Engineers: 1992.

(25) Wang, J.; Goyanes, A.; Gaisford, S.; Basit, A. W., Stereolithographic (SLA) 3D printing of oral modified-release dosage forms. *International journal of pharmaceutics* **2016,** *503* (1), 207-212.

(26) Guinaudeau, A.; Coutelier, O.; Sandeau, A. l.; Mazières, S. p.; Nguyen Thi, H. D.; Le Drogo, V., Destarac, M., Facile access to poly (N-vinylpyrrolidone)-based double hydrophilic block copolymers by aqueous ambient RAFT/MADIX polymerization. *Macromolecules* **2013,** *47* (1), 41-50.

(27) Roka, N.; Kokkorogianni, O.; Pitsikalis, M., Statistical copolymers of N-vinylpyrrolidone and 2-(dimethylamino) ethyl methacrylate via RAFT: Monomer reactivity ratios, thermal properties, and kinetics of thermal decomposition. *J. Polym. Sci., Part A: Polym. Chem.* **2017,** *55* (22), 3776-3787.

(28) Singhal, A.; Chauhan, S., Free Radical Copolymerization of Acrylamide and N-Vinylpyrrolidone Catalyzed by Iron (III) porphyrins in the Presence of Ionic Liquids. *Org. Prep. Proced. Int.* **2018,** *50* (3), 359-371.

(29) Gatica, N.; Fernández, N.; Opazo, A.; Alegría, S.; Gargallo, L.; Radic, D., Synthesis and characterization of functionalized vinyl copolymers. Electronegativity and comonomer reactivity in radical copolymerization. *Polym. Int.* **2003,** *52* (8), 1280-1286.

(30) White, T. J.; Liechty, W. B.; Guymon, C. A., The influence of N-vinyl pyrrolidone on polymerization kinetics and thermo-mechanical properties of crosslinked acrylate polymers. *J. Polym. Sci., Part A: Polym. Chem.* **2007,** *45* (17), 4062-4073.

(31) Lloyd, D. J.; Nikolaou, V.; Collins, J.; Waldron, C.; Anastasaki, A.; Bassett, S. P., . . . Kempe, K., Controlled aqueous polymerization of acrylamides and acrylates and “in situ” depolymerization in the presence of dissolved CO 2. *Chem. Commun.* **2016,** *52* (39), 6533-6536.

(32) Noor, S. A. M.; Sun, J.; MacFarlane, D. R.; Armand, M.; Gunzelmann, D.; Forsyth, M., Decoupled ion conduction in poly (2-acrylamido-2-methyl-1-propane-sulfonic acid) homopolymers. *Journal of materials chemistry a* **2014,** *2* (42), 17934-17943.

(33) Abdullah, M. M.; AlQuraishi, A. A.; Allohedan, H. A.; AlMansour, A. O.; Atta, A. M., Synthesis of novel water soluble poly (ionic liquids) based on quaternary ammonium acrylamidomethyl propane sulfonate for enhanced oil recovery. *Journal of Molecular Liquids* **2017,** *233*, 508-516.

(34) Molyneux, P., *Water-Soluble Synthetic Polymers: Volume I: Properties and Behavior*. CRC press: 2018.

(35) Wang, W.; Liu, R.; Li, Z.; Meng, C.; Wu, Q.; Zhu, F., Synthesis and Self-Assembly of New Double-Crystalline Amphiphilic Polyethylene-block-Poly [oligo (ethylene glycol) Methyl Ether Methacrylate] Coil-Brush Diblock Copolymer. *Macromol. Chem. Phys.* **2010,** *211* (13), 1452-1459.

(36) Leibler, L., Theory of microphase separation in block copolymers. *Macromolecules* **1980,** *13* (6), 1602-1617.

(37) Luo, F.; Sun, T. L.; Nakajima, T.; Kurokawa, T.; Zhao, Y.; Sato, K., . . . Gong, J. P., Oppositely Charged Polyelectrolytes Form Tough, Self-Healing, and Rebuildable Hydrogels. *Adv. Mater.* **2015,** *27* (17), 2722-2727.

(38) Rubinstein, M.; Colby, R. H.; Dobrynin, A. V.; Joanny, J.-F., Elastic modulus and equilibrium swelling of polyelectrolyte gels. *Macromolecules* **1996,** *29* (1), 398-406.

(39) Meka, V. S.; Sing, M. K.; Pichika, M. R.; Nali, S. R.; Kolapalli, V. R.; Kesharwani, P., A comprehensive review on polyelectrolyte complexes. *Drug Discovery Today* **2017**.

4.8 Supplemental

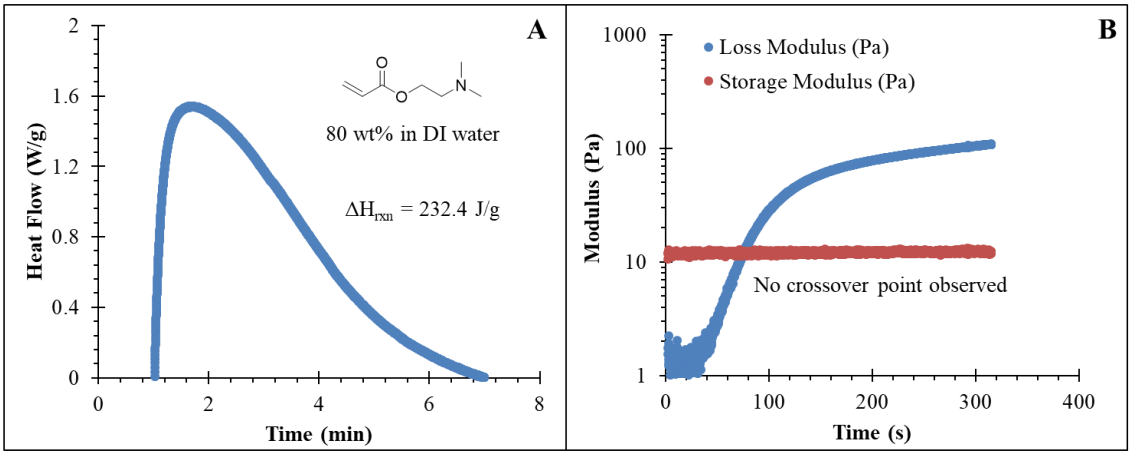

Figure S4.1. (A) Photo-DSC of 2-(dimethylamino)ethyl acrylate in 80 wt% DI water as a non-charged control compared to TMAEA. **(B)** Photo-rheology of the same system where no crossover point is observed, which suggested a solid was not formed.

Table S4.1. Photo-DSC results and subsequent percent conversion calculations of every homopolymer and TMAEA/NVP copolymer system.

Sample	Theoretical $\Delta H_{polymerization}$ (J/g)	Measured $\Delta H_{polymerization}$ (J/g)	Percent Conversion (%)
TMAEA	387	290	75
AAS	360	126	35
AASNa	325	130	40
SPAK	322	145	45
TMAEA/NVP2.5	354	290	82
TMAEA/NVP5	365	317	87
TMAEA/NVP10	342	307	90
TMAEA/NVP20	346	305	88
TMAEA/NVP30	325	292	90

Table S4.2. Tensile results of photopolymerized films of homopolymers.

Sample	Stress at 100 % elongation (MPa)	Elongation (%)
TMAEA	$9.2\ 10^{-2} \pm 0.53$	1250 ± 100
AAS	$6.7\ 10^{-3} \pm 0.21$	250 ± 55

AASNa	$9.7\ 10^{-3} \pm 0.34$	550 ± 130
SPAK	$3.7\ 10^{-3} \pm 0.2$	1130 ± 80
PEGMEA480	$5.1\ 10^{-3} \pm 0.43$	830 ± 240

Table S4.3. Tensile and hysteresis results of photopolymerized films TMAEA/NVP copolymers.

Sample	Stress at 100 % elongation (MPa)	Elongation (%)	Hysteresis (%) Cycle 1	Cycle 2	Cycle 3	Cycle 4	Cycle 5
TMAEA	0.092 ± 0.0053	1250 ± 100	14 ± 2.1	10 ± 3.5	9 ± 1.5	9 ± 2.2	9 ± 2.9
TMAEA/VP2.5	0.11 ± 0.0073	1170 ± 88	20 ± 4	16 ± 3	15 ± 1	13 ± 4	13 ± 4
TMAEA/VP5	0.13 ± 0.0053	1030 ± 69	35 ± 6	28 ± 7	28 ± 5	25 ± 7	24 ± 5
TMAEA/VP10	0.21 ± 0.0081	900 ± 17	41 ± 3.4	35 ± 8.7	33 ± 10	33 ± 3.4	31 ± 6.7
TMAEA/VP20	0.29 ± 0.15	640 ± 49	68 ± 12	54 ± 13	50 ± 9.8	48 ± 10	48 ± 5.3
TMAEA/VP30	2.6 ± 0.47	160 ± 35	87 ± 15	65 ± 17	61 ± 12	55 ± 12	52 ± 13

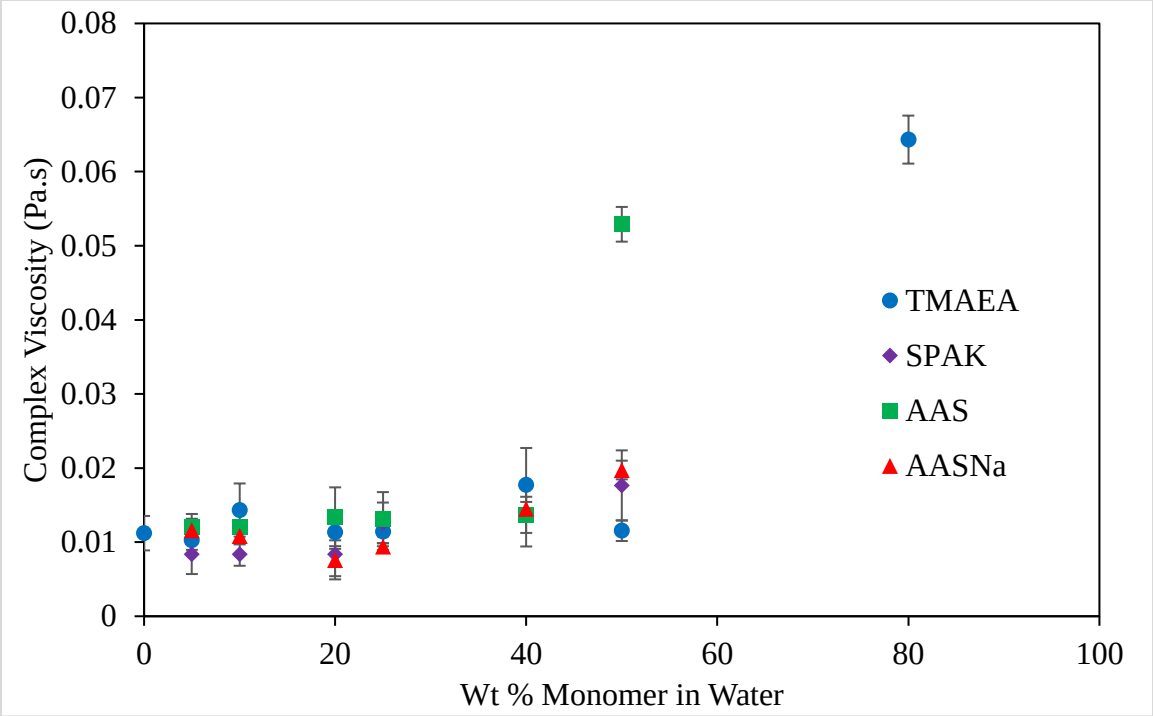

Figure S4.2. Concentric cylinder rheology provides complex viscosity of monomer solutions as a function of monomer concentration ($n = 3$, $p < 0.05$). TMAEA and AAS exhibit increased viscosity at photopolymerization concentration compared to AASNa and SPAK.

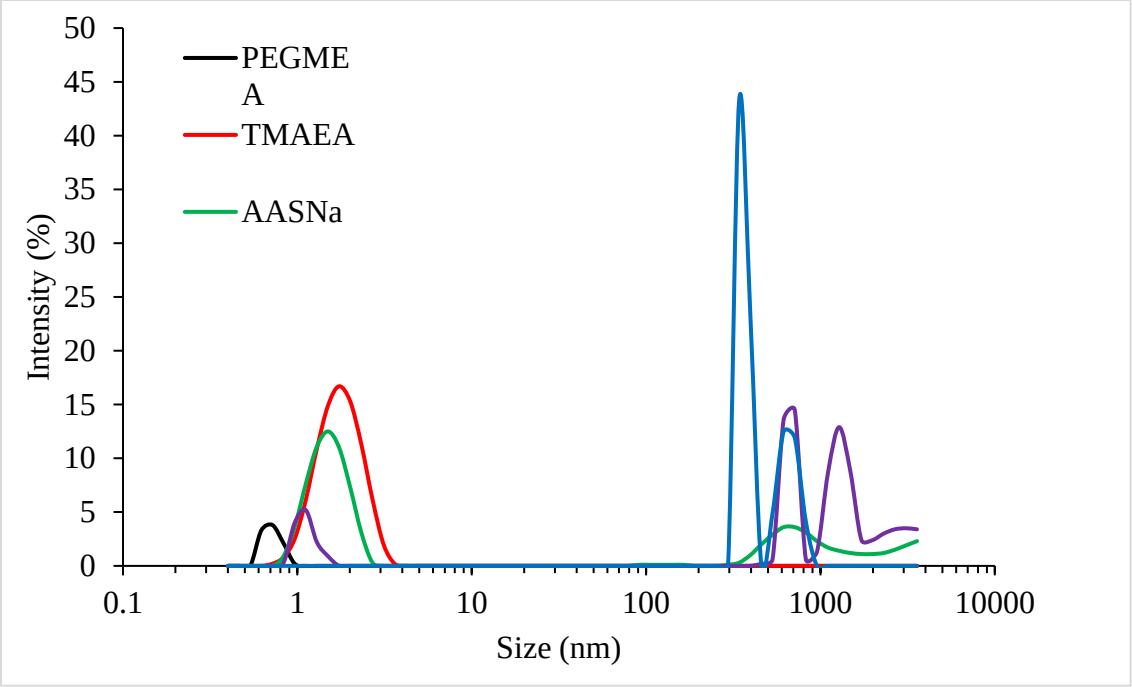

Figure S4.3. Dynamic light scattering reveals ionic aggregation in monomer.

Rheology of monomer solutions revealed complex viscosity as a function of monomer concentration (**Figure S4.2**). The increased viscosity of TMAEA and AAS at monomer concentrations relevant to photopolymerization (80 wt% and 50 wt%, respectively) suggests a role of monomer viscosity on final film modulus. This viscosity decreased significantly upon the addition of water to monomer solutions, confirming aggregate presence in monomer solutions. Interestingly, AASNa and SPAK, which both contain large counterions, failed to exhibit this increase in viscosity at 50 wt% in water. This decreased viscosity corresponded to a decrease in final film modulus, suggesting the potential for solution viscosity to aid in monomer selection for vat photopolymerization.

The discrepancies between monomers based on photo-DSC potentially arises from varied ionic aggregation in the monomer solution prior to polymerization (**Figure S4.3**). As seen in dynamic light scattering, each of the ionic monomers exhibited larger aggregates

as compared to $PEGMEA_{480}$, suggesting a role in monomer aggregation for the successful formation of free-standing films. The size of each of these aggregates and their shape potentially direct both the kinetics of polymerization and the properties of the free-standing film. Further studies as to the particular mechanism and the potential extension of these monomers is currently underway.

Chapter 5: Vat Photopolymerization of Liquid, Biodegradable PLGA-based Oligomers as Tissue Scaffolds

Emily M. Wilts[1], Aleena Gula[1], Corey Davis[1], Nicholas Chartrain[2], Christopher B. Williams[2], and Timothy E. Long[1*]

(Published in *European Polymer Journal*, **2020,** *130*, 109693)

[1]*Department of Chemistry, Macromolecules Innovation Institute, Virginia Tech, Blacksburg, VA 24061*

[2]*Department of Mechanical Engineering, Macromolecules Innovation Institute, Virginia Tech, Blacksburg, VA 24061*

5.1 Abstract

Additive manufacturing (AM) of tissue scaffolds provides medical professionals and patients with personalized treatment options, which align with patients' specific physiology and provide a more efficient and precise manufacturing process. Vat photopolymerization (VP) AM affords biocompatible, degradable, and high-resolution scaffolds capable of achieving specific pore sizes necessary for tissue regeneration. Earlier biodegradable, photoactive polymers for the VP platform usually require dissolution in a solvent or water, which often results in anisotropic shrinkage upon drying and inconsistencies in the final part geometry. This work describes a photoactive oligomeric precursor that eliminates the requirement for water or solvent during VP. Poly(lactide-*co*-glycolide) (PLGA) diacrylates with low number-average molecular weights (< 1400 g mol^{-1}) provided liquid, viscous precursors. Upon crosslinking, the networks exhibited mechanical strength and low cytotoxicity, which are prerequisites for soft tissue scaffolds. Systematically varying the ratios of lactide to glycolide provided a range of degradation rates from 4 to 12 wks. Tailored degradation rates will enable use in different anatomical environments. Cytotoxicity and cell attachment studies revealed crosslinked films that

promoted cell growth and proliferation. This manuscript describes an expanded polymer toolbox for AM of tissue scaffolds with precise resolution in the absence of solvents.

5.2 Introduction

Tissue engineering requires an interdisciplinary strategy of chemistry, biology, and engineering to address inherent complexity.[1,2] Creating a synthetic scaffold to regenerate tissues requires biocompatibility, degradability, and the ability to encourage cell growth and regeneration.[3,4,5] Poly(lactic acid) (PLA), poly(lactic acid-*co*-glycolic acid) copolymers (PLGA), and polycaprolactone (PCL) exemplify popular polymeric scaffolds, where strength and durability targeted to specific tissue dictates selection.[6,7] Morphology is another equally important criterion for scaffolds, where porous, 3D structures best mimic native tissue.[8,9] The implementation of AM for tissue engineering provides unprecedented structures with tunable pore sizes, mechanical properties, and functionality. Unfortunately, the lack of printable biodegradable/biocompatible precursors limits the expansion of this technology. As the availability of functional materials for AM begins to emerge, healthcare providers will improve patient care with personalized tissue scaffolds at an affordable cost without the generation of waste or deleterious byproducts.[6,10]

Vat photopolymerization (VP) of tissue scaffolds continues to provide personalized tissue mimics because of micron-scale resolution and ability to create geometrically complex structures.[6] VP selectively crosslinks or photopolymerizes a liquid, photo-active precursor through exposing the material surface to UV light.[11,12] The liquid precursor resides in a vat where a build platform is partially submerged. Exposure to UV light enables the liquid precursor to solidify, creating the first layer of the print. A recoating

blade or movement of the build platform re-submerges the previous layer into the liquid precursor for a subsequent layer to be printed. For commercially available printers, viscosity constraints restrict the types of photo-active precursors to successfully print using VP.[13] Low viscosity (below 10 Pa·s) photoactive precursors without solvent or monomers improve resolution and reduce the potential for residual reactants in the final scaffold.[14,15]

PLGA copolymers represent versatile and commonly used polymeric materials for tissue scaffolds, medical devices, and drug delivery due to its biocompatibility and established hydrolytic degradation pathways in the body.[16–18] Varying ratios of lactide to glycolide tune degradation rates, as lactide degrades slower than glycolide due to the methyl substituent and concurrent tailoring of crystallinity levels.[19,20] For example, Navarro *et al.* blended PLA and poly(ethylene glycol) (PEG) to achieve increased hydrophilicity and an increased degradation rate while also allowing a range of mechanical properties.[21] Grijpma *et al.* reported an early example of PLGA-based materials as tissue scaffolds using VP. The authors described 4,000 g mol^{-1} PEG as a difunctional initiator with *D,L*-lactide with subsequent end-group functionalization with methacrylic anhydride. VP with 54 wt% water afforded gyroid pore networks, capable of functioning as soft tissue scaffolds.[22] These examples exemplify the potential for PLGA-based materials in VP for tissue scaffolds, however more alternatives are needed to eliminate water and further tune mechanical properties.

This manuscript describes the synthesis and characterization of poly(lactide-*co*-glycolide) (PLGA) copolymers and their subsequent performance in VP for tissue scaffolds. The synthesis and thermal characterization of lactide:glycolide (L:G) molar ratios for 1400 g mol^{-1} copolymers revealed each combination remained as a viscous liquid and exhibited

glass transition temperatures (T_g) of -9 to -10 ^oC. Photorheology and photocalorimetry (photo-DSC) characterized the photo-kinetics of the oligomeric diacrylates, which steered printing parameters. DSC and thermogravimetric analysis (TGA) collectively quantified degradation rates for the crosslinked films in phosphate buffered saline (PBS). As expected, scanning electron microscopy (SEM) further revealed faster degradation rates with higher incorporation of glycolide. Cytotoxicity and cell attachment studies indicated that specific compositions facilitated cell growth while others remained cytotoxic, depending on their relative diacrylate conversions. Finally, VP of 75:25 PLGA-diacrylate afforded a 3D lattice structure as an example of a suitable tissue scaffold.

5.3 Materials and methods

5.3.1 Materials

Lactide and glycolide were purchased from Sigma-Aldrich and recrystallized prior to use in ethanol or toluene, respectively. Poly(ethylene glycol) (M_n = 400 g mol^{-1}) (PEG 400) and potassium carbonate (K_2CO_3) were purchased from Alfa Aesar and Sigma-Aldrich, both dried in vacuo at 40 °C for 24 h. Hexanes, acetone, toluene, chloroform, and aluminum oxide were purchased from Sigma-Aldrich and used as received. Dichloromethane (DCM) (99.99% extra dry over molecular sieves) and acryloyl chloride were purchased from Acros Organics and Sigma-Aldrich and also used without further purification. Stannous(II) 2-ethylhexanoate ($Sn(Oct)_2$) was purchased from Sigma-Aldrich and used in a stock solution (0.0125 g mL^{-1}).

5.3.2 Synthesis of poly(lactic-*co*-glycolic) acid-diol (PLGA-diol)

Six combinations of lactide:glycolide (L:G) molar ratios were synthesized. As an example of the synthesis of a L:G ratio of 50:50 copolymer, lactide (4.0 g, 0.028 mol, 1 eq.), glycolide (3.25 g, 0.028 mol, 1 eq.), $Sn(Oct)_2$ stock solution (0.16 mL), and PEG 400 (2.9 g, 0.00725 mol, 0.26 eq.) were added to a flame-dried 100-mL Schlenk flask and purged with nitrogen for 30 min. A flask containing a mixture of monomers, initiator, and catalyst was submerged in a silicon oil bath with a magnetic stir bar at 120 °C for 6 h, yielding poly(lactic-co-glycolic) acid-diol (PLGA-diol). The flask was removed from the bath to cool for 30 min. PLGA-diol was then dissolved in approximately 15 mL of acetone and the product was precipitated into DI water. The product was then dried at 40 °C in a vacuum oven to remove any residual solvents before further use. The viscous, pale-yellow liquid product was isolated at 90% yield. The structure, number-average molecular weight, and L:G ratio were confirmed using ^{1}H NMR spectroscopy. ^{1}H NMR, 400 MHz ($CDCl_3$): 1.2-1.5 ppm (3H, m), 3.25-3.6 ppm (36H, m), 4.02-4.22 ppm (4H, m), 4.68-5.24 ppm (PLGA backbone), and 5.38-5.47 ppm (2H, m).

5.3.3 Synthesis of poly(lactic-*co*-glycolic) acid-diacrylate (PLGA-diacrylate)

The synthesis of a PLGA diacrylate with a L:G ratio of 50:50 was achieved with PLGA-diol (3.0 g, 0.003 mol, 1 eq.), acryloyl chloride (0.81 g, 0.009 mol, 3 eq.), and K_2CO_3 (2.07 g, 0.015 mol, 5 eq.) in a flame-dried, two-necked round-bottomed flask and purged with nitrogen for 30 min. 30 mL of DCM was added to the flask until the PLGA-diol was dissolved. 12 mL of DCM was mixed with acryloyl chloride in an addition funnel and added dropwise at 0 °C. The mixture reacted for 24 h. Distilled water (1 mL) was added to quench any residual acryloyl chloride. Aluminum oxide was added to neutralize any remaining acid and the mixture was stirred for 30 min. DCM was removed under reduced

pressure to yield a white viscous liquid at an average of 88% yield. Acrylation conversions were confirmed using ^{1}H NMR spectroscopy. ^{1}H NMR, 400 MHz ($CDCl_3$): 1.2-1.5 ppm (3H, m), 3.25-3.6 ppm (36H, m), 4.02-4.22 ppm (4H, m), 4.68-5.24 ppm (PLGA backbone), 5.38-5.47 ppm (2H, m), and 5.8-6.6 ppm (6H, m).

5.3.4 Analytical

Photocalorimetry was performed on a TA Instruments Q2000 with an Omnicure S2000 photo-attachment with fiber optic cable. Tzero pans were loaded as either sample pans or reference pans and equilibrated at 25 °C. Following a 1 min isotherm, the pans were exposed to 8 mW cm^{-2} of 365 nm light. Following 5 min irradiation, the light was turned off and the background heat from the light noted. Integrations of the peaks with background correction afforded the heat of polymerization. To calculate percent conversion, the standard values for ΔH_{rxn} for the homopolymerization of acrylates (86 kJ mol^{-1})[23] were employed. The ΔH_{rxn} values obtained from photocalorimetry were normalized based on the moles of acrylates in the sample. Photorheology occurred on a TA Instruments Discovery HR-2 Rheometer with photo attachment and 20 mm PDMS bottom plate with 20 mm disposable upper geometry. Samples were equilibrated at 25 °C for 30 s to provide baselines for all samples. Samples were oscillated at 1 Hz, providing sampling rates relevant for the second timescale. Following 30 s, samples were irradiated at 20 mW/cm^2 and modulus was monitored. The crossover point was determined as the first instance the storage modulus (G') exceeded loss modulus (G"). Thermogravimetric analysis (TGA) was performed on a TGA Q500 with a 20 min isotherm at 110 ^oC and a ramp at 10 ^oC min^{-1} to 600 ^oC. $T_{d,5\%}$ values were calculated where 5 wt% of the mass was lost and the data was normalized after the isothermal step. Stirring with a magnetic stir bar in chloroform,

acetone, and ethanol, for 48 h each afforded a fully extracted system for the following analytical experiments and cell culture studies. Differential scanning calorimetry (DSC) was performed on a TA Instruments Q2000 with heat/cool/heat cycles of 10 °C min^{-1}, 100 °C min^{-1}, and 10 °C min^{-1}, respectively. Samples were dried at 60 °C under vacuum prior to analysis. Glass transition temperatures (T_gs) were calculated from the second heat inflection point. Tensile testing was performed on film-punched dogbones from photocured films with a crosshead motion of 5 mm min^{-1} and grip-to-grip separation of 26.25 mm on an Intron 5500R. Scanning electron microscopy (SEM) images were taken on a Joel NeoScope JCM-5000 Benchtop SEM, under high vacuum at a 10 kV accelerating voltage.

5.3.5 Cell Culture

MDA-MB-231 human breast cancer cells (American Type Culture Collection) were cultured in 5% CO_2 at 37 ºC in Dulbecco's Modified Eagle's Medium supplemented with F-12 Ham (DMEM), 10% fetal bovine serum (FBS) and 1% penicillin/streptomycin. MDA-MB-231 cells were lifted from the culture flask with 0.25% Trypsin/EDTA, concentrated through centrifugation at 120 g for 5 min and counted for subsequent experiments. MDA-MB-231 cells were maintained in T-75 tissue-culture-treated flasks and passaged when ~80% confluent.

5.3.6 Cytotoxicity

The gels were sterilized through a soak in 70% ethanol/water solution, which then underwent a series of soaks with serum-free DMEM 24 h. MDA-MB-231 cells were seeded

into a tissue-culture-treated 24-well plate at 25,000 cells/well. The cells attached and proliferated for 24 h before films were placed on top of cells. Following a 24 h incubation, the samples were brought to room temperature and films removed from the wells. Equal volumes of serum-containing DMEM and CellTiter-Glo were added to each well, rocked for 2 min, and incubated for 10 min. The samples were subsampled 3 times into a 96-well plate, and the resulting luminescence was read by a SpectraMax G2 plate reader in luminescence. Viability was calculated as a percentage relative to untreated cells cultured on the same plate.

5.3.7 Degradation Study

Films of each L:G molar ratio were prepared in the photorheometer with the same procedure as above. Each film was crosslinked with 0.5 wt% Irgacure 2959 at 20 mW/cm^2 forming a 20 mm diameter and 0.5 mm thick film. The films were dried for 24 h at 60 ^{o}C *in vacuo* and placed into phosphate buffered saline (PBS) at 0.1 g/mL. The mixture remained at 37 ^{o}C and 60% relative humidity. TGA, DSC, and SEM measured the degradation process of the films at 1, 2, 4, 8, 12, and 16 wks.

5.3.8 3D Printing

PLGA-diacrylate 75:25 was prepared for printing upon the addition of TPO photoinitiator (1 wt%) and 2,5-bis(5-*tert*-butyl-benzoxazol-2-yl)thiophene (BBOT) UV absorber (0.01 wt%) to increase resolution during curing. The printer comprised a custom-built mask projection micro vat photopolymerization (MPμVP) printer equipped with a 1080p digital micro-mirror device (DMD) and a 365 nm UV LED light source emitting at an intensity of 9 mW cm^{-2}. A 10-mL glass beaker vat and poly(phenyl sulfone) build plate were used. To

increase adhesion to the build plate, the first layer was over-exposed to generate a “raft” onto which all subsequent layers were printed. The part was printed using 100 μm layers exposed for 2 s per layer. Due to the viscosity of the precursor, the build plate descended a depth of 2.9 mm into the vat and used a time delay of 8 s to allow sufficient material to flow and recoat before each layer.

5.4 Results and Discussion

Ring-opening polymerization and subsequent end-group functionalization yielded PLGA-diacrylates, depicted in **Scheme 5.1**. A copolymerization of *L*-lactide and glycolide with a difunctional initiator, $Sn(Oct)_2$ catalyst, and careful exclusion of water, yielded six compositions of poly(lactic-*co*-glycolic)acid copolymers, ranging from 100 mol % lactide to 25:75 lactide:glycolide (L:G). The PLGA-diol precursors was derivatized with an excess of acryloyl chloride to yield PLGA-diacrylates. The purification process with a basic aluminum oxide column rendered the system free of residual acryloyl chloride or any acid formed during the end-group functionalization. The range of compositions tailored degradation rates for the crosslinked films, utilizing the well-established slower degradation time of lactide relative to glycolide. Previous studies showed pure poly(lactic acid) degrades in more than six months where poly(glycolic acid) degrades in nearly one month in PBS at 37 ^{o}C.[19,24,25] This range of degradation rates enables versatility for a myriad of biomedical applications such as tissue scaffolds, cardiovascular stents, or degradable sutures.

Scheme 5.1. Ring-opening polymerization and subsequent end-group functionalization with acryloyl chloride yielded PLGA-diacrylate.

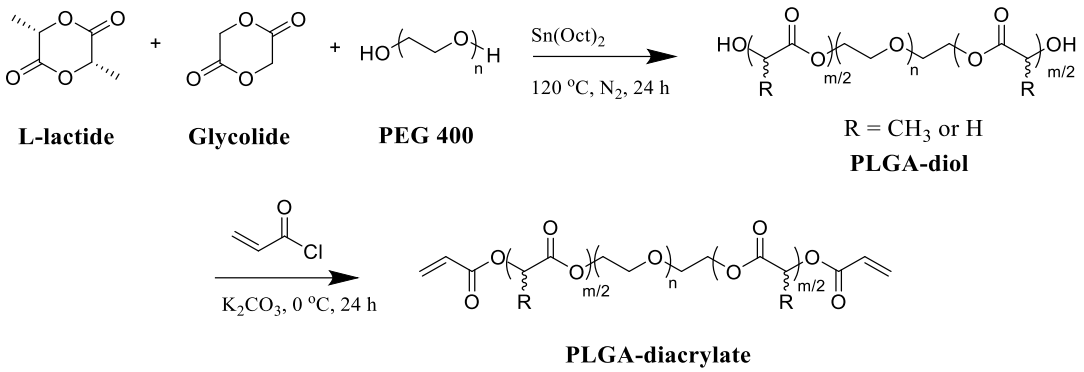

VP requires a liquid photo-active precursor to print high-resolution 3D parts. This restriction tuned the design of the PLGA-diacrylate copolymers where the number-average molecular weight target remained below 1400 g mol^{-1} to yield a liquid, viscous product. The synthesis of varying L:G molar ratios yielded a range of viscosities of the final products resulting from the different reaction rates of lactide and glycolide, which imposed a blocky sequence distribution. The relative reactivity of glycolide compared to lactide is approximately 3:1.[26] Synthesizing copolymers at higher temperatures (150 to 200 °C) produces a more random sequence distribution. Since the monomer mixtures were polymerized at 120 °C, glycolide was more likely to react first and create blocks at the onset of propagation while the lactide blocks were incorporated later in the chains.[26] As a result of the reactivity differences, i.e., the samples containing higher glycolide content likely contained polyglycolide blocks, which ultimately increased the viscosity of the resulting polymer. Although crystallinity was not observed, the polyglycolide blocks presumably induced some degree of ordering thus increasing the zero-shear viscosity.

^{1}H NMR spectroscopy confirmed the PLGA-diacrylate number-average molecular weight (M_n), L:G molar ratios, and acrylation conversions. **Figure 5.1** depicts the annotated ^{1}H NMR spectra where peaks a-c refer to the acrylate, d/g the PLGA backbone,

and e/f the PEG backbone. Integrations from the g peak enabled the calculation of the lactide percentage while subtracting this value from the d peaks, corresponding to the entire PLGA backbone, determined the glycolide percentage. Adding the molecular weight of PEG to the PLGA contribution yielded the total number-average molecular weight of each oligomer, ranging from 1290 to 1400 g mol^{-1}. The integrations of peaks a, b, and c confirmed quantitative conversion of the diol end-groups, where the total integration corresponding to 100% conversion was 6H. Each PLGA-diacrylate exhibited a percent acrylation of ≥ 95%.

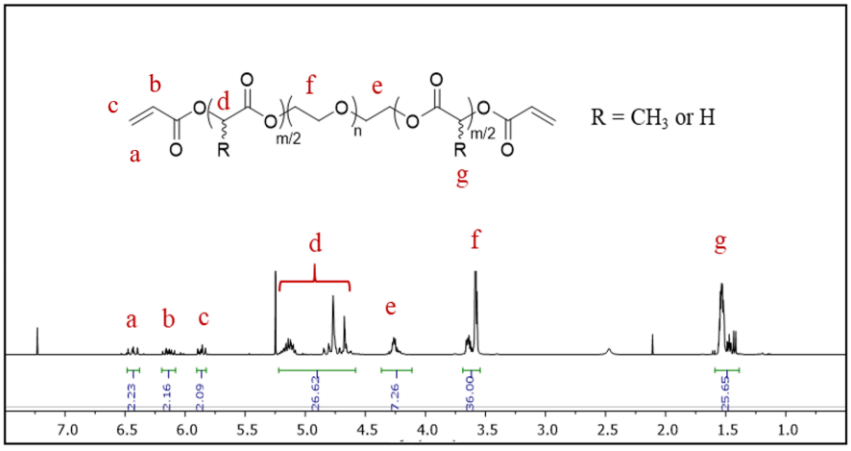

Figure 5.1. ^{1}H NMR spectroscopy revealed structural confirmation of 50:50 PLGA-diacrylate at 1320 g mol^{-1}.

DSC and TGA revealed the thermal properties of the oligomeric precursors and subsequent crosslinked films. **Figure 5.2A** depicts a plot of the glass transition temperatures (T_g) of the PLGA-diol and PLGA-diacrylate crosslinked films as a function of mol % lactide. The PLGA-diols, which were viscous liquids at room temperature, exhibited T_gs between -10 and -9 ^{o}C. After crosslinking, the number-average molecular weight significantly increased, which resulted in an increase of T_gs to 17-20 ^{o}C.

Considering the temperature of the body is 37 ^{o}C and the crosslinked films were flexible above 20 ^{o}C, this system represents an optimal candidate for soft tissue scaffolds. **Figure 5.2B** depicts the relationship of temperatures at 5% weight loss ($T_{d,5\%}$) as a function of mol % lactide. TGA revealed the PLGA-diols and crosslinked PLGA-diacrylates exhibit $T_{d,5\%}$s of 225 to 230 ^{o}C and 245 to 249 ^{o}C, respectively. TGA traces of the PLGA-diols show a shape dependency on glycolide content (**Figure S5.1**). As the glycolide content increases, the loss in mass becomes more gradual, possibly owing to the individual $T_{d,5\%}$ values of polylactide (225 ^{o}C) and polyglycolide (260 ^{o}C).[27,28]

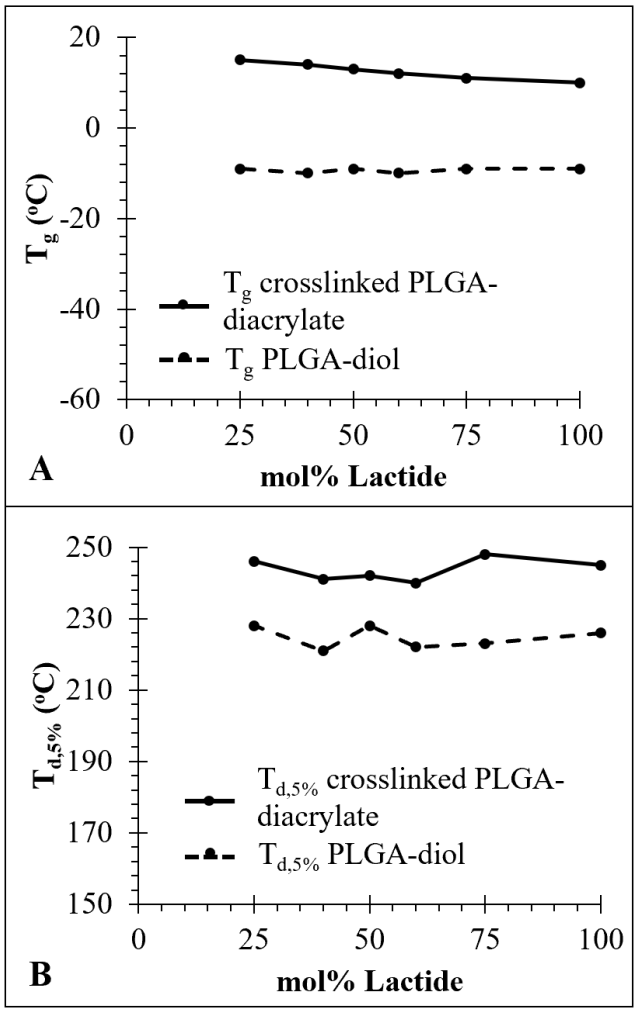

Figure 5.2. (A) T_g as a function of mol % lactide **(B)** and $T_{d,5\%}$ as a function of mol % lactide of PLGA-diol and crosslinked PLGA-diacrylate.

Rheology experiments showcased an increase in zero-shear viscosity as a function of glycolide composition, depicted in **Figure 5.3** SEC-LS analysis, zero-shear viscosities synthesized at different temperatures, and melt rheology experiments of the PLGA-diol copolymers revealed a possible supramolecular structure describing the variation in zero-shear viscosities. SEC-LS analysis of the PLGA-diol copolymers showed a constant Đ of 1.30 to 1.40 across the series and constant M_n of 1200 to 1400 g mol^{-1}, indicating Đ or M_n variation did not contribute to the variable zero-shear viscosities (**Figure S5.3**). Higher reaction temperatures and longer reaction times will result in transesterification after the complete polymerization, which randomizes the sequence distribution.[20] Reacting the copolymers at a higher temperatures (>120 ^oC) and longer reaction times (> 6 h) resulted in a decreased in zero-shear viscosity. A decrease in zero-shear viscosity for 50:50 (**Figure S5.5**) from 32 Pa·s reacted at 120 ^oC to 14.2 Pa·s reacted at 180 ^oC. These experiments suggested a more random micro-structure with a decreased zero-shear viscosity, indicating the presence of ordering in more blocky compositions. Rheology also provided frequency sweeps (**Figure S5.4**) from 1-500 rad s^{-1} of the three samples, where the copolymers were synthesized using the reported reaction conditions (120 ^oC and 6 h). Sample 50:50 begins to show shear thinning at 200 rad s^{-1}, and 100:0 and 75:25 do not show thinning at the examined shear rate range. This displays the dissociation of non-covalent ordering in the 50:50 sample, which may originate from a blocky sequence distribution.

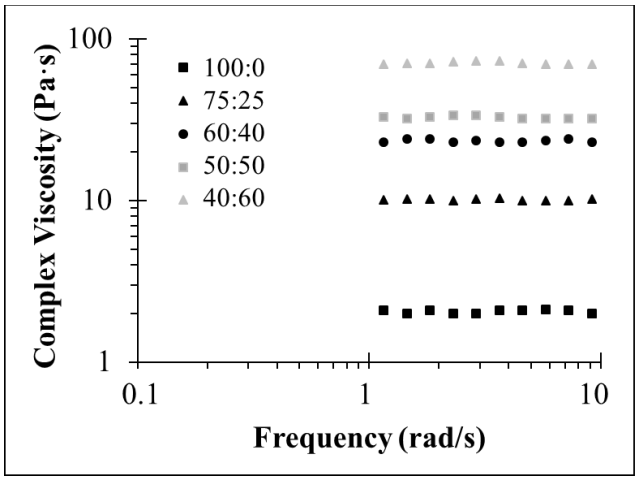

Figure 5.3. Complex viscosity as a function of frequency of PLGA-diacrylates.

Photorheology probed the photocuring kinetics through the determination of crossover time and a plateau storage modulus (G_N^o) following irradiation with UV-Light. **Figure 5.4A** depicts a typical photorheology experiment where the oligomers combined with a photoinitiator (Igracure 2959) were exposed to UV light for 30 s while monitoring the storage and loss moduli. Cytotoxicity studies of various Irgacure® initiators verified Irgacure® 2959 as the least toxic photoinitiator.[29] The plateau storage moduli were defined as the storage modulus after the trace plateaus with less than 5% change over 30 s. The crossover time denoted the time when the storage modulus crosses over the loss modulus, which revealed the polymer transitioned from a more viscous to a more elastic behavior. Photorheology provided a method of measuring relative modulus of the material following photocuring and a timeframe for the photo-active precursor to form a solid film. Further studies excluded 25:75 PLGA-diacrylate since the material was too viscous to perform photo-rheological analysis.

Figure 5.4B depicts the response of the G_N^o and crossover time to as a function of amount of photoinitiator. 60:40 PLGA-diacrylate provided a median zero-shear viscosity value compared to the other samples and thus was used in the photoinitiator optimization study. This analysis determined the optimal photoinitiator concentration to form a crosslinked film with the fastest crossover time and highest G_N^o. In this study, the photoinitiator level increased from 0.25 to 5 wt% compared to the total weight of PLGA-diacrylate. Higher photoinitiator concentration will result in lower molecular weight due to an increase in radical concentration and termination events. The photoinitiator was dissolved in 1 g mL^{-1} of acetone. Solvation of the photoinitiator in 1 g mL^{-1} of acetone prior to addition to the PLGA-diacrylate facilitated efficient incorporation. This led to higher solvent levels with increased photoinitiator concentration.

Figure 5.4B revealed the optimal photoinitiator amount 0.5 wt %, on the basis the highest G_N^o and the lowest crossover time. Incorporation of 0.5 wt% photoinitiator results in a G_N^o of 2 MPa, while further incorporation resulted in a decrease in G_N^o to 0.6 MPa at 5 wt %. The lowering of G_N^o with increasing photoinitiator likely results from two factors; (1) increasing photoinitiator concentration increased the amount of solvent, (2) and a higher radical concentration could lower molecular weight due to a higher termination rate. Plasticization due to solvent and lower molecular weight will both cause a decrease in G_N^o. The crossover time also decreased with increasing photoinitiator incorporation, which could result from increased solvent and lower zero-shear viscosity. These conditions presumably promote faster crosslinking kinetics.

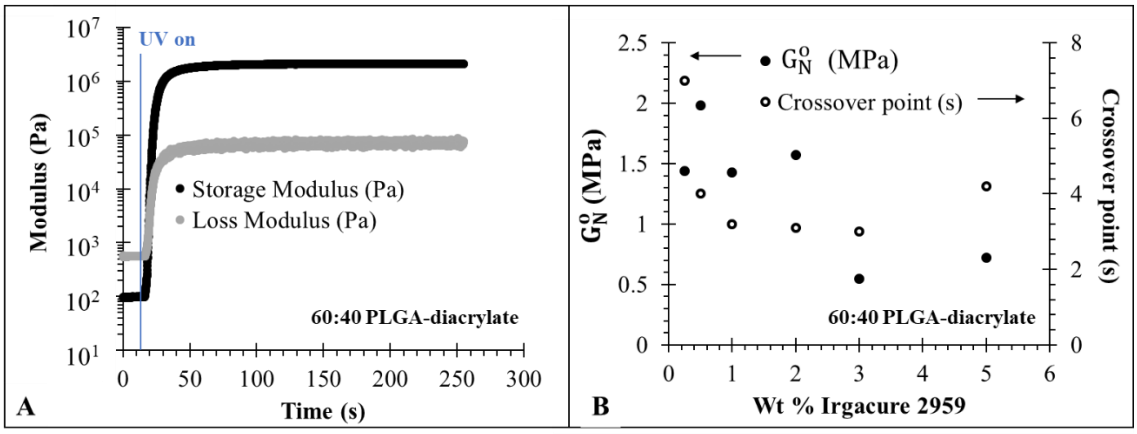

Figure 5.4. (A) Storage and loss modulus as a function of time using photo-rheology. **(B)** wt% Irgacure 2959 as a function of G_N^o and crossover point.

Figure 5.5 depicts further photocalorimetric studies and their relationship to acrylate conversions. **Figure 5.5A** depicts heat flow as a function of time for five of the PLGA-diacrylate samples using the optimized photoinitiator concentration of 0.5 wt %. From these signals, the maximum heat flow and the integration of the peak elucidated the time to peak, which denoted the fastest rate, and the heat of reaction (ΔH_{rxn}), respectively. From the integrations of the traces, the 100:0 PLGA-acrylate sample experienced the largest peak maximum and the 40:60 exhibited the smallest.

Figure 5.5B depicts the relationship between ΔH_{rxn} and time to peak for the various compositions of the PLGA-diacrylate oligomers. The x-axis illustrates the mol % lactide in each sample with glycolide as the remaining component. The solid circles depict the ΔH_{rxn}, and the analysis elucidates an increase in ΔH_{rxn} with increasing mol % lactide. Sample 40:60 afforded a ΔH_{rxn} of 39.5 J g^{-1} and the series plateaus at 75:25 and 100:0 with values of 100.2 and 99.8 J g^{-1}, respectively. This suggested the samples with more lactide enabled further crosslinking of the acrylate end-groups during the time of the experiment.

The open circles depict the time to peak, which denotes the point at which the reaction is the fastest. The samples with higher glycolide content (40:60, 50:50) exhibited a time to peak of ~1.5 s where the remaining samples averaged ~1.25 s. These apparent trends suggested a comparison to gel fraction and zero-shear viscosity data.

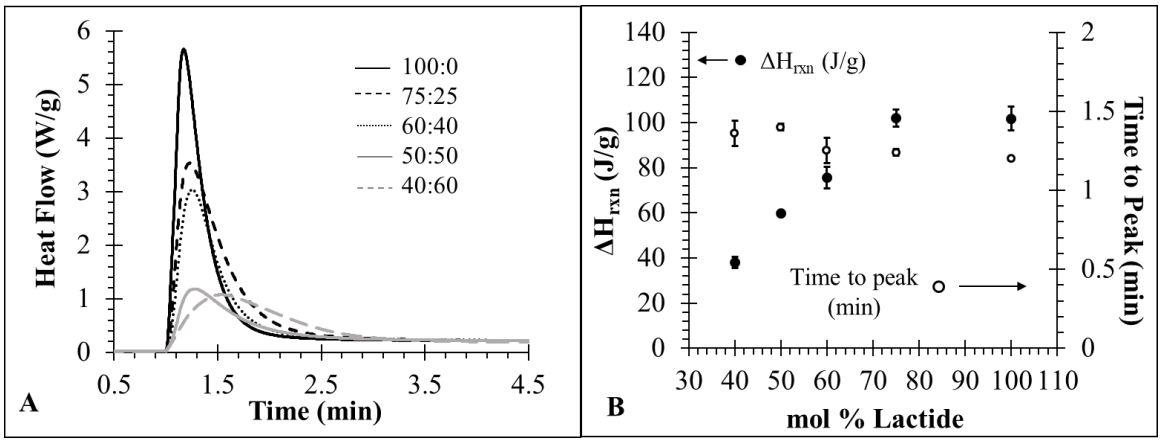

Figure 5.5. (A) Heat flow as a function of time using photo-DSC, **(B)** mol % lactide as a function of ΔH_{rxn} and time to peak.

Figure 5.6A depicts the relationship between gel fraction and relative acrylate conversion with the composition of the PLGA-diacrylate oligomers. Gel fraction describes the quantity of the PLGA-diacrylate in the crosslinked network, although it is possible for only one acrylate to react and remain incorporated into the network. Increased glycolide incorporation afforded lower gel fractions and acrylate conversions. The 100 mol % lactide and 40:60 samples exhibited gel fractions of 93% and 79%, respectively. These relationships confirmed the samples with higher glycolide levels experienced lower conversions, and thus more unreacted diacrylates remained in the films. The lower conversions also suggested the samples containing more glycolide incorporation may have

contained more residual acrylates, which could account for increased cytotoxicity as discussed later.

Figure 5.6B depicts the relationships between zero-shear viscosity and acrylate conversion with the composition of the PLGA-diacrylate oligomers. As the glycolide incorporation increased, photocalorimetry revealed a decrease in conversion. To elucidate the origin of this observation, an analysis of zero-shear viscosity data versus conversion revealed an inverse relationship. As the viscosity of the PLGA-diacrylates increased, the acrylate conversion and number of crosslinks decreased. As viscosity increased, the chain ends were less mobile and unable to react prior to crosslinking. The restricted mobility due to higher viscosity presumably prevented end-groups from reacting, thus resulting in lower conversions.

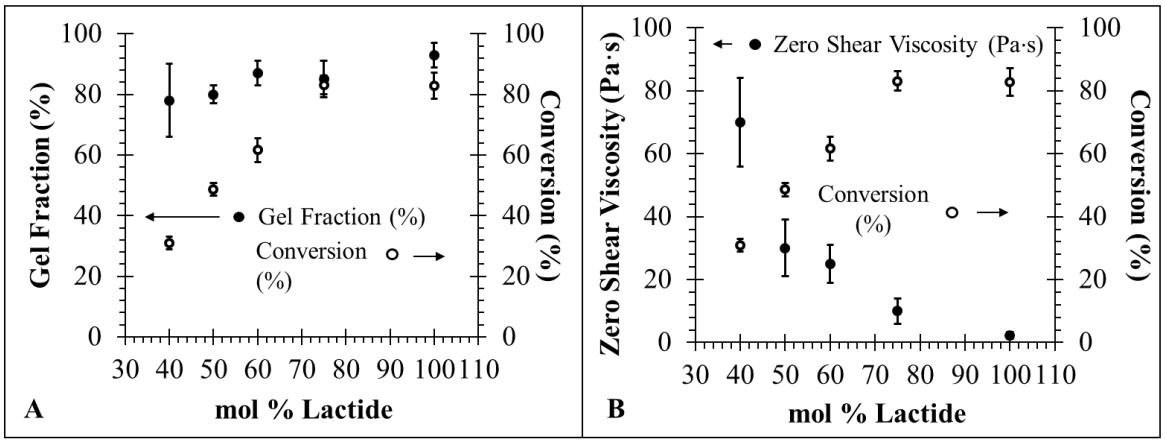

Figure 5.6. (A) Gel fraction and conversion, and **(B)** conversion and zero-shear viscosity as a function of mol % lactide.

Figure 5.7 illustrates the tensile properties of the crosslinked, extracted PLGA-diacrylate films. **Figure 5.7A** depicts the tensile curves where the Young's modulus and elongation-at-break were calculated to elucidate the durability of the crosslinked films.

Figure 5.7B summarizes Young's modulus and percent elongation-at-break as a function of mol % lactide. Samples 100:0 and 75:25 exhibited statistically lower Young's moduli and greater elongation-at-break compared to 60:40, 50:50, and 40:60. As exemplified in the photo-kinetic studies, higher glycolide content resulted in a decrease in conversion. The decreased reaction conversion was expected to decrease film strength resulting from the lower molecular weight and more dangling ends relative to the samples at higher conversions. However, because polyglycolide is a stiffer polymer compared to polylactide, higher glycolide content overcame the shortcomings from low conversion and experienced statistically larger Young's moduli. The elongation-at-break was also inversely related to the Young's moduli data where the stiffer samples showed a lower elongation-at-break. All samples exhibit a Young's modulus of 0.01 to 0.03 MPa, which rendered the systems suitable for soft tissue scaffolds.[30]

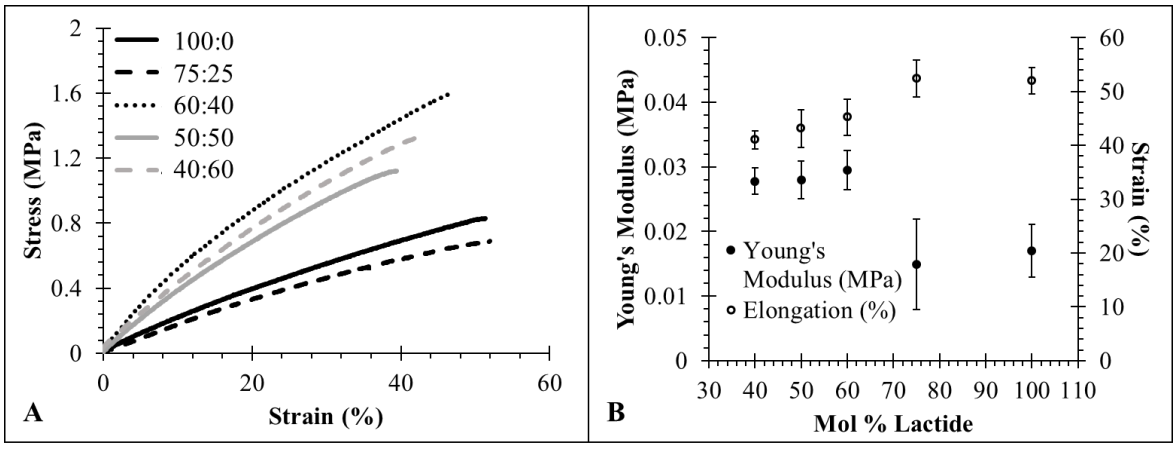

Figure 5.7. (A) Stress vs. strain traces of crosslinked, extracted films. **(B)** Mol % lactide as a function of Young's modulus and strain at break.

Figure 5.8 depicts the thermal analysis of extracted films from a degradation study. This degradation study provided approximate times when crosslinked films optically

degraded and/or dissolved in PBS solution. PLGA degrades through hydrolytic cleavage of the labile ester bonds, resulting in the formation of lactic acid, glycolic acid, and acidic oligomers.[19] The acid formation further catalyzes the degradation of PLGA resulting in autocatalytic hydrolysis. In order to counteract this effect, the degradation study was performed in a buffered solution to prevent a large increases in pH during testing.[31] Acrylate addition during crosslinking results in a non-hydrolytically degradable carbon-carbon backbone. After the entire PLGA backbone degrades, poly(acrylic acid) will remain without backbone degradation, but will dissolve in the water. Therefore for this study, the absence of films and optically transparent PBS qualitatively defined full degradation. Thermal analysis, TGA and DSC, enabled monitoring of the films during degradation. As the films degrade, the $T_{d5\%}$ and T_g should both decrease. $T_{d,5\%}$ denotes where 5 wt% of the sample volatilizes as a function of temperature. As the films degrade, the molecular weight will begin to decrease and volatile by-products will form, resulting in a decrease of $T_{d5\%}$. T_g is also expected to decrease as degradation occurs due to more chain ends.

Figure 5.8A depicts $T_{d,5\%}$ for each crosslinked film as a function of time. All of the samples exhibited $T_{d,5\%}$ values ranging from 240 to 250 ^oC and the onset of a decrease depending on exposure time to the PBS solution. The 100:0 sample remained isolatable after 16 wks and exhibited a final $T_{d5\%}$ of 210 ^oC. This indicated the system degraded and the low molecular weight degradation products contributed to the lower $T_{d,5\%}$. Examining the samples with glycolide content, an apparent trend occurred where the degradation rate, as a function of the slope of the trend, increased as the mol % glycolide content increased. The sample containing the most glycolide content, 40:60, degraded and dissolved in the PBS solution after 4 wks, while the $T_{d5\%}$ lowered to 189 ^oC at week 4.

Figure 5.8B depicts T_g of each crosslinked film as a function of degradation time. The T_g trends follow the $T_{d5\%}$ trends, i.e. 100:0 maintains the highest T_g after 16 wks and 40:60 degrades the fastest with the lowest T_g of -15 ^oC after 4 wks. Similar to the $T_{d5\%}$ data, the 100:0 sample exhibited degradation during the time of the test as the low molecular weight degradation products and newly formed dangling ends created more mobility, which resulted in a decreased T_g. The rapid degradation of 40:60 is also apparent from the T_g, which decreases from 20 ^oC to15 ^oC after 4 wks, with an average drop of 10 ^oC between each time point.

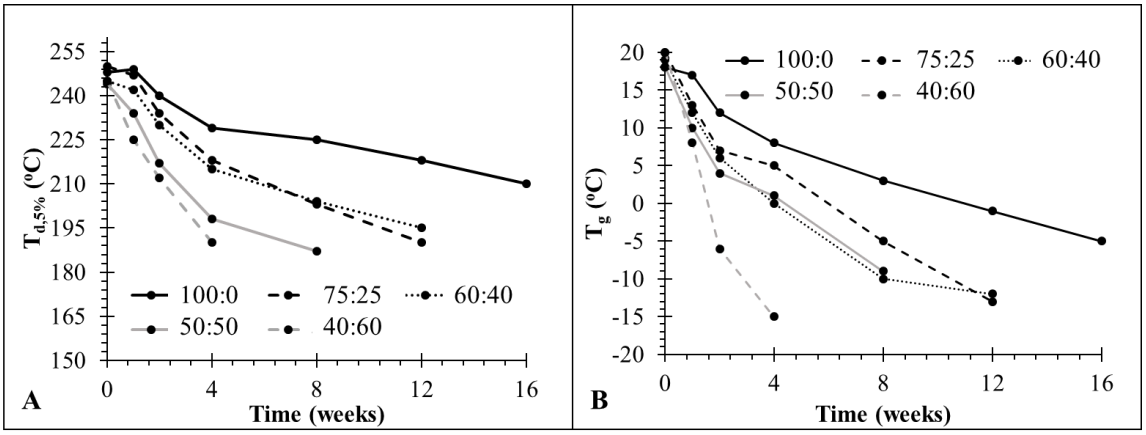

Figure 5.8. DSC and TGA measured the degradation progress. **(A)** $T_{d5\%}$ as a function of degradation time and **(B)** T_g as a function of degradation time.

SEM imaging of each film at each time point elucidated the physical appearance of the films throughout the process. **Figure 5.9** depicts the film surfaces before degradation, and the week before the film fully degraded or dissolved. Each film originally had a relatively smooth surface, however, after exposure to PBS, the films developed voids due to degradation over time. The sample containing 100 mol % lactide survived the full 16

wks, while the 75:25 and 60:40 films could not be recovered after 12 wks. The 50:50 and 40:60 films degraded or dissolved most quickly, 8 and 4 wks, respectively.

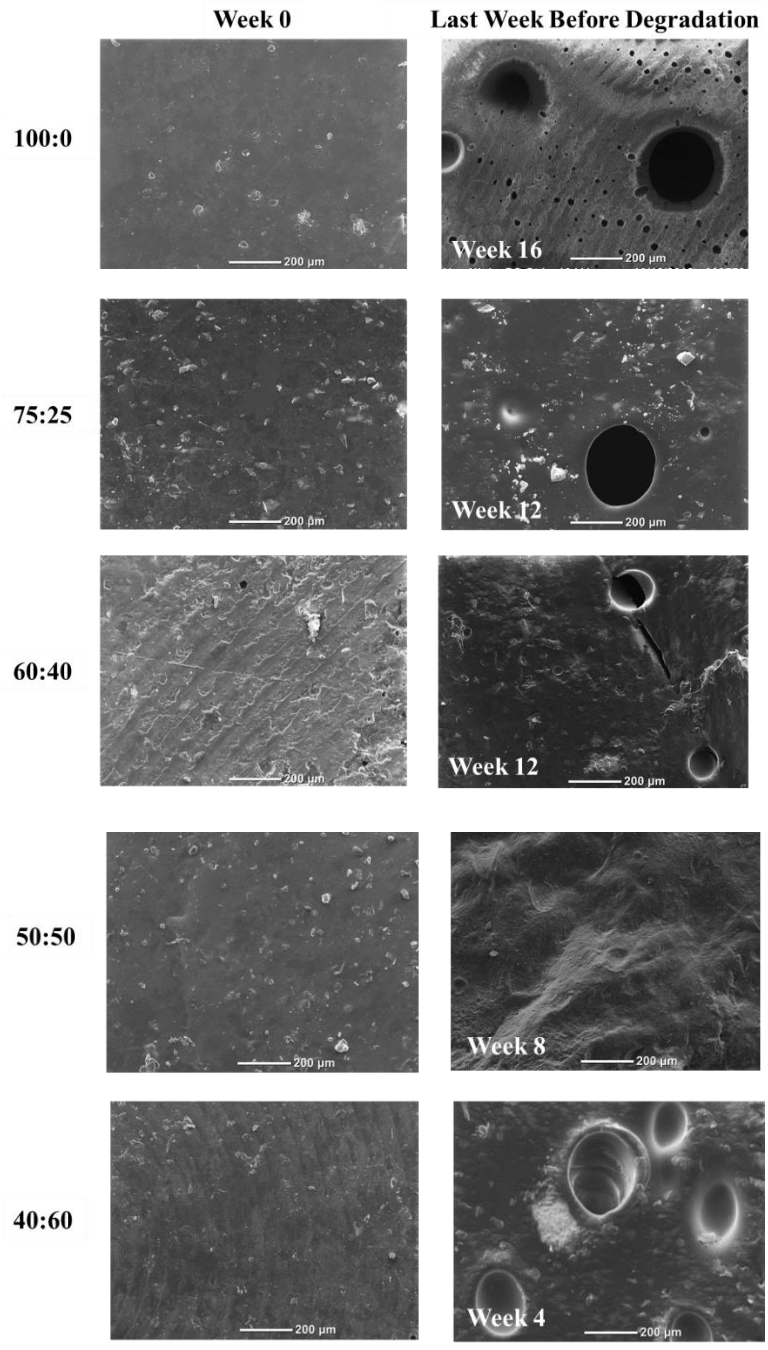

Figure 5.9. SEM images depicting surfaces of week 0 films and the last week before complete degradation.

Cytotoxicity and cell attachment studies determined the feasibility of the discussed PLGA-diacrylates as tissues scaffolds. **Figure 5.10A** depicts cytotoxicity studies of each crosslinked, extracted film over 24, 48, and 72 h. The extraction process ensured the absence of residual diacrylate, photoinitiator, or solvent to solely test the cytotoxicity of the crosslinked films. Although this process extracted residual diacrylates, acrylates may still exist because each system did not reach 100 % conversion. Each sample sustained above 70% viability after 24 h, which provided adequate evidence these materials would cause significant cell death. After 48 h, 100:0, 75:25, 60:40, and 50:50 exhibited an average decrease of viability of 12% with a subsequent decrease after 72 h of an average of 6 %. The crosslinked film 40:60 began with a viability of 66 % after 24 h and dropped to 22 % over the full 48 h, indicating its apparent cytotoxicity. According to the photo-DSC data, 40:60 exhibited the lowest conversion, which may suggest unreacted acrylates play a role in the film's cytotoxicity.

Figure 5.10B depicts cell attachments studies as a function of cell viability on the surface of the crosslinked, extracted films over 24, 48, and 72 h. The 100:0 and 75:25 samples exhibited optimal viability and attachment, and after 72 h, the films maintained viability above 70 %. Attachment studies of 100:0 also revealed in increase in viability after 72 h, which indicated cells proliferation on the film surface. As the incorporation of glycolide increased, samples 60:40, 50:50, and 40:60, all began to incite cell death after 72 h. As discussed previously, increased glycolide incorporation resulted in decreased acrylate conversion. The presence of residual PLGA-diacrylates in the system was eliminated during the extraction process, however free mono-acrylates in the system may facilitate the apparent cytotoxicity.

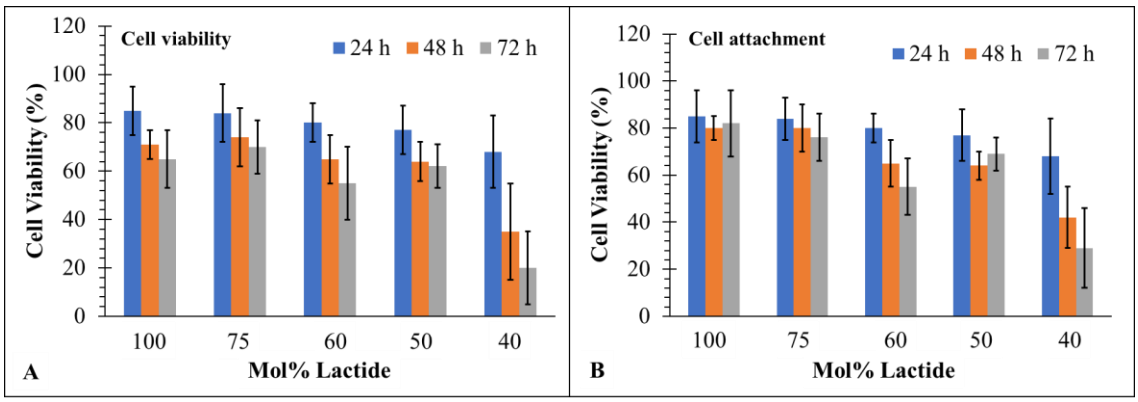

Figure 5.10. (A) Cell viability and **(B)** cell attachment studies over 72 h using extracted films.

As a proof of concept, a custom-built mask projection micro-vat photopolymerization (MPμVP) printer created a 3D lattice structure, depicted in **Figure 5.11**. Printing with a photoinitiator concentration of 1 wt% TPO resulted in over-curing, while the addition of 0.01 wt% UV absorber enabled printing without over-cure, achieving a structure resembling the designed part geometry. **Figure 5.11** depicts SEM images of the structure, which showcase high resolution. Lattice structures, similar to the one depicted, could facilitate tissue regeneration, and this material will be tested to evaluate its feasibility as a 3D tissue scaffold in the future.

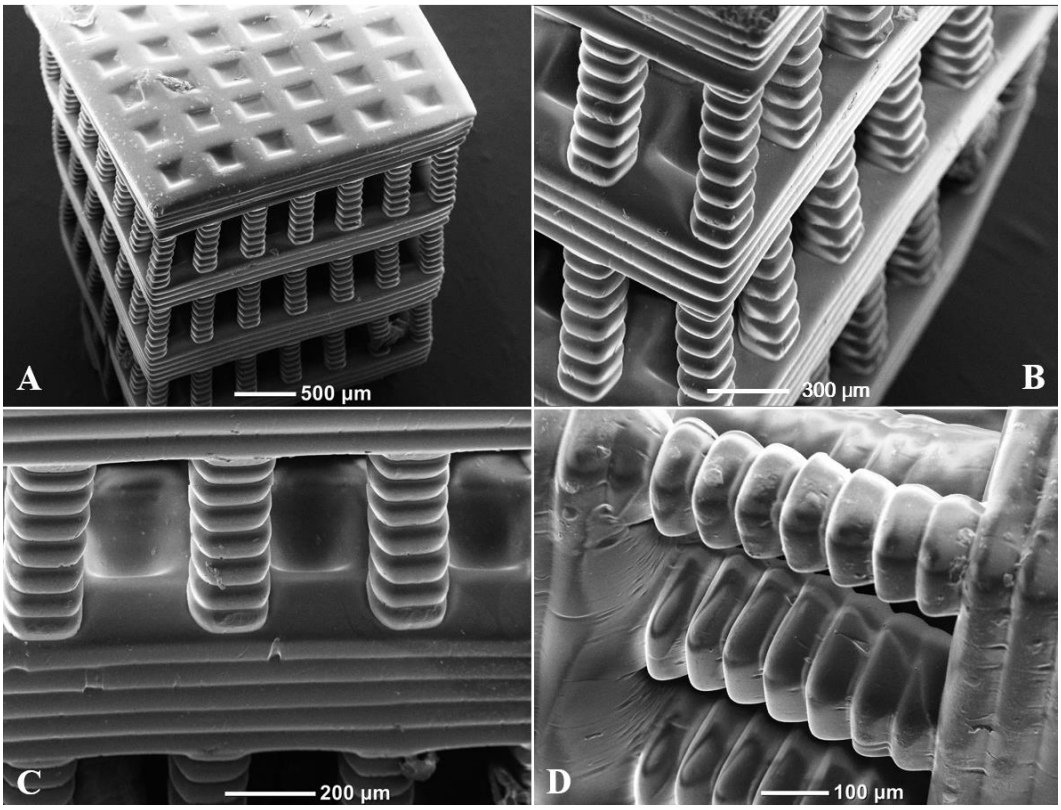

Figure 5.11. SEM images of a 3D printed lattice structure of 75:25 PLGA-diacrylate at **(A)** 27x, **(B)** 80x, **(C)** 100x, and **(D)** 150x magnification.

5.5 Conclusions

This manuscript demonstrated the synthesis, characterization, and VP of oligomeric PLGA-based photoactive precursors for potential use in tissue engineering. Biodegradable, photoactive polymers for VP AM commonly require dissolution in a solvent or water, potentially resulting in shrinkage upon drying and inconsistencies in the final part geometry. The discussed system showcased a photoactive polymer precursor with a low viscosity enabling printing without requiring non-reactive diluents. A series of poly(lactide-*co*-glycolide)diacrylates at low number average molecular weights (< 1400 g mol^{-1}) provided liquid, viscous precursors. The series of crosslinked networks with various L:G ratios

exhibited T_g's ranging from 17 to 20 ^oC and Young's moduli of 0.01 to 0.03 MPa, rendering the systems suitable for soft tissue scaffold applications. Photo-kinetics and rheology experiments revealed that high glycolide composition led to increased zero-shear viscosity and lower acrylate conversions. The cytotoxicity and cell attachment studies revealed a decrease in cell viability with decreased acrylate conversions, suggesting that free acrylate moieties may promote some cell death. In terms of mechanical and cell studies, samples 100:0 and 75:25 provided promising characteristics for soft tissue scaffolds. As a proof of concept, 75:25 was used to print a lattice, where this type of structure will be further used in the production of 3D tissue scaffolds.

5.6 Acknowledgements

The authors would like to thank the National Science Foundation's Research Experience for Undergraduates Program (Award ID Number: CHE-1560240) from the Macromolecules Innovation Institute at Virginia Tech in summer 2018, Keyton Feller for 3D printing support, and Shantel Schexnayder and Allison Pekkanen for preliminary data.

5.7 References

(1) Zhao, N.; Lv, Z.; Ma, J.; Zhu, C.; Li, Q. Fabrication of Hydrophilic Small Diameter Vascular Foam Scaffolds of Poly(ε-Caprolactone)/Polylactic Blend by Sodium Hydroxide Solution. **2018**. https://doi.org/10.1016/j.eurpolymj.2018.11.011.

(2) Etxabide, A.; Long, J.; Guerrero, P.; De La Caba, K.; Seyfoddin, A. 3D Printed Lactose-Crosslinked Gelatin Scaffolds as a Drug Delivery System for Dexamethasone. **2019**. https://doi.org/10.1016/j.eurpolymj.2019.02.019.

(3) Reis, R. L.; Román, J. S.; Román, J. S. *Biodegradable Systems in Tissue Engineering and Regenerative Medicine*; Reis, R., San Román, J., Eds.; CRC Press, 2004. https://doi.org/10.1201/9780203491232.

(4) Dhandayuthapani, B.; Yoshida, Y.; Maekawa, T.; Kumar, D. S. Polymeric Scaffolds in Tissue Engineering Application: A Review. *Int. J. Polym. Sci.* **2011**, *2011*, 1–19. https://doi.org/10.1155/2011/290602.

(5) Moon, N. G.; Mazzini, F.; Pekkanen, A. M.; Wilts, E. M.; Long, T. E. Sugar-Derived Poly(β-Thioester)s as a Biomedical Scaffold. *Macromol. Chem. Phys.* **2018**, *219* (16). https://doi.org/10.1002/macp.201800177.

(6) Mondschein, R. J.; Kanitkar, A.; Williams, C. B.; Verbridge, S. S.; Long, T. E. Polymer Structure-Property Requirements for Stereolithographic 3D Printing of Soft Tissue Engineering Scaffolds. *Biomaterials* **2017**, *140*, 170–188. https://doi.org/10.1016/J.BIOMATERIALS.2017.06.005.

(7) Reed, A. M.; Gilding, D. K. Biodegradable Polymers for Use in Surgery — Poly(Glycolic)/Poly(Iactic Acid) Homo and Copolymers: 2. In Vitro Degradation. *Polymer (Guildf).* **1981**, *22* (4), 494–498. https://doi.org/10.1016/0032-3861(81)90168-3.

(8) Karageorgiou, V.; Kaplan, D. Porosity of 3D Biomaterial Scaffolds and Osteogenesis. *Biomaterials* **2005**, *26* (27), 5474–5491. https://doi.org/10.1016/J.BIOMATERIALS.2005.02.002.

(9) Cox, S. C.; Thornby, J. A.; Gibbons, G. J.; Williams, M. A.; Mallick, K. K. 3D Printing of Porous Hydroxyapatite Scaffolds Intended for Use in Bone Tissue Engineering Applications. *Mater. Sci. Eng. C* **2015**, *47*, 237–247. https://doi.org/10.1016/J.MSEC.2014.11.024.

(10) Do, A.-V.; Khorsand, B.; Geary, S. M.; Salem, A. K. 3D Printing of Scaffolds for Tissue Regeneration Applications. **2015**. https://doi.org/10.1002/adhm.201500168.

(11) Chia, H. N.; Wu, B. M. Recent Advances in 3D Printing of Biomaterials. *J. Biol. Eng.* **2015**, *9* (1), 4. https://doi.org/10.1186/s13036-015-0001-4.

(12) Wilts, E. M.; Pekkanen, A. M.; White, B. T.; Meenakshisundaram, V.; Aduba, D. C.; Williams, C. B.; Long, T. E. Vat Photopolymerization of Charged Monomers: 3D Printing with Supramolecular Interactions. *Polym. Chem.* **2019**, *10* (12). https://doi.org/10.1039/c8py01792a.

(13) Dhariwala, B.; Hunt, E.; Boland, T. Rapid Prototyping of Tissue-Engineering Constructs, Using Photopolymerizable Hydrogels and Stereolithography. *Tissue Eng.* **2004**, *10* (9–10), 1316–1322. https://doi.org/10.1089/ten.2004.10.1316.

(14) Chartrain, N. A.; Williams, C. B.; Whittington, A. R. A Review on Fabricating Tissue Scaffolds Using Vat Photopolymerization. *Acta Biomater.* **2018**, *74*, 90–111. https://doi.org/10.1016/J.ACTBIO.2018.05.010.

(15) Lee, J.-Y.; An, J.; Chua, C. K. Fundamentals and Applications of 3D Printing for Novel Materials. *Appl. Mater. Today* **2017**, *7*, 120–133. https://doi.org/10.1016/J.APMT.2017.02.004.

(16) Chereddy, K. K.; Vandermeulen, G.; Préat, V. PLGA Based Drug Delivery Systems: Promising Carriers for Wound Healing Activity. *Wound Repair Regen.* **2016**, *24* (2), 223–236. https://doi.org/10.1111/wrr.12404.

(17) Lü, J.-M.; Wang, X.; Marin-Muller, C.; Wang, H.; Lin, P. H.; Yao, Q.; Chen, C.

Current Advances in Research and Clinical Applications of PLGA-Based Nanotechnology. *Expert Rev. Mol. Diagn.* **2009**, *9* (4), 325–341. https://doi.org/10.1586/erm.09.15.

(18) Bala, I.; Hariharan, S.; Kumar, M. R. PLGA Nanoparticles in Drug Delivery: The State of the Art; *Crit. Rev. Ther. Drug Carrier Syst.* **2004**, *21* (5), 387–422. https://doi.org/10.1615/CritRevTherDrugCarrierSyst.v21.i5.20.

(19) Gentile, P.; Chiono, V.; Carmagnola, I.; Hatton, P.; Gentile, P.; Chiono, V.; Carmagnola, I.; Hatton, P. V. An Overview of Poly(Lactic-Co-Glycolic) Acid (PLGA)-Based Biomaterials for Bone Tissue Engineering. *Int. J. Mol. Sci.* **2014**, *15* (3), 3640–3659. https://doi.org/10.3390/ijms15033640.

(20) Yu, L.; Zhang, Z.; Ding, J. Influence of LA and GA Sequence in the PLGA Block on the Properties of Thermogelling PLGA-PEG-PLGA Block Copolymers. *Biomacromolecules* **2011**, *12* (4), 1290–1297. https://doi.org/10.1021/bm101572j.

(21) Serra, T.; Ortiz-Hernandez, M.; Engel, E.; Planell, J. A.; Navarro, M. Relevance of PEG in PLA-Based Blends for Tissue Engineering 3D-Printed Scaffolds. *Mater. Sci. Eng. C* **2014**, *38*, 55–62. https://doi.org/10.1016/J.MSEC.2014.01.003.

(22) Seck, T. M.; Melchels, F. P. W.; Feijen, J.; Grijpma, D. W. Designed Biodegradable Hydrogel Structures Prepared by Stereolithography Using Poly(Ethylene Glycol)/Poly(d,l-Lactide)-Based Resins. *J. Control. Release* **2010**, *148* (1), 34–41. https://doi.org/10.1016/J.JCONREL.2010.07.111.

(23) Andrzejewska, E.; Andrzejewski, M. Polymerization Kinetics of Photocurable Acrylic Resins. *J. Polym. Sci. Part A Polym. Chem.* **1998**, *36* (4), 665–673. https://doi.org/10.1002/(SICI)1099-0518(199803)36:4<665::AID-POLA15>3.0.CO;2-K.

(24) Grijpma, D. .; Nijenhuis, A. .; Pennings, A. . Synthesis and Hydrolytic Degradation Behaviour of High-Molecular-Weight l-Lactide and Glycolide Copolymers. *Polymer (Guildf).* **1990**, *31* (11), 2201–2206. https://doi.org/10.1016/0032-3861(90)90096-H.

(25) Cutright, D. E.; Perez, B.; Beasley, J. D.; Larson, W. J.; Posey, W. R. Degradation Rates of Polymers and Copolymers of Polylactic and Polyglycolic Acids. *Oral Surgery, Oral Med. Oral Pathol.* **1974**, *37* (1), 142–152. https://doi.org/10.1016/0030-4220(74)90171-6.

(26) Odile Dechy-Cabaret; Blanca Martin-Vaca, and; Bourissou*, D. Controlled Ring-Opening Polymerization of Lactide and Glycolide. **2004**. https://doi.org/10.1021/CR040002S.

(27) Mitchell, M. R.; Link, R. E.; Yang, M.-H.; Lin, Y.-H. Measurement and Simulation of Thermal Stability of Poly(Lactic Acid) by Thermogravimetric Analysis. *J. Test. Eval.* **2009**, *37* (4), 102271. https://doi.org/10.1520/JTE102271.

(28) Penco, M.; Sartore, L.; Bignotti, F.; D'Antone, S.; Di Landro, L. Thermal Properties of a New Class of Block Copolymers Based on Segments of Poly(D,L-Lactic-

Glycolic Acid) and Poly(ε-Caprolactone). *Eur. Polym. J.* **2000**, *36* (5), 901–908. https://doi.org/10.1016/S0014-3057(99)00155-X.

(29) Williams, C. G.; Malik, A. N.; Kim, T. K.; Manson, P. N.; Elisseeff, J. H. Variable Cytocompatibility of Six Cell Lines with Photoinitiators Used for Polymerizing Hydrogels and Cell Encapsulation. *Biomaterials* **2005**, *26*, 1211–1218. https://doi.org/10.1016/j.biomaterials.2004.04.024.

(30) Polymer Based Systems on Tissue Engineering, Replacement and Regeneration - Google Books https://books.google.com/books?id=25fnCAAAQBAJ&pg=PA28&lpg=PA28&dq=becker+mechanical+strength+of+tissues&source=bl&ots=KJFPyPIDZX&sig=ACfU3U3wHPl5xepRVuj9YCmK4f1pSIHrAA&hl=en&sa=X&ved=2ahUKEwiQvd33lr3nAhU3mHIEHXupCBcQ6AEwDHoECAkQAQ#v=onepage&q=becker mechanical strength of tissues&f=false (accessed Feb 6, 2020).

(31) Agrawal, C. M.; Ray, R. B. Biodegradable Polymeric Scaffolds for Musculoskeletal Tissue Engineering. *J. Biomed. Mater. Res.* **2001**, *55* (2), 141–150. https://doi.org/10.1002/1097-4636(200105)55:2<141::AID-JBM1000>3.0.CO;2-J.

5.8 Supplemental

Figure S5.1. TGA traces of all the L:G ratios depicting temperature (ºC) as a function of mass remaining (%).

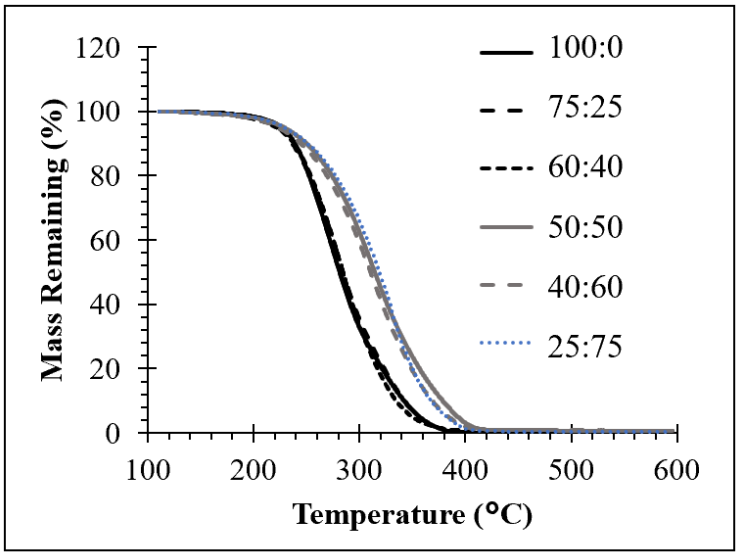

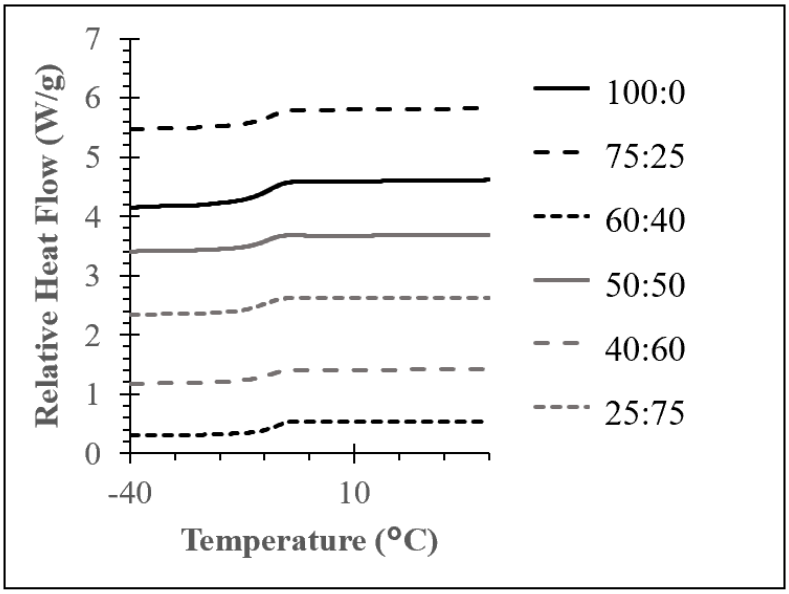

Figure S5.2. DSC traces of all L:G ratios depicting temperature (ºC) as a function of relative heat flow (W/g). The traces are vertically shifted for clarity.

Table S5.1. Tensile results of crosslinked PLGA films.

Sample (L:G)	Young's Modulus (MPa)	Ultimate Stress (MPa)	Elongation (%)
100:0	$1.7 \cdot 10^{-2} \pm 4.1 \cdot 10^{-4}$	0.89 ± 0.10	52.0 ± 2.5
75:25	$1.5 \cdot 10^{-2} \pm 8.7 \cdot 10^{-4}$	$0.75 \pm 5.7 \cdot 10^{-2}$	52.4 ± 3.4
60:40	$2.9 \cdot 10^{-2} \pm 2.5 \cdot 10^{-3}$	1.4 ± 0.14	45.2 ± 5.4
50:50	$2.8 \cdot 10^{-2} \pm 2.9 \cdot 10^{-3}$	1.2 ± 0.14	43.1 ± 3.5
40:60	$2.7 \cdot 10^{-2} \pm 2.0 \cdot 10^{-3}$	1.2 ± 0.11	41.0 ± 1.8

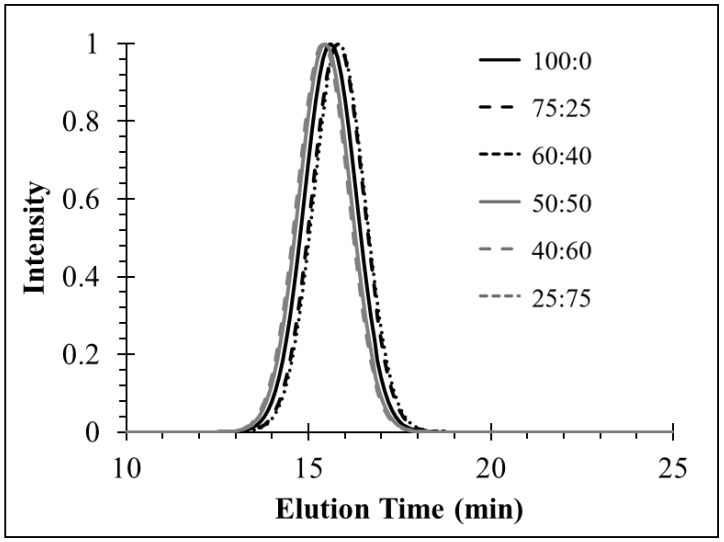

Figure S5.3. SEC-LS analysis in DMF of each PLGA-diol copolymer depicting the light scattering traces.

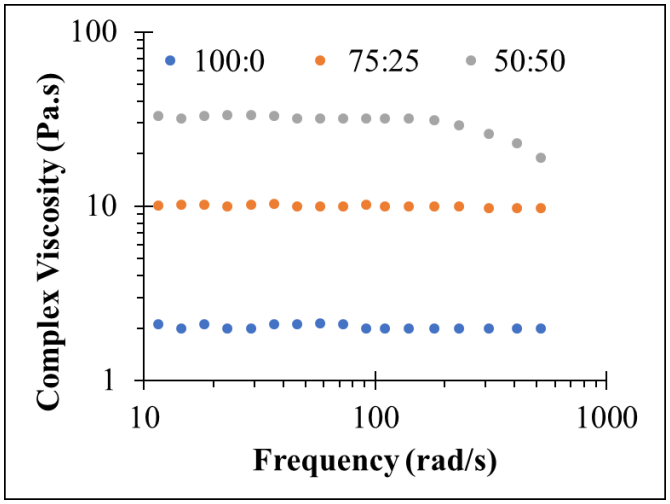

Figure S5.4. Viscosity as a function of frequency for samples 100:0, 75:25, and 50:50.

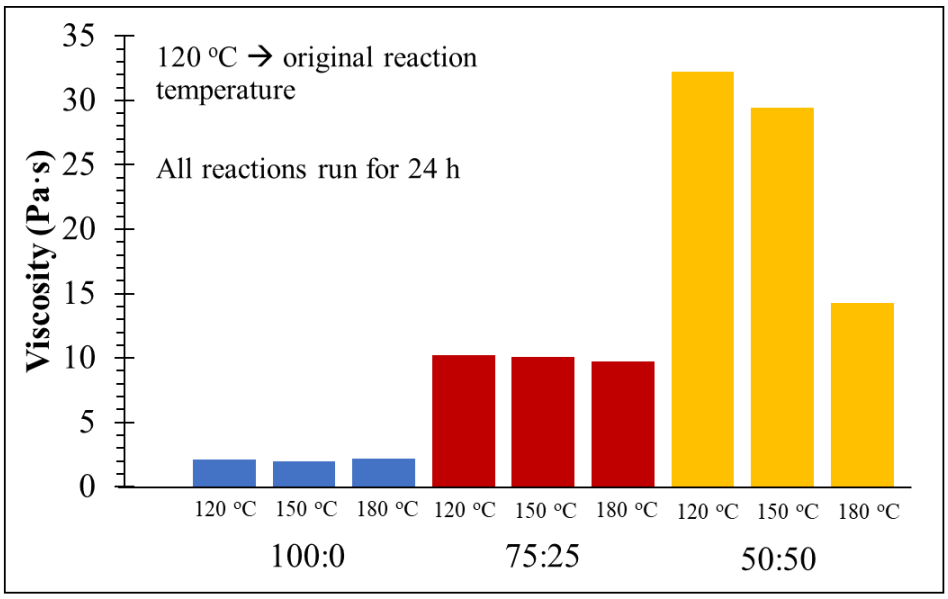

Figure S5.5. Comparison of 100:0, 75:25, and 50:50 reacted at 120, 150, and 180 ºC as a function of zero-shear viscosity.

Chapter 6: Influence of Solution Properties on Photokinetics of Photoactive Precursors for Vat Photopolymerization

Emily M. Wilts, Jose Sintas, Fiona Carter-Todd, and Timothy E. Long*

(Research Chapter)

Department of Chemistry, Macromolecules Innovation Institute, Virginia Tech, Blacksburg, VA 24061

6.1 Abstract

Vat photopolymerization utilizes UV light to selectively cure 3D parts layer-by-layer to enable custom, mass-produced objects unachievable through traditional manufacturing. A plethora of commercially available resins made from polymers, reactive diluents, and oligomers allow commercial use of VP, but commonly lack in strength and durability. Methods to increase strength mainly include dissolving polymers in aqueous and organic solvents to overcome viscosity constraints, but fundamental studies examining viscosity effects on photoactive moiety conversion and photokinetics are lacking. This manuscript describes poly(ethylene glycol)-diacrylate (PEGDA) and amide-containing poly(ethylene glycol)-diacrylamide (PEGDA-mBam) at 2, 8, and 35 kg mol^{-1} dissolved in water to determine viscosity effects on acrylate/acrylamide conversion and photokinetics for VP. Photocalorimetry and photorheology revealed a solution viscosity dependency on acrylate/acrylamide conversion and solidification speed. 2 kg mol^{-1} analogs demonstrated the highest conversions and fastest reaction rate possibly due to maintaining the lowest viscosity and highest concentration of reactive groups. Photocalorimetry failed to detect both 35 kg mol^{-1} analog conversion and PEGDA did not form solid films at any concentration. However, possibly owing to a secondary hydrogen bonding network, PEGDA-mBam formed films above 50 wt %. This study defines printability for VP of

dissolved polymers and serves as a database for conversion and photokinetic information to match specific applications.

6.2 Introduction

Vat photopolymerization selectively solidifies liquid photoactive precursors layer by layer using UV light. Polymers, monomers, reactive dilutes, solid particles, and solvents represent some common materials in photoactive precursors. Rate of reaction, photoactive precursor viscosity, and strength of each layer all contribute to printability of the material. The precursor must react fast enough to solidify in reasonable timeframes (~0-15 s) to enable quick printing. Precursor viscosity defines vat photopolymerization method used where some systems rely on low viscosity (1-10 Pa·s) coalescence to refill the build platform while higher viscosities require a recoating blade.[1] Strength of each layer ensures survival as the next layer is spread across the build platform. These main factors determine how a new material for vat photopolymerization are designed.[2,3] Even though successful printability depends strongly on viscosity, research is lacking of how varying viscosity affects conversion and crosslinking kinetics.[4,5]

Elastic, high-moduli VP parts require high molecular weight between crosslinks (M_c) but factors such as high viscosity and low solubility hinder this effort. High M_c enables polymer entanglements, flexibility, and elasticity. Currently, low molecular weight polymeric precursors create brittle VP parts that do not compare to traditionally manufactured polymers through injection molding or subtractive manufacturing.[6,7] Current solutions to this problem include printing organogels[8,9], simultaneous chain-extension and crosslinking[10,11], and low viscosity colloidal latexes[12]. Dissolving high molecular weight

polymers in organic solvents dramatically increase viscosity therefore resulting in low polymer concentrations (15-30 wt %). While these efforts continue to push the boundaries of printing high molecular weight polymers, literature is lacking that defines photokinetic effects of varying molecular weights and varying viscosity.

High conversion of photoactive moieties in precursor is extremely important for any application involving human contact. Less than 100% conversion runs the risk of leaching precursors and remaining cytotoxic moieties. For example, difunctional photoactive precursors may not incorporate into the network or experience single end-group incorporation. Without extraction, the non-incorporated polymers can leach out or the single photoactive site may lead to cell death for biomedical applications.[13,14] Wilts *et. al.* tested a series of PLGA-diacrylates and found a decrease in acrylate conversion led to increased cytotoxicity in breast cancer epithelial cells.[13] Additive manufacturing is becoming more popular in commercial products and steps to decrease leaching and toxicity are required.

This manuscript describes the synthesis of poly(ethylene glycol)-diacrylate (PEGDA) and hydrogen bond-containing pol(ethylene glycol)-diacrylamide (PEGDA-mBam) and subsequent photokinetic characterization in solution to determine highest acrylate/acrylamide conversions and gel fidelity for vat photopolymerization. Solution rheology revealed critical overlap (C^*) and entanglement concentrations (C_e) transitions, which subsequently elucidated photokinetic dependencies on varying solution regimes. Photocalorimetry and photorheology of 2, 8, and 35 kg mol^{-1} analogs revealed 2 kg mol^{-1} polymers formed the highest moduli gels and comparable acrylate/acrylamide conversions in the semi-dilute entangled regime. PEGDA 35 kg mol^{-1} did not form solid gels at any

concentration but because of hydrogen bonding, PEGDA-mBam 35 kg mol^{-1} formed solid gels at high concentrations (> 50 wt %). Across all samples, as viscosity increased, acrylate/acrylamide conversion decreased, possibly due to decreased chain mobility. No definitive trends emerged relating conversion and viscosity regimes, but all samples did not form solid gels in the dilute regime. The goal of this study is to create a database of different crosslinking kinetics across varying molecular weights, concentrations, and molecular structures to guide readers which concentrations are best for varying applications.

6.3 Experimental

6.3.1 Materials

Thioglycolic acid, acryloyl chloride, basic aluminum oxide, and 1,8-Diazabicyclo[5.4.0]undec-7-ene (DBU) were purchased from Sigma Aldrich and used without further purification. PEG_{2000}, PEG_{8000}, PEG_{35000}, PEG_{6000}, potassium carbonate (K_2CO_3), *p*-toluenesulfonic acid, and *N*,*N* ′-methylenebis(acrylamide) (mBam) were purchased at Sigma Aldrich and dried at 40 ^oC at 10 mbar before use. Dimethyl sulfoxide (DMSO) was purchased from Acros and distilled over calcium hydride. Dichloromethane (DCM), xylenes, and ethyl ether were purchased from Acros and used without further purification.

6.3.2 Synthesis of poly(ethylene)glycol-diacrylate (PEGDA)

The synthesis of poly(ethylene)glycol-diacrylate began with PEG_{2000} (25 g, 0.013 mol, 1 eq.) and K_2CO_3 (10.8 g, 0.078 mol, 6 eq.) in 150 mL of dry dichloromethane (DCM). The reaction vessel was brought to 0 ^oC and a mixture of DCM (20 mL) and acryloyl chloride (4.7 g, 0.052 mol, 4 eq.) was added dropwise over 30 min. The mixture was allowed to stir

for 24 h. The reaction was quenched with 5 mL of water and stirred with 10 mL of basic aluminum oxide for 2 h. The mixture was filtered to remove K_2CO_3 and basic aluminum oxide and subsequently re-dissolved in DCM and run through a basic aluminum oxide column. The product was concentration in vacuo and further dried under high vacuum at 35 ^oC. The solid white product (95% yield) was stored in a freezer without exposure to light. ^1H NMR, 400 MHz (D_2O): 3.5-3.6 ppm (180H, m), 3.7 ppm (4H, m), 4.25 ppm (4H, m), 5.93 ppm (2H, m), 6.12 ppm (2H, m), and 6.42 (2H, m).

6.3.3 Synthesis of poly(ethylene glycol)-dithiol (PEG-SH)

The synthesis of PEG-SH began with PEG_{2000} (10 g, $5.0 \cdot 10^{-3}$ mol, 1 eq.), thioglycolic acid (1.38 g, 0.015 mol, 3 eq.) and *p*-toluenesulfonic acid (0.02 mol %) in xylenes (100 mL). The mixture was purged with nitrogen and heated to 138 ^oC stirred for 24 h at reflux with a Dean-Stark apparatus. After enough water refluxed to signify the reaction completion, the mixture was cooled and precipitated into ether x3. The solid white product (97% yield) was further dried under high vacuum. ^1H NMR, 400 MHz ($CDCl_3$): 1.91 ppm (2H, t), 3.25 ppm (4H, d), 3.41-3.64 ppm (180H, m), and 4.25 ppm (4H, m).

6.3.4 Synthesis of H-bonding poly(ethylene)glycol-diacrylamide (PEGDA-mBam)

PEG-SH (5 g, $2.3 \cdot 10^{-3}$ mol, 0.6 eq.) and mBam (0.59 g, $3.8 \cdot 10^{-3}$ mol, 1 eq.) were dissolved in DMSO (50 mL) and placed in a vat of water. DBU (5 mol %) was added dropwise to prevent local heating. The mixture was stirred at 22 ^oC for 24 h and subsequently precipitated into ether. The slightly yellow solid product was further dried until high vacuum and stored in the freezer without exposure to light. ^1H NMR, 400 MHz ($CDCl_3$): 1.91 ppm (2H, t), 3.25 ppm (4H, d), 3.41-3.64 ppm (180H, m), and 4.25 ppm (4H, m).

6.3.5 Analytical

^{1}H NMR was performed on a 400 MHz Varian Unity in $DMSO_{d6}$, D_2O, and $CDCl_3$. Photocalorimetry was performed on a TA Instruments Q2000 with an Omnicure S2000 photo-attachment with fiber optic cable. T-zero pans were loaded as either sample pans or reference pans and equilibrated at 25 °C. After a 1 min isotherm, the pans were exposed to 20 mW cm^{-2} of a broad-spectrum UV source (320-500 nm). Following 5 min irradiation, the light was turned off and the background heat from the light noted. Integrations of the peaks with background correction afforded the heat of polymerization. To calculate percent conversion, the standard values for ΔH_{rxn} for the homopolymerization of acrylates (86 kJ mol^{-1})[15] were employed. The ΔH_{rxn} values obtained from photocalorimetry were normalized based on the moles of acrylates in the sample. Photorheology occurred on a TA Instruments Discovery HR-2 Rheometer with photo attachment and 20 mm PDMS bottom plate with 20 mm disposable upper geometry. Samples were equilibrated at 25 °C for 30 s to provide baselines for all samples. Samples were oscillated at 1 Hz, providing sampling rates relevant for the second timescale. Following 30 s, samples were irradiated at 20 mW/cm^2 and modulus was monitored. The crossover point was determined as the first instance the storage modulus (G') exceeded loss modulus (G"). A TA Instruments DHR-2 rheometer also measured the solution viscosity of each mixture using a concentric cylinder at 5000 μm gap, steady shear, 10-100 1/s. The zero-shear viscosity was determined by the Newtonian plateau and further used for determination of viscosity vs. concentration transitions. Thermogravimetric analysis (TGA) was performed on a TGA Q500 with a 20 min isotherm at 110 ^{o}C and a ramp at 10 ^{o}C min^{-1} to 600 ^{o}C. $T_{d,5\%}$ values were calculated

where 5 wt% of the mass was lost and the data was normalized after the isothermal step. Stirring with a magnetic stir bar in chloroform, acetone, and ethanol, for 48 h each afforded a fully extracted system for the following analytical experiments and cell culture studies. Differential scanning calorimetry (DSC) was performed on a TA Instruments Q2000 with heat/cool/heat cycles of 10 °C min^{-1}, 100 °C min^{-1}, and 10 °C min^{-1}, respectively. Samples were dried at 60 °C under vacuum prior to analysis. Glass transition temperatures (T_gs) were calculated from the second heat inflection point.

6.3.6 Extraction

After the diacrylates or diacrylamides formed crosslinked films, extraction determined the gel fractions. The gels were dried under high vacuum for 24 h at 50 ^oC, weighed, and wrapped in aluminum foil. The packets were suspended in chloroform for days where the solvent was exchanged every day. The packets were isolated, dried, and weighed to determine the mass difference.

6.4 Results and Discussion

6.4.1 Synthesis and characterization

End-group functionalization and step-growth polymerization yielded two photo-active, water-soluble polymers to compare the photokinetics of non-H-bonding and H-bonding polymers in solution. **Scheme 6.1A** depicts the end-group functionalization of PEG with acryloyl chloride, which created PEGDA at three different M_n. First, a mixture of PEG, K_2CO_3, and DCM were combined and lowered to 0 ^oC to combat the heat production of the subsequent addition. Acryloyl chloride was added dropwise to limit local heating and prevent unwanted side-products. K_2CO_3 acted as a solid acid scavenger at 6

eq. to ensure two acidic additions did not occur and create water. After full substitution, filtration removed K_2CO_3 and multiple purifications through basic alumina oxide removed residual acid. ^{1}H NMR confirmed chemical structure and M_n (**Figure S6.1**).

Scheme 6.1B depicts the synthesis of PEGDA-mBam, which started with the acid-catalyzed end-group functional of PEG with thioglycolic acid. Next, according to the Carother's equation PEG-SH and mBam were combined at a stoichiometric offset with mBam in excess to ensure acrylamide end-groups. Addition of a thiolate anion to an electron-deficient alkene facilitated the base-catalyzed thiol-Michael reaction. Each polymer at different molecular weights contained the same amount of mBam to additionally investigate spacing of hydrogen bonding while rendering the polymers more comparable with similar hydrogen bonding. ^{1}H NMR confirmed chemical structure and M_n (**Figure S6.3**).

Scheme 6.4.1. (A) Synthesis of poly(ethylene glycol)-diacrylate and **(B)** and amide-containing poly(ethylene glycol)-diacrylamide.

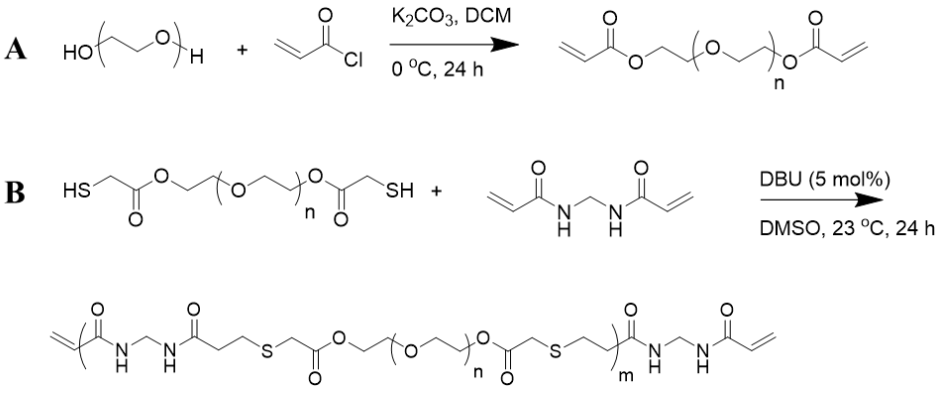

SEC-LS in DMF measured absolute molecular weight and elucidated differences in Đ between PEGDA and PEGDA-mBam. **Figure 6.1** depicts the light scattering traces

of both polymers at 2, 8, and 35 kg mol^{-1}. Each polymer exhibited the targeted M_n within 2 kg mol^{-1} to ensure the photokinetics and molecular weights effects are comparable. The Đ values of PEGDA and PEGDA-mBam at 2, 8, and 35 kg mol^{-1} were 1.41, 1.38, 1.42, and 2.08, 2.13, 1.91, respectively. Ring-opening polymerization yielded PEGDA and common Đ values ranges from 1.5-2 depending on extent of reaction.[16] However, step-growth polymerization created PEGDA-mBam, which exhibits Đ averages of 2 depending on extent of conversion based on the Carother's equation.[17,18] These differences may explain some differences in photokinetics thus not rendering the polymers completely comparable.

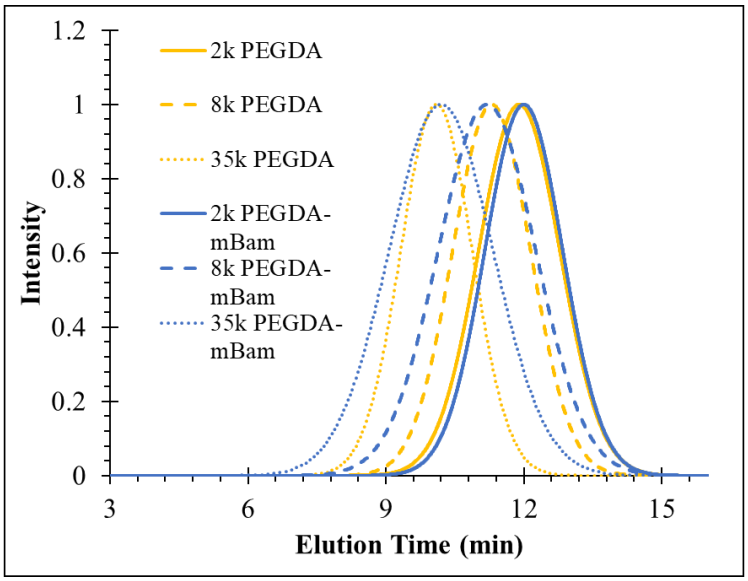

Figure 6.1. SEC-LS in DMF of PEGDA and PEGDA-mBam at 2, 8, and 35 kg mol^{-1}.

6.4.2 Solution properties

Solution rheology elucidated the solution viscosity dependency on concentration and found the critical overlap concentration (C^*) and entanglement concentration (C_e). Dissolution of 2, 8, 35 kg mol^{-1} and 8, and 35 kg mol^{-1} PEGDA-mBam resulted in full

solvation and single coils according to dynamic light scattering. 2 kg mol^{-1} PEGDA-mBam required a 50:50 v:v mixture of water:DMSO to fully solvate, possibly owing to the high concentration of hydrogen bonding units. Specific viscosity (η_{sp}) as a function of concentration elucidated the transitions through the dilute, semi-dilute unentangled, and semi-dilute entangled regimes.[19–21] Single polymer coils in solution corresponded to the dilute regime, where the power law slope ~$C^{1.0}$. As concentration increased, the coils begin to overlap and interact where C* denotes the transition into the semi-dilute unentangled regime with ~$C^{1.25}$.[22–24] Further increase in concentration transitions into the semi-dilute entangles regime where polymers with the ability to entangle induced another increase in slope ~$C^{4.5}$ also marking C_e.[25,26] This study aims to discover if these transitions affect photokinetics in a consistent trend across PEGDA and PEGDA-mBam-type polymers.

Figure 6.2A depicts a representative η_{sp} as a function of concentration plot of PEGDA 8 kg mol^{-1} in water. The dilute (orange), semi-dilute unentangled (gray), and entangled regimes (blue) experienced slopes of $C^{1.3}$, $C^{1.7}$, and $C^{4.1}$, respectively and agree with established values. **Figures 6.2B** and **6.2C** depicts C* and C_e transitions of each M_n of PEGDA and PEGDA-mBam. In general, as the M_n increased, the C^* and C_e decreased because they contained a larger R_g. PEGDA-mBam also exhibited decreased C^* and C_e possibly owing to a less compact solution conformation due to hydrogen bonding with water. The 2 kg mol^{-1} PEGDA and PEGDA-mBam analogs experienced the largest differences in C^* and C_e at 11 and 7, 24 and 18 wt %, respectively. This difference may arise from the high concentration of hydrogen bonding groups compared to the other molecular weight analogs, therefore more association with water and a larger solution conformations.

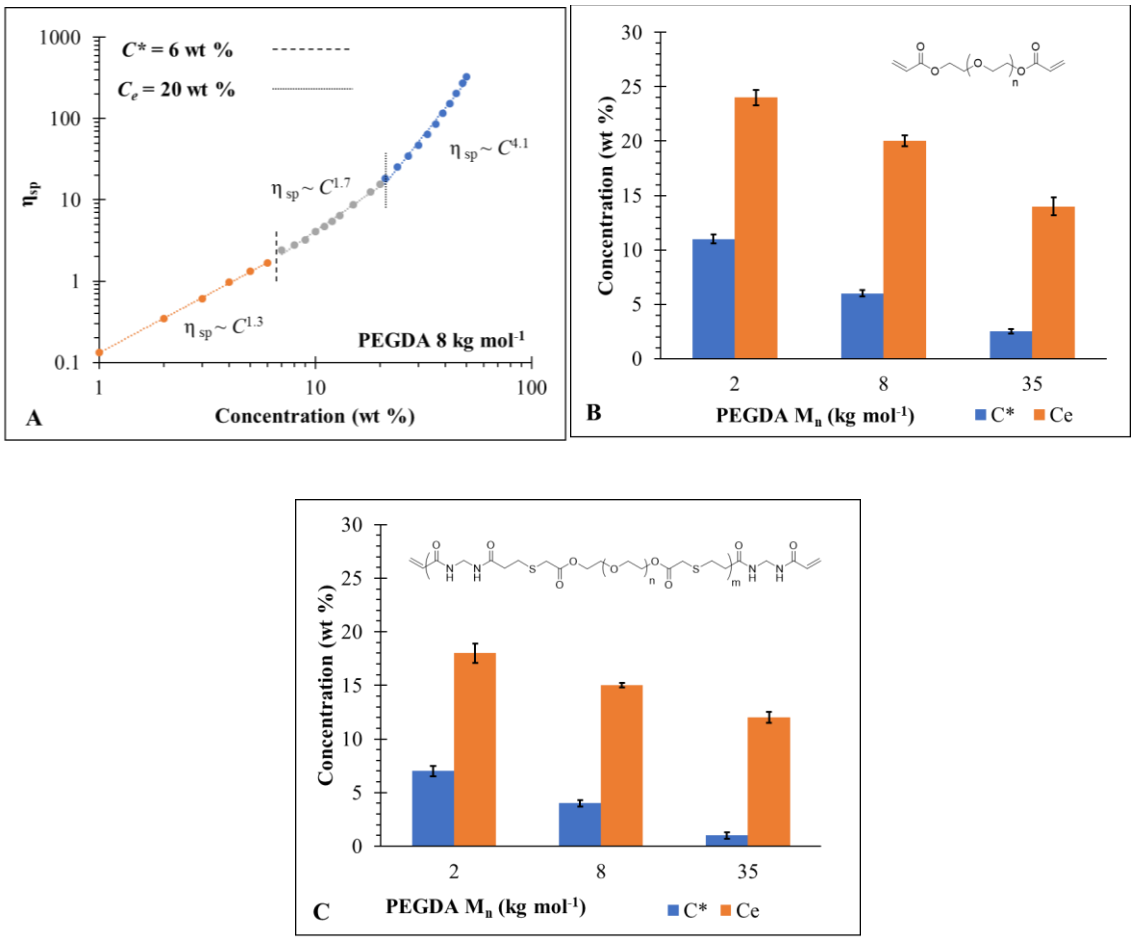

Figure 6.2 (A) η_{sp} as a function of concentration PEGDA 8 kg mol^{-1} example, **(B)** summary of PEGDA and **(C)** PEGDA-mBam C^* and C_e values.

6.4.3 Molecular weight comparison

Comparison of 2, 8, and 35 kg mol^{-1} analogs elucidated which M_ns produced the highest acrylate/acrylamide conversions and high-fidelity gels capable of forming layers in vat photopolymerization. High conversions (close to 100%) is optimal for parts with subsequent uses in biomedical applications. Recent literature suggested free acrylate moieties may be cytotoxic to cells, therefore the highest conversion possible will prevent adverse side-effects and reduce immune responses.[13,14] Higher molecular weight between

crosslinks creates more flexible gels where lower molecular weights produce brittle gels, which hinders final part fidelity. However, achieving high molecular weight between crosslinks remains a challenge because they produce high solution viscosities and have poor crosslink kinetics.[10–12]

Photocalorimetry measured the heat flow as a function of time of the acrylate/acrylamide crosslinking reactions. **Figure 6.3A** shows typical photocalorimetry traces where the exotherm peak denotes the fastest reaction kinetics and the integration represents the heat of reaction (ΔH_{rxn}). UV light exposed the uncovered pan after a 1 minute isotherm and continued to irradiate for 6 min until the reaction was complete, and the trace returned to baseline. In every combination, as the concentration increased, the ΔH_{rxn} increased because higher concentrations of acrylates/acrylamides reacted. **Figure 6.3B** depicts the ΔH_{rxn} as a function of concentration of 2 and 8 kg mol^{-1} PEGDA. Similarly, as molecular weight increased for all combinations the ΔH_{rxn} decreased because a lower number of acrylates/acrylamides reacted.

Calculating acrylate/acrylamide conversions normalized the data and elucidated which molecular weights achieved the highest conversions based on moles of acrylates/acrylamides present. Tissue scaffold literature suggested decreased conversion led to increased cytotoxicity, therefore for biomedical purposes the highest conversion is optimal.[13] Previous studies revealed ΔH_{rxn} of 100% conversion of acrylates and acrylamides is 86 kJ mol^{-1}, which was used for all further calculations.[15] **Figure 6.3C** depicts conversion as a function of concentration for 2 and 8 kg mol^{-1} PEGDA. As a general trend, both molecular weights experienced decreased conversions with increasing concentration. As concentration increased, viscosity increased, which may have hindered

further crosslinking due to decreased chain mobility. When 2 and 8 kg mol^{-1} PEGDA breach 40 wt %, the acrylate conversions begin to deviate where 2 kg mol^{-1} maintained higher conversions. Higher viscosity of 8 kg mol^{-1} or lower concentration of acrylate groups may contribute to decreased conversion at higher concentrations. **Figure 6.3D** depicts conversion as a function of concentration for 2 and 8 kg mol^{-1} PEGDA-mBam. These polymers followed the same trend as PEGDA, besides 2 kg mol^{-1} exhibited lower conversions compared to 8 kg mol^{-1} after 50 wt %. 2 kg mol^{-1} PEGDA-mBam maintained higher concentrations of hydrogen bonding groups and thus experienced higher viscosities than 8 kg mol^{-1} above 40 wt %. The difference in viscosity restricted chain mobility and potentially lowered acrylamide conversions.

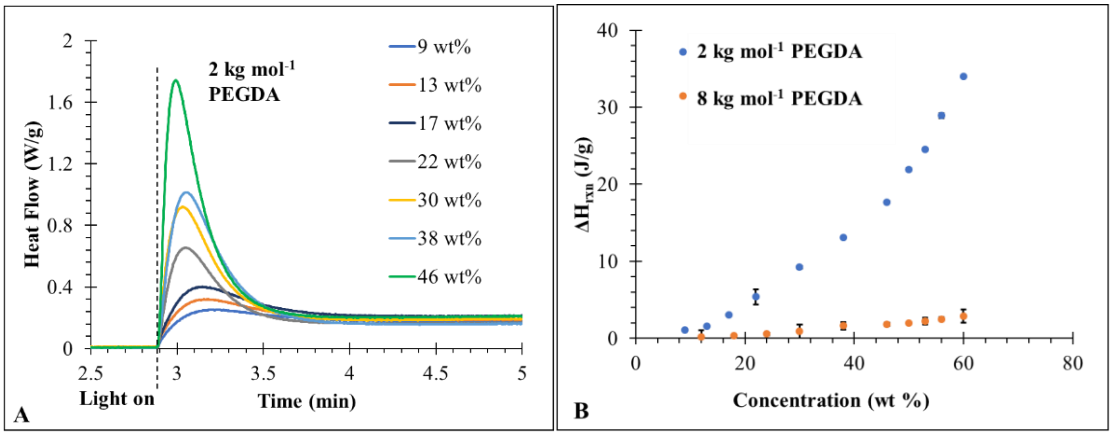

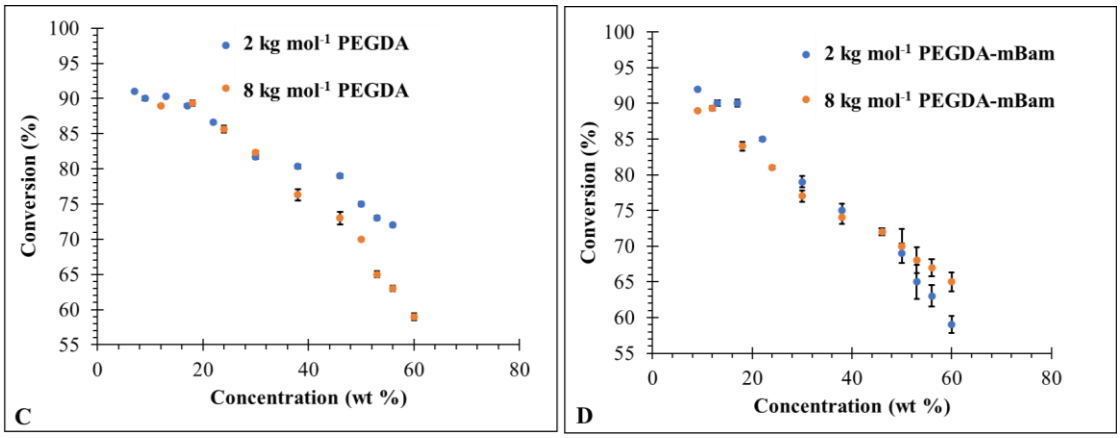

Figure 6.3. (A) Heat flow as a function of time of PEGDA 2 kg mol^{-1} example, **(B)** ΔH_{rxn} as a function of concentration of PEGDA, **(C)** acrylate conversion as a function of concentration of PEGDA, and **(D)** acrylamide conversion as a function of concentration of PEGDA-mBam.

Photorheology probed kinetics and modulus during crosslinking. **Figure 6.4A** depicts representative traces where UV light exposed a 20 mm disc of 8 kg mol^{-1} in DI water. The light irradiated after 15 s and the plateau storage modulus (G_N^o) and crossover time of loss and storage modulus denote relative crosslinked film modulus and relative solid formation. Depending on the vat photopolymerization type, an approximate G_N^o to ensure layers will survive recoating is 10^5 Pa.[1,27] **Figure 6.4B** shows G_N^o as a function of concentration of 2 and 8 kg mol^{-1} PEGDA. 2 kg mol^{-1} PEGDA exhibited higher G_N^o compared to 8 kg mol^{-1} and breached 10^5 Pa at 22 wt %. 8 kg mol^{-1} reached $7.8 \cdot 10^4$ Pa at 60 wt %, which may not survive the recoating process. 2 kg mol^{-1} PEGDA maintained a higher crosslink density compared to 8 kg mol^{-1}, which accounted for the differences in modulus. As a general trend, the crossover time decreased with increasing concentration

owing to a higher concentration of acrylate/acrylamide moieties (**Figure S6.4**). 35 kg mol^{-1} did not form gel solid gels at any concentration tested.

Figure 6.4C shows G_N^o as a function of concentration of 2, 8, and 35 kg mol^{-1} PEGDA-mBam. Similar to the PEGDA trends, as molecular weight increased, G_N^o increased because of higher concentrations of acrylamide groups. However, 35 kg mol^{-1} PEGDA-mBam formed solid gels above 50 wt %, possibly owing to hydrogen bonding preserving the gel fidelity. The G_N^o values were low compared to 2 and 8 kg mol^{-1}, but increasing hydrogen bonding groups in 35 kg mol^{-1} PEGDA-mBam in future studies may increase G_N^o and decrease brittleness.

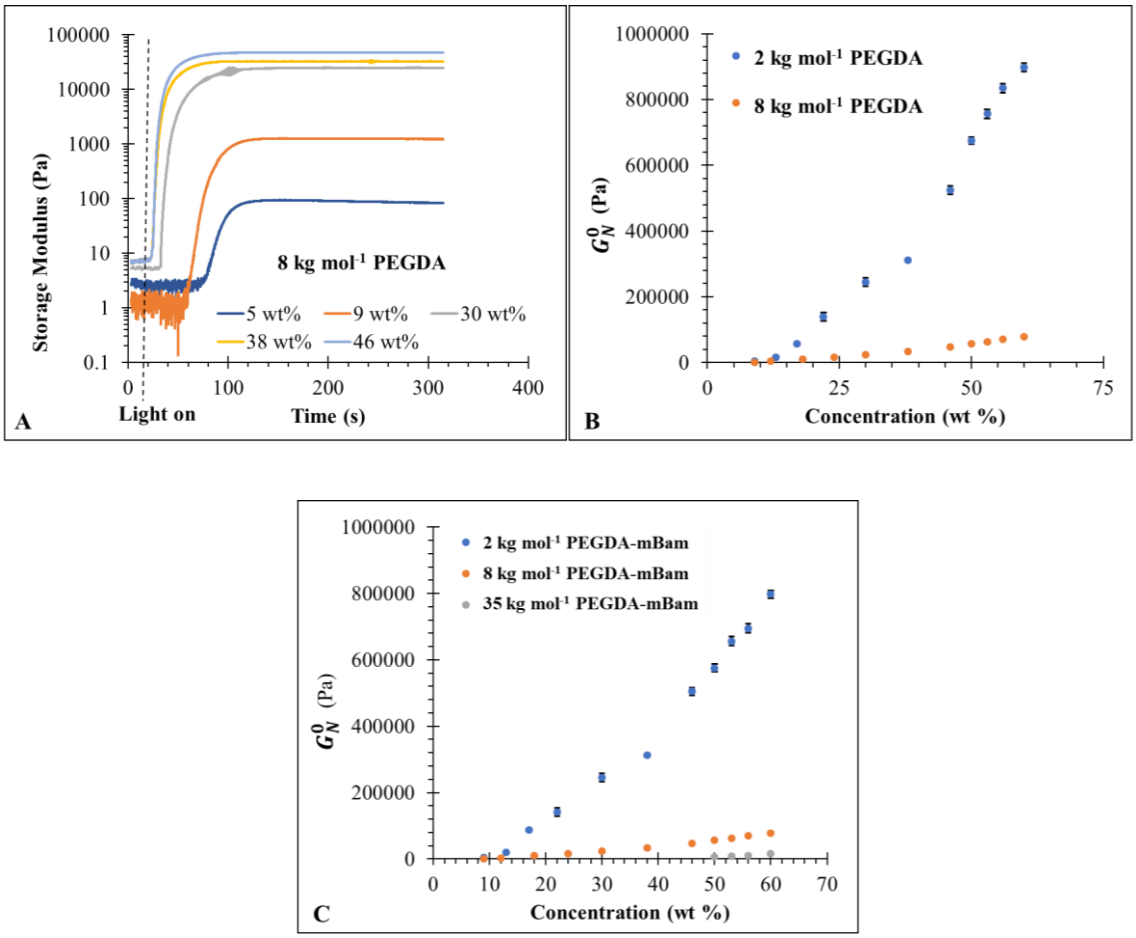

Figure 6.4. (A) Storage modulus as a function of time of PEGDA-mBam 8 kg mol^{-1} example, **(B)** G_N^o as a function of concentration of PEGDA, and **(C)** G_N^o as a function of concentration of PEGDA-mBam.

Gel fraction experiments determined mass percent of starting material incorporated into the network. **Figure 6.5A and B** showcases gel fraction as a function of concentration for 2 and 8 kg mol^{-1} PEGDA, respectively. Similar to the conversion vs. concentration trend, the gel fraction decreased with increasing concentration. 2 kg mol^{-1} experienced a slightly higher gel fraction at each concentration (average 2.3%), possibly owing to high concentrations of acrylate moieties and lower viscosities. For reference, black lines denote $C^*$and C_e on both graphs. In general, after C_e the gel fraction begins to rapidly decrease, but further studies are required to prove its dependency.

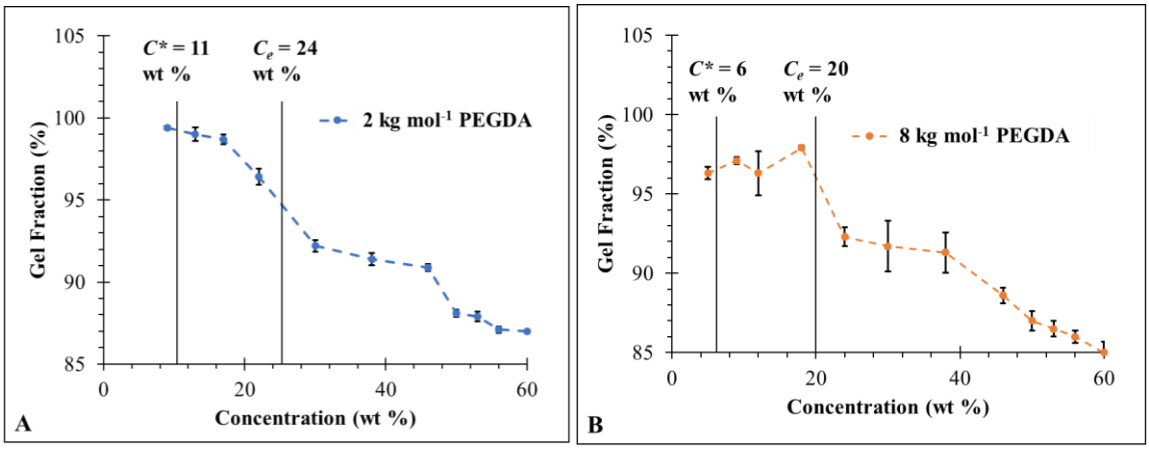

Figure 6.5. Gel fractions as a function of concentration of **(A)** 2 kg mol^{-1} and **(B)** 8 kg mol^{-1} PEGDA.

6.4.4 Non-associating vs. hydrogen bonding comparison

Incorporating hydrogen bonding into the polymer backbone as amide bonds in PEGDA-mBam affected solution viscosity and therefore produced different photokinetic profiles compared to non-associating PEGDA. Polar solvents, such as water, associated with PEGDA-mBam where the carbonyl amide and water hydrogens acted as hydrogen bonding acceptors and donors, respectively. This not only increased the viscosity of the solution but also screened hydrogen bonding between PEGDA-mBam backbones. In one case, 2 kg mol^{-1} PEGDA-mBam, 50:50 v:v water:DMSO was required to dissolve the polymer possibly owing to the highest concentration of amide groups.

Figure 6.6A depicts conversion as a function of concentration for 8 kg mol^{-1} PEGDA and PEGDA-mBam. In some instances, PEGDA-mBam exhibited a lower conversion compared to PEGDA, but in general the acrylate/acrylamide conversions remained the same. The polymers experienced similar viscosities at most concentrations, which could attribute the similar conversion values. **Figure 6.6B** shows the same parameters but comparing 8 kg mol^{-1} PEGDA-mBam in water and chloroform. Chloroform is a non-polar solvent which will not associate to the polymer backbone or screen hydrogen bonding between polymers. The backbone amides associated, which impacted an almost doubling of viscosity for each concentration compared to PEGDA-mBam in water. However, across all concentrations the polymer in chloroform experienced an increase in conversion. The increase in conversion potentially stems from the hydrogen bonding amide bonds templating the crosslinking reaction and therefore overcomes the disadvantage of increased viscosity.[28]

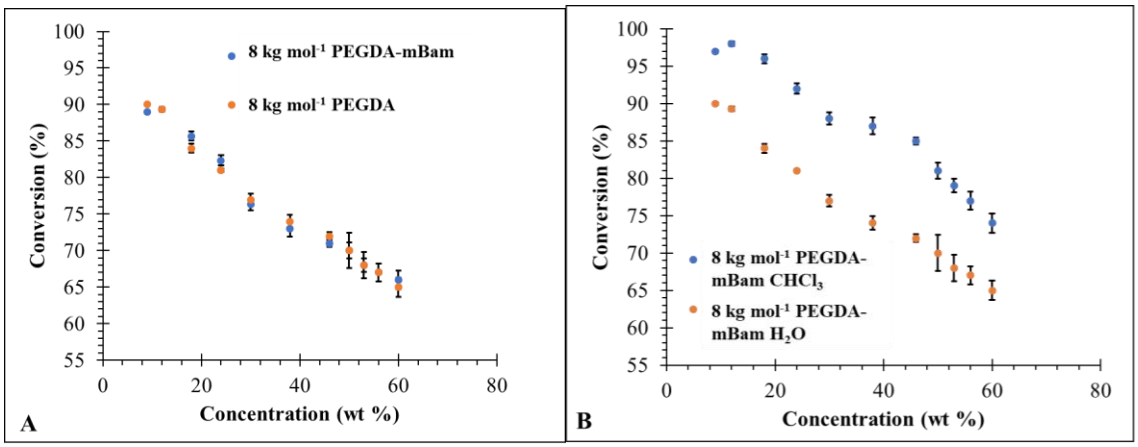

Figure 6.6. (A) Acrylate/acrylamide conversion as a function of concentration of 8 kg mol^{-1} PEGDA and PEGDA-mBam and **(B)** acrylamide conversion of 8 kg mol^{-1} PEGDA-mBam in water and chloroform.

High molecular weight and low crosslinking density hindered the feasibility of printing 35 kg mol^{-1} PEGDA and PEGDA-mBam. For example, **Figure 6.7A** depicts modulus as a function of time of 35 kg mol^{-1} PEGDA to monitor the relative modulus during and after crosslinking. After UV light exposure, both concentrations experienced an increase in modulus, but never exhibited a storage/loss moduli crossover point. The storage/loss moduli crossover denotes a transition from viscous to elastic behavior, or liquid-like to solid-like behavior. The lack of crossover indicates each samples remained a viscous liquid after crosslinking possibly owing to low crosslink density and low conversion. **Figure 6.7B** depicts the same experiment for 35 kg mol^{-1} PEGDA-mBam. After 30 s of light exposure, the network forms a weak, solid film. Solid films formed for all polymers above 50 wt %, but were difficult to remove from the plate and maintained low fidelity. The ability to form a solid network possibly manifested from hydrogen bonding maintaining a secondary network.

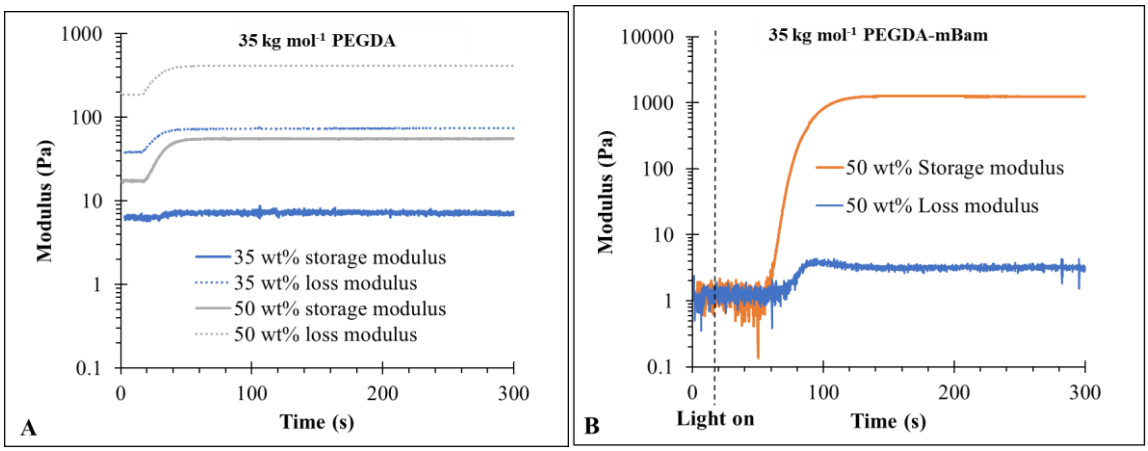

Figure 6.7. Storage/loss moduli as a function of time of **(A)** 35 kg mol^{-1} PEGDA and **(B)** 35 kg mol^{-1} PEGDA-mBam.

Figure 6.8 depicts gel fractions as a function of concentration for 2 kg mol^{-1} PEGDA and PEGDA-mBam. Both gel fractions decreased with increasing concentration, but PEGDA-mBam experienced lower gel fractions after 18 wt % compared to PEGDA. At 60 wt %, PEGDA-mBam exhibited a 78% gel fraction. This trend is mostly likely due to the increased viscosity compared to PEGDA at every wt %. At each wt %, PEGDA-mBam contained almost double the viscosity of PEGDA because water hydrogen bonds with amide moieties, thus increasing the solution viscosity.

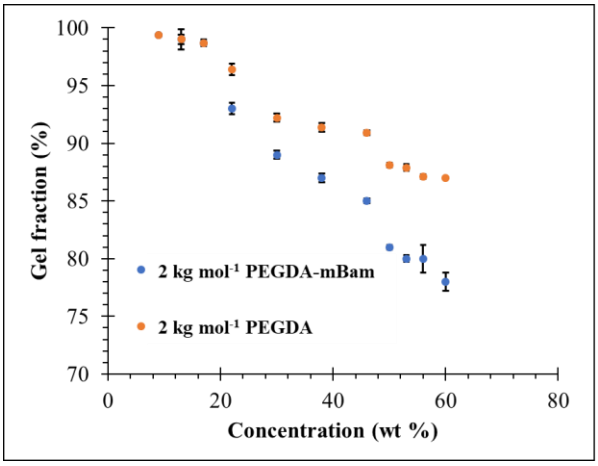

Figure 6.8. Gel fractions as a function of concentration of 2 kg mol^{-1} PEGDA and PEGDA-mBam.

6.5 Conclusions

This manuscript discussed the synthesis, characterization, and subsequent photokinetics in water of poly(ethylene glycol)-diacrylate (PEGDA) and hydrogen bonding poly(ethylene glycol)-diacrylamide (PEGDA-mBam). Determination of C^* and C_e of the two polymers at 2, 8, and 35 kg mol^{-1} revealed increasing molecular weight and addition of hydrogen bonding decreased both transitions. Photocalorimetry and photorheology revealed increased viscosity resulted in decreased acrylate/acrylamide conversion and gel fraction. 2 kg mol^{-1} polymer exhibited the highest relative moduli after crosslinking due to the highest crosslink density compared to other molecular weights. Failure of photocalorimetry for 35 kg mol^{-1} polymers manifested from low concentrations of acrylate/acrylamide groups for detection. Additionally, while 35 kg mol^{-1} PEGDA did not form solid films at any concentration, after 50 wt % in water 35 kg mol^{-1} PEGDA-mBam formed solid films possibly owing to a secondary hydrogen bonded network. This study elucidated conversion dependency on solution viscosity and hydrogen bonding groups effect on crosslinked network moduli.

6.6 Acknowledgements

The authors would like to thank the Timothy Long research group for countless discussions on experimental and analytical design.

6.7 References

(1) Appuhamillage, G. A.; Chartrain, N.; Meenakshisundaram, V.; Feller, K. D.;

Williams, C. B.; Long, T. E. 10th Anniversary: Vat Photopolymerization-Based Additive Manufacturing: Current Trends and Future Directions in Materials Design. **2019**. https://doi.org/10.1021/acs.iecr.9b02679.

(2) Gibson, I.; Rosen, D.; Stucker, B.; Gibson, I.; Rosen, D.; Stucker, B. Vat Photopolymerization Processes. In *Additive Manufacturing Technologies*; Springer New York, 2015; pp 63–106. https://doi.org/10.1007/978-1-4939-2113-3_4.

(3) Huang, Y.; Leu, M. C.; Mazumder, J.; Donmez, A. Additive Manufacturing: Current State, Future Potential, Gaps and Needs, and Recommendations. *J. Manuf. Sci. Eng. Trans. ASME* **2015**, *137* (1). https://doi.org/10.1115/1.4028725.

(4) Stansbury, J.; Materials, M. I.-D.; 2016, undefined. 3D Printing with Polymers: Challenges among Expanding Options and Opportunities. *Elsevier*.

(5) Zandrini, T.; Liaros, N.; Jiang, L. J.; Lu, Y. F.; Fourkas, J. T.; Osellame, R.; Baldacchini, T. Effect of the Resin Viscosity on the Writing Properties of Two-Photon Polymerization. *Opt. Mater. Express* **2019**, *9* (6), 2601. https://doi.org/10.1364/ome.9.002601.

(6) Eckel, Z. C.; Zhou, C.; Martin, J. H.; Jacobsen, A. J.; Carter, W. B.; Schaedler, T. A. Additive Manufacturing of Polymer-Derived Ceramics. *Science (80-.).* **2016**, *351* (6268), 58–62. https://doi.org/10.1126/science.aad2688.

(7) Alvarez-Primo, F.; English, J.; Mireles, J. *Wohlers Report 2016 Appendix E: Material Properties Appendix E: Material Properties*; 2016.

(8) Rau, D. A.; Herzberger, J.; Long, T. E.; Williams, C. B. Ultraviolet-Assisted Direct Ink Write to Additively Manufacture All-Aromatic Polyimides. *ACS Appl. Mater. Interfaces* **2018**, *10* (41), 34828–34833. https://doi.org/10.1021/acsami.8b14584.

(9) Herzberger, J.; Meenakshisundaram, V.; Williams, C. B.; Long, T. E. 3D Printing All-Aromatic Polyimides Using Stereolithographic 3D Printing of Polyamic Acid Salts. *ACS Macro Lett.* **2018**, *7* (4), 493–497. https://doi.org/10.1021/acsmacrolett.8b00126.

(10) Sirrine, J. M.; Meenakshisundaram, V.; Moon, N. G.; Scott, P. J.; Mondschein, R. J.; Weiseman, T. F.; Williams, C. B.; Long, T. E. Functional Siloxanes with Photo-Activated, Simultaneous Chain Extension and Crosslinking for Lithography-Based 3D Printing. *Polymer (Guildf).* **2018**, *152*, 25–34. https://doi.org/10.1016/j.polymer.2018.02.056.

(11) Scott, P. J.; Meenakshisundaram, V.; Chartrain, N. A.; Sirrine, J. M.; Williams, C. B.; Long, T. E. Additive Manufacturing of Hydrocarbon Elastomers via Simultaneous Chain Extension and Cross-Linking of Hydrogenated Polybutadiene. *ACS Appl. Polym. Mater.* **2019**, *1* (4), 684–690. https://doi.org/10.1021/acsapm.8b00150.

(12) Scott, P. J.; Meenakshisundaram, V.; Hegde, M.; Kasprzak, C.; Winkler, C.; Feller, K.; Williams, C. B.; Long, T. E. 3D Printing Latex: A Route to Complex Geometries of High Molecular Weight Polymers. *ACS Appl. Mater. Interfaces* **2020**. https://doi.org/10.1021/acsami.9b19986.

(13) Wilts, E.M.Gula, A; Davis, C.; Chartrain, N.; Williams, C. B.; Long, T. E. Vat Photopolymerization of Liquid, Biodegradable PLGA-Based Oligomers as Tissue Scaffolds. *Eur. Polym. J.* **2020**, *submitted*.

(14) Aduba, D. C.; Margaretta, E. D.; Marnot, A. E. C.; Heifferon, K. V.; Surbey, W. R.; Chartrain, N. A.; Whittington, A. R.; Long, T. E.; Williams, C. B. Vat Photopolymerization 3D Printing of Acid-Cleavable PEG-Methacrylate Networks for Biomaterial Applications. *Mater. Today Commun.* **2019**, *19*, 204–211. https://doi.org/10.1016/j.mtcomm.2019.01.003.

(15) Andrzejewska, E.; Andrzejewski, M. Polymerization Kinetics of Photocurable Acrylic Resins. *J. Polym. Sci. Part A Polym. Chem.* **1998**, *36* (4), 665–673. https://doi.org/10.1002/(SICI)1099-0518(199803)36:4<665::AID-POLA15>3.0.CO;2-K.

(16) Su, W.-F. *RING-OPENING POLYMERIZATION.*; Elsevier Applied Science Publ, 1984; Vol. 1. https://doi.org/10.1007/978-3-642-38730-2_11.

(17) Carothers, W. H. Polymers and Polyfunctionality. *Transactions of the Faraday Society*. The Royal Society of Chemistry January 1, 1936, pp 39–49. https://doi.org/10.1039/TF9363200039.

(18) Tobita, H.; Ohtani, Y. Control of Molecular-Weight Distribution in Step-Growth Polymerization: The Intermediate Monomer Feed Method. *Polymer (Guildf).* **1992**, *33* (4), 801–811. https://doi.org/10.1016/0032-3861(92)90340-3.

(19) Colby, R. H.; Fetters, L. J.; Funk, W. G.; Graessley, W. W. Effects of Concentration and Thermodynamic Interaction on the Viscoelastic Properties of Polymer Solutions. *Macromolecules* **1991**, *24* (13), 3873–3882. https://doi.org/10.1021/ma00013a021.

(20) Gupta, P.; Elkins, C.; Long, T. E.; Wilkes, G. L. Electrospinning of Linear Homopolymers of Poly(Methyl Methacrylate): Exploring Relationships between Fiber Formation, Viscosity, Molecular Weight and Concentration in a Good Solvent. *Polymer (Guildf).* **2005**, *46* (13), 4799–4810. https://doi.org/10.1016/J.POLYMER.2005.04.021.

(21) Matthew G. McKee, †; Garth L. Wilkes, ‡; Ralph. H. Colby, § and; Timothy E. Long*, †. Correlations of Solution Rheology with Electrospun Fiber Formation of Linear and Branched Polyesters. **2004**. https://doi.org/10.1021/MA035689H.

(22) Faraz, M. I. Rheology of Organoclay Dispersions and Modeling of Gelation Behavior and Finding Overlap Concentration. *Arab. J. Sci. Eng.* **2019**, *44* (12), 10117–10126. https://doi.org/10.1007/s13369-019-03960-1.

(23) Wehrman, M. D.; Leduc, A.; Callahan, H. E.; Mazzeo, M. S.; Schumm, M.; Schultz, K. M. Rheological Properties and Structure of Step- and Chain-Growth Gels Concentrated above the Overlap Concentration. *AIChE J.* **2018**, *64* (8), 3168–3176. https://doi.org/10.1002/aic.16062.

(24) Wang, Y.; Fu, J.; Liu, M.; Fu, Q.; Polymer, J. Z.-; 2019, undefined. The Effect of Chain Entanglement State on Melt Crystallization of the Polymer Freeze-Extracted from Solution: The Role of Critical Overlap Concentration. *Elsevier*.

(25) Milner, S. T. Unified Entanglement Scaling for Flexible, Semiflexible, and Stiff Polymer Melts and Solutions. *Macromolecules* **2020**. https://doi.org/10.1021/acs.macromol.9b02684.

(26) Keshavarz, M.; Engelkamp, H.; Xu, J.; Van Den Boomen, O. I.; Maan, J. C.; Christianen, P. C. M.; Rowan, A. E. Confining Potential as a Function of Polymer Stiffness and Concentration in Entangled Polymer Solutions. *J. Phys. Chem. B* **2017**, *121* (22), 5613–5620. https://doi.org/10.1021/acs.jpcb.6b12667.

(27) Wilts, E. M.; Pekkanen, A. M.; White, B. T.; Meenakshisundaram, V.; Aduba, D. C.; Williams, C. B.; Long, T. E. Vat Photopolymerization of Charged Monomers: 3D Printing with Supramolecular Interactions. *Polym. Chem.* **2019**, *10* (12). https://doi.org/10.1039/c8py01792a.

(28) Jansen, J. F. G. A.; Dias, A. A.; Dorschu, M.; Coussens, B. Fast Monomers: Factors Affecting the Inherent Reactivity of Acrylate Monomers in Photoinitiated Acrylate Polymerization. **2003**. https://doi.org/10.1021/ma021785r.

6.9 Supplemental

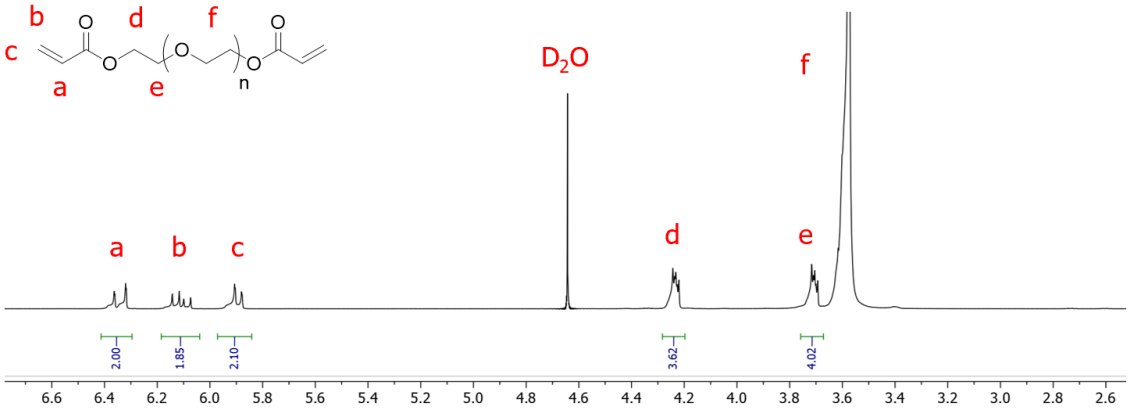

Figure S6.1. Annotated ^{1}H NMR of PEGDA.

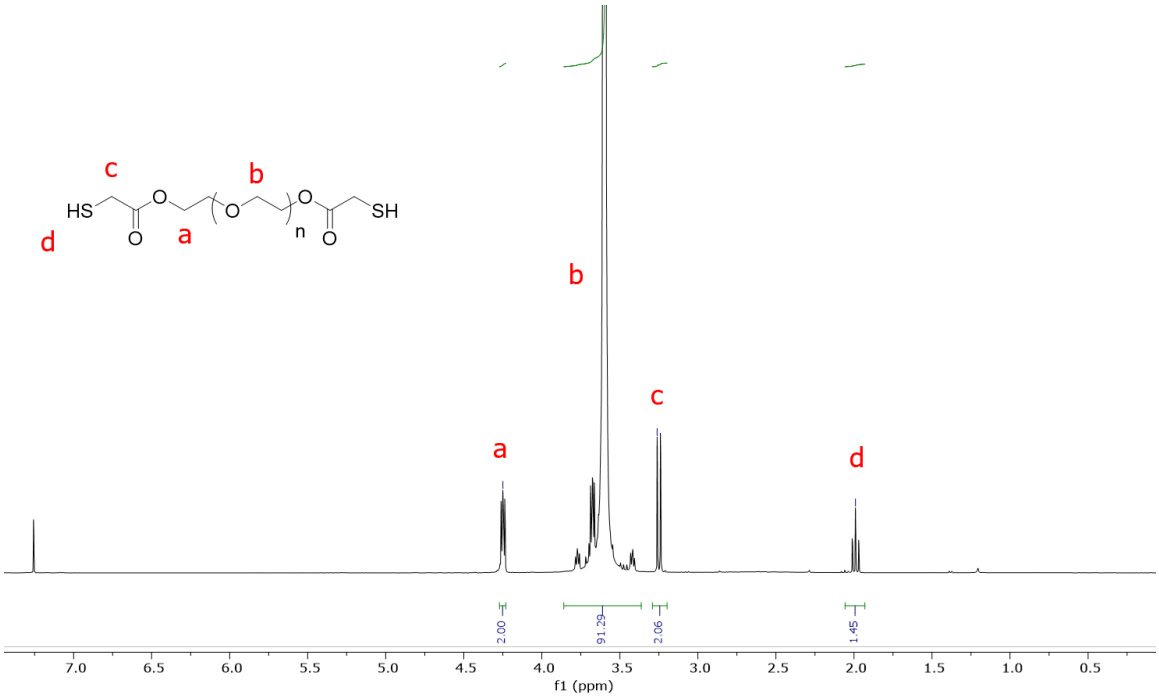

Figure S6.2. Annotated ^{1}H NMR of PEG-SH.

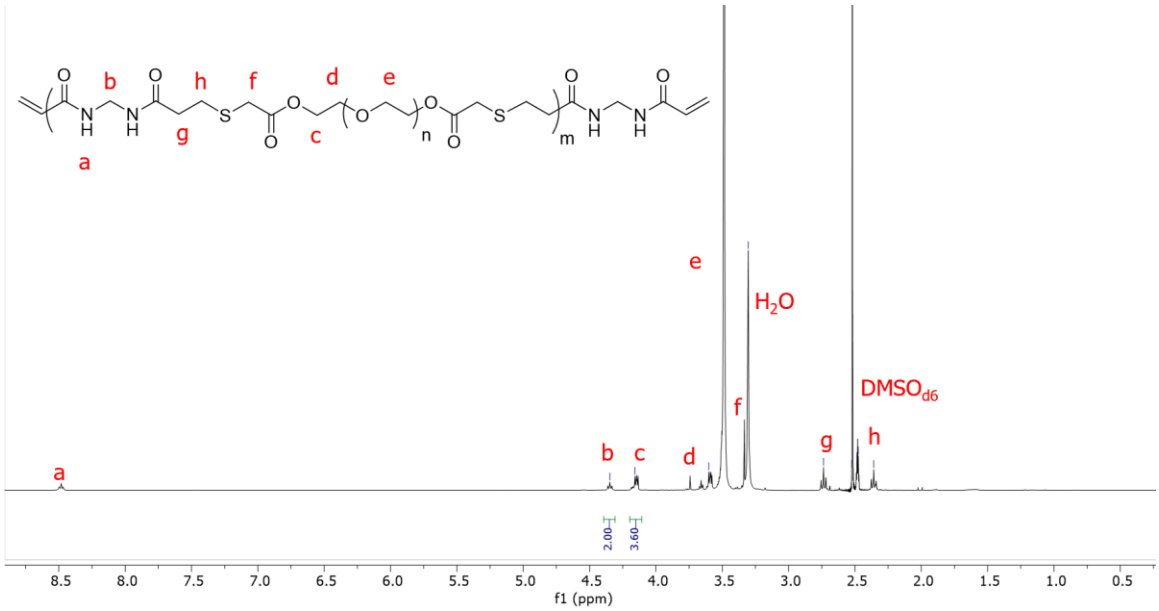

Figure S3. Annotated ^{1}H NMR of PEGDA-mBam.

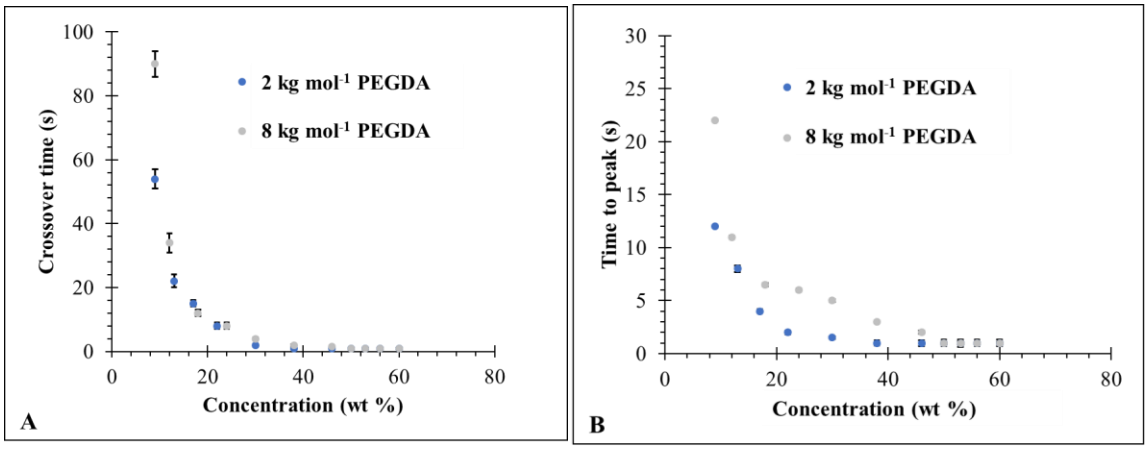

Figure S4. (A) Crossover time as a function of concentration and **(B)** time to peak as a function of concentration.

Chapter 7: Comparison of Linear and 4-arm Star Poly(vinyl pyrrolidone) for Aqueous Binder Jetting Additive Manufacturing of Personalized Dosage Tablets

(Published in *ACS Applied Materials and Interfaces*, **2019**, *10* (27), 23938-23947)

Emily M. Wilts[1], Susan Ma[2], Yun Bai[2], Christopher B. Williams[2] and Timothy E. Long[1*]

[1]*Department of Chemistry, Macromolecules Innovation Institute, Virginia Tech, Blacksburg, VA 24061*

[2]*Department of Mechanical Engineering, Macromolecules Innovation Institute, Virginia Tech, Blacksburg, VA 24061*

7.1 Abstract

Fabrication of personalized dosage oral pharmaceuticals using additive manufacturing (AM) provides patients with customizable, locally manufactured, and cost-efficient tablets, while reducing the probability of side-effects. Binder jetting AM has potential for fabrication of customized dosage tablets, but the resulting parts lack in strength due to solely relying on the binder to produce structural integrity. The selection of polymeric binders is also limited due to viscosity restraints, which limits molecular weight and concentration. To investigate and ameliorate these limitations, this manuscript reports a comprehensive study of linear and 4-arm star poly(vinyl pyrrolidone) (PVP) over a range of molecular weights as polymeric binders for binder jetting additive manufacturing, and their effect on physical tablet properties. Formulation of varying molecular weights and concentrations of linear and 4-arm star PVP in DI water and subsequent jetting revealed relationships between the critical overlap concentrations (C^*) and jettability on binder jetting systems with thermal inkjet systems. After printing with a commercially available ZCorp Spectrum Z510 printer with a HP11 printhead with a lactose and powdered sugar powder bed, subsequent measurement of compressive strength, compressive modulus, and

porosity revealed structure-property relationships between molecular weight, polymer concentration, and linear and 4-arm star architectures with physical properties of binder jetted tablets. This study elucidated the dominating factor to increase compressive strength of a tablet is dependent on the weight percent polymer in the binder, which filled interstitial voids between powder particles. Because 4-arm star polymers have lower solution viscosities compared to linear analogs at the same molecular weights, they were jettable at higher concentrations, thus producing the strongest tablets at a compressive strength of 1.2 MPa. Finally, the inclusion of an active pharmaceutical ingredient (API), acetaminophen, revealed a maintenance of tablet physical properties across 5-50 total wt% API in each tablet.

Keywords: binder jetting, personalized dosage tablets, additive manufacturing, Ohnesorge number, Poly(vinyl pyrrolidone)

7.2 Introduction

Additive manufacturing (AM) of tablets has the potential to provide patients with personalized dosage pharmaceuticals with tunable release profiles.[1,2] An estimated 75-85% of side-effects are a direct result of inaccurate dosing and pharmaceutical combinations because of varying weights and metabolic rates of patients.[3] To ameliorate this problem, researchers strive to use fuse filament fabrication, binder jetting, and selective laser sintering AM technologies to produce personalized dosage tablets, while also transforming the tablet making process into a more time- and cost-efficient process.[4,5] In 2015, Aprecia Pharmaceuticals achieved FDA approval for additively manufactured tablets, called Spritam, using binder jetting AM.[6] The availability of commercially available printers and

the opportunity to use existing excipients from compression molding tablet processes deem this AM method as advantageous for personalized dosage pharmaceuticals. Binder jetting is a powder bed-based system where an adhesive binder is jetted onto a powder surface to make layers. The adhesive used to bind the powder layers usually contains a polymeric binder, solvent, additives to tune solution properties, and often the active pharmaceutical ingredient (API) in certain applications.

Stable droplet formation of drop-on-demand binder jetting systems depends on binder solution properties such as viscosity, surface tension, and density. Three dimensionless numbers called the Reynolds (*Re*) number, Weber (*We*) number, and Ohnesorge (*Oh*) number aim to predict jettability based on the physical properties listed above. The *Re* number (**Eqn. 1**), *We* number (**Eqn. 2**), and *Oh* number (**Eqn. 3**) predict sufficient energy to eject a drop, stable drop formation, general jettability, respectively, where υ, ρ, α, σ, and η represent drop velocity, density, capillary radius of each nozzle, surface tension, and viscosity.[5,7,8] **Eqn. 4** represents the *Z* parameter, another common factor used for predicting jettability, which is the inverse of the *Oh* number. Reis and Derby *et. al.* predicted the *Z* parameter jettable region lies between 1 and 10 using a piezoelectric droplet ejector.[9] Solution viscosity and surface tension mainly govern the ability for a binder to jet where the optimal ranges are 1 to 20 mPa·s and 20 to 40 mN m^{-1}, respectively.[10,11] Recent literature suggests this range varies depending on the use of a piezoelectric or thermal-type printhead, whether the binder contains solid particles, and complex rheology relating to the behavior of polymers, oligomers, and small molecules in binder systems.[7,9,12–16]

$$Re = \frac{v\rho\alpha}{\eta} \qquad \textbf{Eqn. 1}$$

$$We = \frac{v^2\rho\alpha}{\sigma} \qquad \textbf{Eqn. 2}$$

$$\frac{We^{0.5}}{Re} = Oh\ \# = \frac{\eta}{(\sigma\rho\alpha)^{0.5}} \qquad \textbf{Eqn. 3}$$

$$\frac{1}{Oh} = Z \qquad \textbf{Eqn. 4}$$

Another aspect in jetting, specifically polymeric solutions, is considering how viscoelastic effects will impact whether an ink is jettable or not. If the relaxation times of the polymers are longer than the jetting process, they may not be able to jet out of the nozzle. A typical timescale for an actuation pulse is 20 μs, where many concentrated polymeric solutions have relaxation times of ~0.1 s.[17,18] As an example, Hutchings *et. al.* investigated jetting of dilute polymeric solutions and developed a quantitative model which predicts jettability of said solutions based on the system's Weissenberg (*Wi)* number and the polymer extensibility (*L*). Others have investigated the effect of the Wi number on jettability in dilute solutions ($Wi < ½$), but this report aimed to investigate viscoelastic solutions exhibiting higher *Wi* numbers.[17–19] These studies provide comprehensive models and data supporting methods of predicting jettability of linear polymers, but jettability of varying polymer architectures have yet to be explored.

Binder jetting AM employs two different types of drop-ejection mechanisms depending on the type of printhead, termed piezoelectric and thermal. The most popular type, piezoelectric printheads, contain a piezoelectric element, which mechanically moves when a voltage is applied. This movement creates a pressure wave, forcing a drop out of

the nozzle.[5,9] Thermal printheads, the type used in this study, eject drops of binder using a combination of electric pulses and explosive evaporation of a solvent.[14] An electric pulse is sent to the resistor element, which locally heats the binder to the superheat limit temperature (T_{SL}). The T_{SL} is defined as 90% of the critical fluid temperature, which is 312 ^{o}C for water at atmospheric pressure. These temperatures induce the liquid-vapor phase changes to occur through explosive evaporation. The formation of a vapor bubble through this process forces a drop to eject from the nozzle. Considering that the aforementioned printing methods rely on different mechanisms of ejection, it follows that the physical property requirements for binders fall into different jettable ranges.[14]

Linear poly(vinyl pyrrolidone) (PVP) is the most common polymeric binder used in water-based binder jetting AM due to its biocompatibility, water-solubility, and high glass transition temperature.[20,21] PVP, along with other biocompatible polymers, successfully function as binders for AM of tablets, but previous examples solely utilize commercially available materials. Commercially available materials possess limited molecular weight ranges and commonly only allow linear polymer analogs. Moreover, these constraints limit the strength profiles of printed tablets because of the increasing solution viscosity with increasing polymer concentration in the binder. Suwanprateeb *et. al.* demonstrated the higher concentration of oligomeric adhesive in a binder composition maintained higher compressive strengths. They employed combinations of maltodextrin and poly(vinyl alcohol) as adhesive binders in poly(methyl methacrylate) powder, which demonstrated an increase of adhesive content from 10 to 60 wt%, decreased the porosity by 26%, and increased the compressive strength by 22x.[22] Employing the use of varying polymer architectures and a wide molecular weight range in fully water-soluble systems

allows for a more expansive tablet strength profile. For example, star and graft polymers maintain lower solution viscosities compared to linear analogs at the same molecular weight. Star and graft polymers maintain smaller radii of gyration (R_g) compared to linear analogs, which induces less entanglements, thus lowering frictional forces within the solution.[23,24] Branched polymer architectures enable higher polymer loadings in the binder solution while remaining within the jettable range, thus producing a stronger 3D printed part.[25]

This work describes the synthesis of linear and 4-arm star PVP using reversible addition-fragmentation chain-transfer polymerization (RAFT) and their subsequent use in water-based binders for binder jetting AM of personalized dosage tablets. RAFT polymerization enabled the synthesis of 5, 25 and 50 kg mol^{-1} linear and 4-arm star PVP where the formulated binders contained 3, 6, and 9 wt% polymer in DI water and 1 wt% Tween 20® as a surface tension modifier. Steady-state rheology, pendant drop experiments, and density calculations afforded the calculation of the *Oh* number and *Z* parameter, which revealed each combination remained in the theoretically jettable range. Determination of the critical overlap concentration (*C**) of each polymer system also revealed a relationship between jettability and the viscoelastic nature of the polymeric solutions. Binder jetting AM with lactose and powdered sugar formed tablets where compressive strength, compression modulus, and porosity were measured. Using a higher loading of 4-arm star PVP demonstrated an increase in strength of the final printed tablet compared to other water-based binders reported for personalized dosage pharmaceuticals using thermal-type print heads. As the demand for new materials for AM increases, this report describes the role of architecture of polymeric adhesives for binder jetting AM.

7.3 Materials and methods

7.3.1 Materials

(1-Bromoethyl)benzene, 1,2,4,5-tetrakis(bromomethyl)benzene, Tween 20®, silica, acetaminophen, methyl benzoate (99%), and 40k PVP were purchased from Sigma Aldrich and used without further purification. *N*-Vinyl pyrrolidone (NVP) was filtered through a basic aluminum column to remove inhibitor before use. Azobisisobutyronitrile (AIBN) was purchased from Sigma Aldrich and recrystallized from methanol before use. O-ethyl xanthic acid potassium salt was dried at 40 ^{o}C under high vacuum (0.1 mbar) for 24 h before use. Diethyl ether, deionized (DI) water, extra dry acetone (99.9%) and methanol were purchased from Acros and used without further purification. Lactose 315 was purchased from Foremost Farms USA and Kroger Inc. powdered confectioners' sugar (5-30 μm particle size) was purchased from the local store, and both were dried at 60 ^{o}C under vacuum for 24 h and sifted to break up aggregates before use.

7.3.2 Synthetic Methods

7.3.2.1 Synthesis of O-Ethyl-S-(1-ethylphenyl) dithiocarbonate

The synthesis of *O*-ethyl-*S*-(1-ethylphenyl) dithiocarbonate was adopted from Stenzel *et. al*.[26] Briefly, *O*-ethyl xanthic acid potassium salt (5.24 g, 0.033 mol, 1 eq.) was dissolved in 60 mL of dry acetone and purged with nitrogen for 30 min. 1-Bromo ethyl benzene (6.03 g, 0.033 mol, 1 eq.) was added dropwise over 10 min and the reaction stirred for 24 h. Potassium bromide was removed through filtration and the acetone was removed at reduced pressure. The viscous yellow product was used without further purification at 89 % yield. The structure was confirmed using ^{1}H and ^{13}C NMR spectroscopy. ^{1}H NMR ($CDCl_3$):

1.43 (3H, t), 1.57 (3H, d), 4.62 (2H, q), 4.87 (1H, q), 7.36 (5H, m). ^{13}C NMR ($CDCl_3$): 13.6, 21.7, 49.2, 69.6, 127.1-128.7, 141.8, 213.0.

7.3.2.2 Synthesis of 1,2,4,5-Tetrakis[(*O*-ethylxanthyl)methyl]benzene

The synthesis of 1,2,4,5-tetrakis[(*O*-ethylxanthyl)methyl]benzene was adopted from Stenzel *et. al*.[26] Briefly, *O*-ethyl xanthic acid potassium salt (5.24 g, 0.033 mol, 1 eq.) was dissolved in 100 mL of dry acetone and the reaction vessel was purged with N_2 for 30 min. Next, 1,2,4,5-tetrakis(bromomethyl)benzene (3.66 g, 0.0082 mol, 0.25 eq.) was added and the reaction was allowed to stir for 24 h. Potassium bromide was removed through filtration and the acetone was removed at reduced pressure. The residual pale-yellow solid was dissolved in chloroform and purified through column chromatography with 4/1 v/v hexane/ethyl acetate as the mobile phase (55% yield). The structure was confirmed using ^{1}H and ^{13}C NMR spectroscopy. ^{1}H NMR ($CDCl_3$): 1.42 (12H, t), 4.67 (8H, q), 4.38 (8H, s), 7.38 (2H, s). ^{13}C NMR ($CDCl_3$): 13.7, 37.3, 70.2, 132.9, 134.1, 213.1.

7.3.2.3 RAFT polymerization kinetics of *N*-vinyl pyrrolidone

As an example procedure for linear PVP, a stock batch of NVP (35 g, 0.315 mol), O-ethyl-S-(1-ethylphenyl) dithiocarbonate (0.16 g, $7 \cdot 10^{-4}$ mol), and AIBN (11.4 mg, $7 \cdot 10^{-5}$ mol) were mixed and split into six 50-mL round-bottomed flasks and purged with nitrogen for 30 min. The molar ratio of NVP:CTA:AIBN was 450:1:0.1. The mixtures were allowed to react at 60 ^{o}C for 2, 4, 8, 12, 16, and 24 h. ^{1}H NMR spectroscopy of the crude product determined conversion. The reaction mixture was precipitated twice into diethyl ether and stirred for 20 min. Aqueous SEC determined absolute molecular weight of each system.

7.3.3 Binder Preparation

As a general procedure, polymer was placed in DI water and stirred with a magnetic stir bar for 10-15 min until the polymer was fully dissolved. 1 wt% of Tween 20® was subsequently added to tune surface tension and the mixture was stirred for an additional 30 min. After any bubbles dissipated, the binder was syringed through a 2.2 μm filter and used immediately.

7.3.4 Powder Preparation

The lactose was first sifted to <80 μm. Next, a combination of lactose powdered sugar, and silica were placed in a cylindrical container and mixed on a Waverly TR-E roller for 20 min. The powder was placed in the ZCorp printer powder bed and the roller created a flat surface to ensure aggregation did not occur. A ratio of 4:1 lactose:powdered sugar wt:wt was used for every tablet system, and 5 wt% of silica was added to increase spreadability.

7.3.5 Analytical methods

Aqueous SEC was conducted in a 54/23/23 v/v/v mixture of DI water, methanol, and glacial acetic acid with 0.1 M sodium acetate at a pH=4. A Waters Breeze Aqueous SEC with Wyatt miniDAWN treos light scattering and Waters 2414 RI detector with poly(ethylene oxide) (PEO) standards determined absolute molecular weight of each system. Solution viscosity experiments were performed on a DHR Discovery Rheometer in steady state mode with a Peltier plate and concentric cylinder geometries at 20 ^{o}C where n=3. Shear sweeps were conducted from 1-1200 s^{-1} at a 300 or 5000 μm gap with a solvent trap equipped with slightly saturated sponges. Pendant drop experiments were performed

on a FTA 200 Contact Angle Analyzer with a 3 mL 30-gauge syringe. FTA Operator's Software was used to fit the droplet shape to the Young-Laplace equation and yield the liquid-to-air interface surface tension where n=4. Density of the binder solutions was determined through micro-pipetting 1 mL of binder and subsequently weighing the sample, n=5. Compression testing was performed on each printed tablet with a crosshead motion of 1.3 mm min^{-1} on an Instron 4204 with a 1 kN load cell, n=10. Young's modulus was calculated from the slope of the linear elastic region of the stress vs. strain curve, and compressive strength was denoted as the largest stress at the yield point. ^{1}H NMR spectroscopy was conducted on a Varian Unity 400 MHz in D_2O and $DMSO_{d6}$. Scanning electron microscopy (SEM) images were taken on a Joel NeoScope JCM-5000 Benchtop SEM, under high vacuum at a 10 kV accelerating voltage. A micromeritics AccuPyc II 1340 Gas Pycnometer measured apparent density using ultra-pure Helium gas. The porosity of the tablets was calculated using **Eqn. 5,** where the bulk density was calculated using the weight and dimensional measurements of each sample.

$$porosity\ \% = \left(1 - \frac{bulk\ density}{apparent\ density}\right) x\ 100 \qquad \textbf{Eqn. 5}$$

7.3.6 Binder Jetting

All printing was conducted on a Z-Corp Spectrum Z510 3D printer with a HP 11 printhead (11 μm nozzle radius). To print the tablets, a solid model of a 12 mm diameter and 3 mm thick cylindrical tablet was used and uploaded onto the Zprint software and printed with a layer thickness of 0.005 inches at 100% saturation. After the print was complete, the parts were left in the powder bed for 40 min at 60 ^{o}C and subsequently removed from the printer.

7.3.7 Water Dissolution

To test the water dissolution of the binder jetted tablets, each tablet was added to a beaker of DI water at 37 ^{o}C in 1 mg mL^{-1} with a magnetic stir bar. Complete dissolution was denoted when the solution clarified or if the tablet completely broke apart into single particles.

7.3.8 API Determination

^{1}H NMR spectroscopy on a Varian Unity 400 MHz in D_2O determined the amount of API in each tablet. As an example, the 10 wt% API loaded tablets were printed and analyzed as follows. Lactose, powdered sugar, and acetaminophen (API) were all dried at 60 ^{o}C for 24 h before use. The powders were mixed at a ratio of lactose:powdered sugar:acetaminophen 75:15:10 wt:wt:wt and subsequently printed. Samples from the four quadrants and top of and bottom of the tablets were isolated about dissolved in $DMSO_{d6}$. A known amount of methyl benzoate was added to each mixture as an internal standard. To determine the amount of acetaminophen, the integration of the aromatic peaks on methyl benzoate (8.0-8.2, 3H, m) was compared to the aromatic peaks on acetaminophen (6.7, 2H, m; 7.4, 2H, m). An average of each quadrant and the top and bottom of the tablets was used to determine the total acetaminophen amount to ensure an even distribution of API throughout the tablet.

7.3.9 Statistical Analysis

Using Minitab 18 statistical software, an ANOVA test was performed followed by a Tukey's HSD to determine statistical differences between groups with a 95% confidence.

7.4 Results and Discussion

7.4.1 Synthesis and Structural Characterization of Linear and 4-arm Star PVP

RAFT polymerization yielded a series of precise number-average molecular weight (M_n), linear and 4-arm star PVP for subsequent use in water-based binder formulations. RAFT polymerization provides products without residual heavy metal catalysts and other toxic components compared to other reservable-deactivation radical polymerization methods, which deems this method appropriate for pharmaceutical applications.[27–29] This study utilized a specific xanthate-containing chain transfer agent (CTA) to yield controlled molecular weight linear and 4-arm star PVP, depicted in **Scheme 7.1A** and **7.1B**, respectively.[26] A kinetic study of each system revealed first-order kinetics over 24 h with a final conversion of 58% and 45% for the linear and 4-arm star CTAs, respectively. *N*-vinyl pyrrolidone represents a less activated monomer, which subsequently creates a highly reactive propagating radical. A xanthate moiety in the CTA reduces the double bond character compared to a typical dithioate functional group with an adjacent carbon, which helps control the polymerization. Additionally, this CTA contained an ethyl benzyl as a more stable radical-containing leaving group, compared to a common acetate group, which was also hypothesized to help control polymerization.[26,30] Using this system, a range of M_n of linear and 4-arm star PVP were chosen to explore the solution properties of each system and the molecular weight effects on the physical properties of printed tablets.

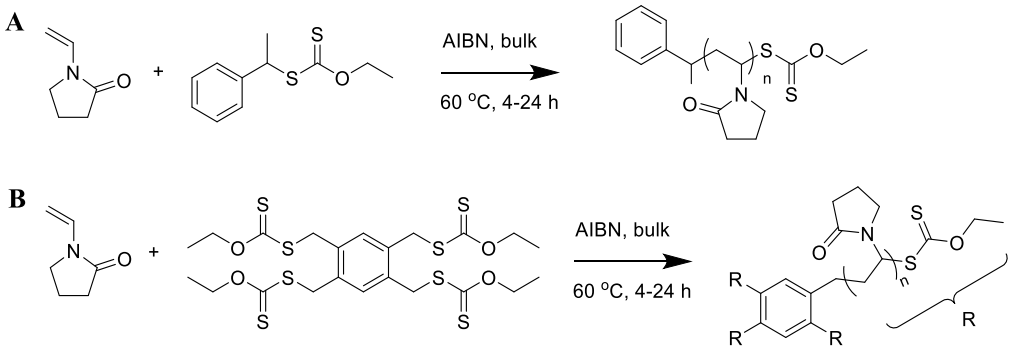

Scheme 7.1. Reversible addition-fragmentation chain-transfer (RAFT) polymerization yielded **(A)** linear and **(B)** 4-arm star poly(vinyl pyrrolidone) (PVP).

Aqueous SEC-MALLS revealed the M_n targets of 5, 25, and 50 kg mol^{-1} were achieved for the linear and 4-arm star PVP systems. **Figure 7.1A** and **7.1B** depicts the light scattering traces of linear and 4-arm star PVP, respectively. Light scattering and refractive index detection confirmed absolute molecular weight of approximately 5, 25, and 50 kg mol^{-1} linear and 4-arm star PVP with all dispersities (Đ) below 1.15, which indicated control of molecular weight owing to the controlled RAFT polymerization process (**Table S7.1**).

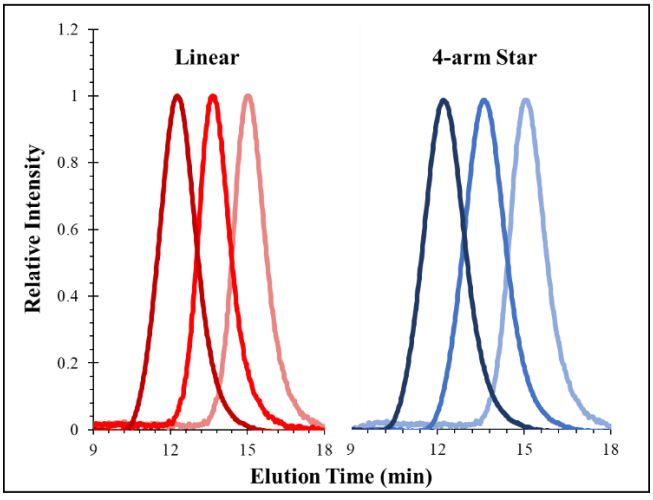

Figure 7.1. Aqueous SEC light scattering traces of linear and 4-arm star PVP depicting signal intensity as a function of elution time.

7.4.2 Binder Solution Properties

Formulations at 3, 6, and 9 wt% solutions in DI water of each M_n of linear and 4-arm star PVP afforded a range of concentrations to not only compare physical tablet properties using increasing wt% polymer, but also demonstrated the ability to jet 4-arm star PVP at higher concentrations compared to linear analogs at the same M_n. The addition of 1 wt% Tween 20®, a surfactant, to each combination lowered the surface tension into a jettable range (41.6 – 47.9 mN m^{-1}). Without the addition of Tween 20®, the binders did not jet from the nozzle, owing to insufficient energy to eject a drop. Density measurements of each binder did not reveal a trend and exhibited similar densities as water, 1.02-1.1 g mL^{-1}.

Figure 7.2A depicts the solution viscosities in DI water at 1000 s^{-1}, and the estimated shear rate of jetting[11], of linear (red) and 4-arm star (blue) PVP as a function of M_n and concentration. Each sample exhibited Newtonian behavior over the measured frequency range of 1-1200 s^{-1}. Increasing concentration and increasing molecular weight for all samples resulted in an increase in solution viscosity, where each data point depicted is statistically different. As concentration increased, the polymer chains exhibited a greater frictional force in solution and began to interact, thus increasing the viscosity. As molecular weight increased, the polymer chains overlap and entangle, which also caused an increase in viscosity. Across all samples, the 4-arm star PVP exhibited lower solution viscosities at all concentrations compared to the corresponding linear analogs at the same M_n. This is

attributed to star polymers experiencing smaller radii of gyration (R_g) compared to linear analogs. These physical properties combined with a compact shape, decreased friction in solution, and decreased entanglements and interactions with other polymer chains resulted in decreased solution viscosities.[31,32] This report discusses using lower solution viscosities to allow for a larger concentration of adhesive polymer to be jetted, which thus produced a stronger tablet in certain combinations.

Figure 7.2B depicts the *Z* parameters of linear (red) and 4-arm star (blue) PVP as a function of M_n and concentration where α=11 μm. The *Z* parameter trends followed similar trends as the solution viscosity data, which suggests tuning solution viscosity had an impact on jettability in this system. Because increasing polymer concentrations increased tablet strength, the goal was to achieve the highest concentration possible. The 4-arm star analogs exhibited lower *Z* parameters compared to the linear analogs, which enabled the ability to print them at higher concentrations.

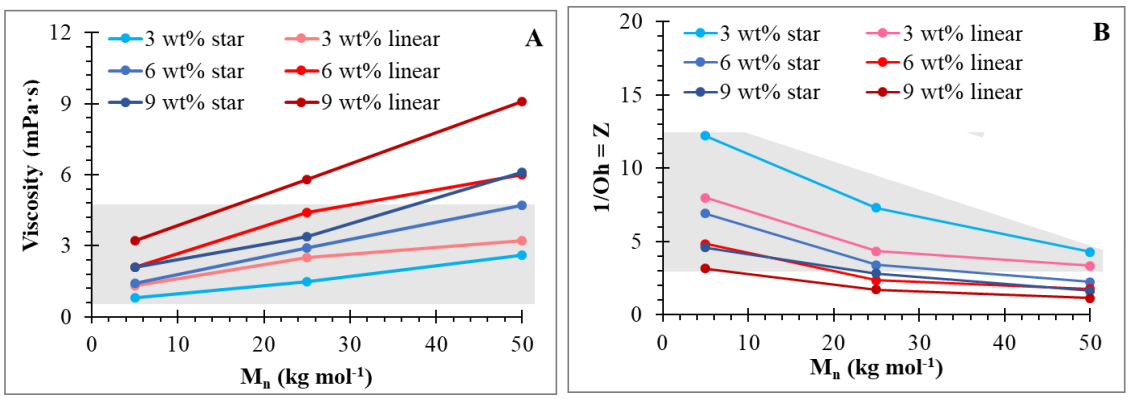

Figure 7.2. (A) Solution viscosities at 1000 s^{-1} and **(B)** Z parameters of 3, 6, and 9 wt% solutions as a function of M_n = 5, 25, and 50 kg mol^{-1} linear (red) and 4-arm star (blue) PVP.

Figure 7.2A and 7.2B depict gray areas representing successfully jetted binder formulations. Based on this comprehensive study, binders with solution viscosities from 0.8 to 4.7 mPa·s and *Z* parameters from 2.2 to 12.4 were jettable on this specific printing system. Binders exhibiting >4.7 mPa·s solution viscosities either partially ejected from the printhead, creating inconsistent layer saturation, or did not eject from the nozzle. This reported jettable range does not align with the accepted jettable *Z* parameter and solution viscosity ranges, 1 to 10 and 1 to 20 mPa·s, respectively. It is important to note that the previously reported range was determined using a piezoelectric printhead with ceramic-containing binders.[9] These differences arise from the different jetting mechanisms of thermal and piezoelectric printheads and the rheological differences between ceramic-containing binders and polymer-containing binders, both discussed extensively in the literature.[7,8,14,17,33] It should also be noted the drop volume could change as much as 15% over the Z parameter range reported, where the lower viscosity binders exhibit larger drop volumes.[34] Considering the small amount of polymer in the binder and the 3 wt% increments between samples, these variations do not significantly contribute to the compressive strength comparisons.

The formulation of polymeric binders also requires consideration of the viscoelastic properties of polymer solutions.[17,25,35,36] As the concentration of polymers in solution increases, the solution exhibits transitions from dilute to semi-dilute unentangled regimes. Dilute solutions behave as Newtonian fluids, and the viscosity of the solution solely depends on the contribution from single-coil polymer chains.[37–39] The critical overlap concentration (*C**) denotes the transition from the dilute to the semi-dilute unentangled regime, where the solution acts as a viscoelastic fluid and the viscosity depends on the

interaction between polymer chains. These transitions and solution viscoelastic behavior also strongly depend on molecular weight and polymer architecture because of the different radii of gyration (R_g).[40–42] Some examples exist for jetting viscoelastic fluids using piezoelectric systems, but systematic studies investigating jetting solution above *C** using thermal jetting systems do not exist in the literature.[43] This study aims to examine the jettability of linear and 4-arm star PVP analogs at varying molecular weights as water-based polymeric binders as a function of *C** in thermal inkjet systems.

Steady-shear solution rheology experiments from 1-20 wt% of linear and 4-arm star PVP in DI water without Tween 20® elucidated the transitions from the dilute to semi-dilute unentangled regimes. **Figure 7.3A** depicts linear and 4-arm star PVP at 25 kg mol^{-1} as an example *C** determination experiment. Scaling theory predicts the power law slope of concentration vs. viscosity in the dilute and semi-dilute unentangled regions for neutral, linear polymers is $C^{1.0}$ and $C^{1.25}$, respectively, where the transition between the two regimes denotes *C**. These experiments revealed *C** for 25 kg mol^{-1} linear and 4-arm star PVP in DI water were 7.0 ± 0.8 and 10.3 ± 0.5 wt%, respectively. 4-Arm star PVP exhibited a higher *C** because of its smaller R_g and the requirement of more polymer in solution to experience the onset of chain overlap compared to the linear analog. Linear and 4-arm star analogs experience slopes of $C^{1.55}$ and $C^{1.4}$ for the dilute regime and $C^{2.0}$ and $C^{1.85}$ for the semi-dilute unentangled regimes, respectively, which does not agree with scaling theory. Although water is considered a good solvent for PVP[44], water also has the ability to hydrogen bond with PVP, which may explain the deviations from known values.

Figure 7.3B depicts the *C** and the maximum jettable wt% of linear and 4-arm star PVP as a function of M_n. Jetting each of these systems revealed the binders could not

successfully eject from the nozzles above *C**. Above *C**, the solution viscosity depends on the interactions between polymer chains, which changes the polymer relaxation times. Literature demonstrated polymer solutions above *C** and with complex rheological behavior are able to print on piezoelectric print heads with larger nozzle diameters.[17,25] This data suggests *C** may predict the maximum concentration of polymer jettability for thermal systems as opposed to a viscosity limit determined by the *Z* parameter ranges. Further studies using polymer architectures with varying *C**'s may better elucidate this dependency. It should also be noted the shape of the drops were not investigated, only whether a single drop jetted out of the nozzle and consistent, uniform tablets were formed.

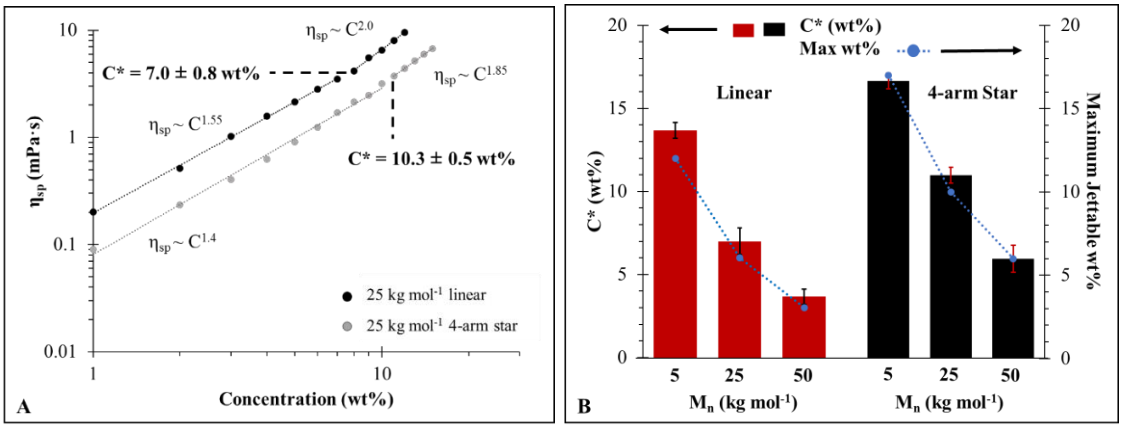

Figure 7.3. (A) Zero shear viscosity as a function of concentration where the dashed line denotes the critical overlap concentration (*C**) **(B)** *C** and the maximum jettable wt% of PVP as a function of M_n and polymer architecture.

7.4.3 Binder Jetting

The optimal ratio of lactose and powdered sugar was initially chosen based on a tradeoff between powder spreadability and printed tablet strength. Preliminary experiments consisting of varying powdered sugar to lactose ratios (0 to 40 wt%) with a constant binder

formulation (5 wt% commercially available 40k linear PVP, 2 wt% Tween 20®) revealed a 4:1 lactose:powdered sugar wt:wt combination provided reproducible spreadability and tablet strength. Incorporation of > 40 wt% powdered sugar resulted in particle aggregation while spreading, and < 20 wt% powdered sugar resulted in tablets exhibiting crushing strengths of < 0.1 MPa. Particle sizes of powdered sugar range from 5-30 μm (**Figure S7.2B**) and particles below 25 μm tended to disrupt flow due to surface energy of the particles.[45] Each successfully printed binder did not produce layer shifting at 100% saturation. Measurements of thickness and diameter of each printed tablet confirmed a less than 5%-dimensional error in each direction of each combination printed. This consistency is extremely important to achieve exact personalized dosage tablets.

7.4.4 Tablet Physical Properties

Tablets for oral personalized dosage pharmaceuticals must maintain compressive strengths above 0.4 MPa to maintain fidelity during possible recoating processes and to survive packaging and handling.[46] **Figure 7.4** depicts the results of compression strength experiments aimed to elucidate the relationships between tablet compressive strength and compressive modulus with polymeric binder M_n's, polymer wt% in the binders, and polymer architectures (**Table S7.2**). **Figure 7.4A** shows the compressive strength of the printed tablets as a function of linear and 4-arm star PVP M_n. Because this experiment aims to compare M_n's, the examples chosen were all printed with 3 wt% PVP in the formulation as higher M_n in some systems produced non-jettable solution viscosities. For both linear and 4-arm star examples, there existed a statistical difference between the compressive strength of tablets printed with 5 kg mol^{-1} and 25 kg mol^{-1} PVP, and 5 kg mol^{-1} and 50 kg mol^{-1} PVP. These relationships revealed a dependence of M_n on tablet compressive strength

as tablets containing 25 and 50 kg mol^{-1} PVP facilitated a stronger tablet than the 5 kg mol^{-1} PVP samples.

Figure 7.4B depicts the compressive strength of printed tablets as a function of wt% PVP in the binder formulations. In each linear and 4-arm star example, there existed a statistical difference between tablet compressive strength with increasing PVP wt% in the binders. These relationships revealed a dependence of wt% PVP in the binder formulations on the tablet compressive strength. Because of viscosity constraints, only 5 kg mol^{-1} linear, 5 kg mol^{-1} 4-arm star, and 25 kg mol^{-1} 4-arm star PVP were jetted at all three concentrations. Moreover, it should be noted the highest compressive strength achieved in this study (1.2 MPa) arose from a binder formulation using 25 kg mol^{-1} 4-arm star PVP at 9 wt% in DI water. As discussed previously, 25 kg mol^{-1} 4-arm star PVP-containing binders were able to print at 9 wt% and 25 kg mol^{-1} linear PVP was not because of C^* values. Above C^*, the solution became viscoelastic and the chains began to overlap, resulting in the requirement of a higher shear rate to enable jetting of the solution.

Figure 7.4C depicts the linear relationships that arose between the compressive strength and compressive modulus as a function of wt% polymer in each binder formulation. As discussed previously, with increasing wt% polymer, the compressive strength and modulus increased. **Figure 7.4D** compares tablet compressive strengths using linear and 4-arm PVP architectures at the same molecular weights all containing 3 wt% polymer in the binder formulations. This data revealed there was no dependence on polymer architecture alone on the tablet compressive strength. The 4-arm star architecture remained important because of its ability to jet at higher concentrations compared to linear polymers at the same molecular weight.

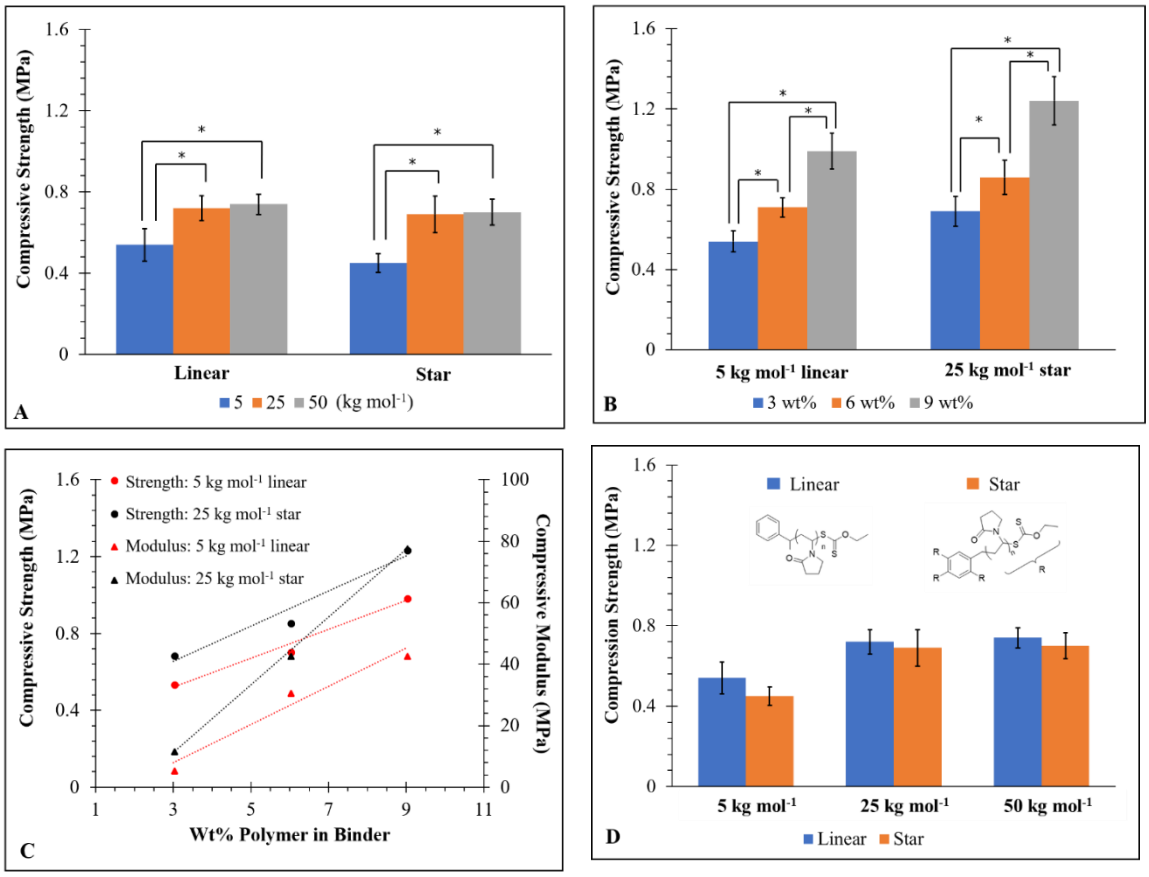

Figure 7.4. (A) Compressive strength of linear and 4-arm star PVP as a function of molecular weight and **(B)** wt%. **(C)** Compressive strength and compressive modulus as a function of wt% polymeric binder. **(D)** Compressive strength as a function of polymer architecture.

Figure 7.5 depicts the relationship between porosity and wt% polymer in the binder composition using 5 kg mol^{-1} linear PVP and 25 kg mol^{-1} 4-arm star PVP as representative examples. In both cases, statistical differences existed between each wt%, indicating a decrease in porosity with increasing wt%. Across all samples, the porosity ranged from 71 to 65%, which is common for binder jetted parts.[22] As a comparison, tablets made through direct compression maintain porosities of 7 to 51%, but do not function as immediate

release tablets.[47] Binder jetted tablets, which usually exhibit porosities from 50 to 80%, provide tablets with sufficient surface area to dissolve immediately. As described previously, the compressive strength and compressive modulus increased with increasing wt% polymer. Increasing the polymeric binder in the composition resulted in decreasing void spaces, which has previously been shown to increase strength of porous materials.[48]

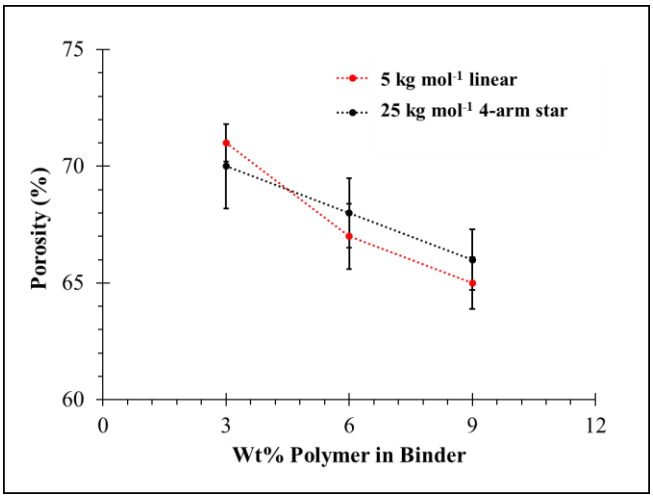

Figure 7.5. Porosity of binder jetted tablets as a function of wt% PVP in each binder composition.

7.4.5 Addition of API

The tablets were intended to provide an immediate release profile, which is common for oral tablets from binder jetting AM. A synergy between high porosity, water-soluble excipients, and water-soluble binders suggested this system as a candidate for immediate release systems. Adding API into the binder provides low-dose tablets with very selective placement of API where API in the powder combinations enables a higher loading. The chosen API, acetaminophen, was combined into the powder system and maintained particle sizes ranging from 5 to 150 μm (**Figure S7.2C**), which could affect tablet dimensional reproducibility and strength. To demonstrate a wide range of API inclusion

and a maintenance of tablet strength and fidelity, various levels of API were introduced into the powder systems.

The addition of 5, 10, 25 and 50 wt% acetaminophen to the powder mixture enabled the printing of API-loaded tablets. The selected API loading amounts demonstrated the ability for this system to function as a candidate for personalized pharmaceuticals. In the future, pharmacies could maintain 3D printers in local offices to fill personalized prescriptions for people of all ages and sizes with multiple medications in each tablet. Each tablet discussed in this system exhibited an average total weight of 200 mg, where API loading of 5, 10, 25, and 50 wt% acetaminophen corresponds to 10, 20, 50, and 100 mg respectively. **Figure 7.6A** depicts the comparison of the theoretical and measured API content in each tablet to ensure consistent and accurate dosing between tablets. ^{1}H NMR spectroscopy of the tablet content revealed the actual amount of the API in each tablet were within a 3% difference of the theoretical values, which asserted feasibility in 3D printed pharmaceuticals.

The varying wt% API showed consistent and agreeable dimensional accuracy and compressive strength compared to tablets without API. Measurements of thickness and diameter revealed an average thickness of 3.12 ± 0.11 mm and average diameter of 12.14 ± 0.15 mm, which confirmed retention of dimensional accuracy. **Figure 7.6B** depicts the compressive strength and modulus as a function of API loading, which elucidated the maintenance of strength with API inclusion. Tablets with 5-50 wt% API maintain the statistically equivalent strength as tablets without API. A statistical difference in theoretical and measured API amounts existed between the non-API containing tablet and the sample

with 50 wt% API possibly due to the large range of API particle sizes creating inconsistent layer spreading and possibly resulting in more void space.

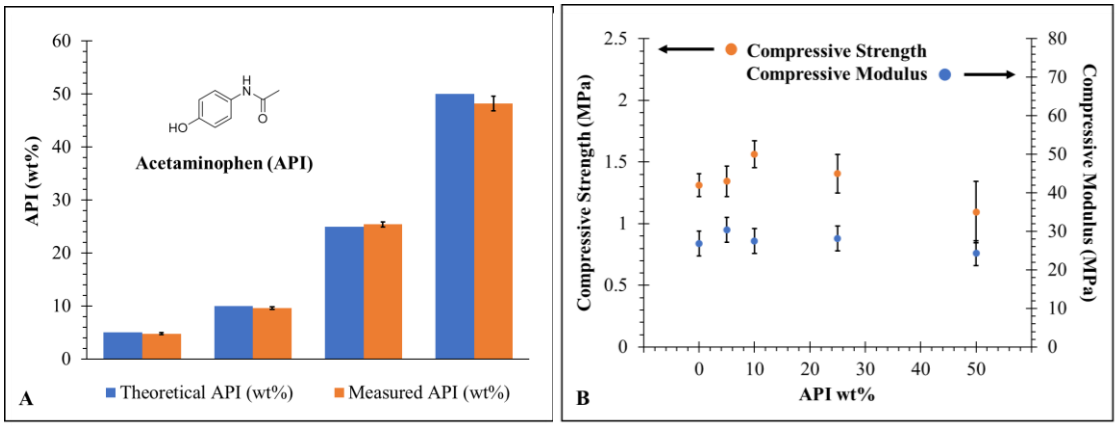

Figure 7.6. (A) Theoretical and measured API in printed tablets and **(B)** compressive strength and modulus as a function of acetaminophen loading at 5, 10, 25, and 50 wt% using 6 wt% 25 kg mol^{-1} 4-arm star PVP in DI water as the binder composition.

Water dissolution of each tablet combination, with and without API, revealed each sample dissolved in below 30 s (**Table S7.3**), which is consistent with immediate release tablets.[49] The samples without API did not show a trend related to concentration of polymer in the binder, architecture of the polymers, or molecular weight of the polymers. Considering lactose and powdered sugar are readily water-soluble, the powder properties combined with the high porosity morphology mostly dominated the dissolution times. An equivalent experiment of API loaded tablets revealed each tablet dissolved in less than 30 s, and there existed a statistical difference in dissolution times between 5 wt% and 50 wt% API loading. Acetaminophen is only slightly soluble in cold water[50], therefore breakup of the tablet into individual particles denoted dissolution. The tablets containing 5 wt% and 50 wt% loading dissolved in 12 and 28 s, respectively, where the hydrophobicity of the

API mainly contributed to the dissolution rates. In the future to achieve a range of dissolution rates, more hydrophobic powders and higher wt% loading of an adhesive agent into the binders will be used.

7.4.6 Printed Tablet Imaging

Figures 7.7A, B, C and 7.**7D, E, F** depict images and SEM images of binder jetted tablets with the same binder, 6 wt% 25 kg mol^{-1} 4-arm star PVP, and powder combinations of 4:1 lactose:powdered sugar and 10:75:15 acetaminophen:lactose:powdered sugar (10 wt% API), respectively. On a macroscopic scale as depicted in **Figures 7.7A** and 7.**7B**, the two tablets had similar appearances. **Figures 7.7B** and **7.7E** depict SEM images of the surfaces of binder jetted tablets. Both surfaces appear similar where surface roughness is apparent. **Figures 7.7C** and **7.7F** depict SEM images of freeze-fractured, cross-sectional areas of each tablet. Both images reveal void spaces within the tablets, which agreed with quantitative porosity calculations.

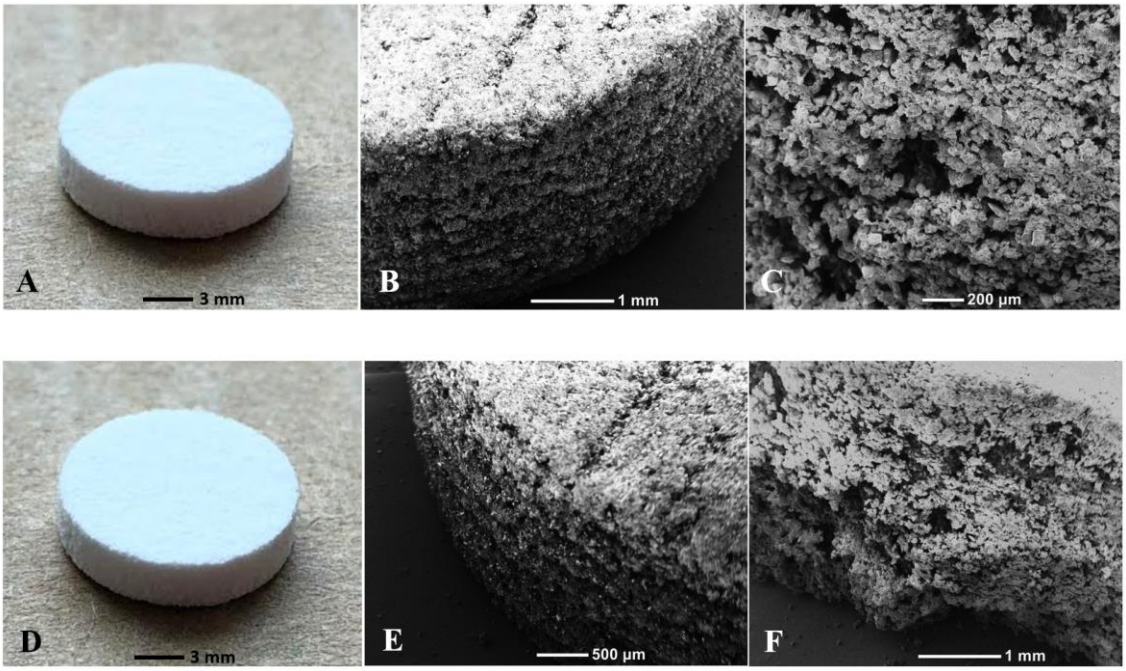

Figure 7.7. (A) Image of a binder jetted tablet with 5:1 lactose:powdered sugar with 6 wt% 25 kg mol^{-1} 4-arm star PVP. **(B)** SEM image of the tablet surface at 24x magnification and **(C)** a SEM image of the freeze-fractured cross-sectional area at 60x magnification. **(D)** Image of a binder jetted tablet with 10:75:15 acetaminophen/lactose/powdered sugar with 6 wt% 25 kg mol^{-1} 4-arm star PVP. **(E)** SEM image of the tablet surface at 30x magnification and **(F)** a SEM image of the freeze-fractured cross-sectional area at 24x magnification.

7.5 Conclusion

The development of AM of personalized dosage pharmaceuticals has the potential to revolutionize manufacturing of oral tablets, but improvements are still required. Currently, the field of binder jetting AM for tablets is limited due to the lack of literature on polymeric binders other than commercially available options. This investigation of linear and 4-arm star PVP architectures, molecular weights, and polymer concentration effects on tablets physical properties aims to not only expand the materials toolbox for binder jetting AM, but also elucidate structure-property relationships between molecular structures and printed parts. While M_n above 25 kg mol^{-1} polymers increased tablet compressive strength, the largest factor in increasing compressive strength was an increase in polymer concentration in the binder compositions. Star PVP with 4 arms printed at the highest concentration compared to linear analogs at the same M_n because of decreased solution viscosity and increased C^* in DI water. The results of this study not only elucidated the relationships between polymer solution properties and jettability on a thermal printhead, but also indicated these materials are strong candidates for future personalized dosage pharmaceuticals.

7.6 Acknowledgements

The authors would like to thank Candace Wall, Dr. Charles Carfagna, and Ashwath Kumar for conducting surface tension experiments, conducting aqueous SEC experiments, and helpful binder jetting AM discussions, respectively.

Supporting Information

Supporting information includes comprehensive tables and summaries of all data collected in this manuscript including SEC-MALS, solution rheology, compression, and water dissolution data.

7.7 References

(1) Yu, D. G.; Zhu, L.-M.; Branford-White, C. J.; Yang, X. L. Three-Dimensional Printing in Pharmaceutics: Promises and Problems. *J. Pharm. Sci.* **2008**, *97* (9), 3666–3690. https://doi.org/10.1002/jps.21284.

(2) Moulton, S. E.; Wallace, G. G. 3-Dimensional (3D) Fabricated Polymer Based Drug Delivery Systems. *J. Control. Release* **2014**, *193*, 27–34. https://doi.org/10.1016/J.JCONREL.2014.07.005.

(3) Cohen, J. S. Ways to Minimize Adverse Drug Reactions. *Postgrad. Med.* **1999**, *106* (3), 163–172. https://doi.org/10.3810/pgm.1999.09.688.

(4) Raijada, D.; Genina, N.; Fors, D.; Wisaeus, E.; Peltonen, J.; Rantanen, J.; Sandler, N. A Step Toward Development of Printable Dosage Forms for Poorly Soluble Drugs. *J. Pharm. Sci.* **2013**, *102* (10), 3694–3704. https://doi.org/10.1002/JPS.23678.

(5) Prasad, L. K.; Smyth, H. 3D Printing Technologies for Drug Delivery: A Review. *Drug Dev. Ind. Pharm.* **2016**, *42* (7), 1019–1031. https://doi.org/10.3109/03639045.2015.1120743.

(6) rebuffs Monsanto, S. First 3D-Printed Pill. *Nature* **2015**, *33*, 1014.

(7) Derby, B. Inkjet Printing Ceramics: From Drops to Solid. *J. Eur. Ceram. Soc.* **2011**, *31* (14), 2543–2550. https://doi.org/10.1016/J.JEURCERAMSOC.2011.01.016.

(8) Fromm, J. E. Numerical Calculation of the Fluid Dynamics of Drop-on-Demand Jets. *IBM J. Res. Dev.* **1984**, *28* (3), 322–333. https://doi.org/10.1147/rd.283.0322.

(9) Reis, N.; Ainsley, C.; Derby, B. Ink-Jet Delivery of Particle Suspensions by Piezoelectric Droplet Ejectors. *J. Appl. Phys.* **2005**, *97* (9), 094903.

https://doi.org/10.1063/1.1888026.

(10) Hon, K. K. B.; Li, L.; Hutchings, I. M. Direct Writing Technology—Advances and Developments. *CIRP Ann.* **2008**, *57* (2), 601–620. https://doi.org/10.1016/J.CIRP.2008.09.006.

(11) Friederich, A.; Binder, J. R.; Bauer, W. Rheological Control of the Coffee Stain Effect for Inkjet Printing of Ceramics. *J. Am. Ceram. Soc.* **2013**, *96* (7), 2093–2099. https://doi.org/10.1111/jace.12385.

(12) Jang, D.; Kim, D.; Moon, J. Influence of Fluid Physical Properties on Ink-Jet Printability. *Langmuir* **2009**, *25* (5), 2629–2635. https://doi.org/10.1021/la900059m.

(13) Mckinley, G. H. *Dimensionless Groups For Understanding Free Surface Flows of Complex Fluids*; 2005.

(14) Özkol, E.; Ebert, J.; Telle, R. An Experimental Analysis of the Influence of the Ink Properties on the Drop Formation for Direct Thermal Inkjet Printing of High Solid Content Aqueous 3Y-TZP Suspensions. *J. Eur. Ceram. Soc.* **2010**, *30* (7), 1669–1678. https://doi.org/10.1016/J.JEURCERAMSOC.2010.01.004.

(15) Nallan, H. C.; Sadie, J. A.; Kitsomboonloha, R.; Volkman, S. K.; Subramanian, V. Systematic Design of Jettable Nanoparticle-Based Inkjet Inks: Rheology, Acoustics, and Jettability. *Langmuir* **2014**, *30* (44), 13470–13477. https://doi.org/10.1021/la502903y.

(16) Liu, Y.; Derby, B. Experimental Study of the Parameters for Stable Drop-on-Demand Inkjet Performance. *Phys. Fluids* **2019**, *31* (3), 032004. https://doi.org/10.1063/1.5085868.

(17) Hoath, S. D.; Harlen, O. G.; Hutchings, I. M. Jetting Behavior of Polymer Solutions in Drop-on-Demand Inkjet Printing. *J. Rheol. (N. Y. N. Y).* **2012**, *56* (5), 1109–1127. https://doi.org/10.1122/1.4724331.

(18) Vadillo, D. C.; Tuladhar, T. R.; Mulji, A. C.; Jung, S.; Hoath, S. D.; Mackley, M. R. Evaluation of the Inkjet Fluid's Performance Using the "Cambridge Trimaster" Filament Stretch and Break-up Device. *J. Rheol. (N. Y. N. Y).* **2010**, *54* (2), 261–282. https://doi.org/10.1122/1.3302451.

(19) Hoath, S. D.; Vadillo, D. C.; Harlen, O. G.; McIlroy, C.; Morrison, N. F.; Hsiao, W.-K.; Tuladhar, T. R.; Jung, S.; Martin, G. D.; Hutchings, I. M. Inkjet Printing of Weakly Elastic Polymer Solutions. *J. Nonnewton. Fluid Mech.* **2014**, *205*, 1–10. https://doi.org/10.1016/J.JNNFM.2014.01.002.

(20) Katstra, W. .; Palazzolo, R. .; Rowe, C. .; Giritlioglu, B.; Teung, P.; Cima, M. . Oral Dosage Forms Fabricated by Three Dimensional Printing™. *J. Control. Release* **2000**, *66* (1), 1–9. https://doi.org/10.1016/S0168-3659(99)00225-4.

(21) Rowe, C. .; Katstra, W. .; Palazzolo, R. .; Giritlioglu, B.; Teung, P.; Cima, M. . Multimechanism Oral Dosage Forms Fabricated by Three Dimensional Printing™. *J. Control. Release* **2000**, *66* (1), 11–17. https://doi.org/10.1016/S0168-3659(99)00224-2.

(22) Patirupanusara, P.; Suwanpreuk, W.; Rubkumintara, T.; Suwanprateeb, J. Effect of

Binder Content on the Material Properties of Polymethyl Methacrylate Fabricated by Three Dimensional Printing Technique. *J. Mater. Process. Technol.* **2008**, *207* (1–3), 40–45. https://doi.org/10.1016/J.JMATPROTEC.2007.12.058.

(23) Kilb, R. W.; Bueche, A. M. Solution and Fractionation Properties of Graft Polymers. *J. Polym. Sci.* **1958**, *28* (117), 285–294. https://doi.org/10.1002/pol.1958.1202811704.

(24) N. Hadjichristidis, M. P., Hermis Iatrou, P. Driva, M. Chatzichristidi, Georgios Sakellariou, D. J. Lohse. No Title. *Encyclopedia Of Polymer Science and Technology*; Wiley and Sons Inc., 2010.

(25) de Gans, B.-J.; Xue, L.; Agarwal, U. S.; Schubert, U. S. Ink-Jet Printing of Linear and Star Polymers. *Macromol. Rapid Commun.* **2005**, *26* (4), 310–314. https://doi.org/10.1002/marc.200400503.

(26) Nguyen, T. L. U.; Eagles, K.; Davis, T. P.; Barner-Kowollik, C.; Stenzel, M. H. Investigation of the Influence of the Architectures of Poly(Vinyl Pyrrolidone) Polymers Made via the Reversible Addition–Fragmentation Chain Transfer/Macromolecular Design via the Interchange of Xanthates Mechanism on the Stabilization of Suspension Polymerizations. *J. Polym. Sci. Part A Polym. Chem.* **2006**, *44* (15), 4372–4383. https://doi.org/10.1002/pola.21518.

(27) Boyer, C.; Bulmus, V.; Davis, T. P.; Ladmiral, V.; Liu, J.; Perrier, S. Bioapplications of RAFT Polymerization. *Chem. Rev.* **2009**, *109* (11), 5402–5436. https://doi.org/10.1021/cr9001403.

(28) Lowe, A. B.; McCormick, C. L. Reversible Addition–Fragmentation Chain Transfer (RAFT) Radical Polymerization and the Synthesis of Water-Soluble (Co)Polymers under Homogeneous Conditions in Organic and Aqueous Media. *Prog. Polym. Sci.* **2007**, *32* (3), 283–351. https://doi.org/10.1016/J.PROGPOLYMSCI.2006.11.003.

(29) Nicolas, J.; Mantovani, G.; Haddleton, D. M. Living Radical Polymerization as a Tool for the Synthesis of Polymer-Protein/Peptide Bioconjugates. *Macromol. Rapid Commun.* **2007**, *28* (10), 1083–1111. https://doi.org/10.1002/marc.200700112.

(30) Coote*, M. L. Ab Initio Study of the Addition−Fragmentation Equilibrium in RAFT Polymerization: When Is Polymerization Retarded? **2004**. https://doi.org/10.1021/MA049444W.

(31) Roovers, J. Dilute Solution Properties of Regular Star Polymers. *Plast. Eng.* **1999**, *53*, 285–341.

(32) Ronda Plummer; David J. T. Hill, and; Whittaker*, A. K. Solution Properties of Star and Linear Poly(N-Isopropylacrylamide). **2006**. https://doi.org/10.1021/MA0614545.

(33) Ozkol, E. €. Rheological Characterization of Aqueous 3Y-TZP Inks Optimized for Direct Thermal Ink-Jet Printing of Ceramic Components. **2013**. https://doi.org/10.1111/jace.12285.

(34) Tekin, E.; Smith, P. J.; Schubert, U. S. Inkjet Printing as a Deposition and

Patterning Tool for Polymers and Inorganic Particles. *Soft Matter* **2008**, *4* (4), 703. https://doi.org/10.1039/b711984d.

(35) Tirtaatmadja, V.; McKinley, G. H.; Cooper-White, J. J. Drop Formation and Breakup of Low Viscosity Elastic Fluids: Effects of Molecular Weight and Concentration. *Phys. Fluids* **2006**, *18* (4), 043101. https://doi.org/10.1063/1.2190469.

(36) de Gans, B.-J.; Duineveld, P. C.; Schubert, U. S. Inkjet Printing of Polymers: State of the Art and Future Developments. *Adv. Mater.* **2004**, *16* (3), 203–213. https://doi.org/10.1002/adma.200300385.

(37) Matthew G. McKee; Matthew T. Hunley; John M. Layman, and; Long*, T. E. Solution Rheological Behavior and Electrospinning of Cationic Polyelectrolytes. **2005**. https://doi.org/10.1021/MA051786U.

(38) Matthew G. McKee, †; Garth L. Wilkes, ‡; Ralph. H. Colby, § and; Timothy E. Long*, †. Correlations of Solution Rheology with Electrospun Fiber Formation of Linear and Branched Polyesters. **2004**. https://doi.org/10.1021/MA035689H.

(39) Gupta, P.; Elkins, C.; Long, T. E.; Wilkes, G. L. Electrospinning of Linear Homopolymers of Poly(Methyl Methacrylate): Exploring Relationships between Fiber Formation, Viscosity, Molecular Weight and Concentration in a Good Solvent. *Polymer (Guildf).* **2005**, *46* (13), 4799–4810. https://doi.org/10.1016/J.POLYMER.2005.04.021.

(40) Colby, R. H.; Fetters, L. J.; Funk, W. G.; Graessley, W. W. *Effects of Concentration and Thermodynamic Interaction on the Viscoelastic Properties of Polymer Solutions*; 1991; Vol. 24.

(41) Polymer, W. G.-; 1980, undefined. Polymer Chain Dimensions and the Dependence of Viscoelastic Properties on Concentration, Molecular Weight and Solvent Power. *Elsevier*.

(42) Wendy E. Krause, †; Enrico G. Bellomo, ‡ and; Ralph H. Colby*, ‡. Rheology of Sodium Hyaluronate under Physiological Conditions. **2001**. https://doi.org/10.1021/BM0055798.

(43) Hoath, S. D.; Hutchings, I. M.; Martin, G. D.; Tuladhar, T. R.; Mackley, M. R.; Vadillo, D. Links Between Ink Rheology, Drop-on-Demand Jet Formation, and Printability. *J. Imaging Sci. Technol.* **2009**, *53* (4), 041208. https://doi.org/10.2352/J.ImagingSci.Technol.2009.53.4.041208.

(44) EL Aferni, A.; Guettari, M.; Tajouri, T. Effect of Polymer Conformation on Polymer-Surfactant Interaction in Salt-Free Water. *Colloid Polym. Sci.* **2016**, *294* (7), 1097–1106. https://doi.org/10.1007/s00396-016-3869-8.

(45) Ziegelmeier, S.; Christou, P.; Wöllecke, F.; Tuck, C.; Goodridge, R.; Hague, R.; Krampe, E.; Wintermantel, E. An Experimental Study into the Effects of Bulk and Flow Behaviour of Laser Sintering Polymer Powders on Resulting Part Properties. *J. Mater. Process. Technol.* **2015**, *215*, 239–250. https://doi.org/10.1016/J.JMATPROTEC.2014.07.029.

(46) Shabana, M. A Review on the Quality Control Analysis of Oral Dosage Form: Tablets. *Res. Rev. J. Pharm. Pharm. Sci.* **2016**, *5* (2), 108–114.

(47) Hancock, B. C.; Colvin, J. T.; Mullarney, M. P.; Zinchuk, A. V. *The Relative Densities of Pharmaceutical Powders, Blends, Dry Granulations, and Immediate-Release Tablets*; 2003.

(48) Lorna J. Gibson, M. F. A. *Cellular Solids: Structure and Properties - Lorna J. Gibson, Michael F. Ashby - Google Books*; Pergamon Press, 1999.

(49) Garg, G.; Siddiqui, M. N.; Sharma, K. *Fast Dissolving Tablets: Preparation, Characterization and Evaluation: An Overview*; 2010; Vol. 4.

(50) and, R. A. G.; Rasmuson*, Å. C. Solubility of Paracetamol in Pure Solvents. **1999**. https://doi.org/10.1021/JE990124V.

7.8 Supplemental

Table S7.1. Summary of Aqueous SEC data of linear and 4-arm star polyvinylpyrrolidone (PVP).

Topology	M_n (kg mol^{-1})	M_w (kg mol^{-1})	Đ
Linear	5.1	5.7	1.12
Linear	24.6	26.6	1.08
Linear	48.8	55.6	1.14
4-Arm Star	4.8	5.5	1.14
4-Arm Star	25.2	27.5	1.09
4-Arm Star	49.5	54.9	1.11

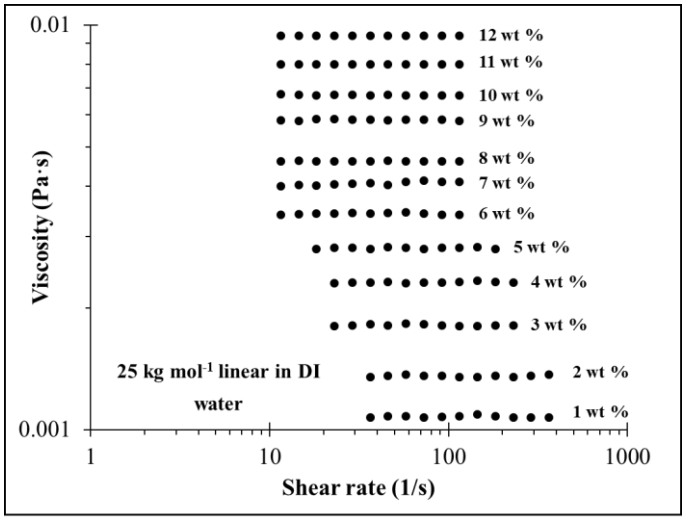

Figure S7.1. Steady-state shear sweeps of 25 kg mol^{-1} linear PVP from 1 to 12 wt% in DI water.

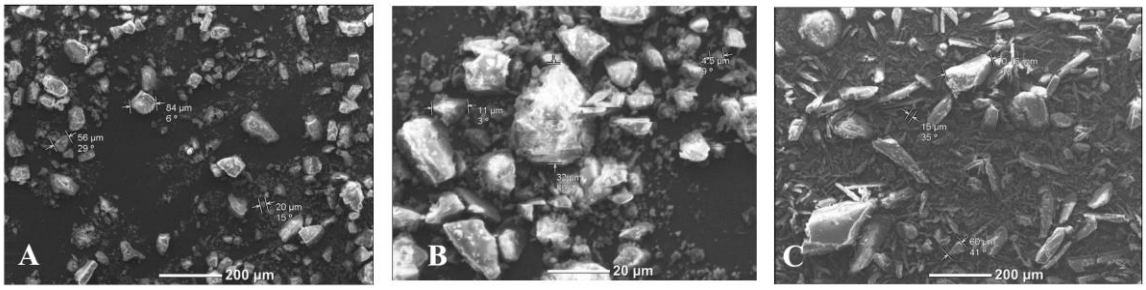

Figure S7.2. SEM images of **(A)** lactose, **(B)** powdered sugar, **(C)** and acetaminophen.

Table S7.2. Physical properties summary of jettable linear and 4-arm star PVP combinations.

Topology	Targeted M_n (kg mol^{-1})	Concentration (wt%)	Compressive strength (MPa)
Linear	5	3	0.54 ± 0.05
Linear	5	6	0.71 ± 0.05
Linear	5	9	0.99 ± 0.09
4-Arm Star	5	3	0.43 ± 0.05
4-Arm Star	5	6	0.67 ± 0.08
4-Arm Star	5	9	0.97 ± 0.13
Linear	25	3	0.72 ± 0.06
Linear	25	6	1.01 ± 0.09
4-Arm Star	25	3	0.69 ± 0.07
4-Arm Star	25	6	0.86 ± 0.09
4-Arm Star	25	9	1.24 ± 0.11
Linear	50	3	0.74 ± 0.07
4-Arm Star	50	3	0.70 ± 0.06
4-Arm Star	50	6	0.96 ± 0.15

Table S7.3. Water dissolution summary of jettable tablets with and without API.

Topology/MW (kg mol^{-1})	API in powder (wt%)	Concentration in binder (wt%)	Dissolution Time (s)
Linear/5	0	3	24 ± 13
Linear/5	0	6	20 ± 14
Linear/5	0	9	12 ± 12
4-Arm Star/5	0	3	19 ± 13
4-Arm Star/5	0	6	13 ± 11
4-Arm Star/5	0	9	19 ± 10
Linear/25	0	3	10 ± 8
Linear/25	0	6	22 ± 12
4-Arm Star/25	0	3	21 ± 12
4-Arm Star/25	0	6	13 ± 10
4-Arm Star/25	0	9	22 ± 12
Linear/50	0	3	20 ± 11
4-Arm Star/50	0	3	14 ± 11
4-Arm Star/50	0	6	13 ± 9
4-Arm Star/25	5	6	12 ± 9
4-Arm Star/25	10	6	18 ± 12
4-Arm Star/25	25	6	24 ± 13
4-Arm Star/25	50	6	28 ± 9

Chapter 8: Thiol-Ene Addition Enables Tailored Synthesis of Poly(2-oxazoline)-*graft*- Poly(vinyl pyrrolidone) Copolymers for Binder Jetting 3D Printing

Emily M. Wilts and Timothy E. Long*

(Published in *Polymer International*, **2020**)

Department of Chemistry, Macromolecules Innovation Institute, Virginia Tech, Blacksburg, VA 24061

8.1 Abstract

The rising popularity of graft copolymers manifests from unique solution properties and potential for a myriad of biomedical applications. Poly(vinyl pyrrolidone) (PVP) is an amorphous, water-soluble polymer used for polymeric adhesives for binder jetting additive manufacturing, fillers in cosmetic products, and subcutaneous drug delivery systems. This work describes the synthesis of graft poly(2-oxazoline) and PVP copolymers using "grafting to" methodology and thiol-ene 'click' chemistry. Copolymerization of 2-methyl-2-oxazoline and 2-(3-butenyl)-2-oxazoline formed vinyl grafting sites at a controlled absolute molecular weight. In a separate reaction, reversible addition fragmentation transfer (RAFT) polymerization and subsequent aminolysis yielded defined, oligomeric, thiol-terminated PVP. Thiol-ene 'click' chemistry facilitated the formation of poly(2-oxazoline)-*graft*-poly(vinyl pyrrolidone) (PMeOx-*g*-PVP) at varying mol % grafting sites and PVP graft length. ^{1}H NMR spectroscopy, aqueous SEC-MALS, and bromine titrations confirmed chemical structure and differential scanning calorimetry (DSC) and thermogravimetric analysis (TGA) elucidated thermal transitions. Aqueous SEC-MALS and ^{1}H NMR also determined number- and weight-average molecular weight and average grafting percentages, which helped determine optimal reaction conditions. Zero-shear viscosities of 5 and 10 wt % solutions in DI water of each graft copolymer compared to

their linear analogs revealed a 31% decrease in viscosity at the same number-average molecular weight. This large decrease in solution viscosity deemed PMeOx-*g*-PVP compositions as potential candidates for binder jetting additive manufacturing.

8.2 Introduction

'Click' chemistry is a class of reactions used for linear polymerization, crosslinking, and the fabrication of complex polymer architectures.[1,2] These reactions commonly facilitate the production of graft copolymers, consisting of a linear backbone and ordered or random branches. Click-type chemistry enables "grafting to" methodology to produce graft copolymers where azide-alkyne or thiol-ene reaction pairs covalently attach branches onto polymer backbones.[2–4] As an example, Demirci *et. al.* synthesized (polystyrene-*g*-poly(ε-caprolactone) and poly(vinyl chloride)-*g*-poly(ε-caprolactone)) using azide-alkyne methodologies resulting in a miscible copolymer containing a single T_g and even grafting distribution.[5] Thermoplastic elastomers, impact resistant materials, self-assembled micelles, and stabilizers for emulsion-type polymerization methods represent common applications for graft copolymers.[6–9] Graft copolymers are also used in some biomedical applications, but development of new compositions and functions is still needed.[10,11]

Poly(2-oxazoline)s and poly(vinyl pyrrolidone) (PVP) are two groups of water-soluble polymers used for drug delivery, solution-based therapeutics, and other biomedical applications.[12–14] Linear PVP between 2.5 and 1000 kg mol^{-1} are non-toxic below 100 mg kg^{-1} if ingested and are thermally, chemically, and pH stable. In pharmaceuticals, PVP acts as binders, coatings, disintegrating agents, and stabilizers. Other applications include fillers for cosmetics and stabilizers for two-phase polymerization methods.[14] Poly(2-oxazoline)s

represent a group of polymers used for subcutaneous drug delivery and a myriad of other biomedical applications.[15,16] The synthetic tunability of poly(2-oxazoline)s in concert with the non-toxic and water solubility properties of both compositions render a graft copolymer combination potentially relevant in biomedical applications.

Applications of water-soluble graft copolymers include improving mechanical properties of binder jetted (BJ) additively manufactured (AM) parts and stabilizing suspension polymerization processes. Binder jetting additive manufacturing (BJ AM) is a powder-bed system where adhesive binder ejects onto a powder surface to create layers.[17–19] When using polymeric binders for BJ AM, higher concentrations of polymer in the binder lead to filling void spaces in the powder matrix, resulting in higher compressive strengths.[20,21] As number-average molecular weight (M_n) and concentration of polymers in solution increases, solution viscosity increases, which eventually reaches viscosity limits for inkjet systems. Varying architectures, such as star or graft polymers, experience lower solution viscosities compared to linear analogs at the same M_n. [22,23] Wilts *et. al.* compared linear and 4-arm star PVP for BJ AM polymeric binders and found 25 kg mol^{-1} 4-arm star PVP printed at 9 wt %, a higher concentration compared to 25 kg mol^{-1} linear PVP, to produce stronger tablets for personalized dosage pharmaceuticals. Building on this work, designed graft copolymers could provide even lower solution viscosities compared to 4-arm star analogs to achieve higher polymer concentrations in the binder and stronger printed parts.[21] Another potential application of graft PVP is as a stabilizer in suspension polymerization.[24,25] Stenzel *et. al.* showed 4-arm star PVP lowered the interfacial tension between water and monomer droplets, resulting in a more stable suspension and more

uniform drops compared to linear analogs, where graft polymers may also have this effect.[26]

This paper describes the synthetic methods of PMeOx-*g*-PVP graft copolymers using 5, 10 and 25 mol % grafting sites with 2.5 and 5 kg mol^{-1} PVP grafts. Cationic ring-opening polymerization yielded a poly(2-oxazoline) backbone containing vinyl grafting sites, and RAFT polymerization with subsequent aminolysis yielded thiol-terminated PVP. Aqueous SEC-MALS and bromine titrations confirmed grafting percentages where the higher mol % grafting sites led to lower conversion of vinyl groups. Kinetic studies exploring type of initiator, initiator concentration, time of UV light exposure, and thiol equivalent compared to the vinyl moieties revealed optimal reaction conditions for the thiol-ene grafting reaction. Thermal analysis using differential scanning calorimetry (DSC) revealed differences in glass transition temperatures (T_g) between varying graft copolymer compositions and differences compared to Fox T_g estimations. Finally, solution rheology experiments of graft copolymers in DI water revealed an average 31% decrease in solution viscosity compared to linear PVP analogs of the same M_n. The large decrease in solution viscosity could render this system advantageous for BJ AM or stabilizers for suspension polymerization.

8.3 Experimental

8.3.1 Materials

Diisopropylamine and methyl oxazoline were purchased from Sigma Aldrich and distilled over calcium hydride before use. *N*-butyl-lithium, allyl bromide, methyl triflate, piperidine, vinyl pyrrolidone, *O*-ethyl xanthic acid potassium salt, silver nitrate, sodium hydroxide,

and 1-bromo ethyl benzene were purchased from Sigma Aldrich and used without further purification. Saturated bromine water was purchased from ITW Reagents and diluted with DI water to 0.1 M before use. Azobisisobutyronitrile (AIBN) was purchased from Sigma Aldrich and recrystallized over methanol before use. Extra dry acetonitrile, chloroform, tetrahydrofuran, dichloromethane, methanol, pyridine and acetone were purchased from Acros and used without further purification.

8.3.2 2-(3-butenyl)-2-oxazoline (EneOx) synthesis

2-(3-butenyl)-2-oxazoline was prepared through a synthesis reported by Hoogenboom et. al.[27] Briefly, a fresh LDA solution was prepared through dropwise addition of *n*-butyl-lithium (2.5 M, 44.7 mL, 0.11 mol, 0.95 eq.) to diisopropylamine (16.5 mL, 0.12 mol, 1 eq.) in dry THF at -78 ^{o}C and stirred for 1 h. Next, 2-methyl-2-oxazoline (MeOx) (10.0 g, 0.12 mol, 1 eq.) was added dropwise to the LDA solution and stirred for 1 h. Allyl bromide (9.1 mL, 0.105 mol, 0.9 eq.) was then added dropwise and the solution was brought to room temperature and allowed to stir for 24 h. The reaction was quenched with methanol, the solvents were removed under reduced pressure, and the residual was dissolved in dichloromethane. The solution was washed three times with water and twice with brine. Before use, the product was vacuum distilled (3 mbar, 70 ^{o}C) to produce a clear liquid at 61% yield. The structure was confirmed using ^{1}H and ^{13}C NMR spectroscopy and mass spectroscopy. ^{1}H NMR (400 MHz, $CDCl_3$): 2.27 (4H, s), 3.70 (2H, t), 4.16 (2H, t), 4.95-5.10 (2H, m), 5.80-5.87 (1H, m). ^{13}C NMR (400 MHz, $CDCl_3$): 26.6, 29.4, 53.9, 66.6, 115.0, 137.2, 166.1. Mass spectroscopy, expected: 41.09310 g mol^{-1}, measured: 41.09671 g mol^{-1}.

8.3.3 Poly(2-methyl-2-oxazoline) and poly[2-(3-butenyl)-2-oxazoline]) copolymer synthesis (PMeEneOx)

2-Methyl-2-oxazoline (15 g, 0.18 mol, 9 eq.), 2-(3-butenyl)-2-oxazoline (2.47 g, 0.0198 mol, 1 eq.), and acetonitrile at 20 wt % solids were added to a 500-mL round bottomed flask and purged with nitrogen for 30 min. Methyl triflate (0.22 g, $1.35 \cdot 10^{-3}$ mol) was added and the mixture was stirred for 60-72 h at 80 ^{o}C. The reaction was cooled to room temperature, piperidine (0.255 g, $3 \cdot 10^{-3}$ mol) was added, and the mixture was reacted at 60 ^{o}C for 24 h. The acetonitrile was removed under reduced pressure and the solid polymer was dissolved in 50 mL of deionized water. The solution was extracted three times with chloroform and the collected organic fractions were combined. The product was then precipitated twice in diethyl ether and dried under high vacuum at 40 ^{o}C to yield a white solid at 90% yield. ^{1}H NMR ($CDCl_3$): 1.90-2.17 (3H, m), 2.28-2.50 (4H, m), 3.3-3.55 (4H, m), 4.93-5.08 (2H, m), 5.75-5.88 (1H, m).

8.3.4 O-Ethyl-S-(1-ethylphenyl) dithiocarbonate synthesis

The synthesis of *O*-ethyl-*S*-(1-ethylphenyl) dithiocarbonate was adopted from Stenzel *et. al.* Briefly, *O*-ethyl xanthic acid potassium salt (5.24 g, 0.033 mol, 1 eq.) was dissolved in 60 mL of dry acetone and purged with nitrogen for 30 min. 1-bromo ethyl benzene (6.1 g, 0.033 mol, 1 eq.) was added dropwise over 10 min and the reaction stirred for 24 h. Potassium bromide was removed through filtration and the acetone was removed at reduced pressure. The viscous yellow product was used without further purification at 89%

yield. The structure was confirmed using ^{1}H and ^{13}C NMR spectroscopy and mass spectroscopy. ^{1}H NMR ($CDCl_3$): 1.43 (3H, t), 1.57 (3H, d), 4.62 (2H, q), 4.87 (1H, q), 7.36 (5H, m). ^{13}C NMR ($CDCl_3$): 13.6, 21.7, 49.2, 69.6, 127.1-128.7, 141.8, 213.0. Mass spectroscopy, expected: 226.35 g mol^{-1}, measured: 226.57 g mol^{-1}.

8.3.5 RAFT polymerization kinetics of vinyl pyrrolidone

A stock batch of vinyl pyrrolidone (35 g, 0.315 mol) and *O*-ethyl-*S*-(1-ethylphenyl) dithiocarbonate (0.16 g, $7 \cdot 10^{-4}$ mol), and AIBN (11.4 mg, $7 \cdot 10^{-5}$ mol) were mixed and split into six 50 mL round bottomed flasks and purged with nitrogen for 30 min. The mixtures were allowed to react at 60 ^{o}C for 2, 4, 8, 12, 16, and 24 h where exposure to oxygen terminated the reaction. ^{1}H NMR determined conversion and M_n. This procedure was also used to synthesize the linear PVP analogs at the same M_n as the graft copolymers.

8.3.6 Thiol-terminated poly(vinyl pyrrolidone) (PVP-SH)

N-vinyl pyrrolidone (5 g, 0.045 mol, 1 eq.), *O*-ethyl-*S*-(1-ethylphenyl) dithiocarbonate (0.264 g, 0.001 mol), and AIBN (0.0264 g, $1 \cdot 10^{-4}$ mol) was added into a 250-mL round bottomed flask and purged with nitrogen for 30 min. The reaction stirred at 60 ^{o}C for 24 h. The flask was exposed to air to terminate the reaction and after being cooled to room temperature, the product was precipitated twice into diethyl ether and subsequently dried under high vacuum at 80 ^{o}C. The product was a pale yellow solid at 96% yield. The purified PVP (2 g, $4 \cdot 10^{-4}$ mol, 1 eq.) and 100 mL of chloroform was added to a 250 mL round bottomed flask with butylamine (0.15 g, $2 \cdot 10^{-3}$ mol, 5 eq.) and catalytic amounts of tributyl phosphine as a reducing agent. The reaction mixture was stirred at room temperature for 24 h and used without purification for the next step to prevent thiol-thiol coupling.

Considering the PVP backbone covered the thiol moiety in ^{1}H NMR spectroscopy, a thiol titration assay was used to confirm and quantify the thiol formation.[28]

8.3.7 Graft copolymer synthesis (PMeOx-g-PVP)

PMeEneOx (1 g, $1 \cdot 10^{-4}$ mol, 1 eq.) and diphenyl(2,4,6-trimethylbenzoyl)phosphine oxide (TPO) (9.7 mg, 0.3 eq.) were dissolved in chloroform (15 wt % solids) and added to the PVP-SH reaction mixture. The mixture was purged with nitrogen for 30 min and exposed to a broad spectrum (320-500 nm) UV light for 10 min and stirred for an additional 24 h. Chloroform was removed under reduced pressure and the product was dissolved in methanol. The solution was put into dialysis for five days against methanol with 3.5 kg mol^{-1} pores. After five days the methanol was removed, and the product was precipitated into diethyl ether and dried under high vacuum at 80 ^{o}C.

8.3.8 Analytical Methods

Differential scanning calorimetry (DSC) was ran at 50 mL min^{-1} nitrogen flow at a 10 ^{o}C per min heating rate and 100 ^{o}C per min cooling rate on a TA instruments Q2000 with indium (mp = 156.60 °C) and zinc (mp = 419.47 °C) standards. Glass transition temperatures (T_g) were determined from the midpoint of the endothermic transition. TA Instruments Q50 measured for thermogravimetric analysis (TGA) started with a 30 min isotherm at 120 °C and a ramp 10 °C/min from 120 to 600 °C. Aqueous SEC was conducted in a 54/23/23 v/v/v mixture of DI water, methanol, and glacial acetic acid with 0.1 M sodium acetate at a pH=4. A Waters Breeze Aqueous SEC with Wyatt miniDAWN treos light scattering and Waters 2414 RI detector with poly(ethylene oxide) (PEO) standards determined absolute molecular weight of each system. A DHR Rheometer in steady state

mode measured the solution viscosity of the discussed polymers in DI water with a concentric cylinder geometry at 20 ^{o}C where n=3. Shear sweeps were conducted from 1-100 s^{-1} at a 5000 μm gap with a solvent trap equipped with slightly saturated sponges.

8.3.9 Thiol titration assay

PVP-SH (0.25 g, $1 \cdot 10^{3}$ mol) was dissolved in 3 mL of pyridine. An aqueous silver nitrate solution (0.4 M, 1 mL) was added stirred with a magnetic stir bar for 10 min with the subsequent addition of 20 mL of DI water and phenolphthalein. Titration with 0.1 M sodium hydroxide revealed a light pink color after completion.[28]

8.3.10 Alkene titration assay

PMeOx-*g*-PVP (5 g, $1.4 \cdot 10^{4}$ mol) was dissolved in 20 mL of DI water and titrated with bromine water (0.1 M). The completion of the titration was determined when the orange bromine water became colorless.[29]

8.3.11 Nomenclature

The six polymers in the discussed graft copolymer series follow the naming sequence "xx%, yy" where "xx" represents the mol % grafting sites and "yy" represents the PVP graft molecular weight, displayed in **Table 1**. The six polymers contain 5, 10, and 25 mol % grafting sites and 2.5 and 5 kg mol^{-1} PVP grafts.

Table 8.1. Summary of graft copolymer nomenclature.

Name	M_n PVP (kg mol^{-1})	Me:Ene mol %
5%, 2.5	2.5	95:5
5%, 5	5	95:5
10%, 2.5	2.5	90:10
10%, 5	5	90:10
25%, 2.5	2.5	75:25
25%, 5	5	75:25

8.4 Results and Discussion

Scheme 8.1 depicts the synthesis of 2-(3-butenyl)-2-oxazoline (**Scheme 8.1, 2**), containing a fresh LDA solution with n-butyllithium and diisopropylamine in THF with exclusion of water. After a stoichiometric addition of 2-methyl-2-oxazoline (**Scheme 8.1, 1**), the LDA enabled deprotonation. The unstable, anionic 2-methyl-2-oxazoline facilitated addition of allyl bromide and enabled formation of a vinyl-containing oxazoline monomer. A water and brine workup removed residual starting materials and distillation over CaH_2 removed water and any remaining impurities.[27]

Scheme 8.1. Synthesis of 2-(3-butenyl)-2-oxazoline.

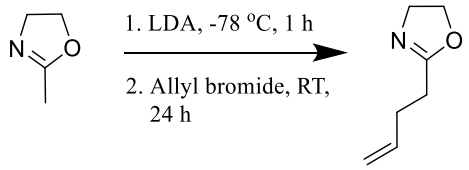

1 **2**

Scheme 8.2 depicts the synthesis of PMeOx-*g*-PVP beginning with cationic copolymerization of 2-methyl-2-oxazoline (**Scheme 8.2, 1**) and 2-(3-butenyl)-2-oxazoline (**Scheme 8.2, 2**) with exclusion of water to prevent chain termination. Methyl triflate

initiated the polymerization and stirring for 60 h at 80 ºC achieved the targeted M_n of 10 kg mol^{-1}. Piperidine quenched the cationic propagating species where 24 h of additional stirring produced full substitution. Initiation with methyl triflate and end-capping with piperidine ensured non-reactive end groups. Additionally, the chosen vinyl side-chain was not susceptible to radical polymerization, which prevented competing reactions during grafting.[27] 2-(3-butenyl)-2-oxazoline reacted slower than 2-methyl-2-oxazoline creating a gradient sequence distribution. This resulted in a concentration of 2-(3-butenyl)-2-oxazoline at the end of the polymer chain.[15,30]

RAFT polymerization kinetic studies of *N*-vinyl pyrrolidone determined reaction times yielding varying M_n, ranging from 1 to 50 kg mol^{-1}. Stenzel *et. al.* previously reported success in using xanthate-containing chain transfer agents (CTA) (**Scheme 8.2, 4**) for controlled polymerization of *N*-vinyl pyrrolidone.[26] As a less activated monomer, *N*-vinyl pyrrolidone manifested a highly reactive propagating radical. CTAs containing xanthate moieties help control the polymerization through the reduction of double bond character compared to a typical dithioate functional group with an adjacent carbon. The ethyl benzyl group also helped control the polymerization as a more stable radical-containing leaving group, compared to a common acetate group.[21,26] RAFT polymerization afforded 2.5 and 5 kg mol^{-1} PVP (**Scheme 8.2, 6**), which were precipitated into ethyl ether to remove residual monomer and dried under high vacuum. PVP (**Scheme 8.2, 6**) then underwent aminolysis with butylamine and tributyl phosphine as a reducing agent. The mixture reacted for 24 h and immediate use in the final step of the synthesis prevented disulfide coupling. Nicolay *et. al.* previously reported that immediate use of thiol-terminated molecules in thiol-ene reactions prevented thiol-thiol coupling in the purification process

or during storage.[31] Isolation of reaction aliquots and subsequent thiol titration assays confirmed 100% conversion to thiol end-groups. Thiol-ene 'click' chemistry with TPO and UV light afforded attachment of thiol-terminated PVP (**Scheme 8.2, 7**) to the poly(2-oxazoline) backbone (**Scheme 8.2, 3**). Exposure to oxygen terminated the reaction after completion.

Scheme 8.2. Synthesis of PMeOx-*g*-PVP using thiol-ene 'click' chemistry.

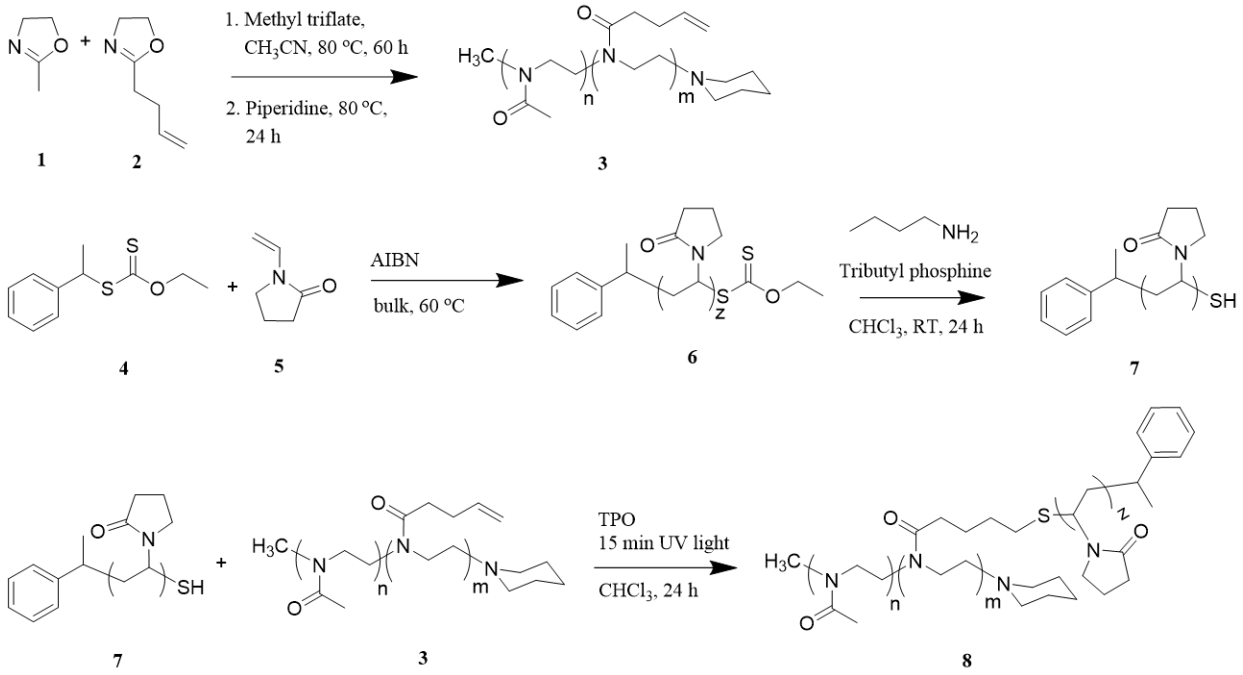

Aqueous SEC-MALS, ^{1}H NMR spectroscopy, and bromine titrations quantified the conversion of backbone vinyl groups, indicating attachment of PVP grafts. Peaks at 4.93-5.08 (2H, m) and 5.75-5.88 (1H, m) revealed remaining vinyl moieties after attempts to attach the PVP grafts (**Figure S8.5**). However, this method remained valid only when measuring 5%, 2.5 and 10%, 2.5 copolymers. Other copolymers contained higher concentrations of PVP grafts and higher M_n grafts, which resulted in dilution of vinyl signals. Aqueous SEC-MALS and titration provided two quantifiable methods to measure

the conversion of vinyl moieties. **Figure 8.1** depicts light scattering traces of 10%, 2.5, 10%, 5 and their corresponding precursors. The dashed lines represent the precursors, the PMeEneOx backbone, 2.5 kg mol^{-1}, and 5 kg mol^{-1} PVP. Both graft copolymers experienced peak broadening compared to corresponding precursors.

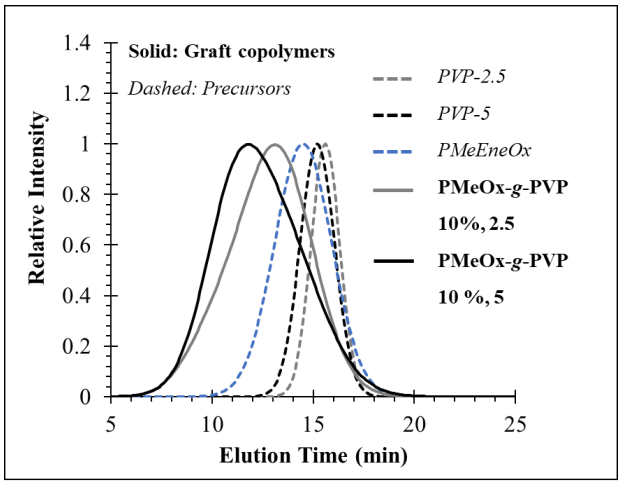

Figure 8.1. Aqueous SEC-MALS light scattering traces depicting relative intensity as a function of elution time of two example graft copolymer systems and the corresponding precursors.

Table 8.2 summaries the graft copolymer aqueous SEC-MALS data. The targeted M_n values represent 100% vinyl groups converted and all available grafting sites containing a PVP chain. Two methods determined mol % grafting, aqueous SEC-MALS and bromine titration, where both measurements agreed. Samples 5%, 2.5, 5%, 5, and 10%, 2.5 all exhibited 100% conversion of vinyl groups. However, as mol % grafting sites and M_n of PVP grafts increased, conversion of vinyl groups decreased. Samples 10%, 5, 25%, 2.5, and 25%, 5 exhibited average conversions of 95%, 78%, and 60% respectively. The suspected gradient sequence of the poly(2-oxazoline) backbone resulted in a high

concentration of vinyl moieties resonating at the terminal chain end. The proximity of vinyl groups may result in steric hinderance impacting substitution of PVP grafts. This is a common issue with grafting-to methodology depending on the proximity of the grafting moieties and M_n of the grafts.[3,4,32]

Table 8.2. Summary of aqueous SEC-MALS data.

Name	Target MW (kg mol^{-1})[a]	M_n (kg mol^{-1})	Đ	Target grafting mol %	Grafting mol %[b]	Grafting mol %[c]
5%, 2.5	22.5	23	1.61	5	5	5.0
5%, 5	35	33.1	1.54	5	5	5.0
10%, 2.5	35	33.4	1.78	10	10	9.8
10%, 5	60	55.2	1.85	10	9	9.9
25%, 2.5	72.5	56.6	2.67	25	19	20.3
25%, 5	135	87.8	2.34	25	16	14.6

[a]Target MW: MW at 100% conversion of vinyl groups
[b]Measured grafting mol % based on SEC-MALS
[c]Measured based on bromine titration of vinyl moieties

Figure 8.2 depicts Đ as a function of graft copolymer composition where the empty bars represent the Đs of PMeEneOx backbones. As the incorporation of 2-(3-butenyl)-2-oxazoline increased, Đ increased because of increased reaction times. Ranging from 5 to 25 mol % 2-(3-butenyl)-2-oxazoline, the reaction times increased from 48 to 62 h. Extended reaction times exposed poly(2-oxazoline)s to side-reactions due to monomer transfer reactions, where the oxazoline monomer α-proton is transferred onto the oxazolinium propagating species, resulting in an increased in Đ.[33–35] The graft copolymer compositions also exhibited an increase in Đ as mol % grafting sites increased. As mol % grafting sites increased, the attachment of PVP grafts decreased, leading to more variability in the polymer structure.

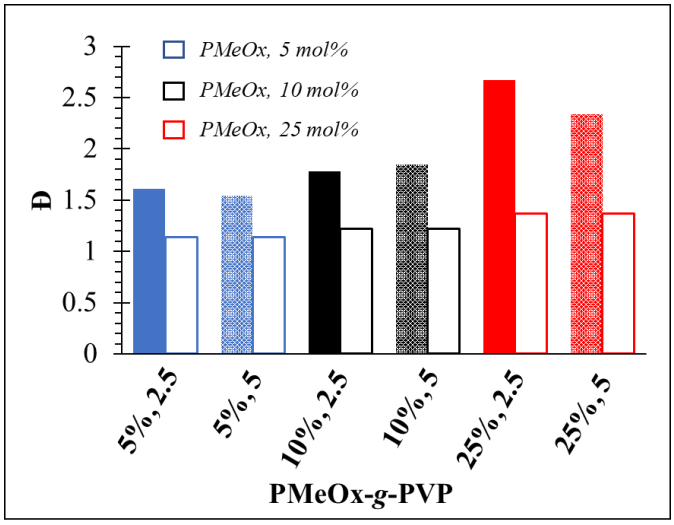

Figure 8.2. Đ as a function of PMeOx-*g*-PVP compositions.

Figure 8.3 depicts radical kinetics associated with the thiol-ene 'click' attachment of the PVP grafts to the poly(2-oxazoline) backbone. First, measuring conversion of vinyl groups as a function of time using both a thermal (AIBN) and photo (TPO) initiators established which initiator produced the most PVP graft substitutions. **Figure 8.3A** depicts the conversion of vinyl groups as a function of time using both initiators with copolymers 10%, 2.5 and 5%, 2.5. After 15 min of UV light exposure and an additional 24 h of stirring, the samples using TPO as an initiator reached 100% conversion of vinyl groups. Copolymers heated to 65 ºC and using AIBN as an initiator achieved 90% and 92% conversion for 10%, 2.5 and 5%, 2.5, respectively. Previous studies reported the higher temperatures encourage more thiol-thiol coupling, which may have led to the lower conversion values using AIBN in this study.[36]

After TPO proved to produce the highest conversion of vinyl groups, a study of conversion as a function of mol % TPO revealed 3 mol % produced the highest conversion in samples 5%, 2.5 and 10%, 2.5. **Figure 8.3B** elucidates 3 mol % TPO produced both

samples with 100% conversion of vinyl groups. **Figure 8.3C** depicts conversion as a function of UV light exposure time, which revealed the optimal time was 10 min. The last kinetic study, **Figure 8.3D**, examined conversion as a function thiol equivalent, compared to the mol % graft sites, which revealed three equivalents produced the highest conversions. All copolymers containing 25 mol % grafting sites failed to breach 81% grafting. Attempting extremes in all categories, 6 mol % TPO, 30 min of UV light exposure, and 6 thiol equivalents, still only produced conversions of 81 and 58% conversion for 25%, 2.5 and 25%, 5, respectively.

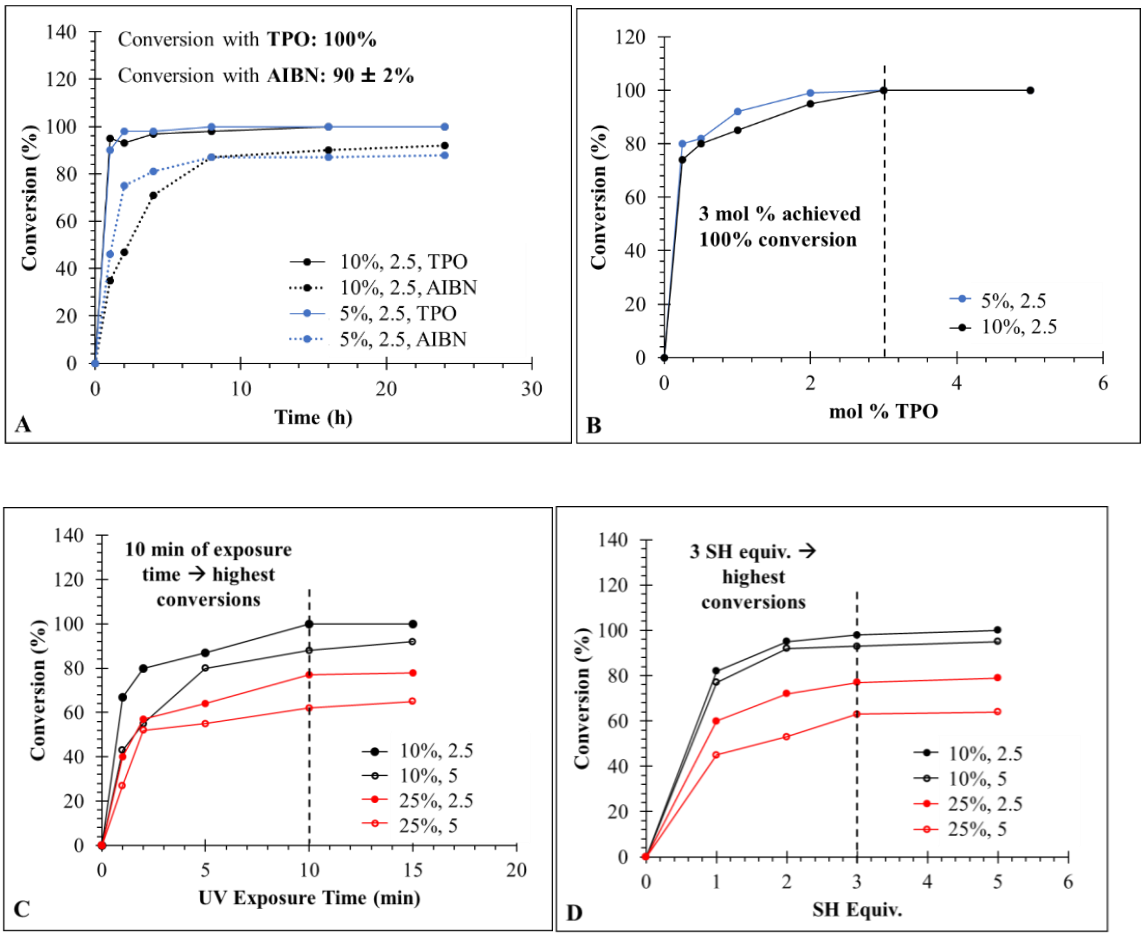

Figure 8.3. Photokinetics of the thiol-ene click grafting reaction where **(A)** elucidates a thermal vs. photoinitiator depicting conversion (%) vs. time, **(B)** depicts conversion (%) as a function of mol % TPO, **(C)** depicts conversion (%) as a function of UV exposure time, and **(D)** depicts conversion as a function of SH equivalents.

A poly(2-(3-butenyl)-2-oxazoline homopolymer, containing grafting sites on each repeat unit, elucidated the steric hinderance effects on subsequent PVP grafting. **Figure 8.4A** depicts conversion as a function of PVP graft M_n on a 6 kg mol^{-1} poly(2-(3-butenyl)-2-oxazoline backbone. Grafting with 2.5 and 5 kg mol^{-1} PVP chains resulted in conversions of 45% and 38%, respectively, which suggested steric hinderance impacts. Increasing PVP graft attachment prevented further substitution on adjacent grafting sites, resulting in low conversions and low grafting percentages. **Figure 8.4B** depicts a summary of conversion as a function of mol % grafting sites on the poly(2-oxazoline) backbones. Samples 5%, 2.5, 5%, 5, and 10%, 2.5, achieved 100% conversion possibly owing to the comparatively low number of grafting sites on the backbone. As PVP graft M_n and mol % graft sites increased, a decrease in conversion occurred. Samples 25%, 2.5 and 25%, 5 resulted in conversions of 78% and 62%, respectively, possibly owing to the gradient sequencing of the poly(2-oxazoline) backbone.

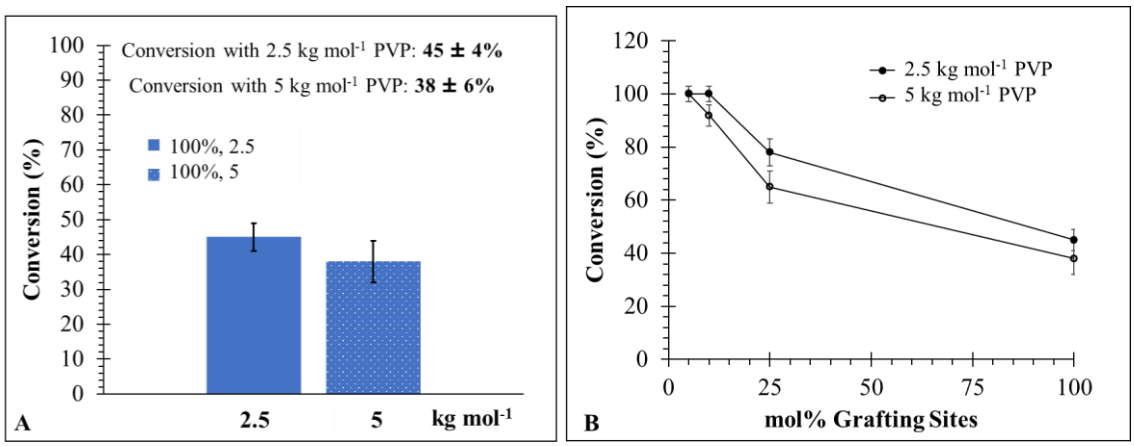

Figure 8.4. Using poly(2-(3-butenyl)-2-oxazoline, 100 mol % grafting sites, to explore steric hindrance effects on vinyl conversion where **(A)** depicts conversion as a function of PVP graft M_n and **(B)** summarizes all of the grafting results depicting conversion as a function of mol % grafting sites.

Differential scanning calorimetry (DSC) revealed a single glass transition temperature (T_g) for each graft copolymer. Graft copolymers often experience two T_gs; One associated to the backbone segmental motion and another related to grafts.[2,37] Other copolymers exhibit one T_g that follows the Fox equation for copolymer systems, indicating a miscible copolymer. The Fox equation (**Eqn. 1**) expresses the change in T_g of miscible copolymers based on free volume theory, where w and T_g correspond to the wt % and T_g of each composition. This equation is used as an estimation of graft copolymer systems but falls short due to not considering end-group effects and decreased segmental backbone movement due to high graft concentrations.[38,39]

$$\frac{1}{T_g} = \frac{w_1}{T_{g,1}} + \frac{w_2}{T_{g,2}} \qquad \textbf{Eqn. 1}$$

Figure 8.5A depicts the T_gs of each graft copolymer (filled bars), showing an increase with increasing mol % grafting sites and PVP graft M_n. **Figure 8.5A** also depicts

the Fox T_g estimations (open bars) as a comparison. At the highest conversion possible, the graft copolymers contained 55, 71, 71, 81, 83, and 89 wt % PVP, respectively, indicating T_g dependency on wt % PVP. **Table S8.1** summarizes the T_gs of the poly(2-oxazoline) backbones and PVP grafts to demonstrate changes after grafting. As seen in the Fox T_g estimations, the graft copolymers deviated from the predictions for compositions containing above 5 mol % grafting sites. PMeOx-*g*-PVP containing 5 mol % grafting sites experience T_gs between the backbone and PVP grafts, 88 and 95 ^oC for 5%, 2.5 and 5%, 5, respectively, which also align with the corresponding Fox estimations, 87 and 98 ^oC, respectively. As the mol % grafting sites increased, an increase in PVP wt % restricted segmental motion and dominated the T_g. For example, 10%, 2.5 and 10%, 5 experienced T_gs of 96 and 111 ^oC, respectively, which exceeds and borders the 2.5 and 5 kg mol^{-1} PVP graft precursors T_gs of 102 and 123 ^oC, respectively. A similar trend was observed for 25%, 2.5 and 25%, 5 with T_gs of 112 and 119 ^oC, respectively. The copolymers containing more than 5 mol % graft sites deviated from the Fox estimations by over 5 ^oC, which indicated the restriction of segmental motion because of the increase grafting percentages.

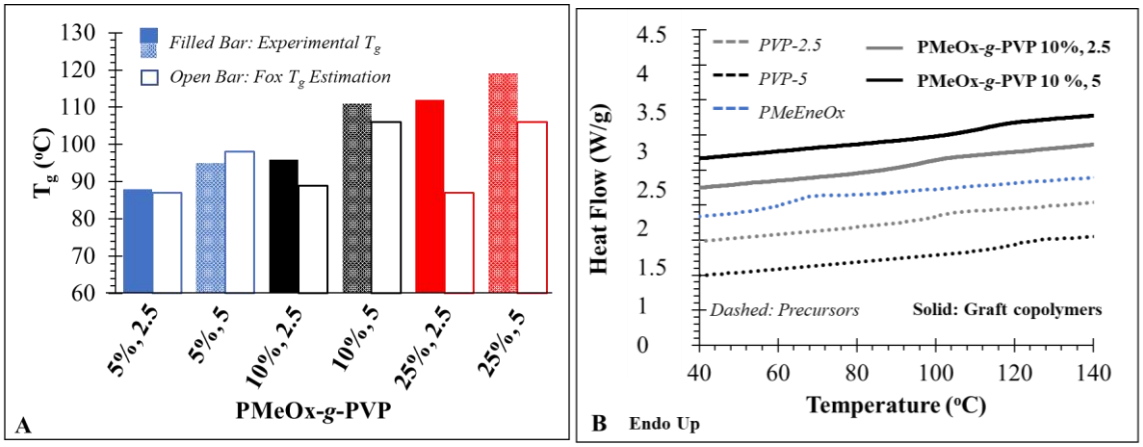

Figure 8.5. DSC reveals glass transition temperatures (T_g) of each graft copolymer system compared to Fox T_g estimations. **(A)** depicts T_g and Fox T_g estimation as a function of graft copolymer composition and **(B)** shows heat flow as a function of temperature for two example graft copolymers and their corresponding precursors.

Graft copolymers exhibit unique solution properties owing to their compact size and worm-like conformations. They also experience smaller hydrodynamic radii and volumes compared to their linear analogs at the same M_n, which corresponds to lower solution viscosities.[40–42] This quality is advantageous for applications such as BJ AM and stabilizers in suspension polymerization because solution viscosity will not increase as quickly with increasing concentration compared to linear analogs. Solution rheology with a concentric cylinder geometry afforded the zero-shear viscosities of each graft copolymer in DI water, depicted in **Figure 8.6A**. As a reference, 40 kg mol^{-1} linear PVP exhibited a zero-shear viscosity of 4.4 mPa·s at 5 wt %, which is a common structure and concentration for BJ AM. On some printers, solutions containing more than 5 wt % will not print because of excessive viscosities. Using the discussed graft copolymers, 10, 2.5 in particular, higher polymer concentration will result in a minimum increase in viscosity and thus remain within the printable range and lead to fabrication of stronger printed parts.[21]

Figure 8.6B depicts solution rheology frequency sweeps of 10%, 2.5 and linear 35 kg mol^{-1} PVP at 5 and 10 wt % in DI water. RAFT polymerization afforded linear PVP analogs at the same total M_n of the graft copolymers, where the zero-shear viscosities are summarized in **Table S8.2**. Linear polymers compared to graft polymers at the same M_n exhibit larger hydrodynamic radii, more entanglements, and induce more drag in solution resulting in an average of 20-30% reduction in solution viscosity.[21,22,43] In this study, on

average, the graft copolymers experienced 31% lower zero-shear viscosities at the same concentration as the linear analogs. **Figure 8.6B** elucidates the difference in solution viscosities of 10%, 2.5 and linear 35 kg mol^{-1} PVP at 5 and 10 wt % in DI water. The 5 wt % and 10 wt % pairs exhibit a 32% and 37% difference in viscosity, respectively.

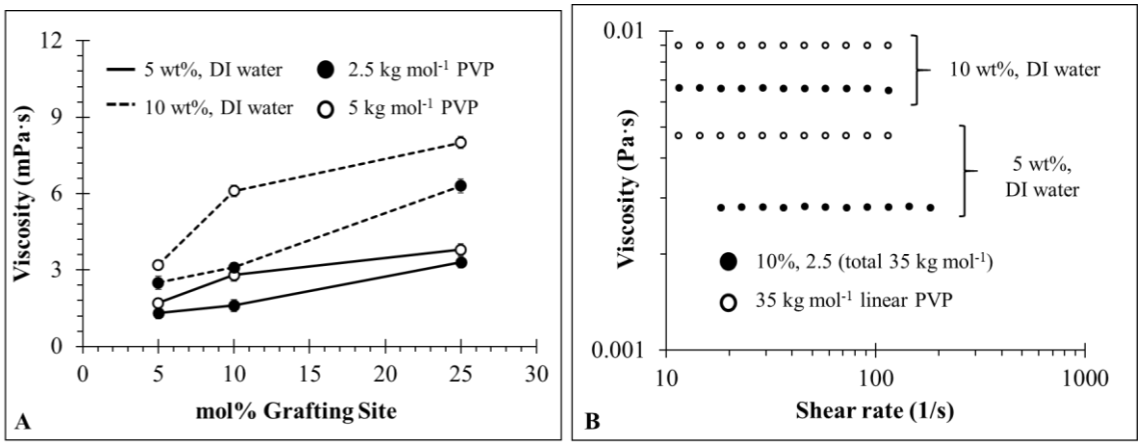

Figure 8.6. (A) Zero-shear viscosity as a function of mol % grafting sites in DI water and **(B)** elucidates solution viscosity as a function of shear rate depicting 10%, 2.5 and a linear PVP analog at the same M_n.

Conclusions

RAFT polymerization, cationic ring-opening polymerization, and thiol-ene 'click' chemistry afforded a series of water-soluble, graft copolymers with poly(2-oxazoline) backbones and PVP grafts. Poly(2-oxazoline)s containing vinyl moieties at 5, 10, and 25 mol % with 2.5 and 5 kg mol^{-1} PVP grafts produced a series of polymers with T_gs ranging from 88 to 119 ^oC. Kinetic studies examining thermal vs. photo initiators, mol % initiator, UV light exposure time, and thiol equivalents revealed the optimal reaction conditions to achieve the highest conversion of vinyl groups. Samples 5%, 2.5, 5%, 5, and 10%, 2.5, achieved 100% conversion possibly owing to the comparatively low number of grafting

sites on the backbone. Even after optimization of the thiol-ene 'click' step, as the PVP graft M_n and mol % graft sites increased, a decrease in conversion occurred. Samples 25%, 2.5 and 25%, 5 resulted in conversions of 78% and 62%, respectively, possibly owing to the gradient sequencing of the poly(2-oxazoline) backbone. Solution rheology experiments to determine zero-shear viscosities of the graft copolymers and linear analogs at the same total M_n revealed an average 31% decrease in viscosity. Applications of water-soluble graft copolymers include improving mechanical properties of BJ AM parts and stabilizing suspension polymerization processes. Future manuscripts will demonstrate the effectiveness of these polymer systems in BJ AM.

8.5 Acknowledgements

The authors would like to thank Dr. Charles Carfagna for performing SEC-MALS experiments and analysis.

8.6 References

(1) Kolb, H. C.; Finn, M. G.; Sharpless, K. B. Click Chemistry: Diverse Chemical Function from a Few Good Reactions. *Angew. Chemie Int. Ed.* **2001**, *40* (11), 2004–2021. https://doi.org/10.1002/1521-3773(20010601)40:11<2004::AID-ANIE2004>3.0.CO;2-5.

(2) Hong, S. C.; Pakula, T.; Matyjaszewski, K. Preparation of Polyisobutene-Graft-Poly(Methyl Methacrylate) and Polyisobutene-Graft-Polystyrene with Different Compositions and Side Chain Architectures through Atom Transfer Radical Polymerization (ATRP). *Macromol. Chem. Phys.* **2001**, *202* (17), 3392–3402. https://doi.org/10.1002/1521-3935(20011101)202:17<3392::AID-MACP3392>3.0.CO;2-4.

(3) and, H. G.; Matyjaszewski*, K. Synthesis of Molecular Brushes by "Grafting onto" Method: Combination of ATRP and Click Reactions. **2007**. https://doi.org/10.1021/JA0711617.

(4) Brent S. Sumerlin; Nicolay V. Tsarevsky; Guillaume Louche; Robert Y. Lee, and; Matyjaszewski*, K. Highly Efficient "Click" Functionalization of Poly(3-Azidopropyl Methacrylate) Prepared by ATRP. **2005**. https://doi.org/10.1021/MA0511245.

(5) Demirci, G.; Tasdelen, M. A. Synthesis and Characterization of Graft Copolymers by Photoinduced CuAAC Click Chemistry. *Eur. Polym. J.* **2015**, *66*, 282–289. https://doi.org/10.1016/j.eurpolymj.2015.02.029.

(6) Feng, C.; Li, Y.; Yang, D.; Hu, J.; Zhang, X.; Huang, X. Well-Defined Graft Copolymers: From Controlled Synthesis to Multipurpose Applications. *Chem. Soc. Rev.* **2011**, *40* (3), 1282–1295. https://doi.org/10.1039/B921358A.

(7) Darcos, V.; El Habnouni, S.; Nottelet, B.; El Ghzaoui, A.; Coudane, J. Well-Defined PCL-Graft-PDMAEMA Prepared by Ring-Opening Polymerisation and Click Chemistry. *Polym. Chem.* **2010**, *1* (3), 280–282. https://doi.org/10.1039/c0py00004c.

(8) Pan, Y.; Bao, H.; Sahoo, N. G.; Wu, T.; Li, L. Water-Soluble Poly(N-Isopropylacrylamide)-Graphene Sheets Synthesized via Click Chemistry for Drug Delivery. *Adv. Funct. Mater.* **2011**, *21* (14), 2754–2763. https://doi.org/10.1002/adfm.201100078.

(9) Yuan, W.; Li, X.; Gu, S.; Cao, A.; Ren, J. Amphiphilic Chitosan Graft Copolymer via Combination of ROP, ATRP and Click Chemistry: Synthesis, Self-Assembly, Thermosensitivity, Fluorescence, and Controlled Drug Release. *Polymer (Guildf).* **2011**, *52* (3), 658–666. https://doi.org/10.1016/j.polymer.2010.12.052.

(10) Park, I. K.; Ihm, J. E.; Park, Y. H.; Choi, Y. J.; Kim, S. I.; Kim, W. J.; Akaike, T.; Cho, C. S. Galactosylated Chitosan (GC)-Graft-Poly(Vinyl Pyrrolidone) (PVP) as Hepatocyte-Targeting DNA Carrier: Preparation and Physicochemical Characterization of GC-Graft-PVP/DNA Complex (1). *J. Control. Release* **2003**, *86* (2–3), 349–359. https://doi.org/10.1016/S0168-3659(02)00365-6.

(11) Seung, E. C.; In, K. P.; Eun, M. K.; Hwan, J. J.; Tae, G. P.; Yun, J. C.; Akaike, T.; Chong, S. C. Galactosylated Polyethylenimine-Graft-Poly(Vinyl Pyrrolidone) as a Hepatocyte-Targeting Gene Carrier. *J. Control. Release* **2005**, *105* (1–2), 151–163. https://doi.org/10.1016/j.jconrel.2005.03.011.

(12) Nair, B. Final Report On the Safety Assessment of Polyvinylpyrrolidone (PVP). *Int. J. Toxicol.* **1998**, *17* (4_suppl), 95–130. https://doi.org/10.1177/109158189801700408.

(13) Bauer, M.; Schroeder, S.; Tauhardt, L.; Kempe, K.; Schubert, U. S.; Fischer, D. *In Vitro* Hemocompatibility and Cytotoxicity Study of Poly(2-Methyl-2-Oxazoline) for Biomedical Applications. *J. Polym. Sci. Part A Polym. Chem.* **2013**, *51* (8), 1816–1821. https://doi.org/10.1002/pola.26564.

(14) Haaf, F.; Sanner, A.; Straub, F. Polymers of N-Vinylpyrrolidone: Synthesis, Characterization and Uses. *Polym. J.* **1985**, *17* (1), 143–152. https://doi.org/10.1295/polymj.17.143.

(15) Lava, K.; Verbraeken, B.; Hoogenboom, R. Poly(2-Oxazoline)s and Click Chemistry: A Versatile Toolbox toward Multi-Functional Polymers. *Eur. Polym. J.* **2015**, *65*, 98–111. https://doi.org/10.1016/j.eurpolymj.2015.01.014.

(16) Glassner, M.; Vergaelen, M.; Hoogenboom, R. Poly(2-Oxazoline)s: A Comprehensive Overview of Polymer Structures and Their Physical Properties. *Polym. Int.*

2018, *67* (1), 32–45. https://doi.org/10.1002/pi.5457.

(17) Prasad, L. K.; Smyth, H. 3D Printing Technologies for Drug Delivery: A Review. *Drug Dev. Ind. Pharm.* **2016**, *42* (7), 1019–1031. https://doi.org/10.3109/03639045.2015.1120743.

(18) Reis, N.; Ainsley, C.; Derby, B. Ink-Jet Delivery of Particle Suspensions by Piezoelectric Droplet Ejectors. *J. Appl. Phys.* **2005**, *97* (9), 094903. https://doi.org/10.1063/1.1888026.

(19) Bai, Y.; Wagner, G.; Williams, C. B. Effect of Particle Size Distribution on Powder Packing and Sintering in Binder Jetting Additive Manufacturing of Metals. *J. Manuf. Sci. Eng.* **2017**, *139* (8), 081019. https://doi.org/10.1115/1.4036640.

(20) Patirupanusara, P.; Suwanpreuk, W.; Rubkumintara, T.; Suwanprateeb, J. Effect of Binder Content on the Material Properties of Polymethyl Methacrylate Fabricated by Three Dimensional Printing Technique. *J. Mater. Process. Technol.* **2008**, *207* (1–3), 40–45. https://doi.org/10.1016/J.JMATPROTEC.2007.12.058.

(21) Wilts, E.; Ma, D.; Bai, Y.; Williams, C. B.; Long, T. E. Comparison of Linear and 4-Arm Star Poly(Vinyl Pyrrolidone) for Aqueous Binder Jetting Additive Manufacturing of Personalized Dosage Tablets. *ACS Appl. Mater. Interfaces* **2019**, acsami.9b08116. https://doi.org/10.1021/acsami.9b08116.

(22) Kilb, R. W.; Bueche, A. M. Solution and Fractionation Properties of Graft Polymers. *J. Polym. Sci.* **1958**, *28* (117), 285–294. https://doi.org/10.1002/pol.1958.1202811704.

(23) N. Hadjichristidis, M. P., Hermis Iatrou, P. Driva, M. Chatzichristidi, Georgios Sakellariou, D. J. Lohse. No Title. *Encyclopedia Of Polymer Science and Technology*; Wiley and Sons Inc., 2010.

(24) Dowding, P. J.; Vincent, B. Suspension Polymerisation to Form Polymer Beads. *Colloids Surfaces A Physicochem. Eng. Asp.* **2000**, *161* (2), 259–269. https://doi.org/10.1016/S0927-7757(99)00375-1.

(25) Mendizabal, E.; Castellanos-Ortega, J. R.; Puig, J. E. A Method for Selecting a Polyvinyl Alcohol as Stabilizer in Suspension Polymerization. *Colloids and Surfaces* **1992**, *63* (3–4), 209–217. https://doi.org/10.1016/0166-6622(92)80242-T.

(26) Nguyen, T. L. U.; Eagles, K.; Davis, T. P.; Barner-Kowollik, C.; Stenzel, M. H. Investigation of the Influence of the Architectures of Poly(Vinyl Pyrrolidone) Polymers Made via the Reversible Addition–Fragmentation Chain Transfer/Macromolecular Design via the Interchange of Xanthates Mechanism on the Stabilization of Suspension Polymerizations. *J. Polym. Sci. Part A Polym. Chem.* **2006**, *44* (15), 4372–4383. https://doi.org/10.1002/pola.21518.

(27) Dargaville, T. R.; Lava, K.; Verbraeken, B.; Hoogenboom, R. Unexpected Switching of the Photogelation Chemistry When Cross-Linking Poly(2-Oxazoline) Copolymers. *Macromolecules* **2016**, *49* (13), 4774–4783. https://doi.org/10.1021/acs.macromol.6b00167.

(28) Saville, B. A Simple Titrimetric Method for the Assay of Thiols. *Analyst* **1961**, *86* (1018), 29. https://doi.org/10.1039/an9618600029.

(29) Morrell, J. C.; Levine, I. M. Determination of Olefins by Bromine Titration. *Ind. Eng. Chem. Anal. Ed.* **1932**, *4* (3), 319–321. https://doi.org/10.1021/ac50079a035.

(30) Anja Gress; Antje Völkel, and; Schlaad*, H. Thio-Click Modification of Poly[2-(3-Butenyl)-2-Oxazoline]. **2007**. https://doi.org/10.1021/MA071357R.

(31) Le Neindre, M.; Magny, B.; Nicolaÿ, R. Evaluation of Thiocarbonyl and Thioester Moieties as Thiol Protecting Groups for Controlled Radical Polymerization. *Polym. Chem.* **2013**, *4* (22), 5577. https://doi.org/10.1039/c3py00754e.

(32) Nicolay V. Tsarevsky; Sidi A. Bencherif, and; Matyjaszewski*, K. Graft Copolymers by a Combination of ATRP and Two Different Consecutive Click Reactions. **2007**. https://doi.org/10.1021/MA070705M.

(33) Litt, M.; Levy, A.; Herz, J. Polymerization of Cyclic Imino Ethers. X. Kinetics, Chain Transfer, and Repolymerization. *J. Macromol. Sci. Part A - Chem.* **1975**, *9* (5), 703–727. https://doi.org/10.1080/00222337508065890.

(34) Kourti, M.-E.; Vougioukalakis, G. C.; Hadjichristidis, N.; Pitsikalis, M. Metallocene-Mediated Cationic Ring-Opening Polymerization of 2-Methyl- and 2-Phenyl-Oxazoline. *J. Polym. Sci. Part A Polym. Chem.* **2011**, *49* (11), 2520–2527. https://doi.org/10.1002/pola.24679.

(35) Baumgaertel, A.; Weber, C.; Knop, K.; Crecelius, A.; Schubert, U. S. Characterization of Different Poly(2-Ethyl-2-Oxazoline)s via Matrix-Assisted Laser Desorption/Ionization Time-of-Flight Tandem Mass Spectrometry. *Rapid Commun. Mass Spectrom.* **2009**, *23* (6), 756–762. https://doi.org/10.1002/rcm.3933.

(36) Uygun, M.; Tasdelen, M. A.; Yagci, Y. Influence of Type of Initiation on Thiolâ€“Ene Â€œClickâ€• Chemistry. *Macromol. Chem. Phys.* **2010**, *211* (1), 103–110. https://doi.org/10.1002/macp.200900442.

(37) Yamashita, K.; Ito, K.; Tsuboi, H.; Takahama, S.; Tsuda, K.; Otsu, T. Graft Copolymerization by Iniferter Method; Structural Analyses of Graft Copolymer by Glass Transition Temperature. *J. Appl. Polym. Sci.* **1990**, *40* (910), 1445–1452. https://doi.org/10.1002/app.1990.070400903.

(38) Brostow, W.; Chiu, R.; Kalogeras, I. M.; Vassilikou-Dova, A. Prediction of Glass Transition Temperatures: Binary Blends and Copolymers. *Mater. Lett.* **2008**, *62* (17–18), 3152–3155. https://doi.org/10.1016/j.matlet.2008.02.008.

(39) FOX; G., T. Influence of Diluent and of Copolymer Composition on the Glass Temperature of a Poly-Mer System. *Bull. Am. Phys. Soc.* **1956**, *1*, 123.

(40) Matthew G. McKee, †; Garth L. Wilkes, ‡; Ralph. H. Colby, § and; Timothy E. Long*, †. Correlations of Solution Rheology with Electrospun Fiber Formation of Linear and Branched Polyesters. **2004**. https://doi.org/10.1021/MA035689H.

(41) Colby, R. H.; Fetters, L. J.; Funk, W. G.; Graessley, W. W. *Effects of Concentration*

and Thermodynamic Interaction on the Viscoelastic Properties of Polymer Solutions; 1991; Vol. 24.

(42) Lee, A. S. S.; Choi, S.-S.; Baek, K.-Y.; Hwang, S. S. Thiol-Ene Photopolymerization of Well-Defined Hybrid Graft Polymers from a Ladder-like Polysilsesquioxane. *Macromol. Res.* **2015**, *23* (1), 60–66. https://doi.org/10.1007/s13233-015-3004-6.

(43) Bywater, S. Preparation and Properties of Star-Branched Polymers. In *Physical Chemistry*; Springer Berlin Heidelberg: Berlin, Heidelberg, 1979; pp 89–116. https://doi.org/10.1007/3-540-09199-8_2.

8.7 Supplemental

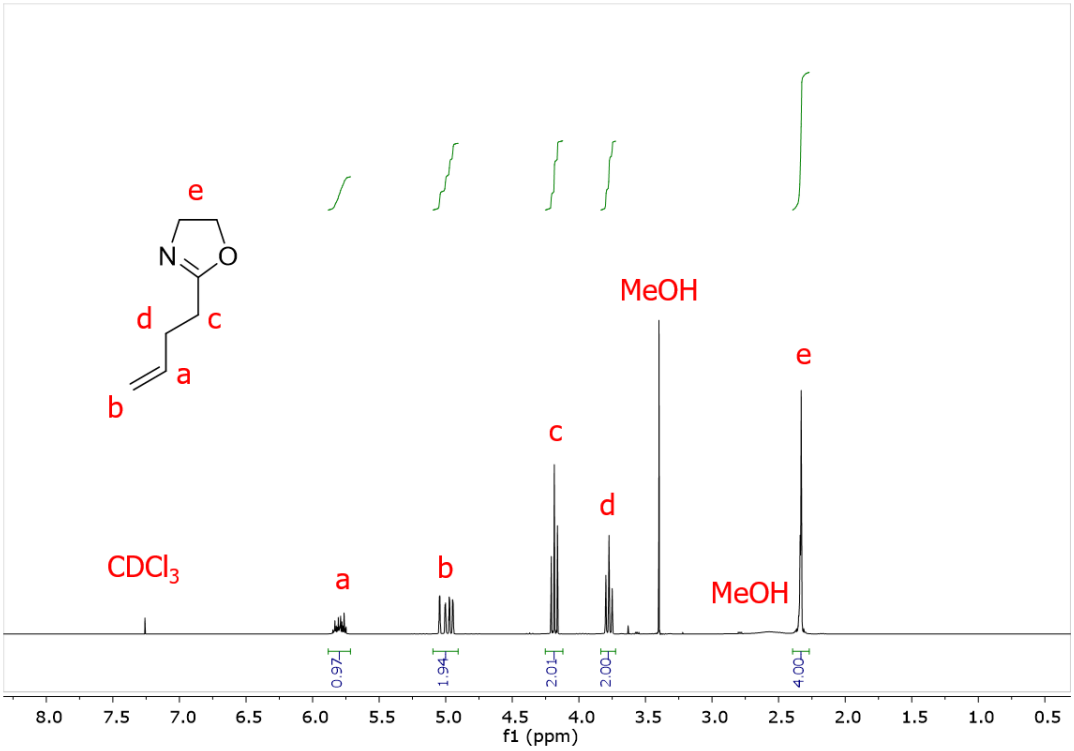

Figure S8.1. ^{1}H NMR spectroscopy of 2-(3-butenyl)-2-oxazoline in $CDCl_3$.

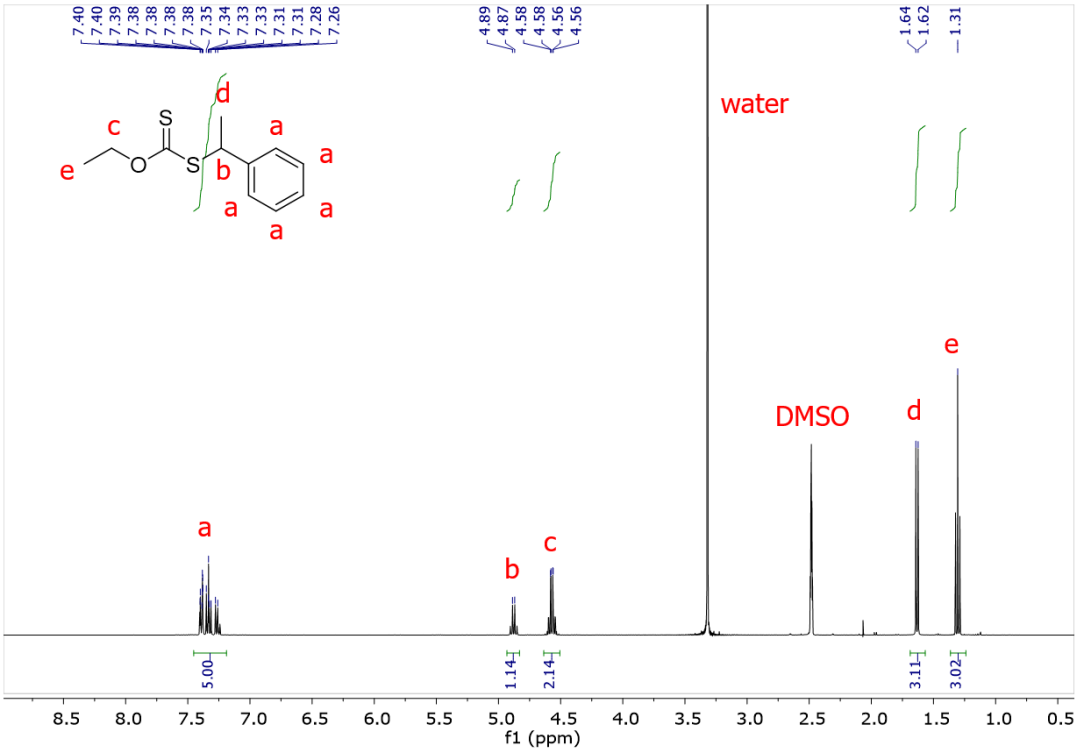

Figure S8.2. ^{1}H NMR spectroscopy of *O*-ethyl-*S*-(1-ethylphenyl) dithiocarbonate in $DMSO_{d6}$.

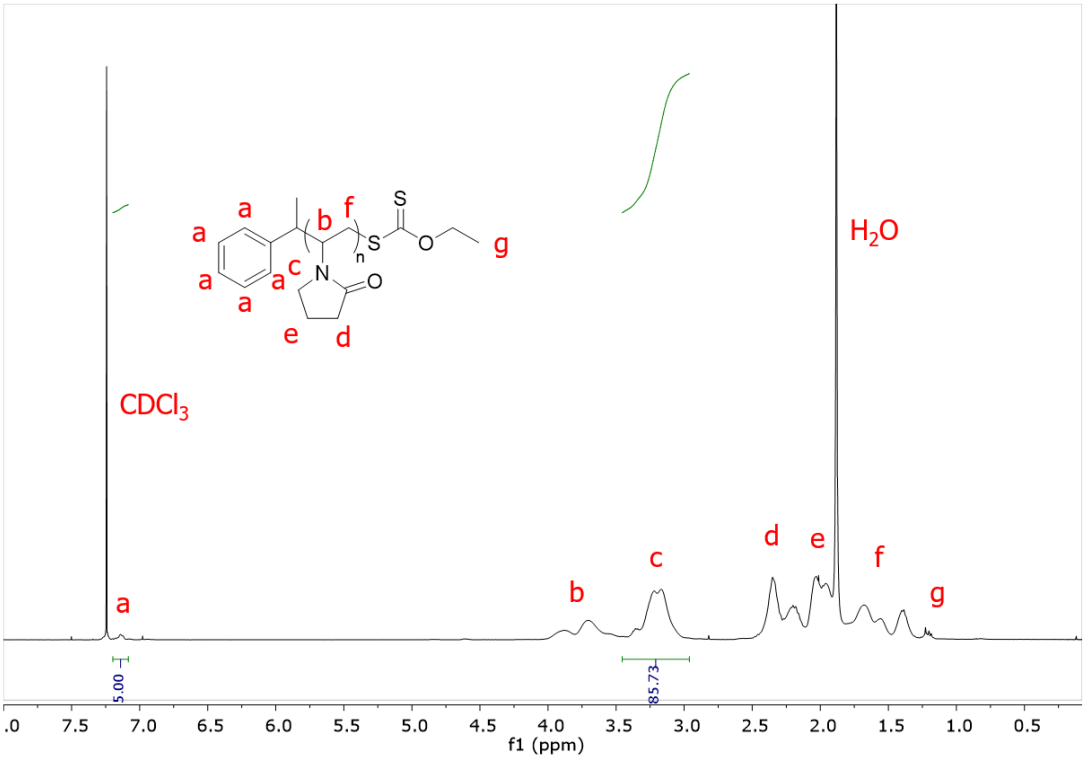

Figure S8.3. ^{1}H NMR spectroscopy of 5k PVP in $CDCl_3$.

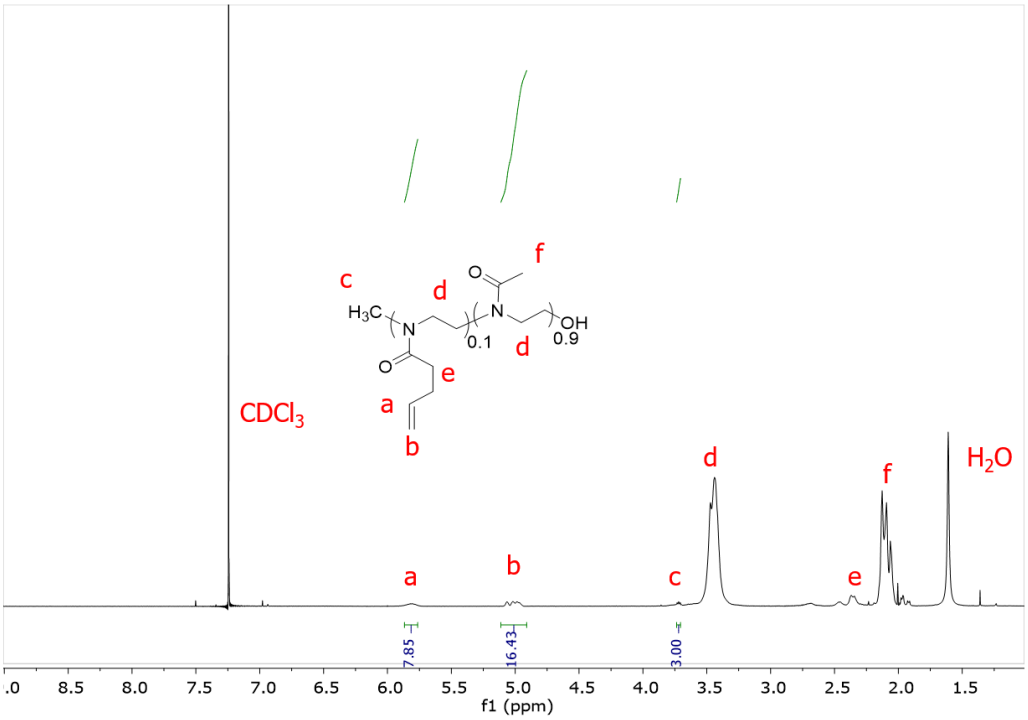

Figure S8.4. ^{1}H NMR spectroscopy of 90:10 PMeOx-*co*-PEneOx (PMeEneOx) in $CDCl_3$.

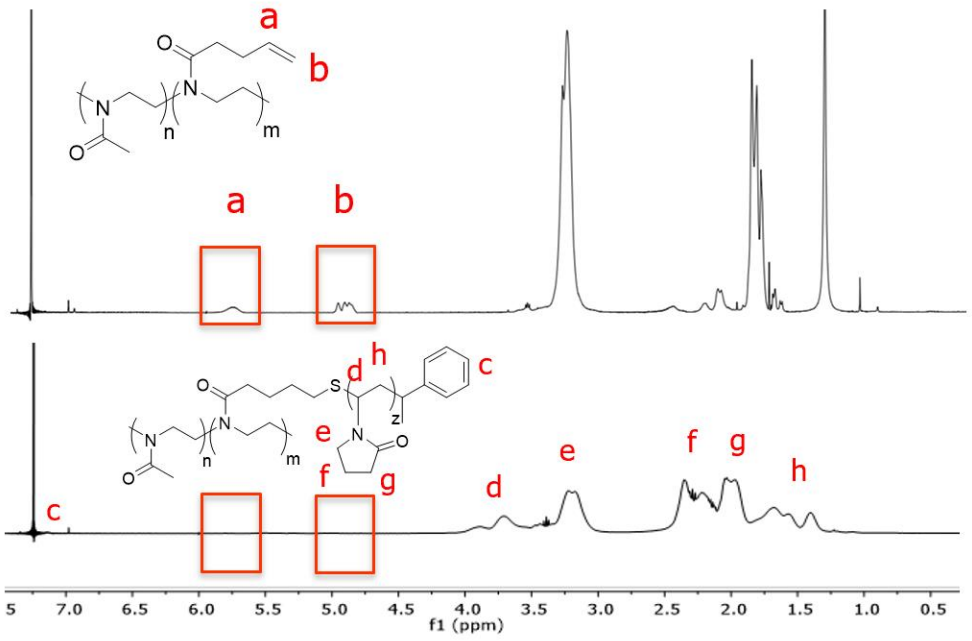

Figure S8.5. ^{1}H NMR spectroscopy of PMeEneOx 90:10 and 2.5 kg mol^{-1} depicts the elimination of the vinyl peaks at 5.8 to 4.8 ppm indicating full conversion of grafting sites.

Table S8.1. Thermals transitions and molecular weight of precursors of PMeOx-*g*-PVP samples.

Sample Name	T_g (°C)	M_n, aqueous SEC (kg mol^{-1})	PDI
2.5 kg mol^{-1} PVP	102	2.9	1.06
5 kg mol^{-1} PVP	123	5.3	1.05
PMeEneOx, 95:5	75	10.0	1.2
PMeEneOx, 90:10	67	10.2	1.22
PMeEneOx, 75:25	51	9.5	1.37

Table S8.2. Zero-shear viscosity values of PMeOx-*g*-PVP samples and the corresponding linear analogs in 5 wt %, DI water.

Sample Name	M_n (kg mol^{-1})	Đ	Architecture	Zero-shear viscosity (mPa·s)
5%, 2.5	23	1.61	Graft copolymer	1.3
5%, 5	33.1	1.54	Graft copolymer	1.7
10%, 2.5	33.4	1.78	Graft copolymer	1.6
10%, 5	55.2	1.85	Graft copolymer	2.8
25%, 2.5	56.6	2.67	Graft copolymer	3.3
25%, 5	87.8	2.34	Graft copolymer	3.8
PVP25k	25.1	1.1	Linear	4.2
PVP35k	34.8	1.13	Linear	4.7
PVP55k	55.4	1.14	Linear	6.9
PVP88k	89.7	1.15	Linear	12.9

Chapter 9: Role of Entanglements on the Performance of Branched Polymers as Aqueous Adhesives in Binder Jetting Additive Manufacturing of Pharmaceuticals

Emily M. Wilts[1], Susan Ma[2], Christopher B. Williams[2], and Timothy E. Long[1*]

(Submitting to *Molecules*, **2020**)

[1]Department of Chemistry, Macromolecules Innovation Institute, Virginia Tech, Blacksburg, VA 24061

[2]Department of Mechanical Engineering, Macromolecules Innovation Institute, Virginia Tech, Blacksburg, VA 24061

*To whom correspondence should be addressed: E-mail: telong@vt.edu. TEL: (540) 231-2480

FAX: (540) 231-8517

9.1 Abstract

Personalized dosage pharmaceuticals provide patients with exact dosing based on metabolic and genomic screenings with the avoidance of multi-drug interactions and adverse side-effects from incorrect dosing. Additive manufacturing facilitates the production of oral tablets and implantable devices capable of personalized dosage through its inherently tunable process. Binder jetting advantageously creates oral tablets with the ability to deliver very small doses, usage of common excipients, and the versatility of a multi-material system. However, polymers as adhesives for binders sustain limitations, where the viscosity constraints of binder jetting limit the molecular weight and polymer concentration in the binder. To ameliorate this problem, this manuscript describes designed graft copolymers with low or nonexistent entanglements as polymeric binders, which provided decreased solution viscosity at higher concentrations compared to linear polymers at the same molecular weight. Higher concentrations of polymer fill in interstitial voids and increases the strength of binder jetted parts. Previously, 4-arm star poly(vinyl

pyrrolidone) (PVP) demonstrated an increase in compressive strength compared to linear analogs at the same molecular weight. This manuscript aims to use graft PVP (PMeOx-*g*-PVP), strategically designed to obtain an even lower solution viscosity compared to previous examples. In this study, PMeOx-*g*-PVP in DI water printed at a higher wt %, 14 wt %, compared to linear and 4-arm star analogs, which produced the strongest tablet of the architecture series, 1.6 MPa. Increased critical overlap concentrations (*C**) enabled solutions of PMeOx-*g*-PVP to print at higher concentrations compared to linear and 4-arm star analogs, which also predicted the copolymer maximum jettable concentrations printed on a thermal printhead.

9.2 Introduction

Additively manufactured pharmaceuticals provide healthcare professionals and patients oral doses with complex geometries, personalized amounts of active ingredients, and rapid production.[1–3] Complex geometries enable near zero-order release profiles and precise placements of active ingredients.[4–6] Complex geometries facilitate personalized dosages, drug combinations, and release profiles for individuals based on metabolic rates and current health. Rapid manufacturing of oral doses enables this technology effective in emergency situations and helps the drug development process through reducing production time. These unique advantages improve drug efficacy, reduce side-effects, reduce drug-drug interactions, and reduce the time to commercialize novel pharmceticals.[7] For example, a patient taking five different pills multiple times per day may experience side-effects because of drug interactions and incorrect dosing, while also struggling to remember to take multiple medications. In the future, additive manufacturing will enable this patient to

take one pill, with exact dosing and tailored release rates to improve the patient's overall quality of life.

Binder jetting additive manufacturing (BJ AM) facilitated the first FDA approved printed oral tablet in 2015 called Spritam from Aprecia Pharmaceuticals.[8] BJ AM enables layer-by-layer manufacturing through precise ejection of binder onto a powder bed. After each layer ejection, a roller pushes a new layer of powder over the build area to prepare for subsequent deposits. For pharmaceutical applications, BJ AM provides the precise placement of active pharmaceutical ingredients (API) and adapts excipients already used in the pharmaceutical industry. Two types of printheads, piezoelectric and thermal, enable jetting out of the nozzles. In piezoelectric printheads, an applied voltage creates a mechanical response forcing a drop out of a nozzle.[6,9] Thermal printheads rely on explosive evaporation of solvent to create a vapor bubble, which eject drops out of the nozzle. Previous studies suggest each ejection mechanism requires different binder solution properties for successful jettability.[10]

Binder development requires four dimensionless equations to predict successful jetting called the Reynolds number (*Re*) (**Eqn. 1**), Weber number (*We*) (**Eqn. 2**), Ohnesorge number (*Oh*) (**Eqn. 3**), and Z parameter (*Z*) (**Eqn. 4**). The *Re* number represents the viscosity contribution and predicts sufficient energy to eject a drop while the *We* number represents the surface tension contribution and predicts stable drop formation. In **Eqn. 3**, η, σ, ρ, and α represent solution viscosity, surface tension, density, and nozzle radius, which come together to predict if stable drop formation and successful ejection is possible. The reciprocal of the *Oh* number is the *Z* parameter where a range from 1-10 is considered the jettable range.[6,11,12] Jetting polymeric solutions also requires the

consideration of viscoelastic properties of polymers. Previous studies and predictive models consider polymer relaxation times using the Weissenberg number (*Wi*) and polymer extensibility (*L*) for linear polymers in good solvents.[13–15] Other studies using 4-arm star polymers found the critical overlap concentration (*C**) can also predict maximum jettable concentrations using thermal printheads.[16]

$$Re = \frac{v\rho\alpha}{\eta} \qquad \textbf{Eqn. 1}$$

$$We = \frac{v^2\rho\alpha}{\sigma} \qquad \textbf{Eqn. 2}$$

$$\frac{We^{0.5}}{Re} = Oh\ \# = \frac{\eta}{(\sigma\rho\alpha)^{0.5}} \qquad \textbf{Eqn. 3}$$

$$\frac{1}{Oh} = Z \qquad \textbf{Eqn. 4}$$

While jettability of linear polymer solutions using piezoelectric printheads is well-studied, the investigation of varying architectures of polymers using a thermal printhead is lacking. Wilts *et. al.* demonstrated *C** predicted the maximum jettable concentration of linear and 4-arm poly(vinyl pyrrolidone) (PVP) at molecular weights from 5 to 50 kg mol^{-1}. They also found 4-arm star polymers provided lower solution viscosities, enabling higher polymer concentrations, and thus stronger printed tablets compared to linear analogs.[16] Branched and graft copolymers also possess lower solution viscosities compared to linear analogs because of the more compact sizes and low entanglements.[17–19] Investigating these architectures and other compact polymer architectures to produce stronger printed tablets and create predictive jettability qualifications will continue to expand the toolbox of novel materials for AM.

This manuscript describes binder jetting AM with a thermal printhead of graft poly(2-oxazoline) and poly(vinyl pyrrolidone) copolymers (PMeOx-*g*-PVP) as polymeric adhesives for personalized dosage pharmaceuticals. The reported data adds to and complements previous binder jetting AM studies using linear and 4-arm star PVP and demonstrates the success in using varying polymer architectures as binders for stronger printed parts.[16] To predict jettability in DI water, this manuscript showed the calculation and measurement of both the *Z* parameter and *C**, which both predict printability using thermal printheads. Next, compression testing and porosity experiments revealed higher concentrations of polymer in the binder formulation resulted in increased compressive strength and decreased porosity. Solution viscosity experiments revealed *C** values for each graft PVP combination and subsequent printing demonstrated the maximum jettable wt % resonated around *C**. Thermogravimetric sorption analysis revealed water uptake of the graft copolymers and the tablets, where the powder adsorption properties predominately governed this property. Throughout the manuscript, comparison between linear, 4-arm star, and graft PVP revealed the advantages of utilizing lower viscosity and lower entanglement polymer architectures for stronger printed parts.

9.3 Experimental

9.3.1 Materials

Diisopropylamine and methyl oxazoline were purchased from Sigma Aldrich and distilled over calcium hydride before use. *N*-butyl-lithium, allyl bromide, methyl triflate, piperidine, vinyl pyrrolidone, *O*-ethyl xanthic acid potassium salt, and 1-bromo ethyl benzene were purchased from Sigma Aldrich and used without further purification. Diphenyl(2,4,6-

trimethylbenzoyl)phosphine oxide (TPO) was purchased from Sigma Aldrich and recrystallized over methanol before use. Extra dry acetonitrile, chloroform, tetrahydrofuran, dichloromethane, methanol, and acetone were purchased from Acros and used without further purification.

9.3.2 Graft copolymer synthesis (PMeOx-*g*-PVP)

The following synthetic procedure was adopted from Wilts *et. al.* and only the final steps are noted for conciseness.[20] A copolymer of poly(2-methyl-2-oxazoline) and poly[2-(3-butenyl)-2-oxazoline]) with 10 mol % poly[2-(3-butenyl)-2-oxazoline]) (1 g, $1 \cdot 10^{-4}$ mol, 1 eq.) was combined with diphenyl(2,4,6-trimethylbenzoyl)phosphine oxide (TPO) (9.7 mg, 0.3 eq.) and dissolved in chloroform (15 wt % solids). The mixture was added to a solution of thiol-terminated PVP (2 g, $4 \cdot 10^{-4}$ mol, 15 wt % solids) and purged with nitrogen for 30 min. The flask was exposed to a broad spectrum (320-500 nm) UV light for 10 min and stirred for an additional 24 h. The residual solvent was removed under reduced pressure and the product was dissolved in methanol. The solution was subjected to dialysis for five days against methanol with a 3.5 kg mol^{-1} pore cut off. After five days the methanol was removed, and the product was precipitated into diethyl ether and dried under high vacuum at 80 ^{o}C.

9.3.3 Binder Preparation

As an example, procedure to produce a 5 wt % solution, 5 g of polymer was dissolved and stirred with a magnetic stir bar in 95 g of DI water for 10-15 min until the polymer was fully dissolved. After the polymer was dissolved, the surfactant, Tween 20®, was added to lower surface tension and the mixture was stirred for an additional 30 min. After any

bubbles dissipated, the binder was filtered through a PTFE 2.2 μm filter and used immediately.

9.3.4 Powder Preparation

To achieve a smaller particle size distribution and remove larger powders that may cause inconsistent spreading, the lactose was first sifted to <80 μm. To combine the lactose, powdered sugar, and silica, the powders were placed in a cylindrical container and mixed on a Waverly TR-E roller for 20 min. The powder was placed into and tested on the ZCorp Spectrum Z510 3D printer to ensure the roller created a flat, consistent surface. A ratio of 4:1 lactose:powdered sugar wt:wt was used for every tablet system, and 5 wt % of silica was added to increase spreadability.

9.3.5 Analytical

Aqueous SEC was conducted in a 54/23/23 v/v/v mixture of DI water, methanol, and glacial acetic acid with 0.1 M sodium acetate at a pH=4. A Waters Breeze Aqueous SEC with Wyatt miniDAWN treos light scattering and Waters 2414 RI detector with poly(ethylene oxide) (PEO) standards determined absolute molecular weight of each system. Solution viscosity experiments were performed on a DHR Discovery Rheometer in steady state mode with a Peltier plate and concentric cylinder geometries at 20 ^{o}C where n=3. Shear sweeps were conducted from 1-1200 s^{-1} at a 300 or 5000 μm gap with a solvent trap equipped with slightly saturated sponges. Pendant drop experiments were performed on a FTA 200 Contact Angle Analyzer with a 3 mL 30-gauge syringe. FTA Operator's Software was used to fit the droplet shape to the Young-Laplace equation and yield the liquid-to-air interface surface tension where n=4. Density of the binder solutions was

determined through micro-pipetting 1 mL of binder and subsequently weighing the sample, n=5. Compression testing was performed on each printed tablet with a crosshead motion of 1.3 mm min^{-1} on an Instron 4204 with a 1 kN load cell, n=10. Young's modulus was calculated from the slope of the linear elastic region of the stress vs. strain curve, and compressive strength was denoted as the largest stress at the yield point. ^{1}H NMR spectroscopy was conducted on a Varian Unity 400 MHz in D_2O and $DMSO_{d6}$. Scanning electron microscopy (SEM) images were taken on a Joel NeoScope JCM-5000 Benchtop SEM, under high vacuum at a 10 kV accelerating voltage. Water-uptake was performed on a TA Instruments Q5000 DA Thermogravimetric Sorption Analyzer from 0 to 95% humidity. A micromeritics AccuPyc II 1340 Gas Pycnometer measured apparent density using ultra-pure Helium gas. The porosity of the tablets was calculated using **Eqn. 5,** where the bulk density was calculated using the weight and dimensional measurements of each sample.

$$porosity\ \% = \left(1 - \frac{bulk\ density}{apparent\ density}\right) x\ 100 \qquad \textbf{Eqn. 5}$$

9.3.6 Binder Jetting

A Z-Corp Spectrum Z510 3D printer with a HP 11 printhead (11 μm nozzle radius) conducted all tablet and shape printing. A model of a cylindrical tablet with a 12 mm diameter and 3 mm height was constructed on Zprint software. The part was printed at 0.005 inch layer thickness and 100 saturation where the part was left in the printer after completion for 40 min at 60 ^{o}C before removal.

9.3.7 Water Dissolution

Each printed tablet was placed in DI water at 1 mg mL^{-1} at 37 ^{o}C with a magnetic stir bar to test the dissolution properties. Dissolution was detected after the tablet and its particles were no longer visible and the solution was clear.

9.3.8 API Determination

This procedure was adopted from Wilts *et. al.*[16] and in short, ^{1}H NMR spectroscopy on a Varian Unity 400 MHz in D_2O determined the amount of API in each tablet. As an example, the 10 wt % API loaded tablets were printed and analyzed as follows. Lactose, powdered sugar, and acetaminophen (API) were all dried at 60 ^{o}C for 24 h before use. The powders were mixed at a ratio of lactose:powdered sugar:acetaminophen 75:15:10 wt:wt:wt and subsequently printed. Samples from the four quadrants and top of and bottom of the tablets were isolated about dissolved in $DMSO_{d6}$. A known amount of methyl benzoate was added to each mixture as an internal standard. To determine the amount of acetaminophen, the integration of the aromatic peaks on methyl benzoate (8.0-8.2, 3H, m) was compared to the aromatic peaks on acetaminophen (6.7, 2H, m; 7.4, 2H, m). An average of each quadrant and the top and bottom of the tablets was used to determine the total acetaminophen amount to ensure an even distribution of API throughout the tablet.

9.3.9 Statistical Analysis

Minitab 18 statistical software measured statistical differences between samples at 95% confidence with an ANOVA test followed by a Tukey's HSD.

9.3.10 Nomenclature

The six polymers in the discussed graft copolymer series follow the naming sequence “xx%, yy” where “xx” represents the mol % grafting sites and “yy” represents the PVP graft

molecular weight, displayed in **Table 9.1**. The six polymers contain 5, 10, and 25 mol % grafting sites and 2.5 and 5 kg mol^{-1} PVP grafts.

Table 9.1 Summary of graft copolymer nomenclature.

Name	M_n PVP (kg mol^{-1})	Me:Ene mol %
5%, 2.5	2.5	95:5
5%, 5	5	95:5
10%, 2.5	2.5	90:10
10%, 5	5	90:10
25%, 2.5	2.5	75:25
25%, 5	5	75:25

9.4 Results and Discussion

Wilts *et. al.* first reported the synthesis of PMeOx-*g*-PVP using thiol-ene click chemistry to covalently attach PVP grafts to a poly(2-oxazoline) backbone, depicted in **Scheme 9.1**.[20] The copolymerization of 2-methyl-2-oxazoline and 2-(3-butenyl)-2-oxazoline created a gradient copolymer, where 2-(3-butenyl)-2-oxazoline reacted slower than 2-methyl-2-oxazoline, resulting in a concentration of vinyl-containing units at the terminal chain end. Even with the gradient structure of the backbone, 100% substitution of the PVP grafts was achieved with 2.5 kg mol^{-1} PVP grafts and backbones containing 5 and 10 mol % grafting sites. Samples with 25 mol % grafting sites resulted in incomplete substitution of the PVP grafts, at 76 and 64% with 2.5 and 5 kg mol^{-1} PVP grafts, respectively. Even with incomplete substitution in some combinations, the graft copolymers resulted in lower solution viscosities compared to PVP linear analogs at the same total molecular weight. These viscosity advantages render the discussed systems ideal

for binder jetting to achieve a higher polymer loading in the binder solution without exceeding the viscosity limit.

Scheme 9.1. Synthesis of PMeOx-*g*-PVP using thiol-ene 'click' chemistry.

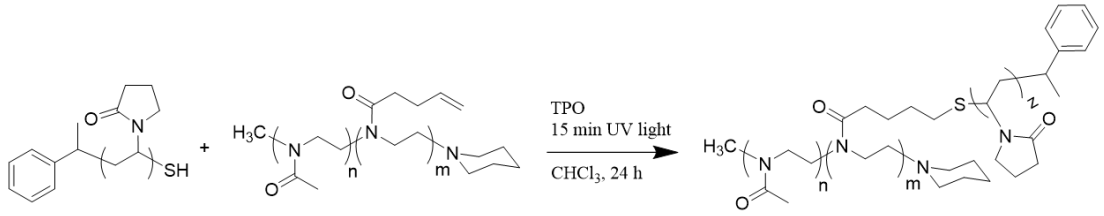

PVP-SH PMeEneOx PMeOx-*g*-PVP

The motivation to use the described graft copolymers for BJ AM of personalized dosage pharmaceuticals stems from decreased solution viscosity and increased critical overlap concentration (*C**) in some combinations compared to linear and 4-arm star analogs. The biocompatible components also enabled a safe polymer adhesive for ingestion. Wilts *et. al.* described a study using linear and 4-arm star PVP to show *C** may act as the maximum jettable wt % in BJ AM when using thermal printheads. 4-Arm star exhibited higher *C** values compared to linear analogs at the same molecular weights, enabling higher concentrations in the binder, filling in more powder void spaces, and thus producing a stronger printed part.[16] The higher *C** value of the 4-arm star PVP samples stems from the smaller hydrodynamic radius (R_g).[21,22] Graft copolymers enable tunability of R_g and entanglements through length of backbone and length of grafts. Some combinations in this study, for example 10%, 2.5, experienced a higher *C** compared to 4-arm star analogs and thus was printed at a higher concentration compared to linear and 4-arm star examples. Poly(2-oxazoline)s and PVP are also already used for biomedical applications such as drug

delivery and implantable devices, which renders these copolymers possibly suitable for personalized dosage pharmaceuticals.

The backbone length and length of arms contribute to designing the compactness of the polymer structure and ability to entangle. When comparing branched and linear polymers at the same molecular weight, the branched polymer will exhibit a smaller hydrodynamic radius and therefore will exhibit lower melt and solution viscosities. This effect grows with inclusion of additional branches or arms.[23,24] The ability for branched polymers to entangle depends solely on the molecular weight of the branch or arm. Long chain branching will increase viscosity because more entanglements per chain exist. Alternatively, short chain branching hinders entanglement through inefficient packing and steric hinderances preventing interactions.[25,26] When designing the graft copolymers, both compactness and ability to entangle dictated the chemical structure to create lower solution viscosities compared to linear and 4-arm star analogs. A comprehensive study of 5, 10, and 25 mol % grafting combined with low arm length, 2.5 and 5 kg mol^{-1}, uncovered the optimal structure for a low viscosity, high concentration binder.

Figure 9.1 depicts solution viscosity at 1000 s^{-1}, the estimated shear rate for jetting,[27] and the *Z* parameter for each graft copolymer composition in DI water at 5 and 10 wt %. **Figure 9.1A** demonstrates the solution viscosity at 1000 s^{-1} where it increases with increasing concentration. Solution viscosity also increases with increasing total molecular weight, mol % grafting sites, and wt % PVP in the copolymer composition. Depicted in **Figure 9.1B,** these values combined with the measured surface tension, density, and nozzle radius enabled the calculation of the *Z* parameter for each solution according to **Eqn. 4**. The surface tension and density of each combination ranged from 35.1-46.2 mN

m^2 and 1.05-1.1 g mL^{-1}, respectively. The main factor of variation in *Z* parameter was viscosity and as seen in **Figure 9.1B**, where the *Z* parameter decreased with increased solution viscosity. The ideal printable range for the *Z* parameter is hypothesized to be 1-10, but recent literature suggests depending on the contents of the binder, for example small molecules, polymers or ceramic particles, this ideal printable range may vary.[9,10,12,28–32]

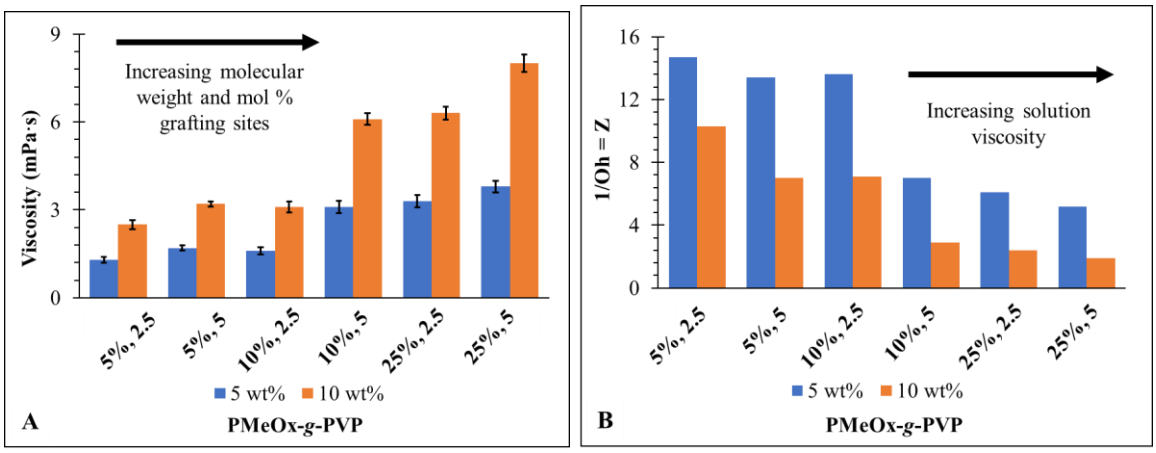

Figure 9.1. (A) Solution viscosity as a function of PMeOx-*g*-PVP composition and **(B)** Z parameter as a function of PMeOx-*g*-PVP composition.

While the *Z* parameter is important when predicting binder jettability, viscoelastic properties of polymeric solutions also need to be considered. Wilts *et. al.* compared jettability of linear and 4-arm star PVP and found the critical overlap concentration (*C**) predicted binder jettability using thermal printheads.[16] Other examples of exploring polymer viscoelasticity in relation to jetting include Hutchings *et. al.*, who investigated jetting of dilute polymer solutions. Based on the polymeric solution Weissenberg number (*Wi*) and polymer extensibility (*L*), a quantitative model was developed to predict jettability of the investigated solutions.[33,34] While the *Z* parameter predicts common viscosity and surface tension ratios for printability, the ideal range, 1 – 10, was determined using binders

containing ceramic particles with a piezoelectric printhead. Other studies explored the differences in ideal *Z* parameter ranges using small molecules, ceramic particles, and polymers in the binder and also investigating the difference between piezoelectric and thermal printheads.[10,12,35]

Figure 9.2 depicts the specific viscosity (η_{sp}) as a function of concentration of 10%, 2.5 and 25%, 5 as examples in DI water, where *C** is noted through the dashed lines. When plotting η_{sp} as a function of concentration, linear, neutral polymers experience four main viscoelastic regimes where changes in the power law slope denotes the beginning and end of each regime. The dilute and semi-dilute unentangled regimes physically represent where dissolved polymer chains do not overlap, transitioning to chain overlap, which causes an increase in viscosity.[19,36–38] In extensive studies of solution viscosity of branched polymers, the slope of a η_{sp} as a function of concentration in entangled species should not fit linearly to the power law, but rather increase exponentially. The graft copolymers discussed do not exhibit an exponential increase in η_{sp} as a function of concentration and therefore likely lack entanglements or the potential to entangle.[25,26,39,40] **Figure 9.2** shows the first two regimes where the interface represents the critical overlap concentration (*C**). Above *C** denotes when a polymeric solution begins to exhibit viscoelastic properties and thus is further used to predict jettability in this study.

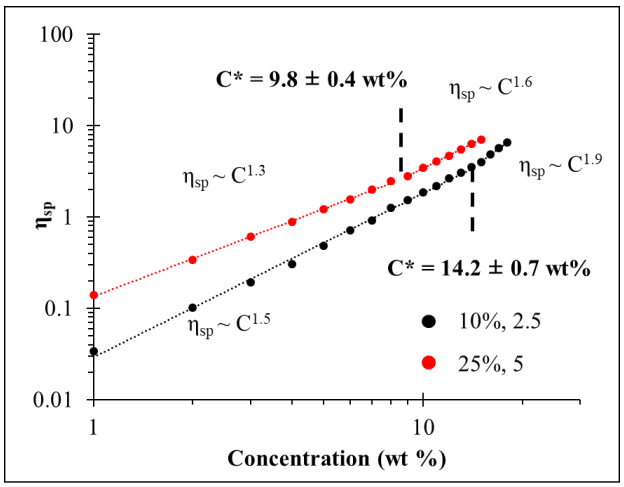

Figure 9.2. Specific viscosity (η_{sp}) as a function of concentration of 10%, 2.5 and 25%, 5 where the inflection point denotes *C**.

Figure 9.3A depicts the compressive strength results of tablets made with each graft copolymer at 5 and 10 wt % in DI water. Each tablet exhibited compressive strengths above 0.4 MPa, which is the industry standard to survive recoating processes, shipping, and storing.[41] Across all samples, tablets printed with a concentration of 10 wt % compared to 5 wt % exhibited an average of 0.61 MPa larger in compressive strength. This suggests the higher concentration is filling in powder void spaces and increasing the compressive strength. Binder jetted tablets are an example of a homogenous porous material and fails through compression via progressive microfracturing. Each microfracture begins at a void space, thus larger sizes and increased void spaces in a porous structure induce weaker parts.[42,43] Filling spaces will decrease the voids and thus increase the compressive strength. It should also be noted that the volume of drops will vary with different viscosities, but the differences were determined to be negligible for this study.

Figure 9.3B demonstrates the effectiveness of PMeOx-*g*-PVP as a polymeric adhesive for BJ AM, showing a comparison of the compressive strength of tablets printed with linear, 4-arm star, and graft PVP in DI water as binders with data repeated from Wilts *et. al.*[16] A ZCorp printer attempted to print linear (25 kg mol^{-1}), 4-arm star (25 kg mol^{-1}), and 10%, 2.5 (35 kg mol^{-1}), at 5 and 10 wt %. 4-Arm star PVP and 10%, 2.5 both printed at 10 wt %, but linear PVP did not. This is due to linear PVP exhibiting a C^* value of 6 wt %, and therefore failed to jet at 10 wt %. This emphasizes the advantages of using varying architectures for BJ AM as the decreased viscosity allows for higher polymer concentrations, and thus stronger printed parts.

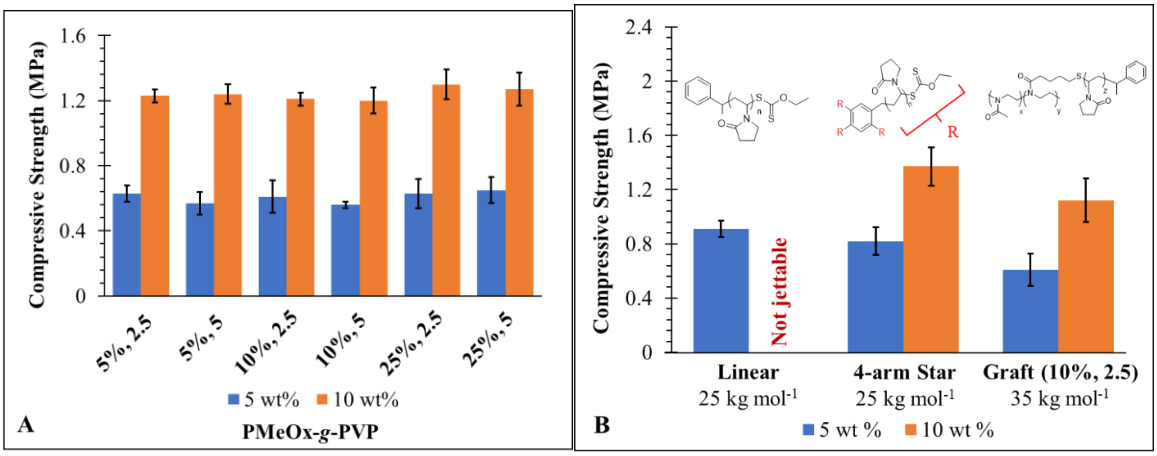

Figure 9.3. (A) Compressive strength as a function of PMeOx-*g*-PVP composition and **(B)** compressive strength comparison of linear, 4-arm star, and graft PVP at similar molecular weights. (Data reproduced with permission from Wilts et. al.[16])

A gas pycnometer measured the apparent density of each tablet to identify whether the increased polymer concentration in the binder resulted in lower apparent density in the tablets, and thus lower porosity. **Figure 9.4A** depicts the porosity calculations, according to **Eqn. 5**, of tablets printed from 5%, 2.5, 10%, 2.5, and 25%, 2.5 at 5 at 10 wt %. The

tablets printed with 5 wt % polymer resulted in a higher porosity compared to 10 wt %. At 10 wt %, more polymer filled powder void spaces and thus created parts with lower porosity. As discussed previously, this decrease in porosity also resulted in stronger tablets because of the lower potential to fail through microcracking, which begins at void spaces. Consistent with literature and common porosity values for binder jetted parts, these tablets experienced 67 to 62% porosity.[44] Other tablets that do not function as immediate release pills made through compression molding experience 7 to 51% porosity.[45] **Figure 9.4B** depicts a tablet porosity comparison printed with linear, 4-arm star, and graft PVP. The different polymer architectures did not produce a difference in porosity, but the increased wt % polymer in the binder, only available at 10 wt % with 4-arm star and graft PVP, resulted in decreased porosity.

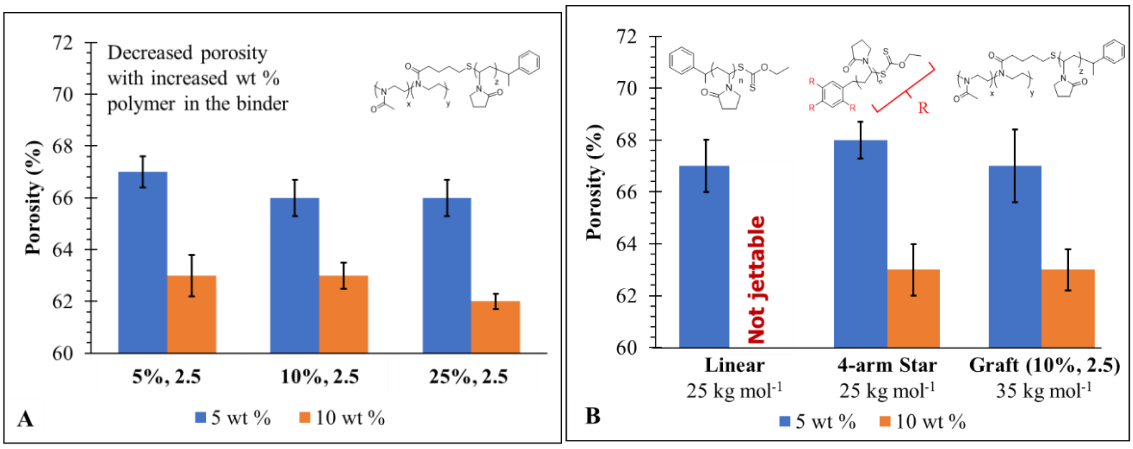

Figure 9.4. (A) Porosity % as a function of graft copolymer composition and **(B)** porosity % as a function of linear, 4-arm star, and graft PVP at comparable molecular weights. (Data reproduced with permission from Wilts et. al.[16])

BJ AM tablets are highly porous and optimal for immediate release oral pills. The excipient porosity and hydrophilicity help the tablet dissolve immediately on the tongue to

help patients who have difficulty swallowing pills. The tablets dissolved completely in DI water with a magnetic stirrer from 15 to 25 s (**Table S9.2**), which is optimal for immediate release tablets and consistent with previous dissolution rates reported.[46] The excipient composition mainly controlled the water dissolution and these results did not show statistically different dissolution rates depending on polymer concentration in the binder or graft copolymer compositions.

After measuring *C** values for each graft copolymer composition, a total of six concentrations ranging from 4 wt % below and above *C** were tested on the ZCorp printer to identify jettability. Complete failure or only partial jetting out of the nozzle resulted in a non-jettable result. **Figure 9.5A** depicts *C** values and the maximum jettable wt % as a function of graft copolymer composition. The black circles denote the maximum jettable wt % of each composition, which remained at or below *C**. After the *C** transition, polymer chains begin to overlap causing an increase in viscosity and the beginning of viscoelastic properties. The inability to jet above *C** using thermal printheads may be a result of the jetting process inability to overcome viscoelastic effects of the polymeric solution. *C** may better predict maximum jettable concentrations for polymer solutions using thermal printheads as opposed to the Z parameter. However, literature describes instances where more concentrated polymer solutions with complex rheological behavior and above *C** jet on piezoelectric printheads with larger nozzle diameters.[13,47]

Figure 9.5B depicts 10%, 2.5 in DI water jetted from 5 to 16 wt % where the maximum jettable wt % was 14 wt %. This binder combination did not jet over 14 wt % because it could not exceed the *C** value. This combination represented the strongest tablet produced, owing to its ability to print at a larger wt % and the high wt % of PVP in the

graft copolymer composition. 5%, 2.5 jetted at 18 wt %, which resulted in tablet a compressive strength of 1.49 MPa. This graft copolymer combination contains 55 wt % PVP with a glass transitions temperature (T_g) of 87 ^oC compared to 10%, 2.5 at 71 wt % PVP and a T_g of 95 ^oC.[20] These chemical and thermal differences may account for the decreased compressive strength of 5%, 2.5 printed at 18 wt % compared to 10%, 2.5 printed at 14 wt %.

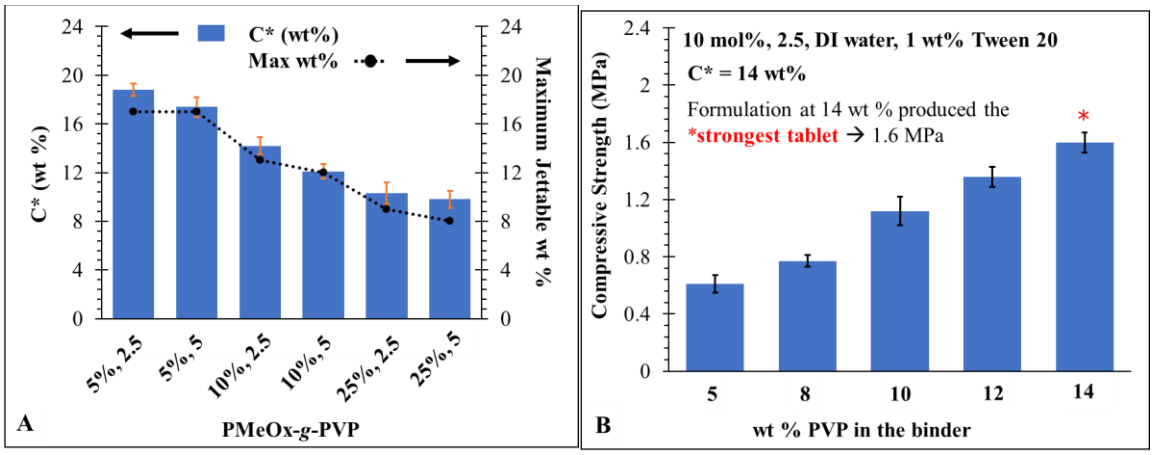

Figure 9.5. (A) Maximum jettable wt % of polymer in each binder formulation as a function of the PMeOx-*g*-PVP C* values and **(B)** compression strength as a function of wt % PVP in the binder of 10%, 2.5 to demonstrate the stronger tablet produced from this study.

Figure 9.6 depicts images of binder jetted parts printed with 10%, 2.5 at 10 wt %. **Figure 9.6A** and 9.**6B** illustrate the tablets used for compression and porosity testing where the dimensional accuracy remained below 3% error in 3-dimensions. **Figures 9.6C, D, E,** and **F** depict other binder jetted shapes to demonstrate the versatility and effectiveness of the binder.

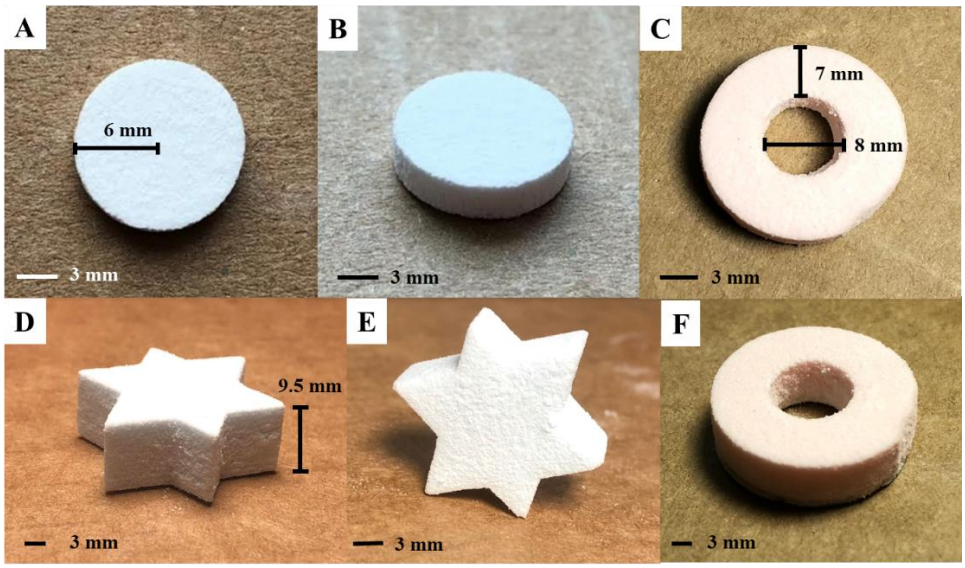

Figure 9.6. **(A, B)** Image of a binder jetted tablet, the shape and size used for compression and porosity testing, **(C, F)** a printed ring, and **(D, E)** a printed star to demonstrate varying printed geometries. All tablets were printed with 10%, 2.5, 10 wt %, in DI water with 1 wt % Tween 20.

Another consideration when manufacturing, packaging, and shipping oral tablets is the hydroscopic properties of the materials. If a tablet absorbs water in any part of the process, it could affect the strength and release rate of the pill. A thermogravimetric sorption analyzer (TGA-SA) measured the weight gain of select, neat graft copolymers and printed tablets of humidity levels from 0 to 100%. **Figure 9.7** depicts the weight gain from water as a function of relative humidity of the two powder components, powdered sugar and lactose, 25%, 2.5, and a tablet printed with 10 wt % 25%, 5. Powdered sugar and lactose both begin adsorbing water at 70% relative humidity and gain 22 and 19% compared to the original sample weight, respectively. 25%, 2.5 begins to adsorb water at 10% relative humidity and gained 80% water total at 95% relative humidity. The printed

tablet manufactured with 10 wt % 25%, 5 began absorbing water at 60% relative humidity and gained a total of 32% water at 95% humidity. This data reveals the powder components of the pill mainly control the hydroscopic properties of the tablet because the powders represent >95% of the total weight of the printed part.

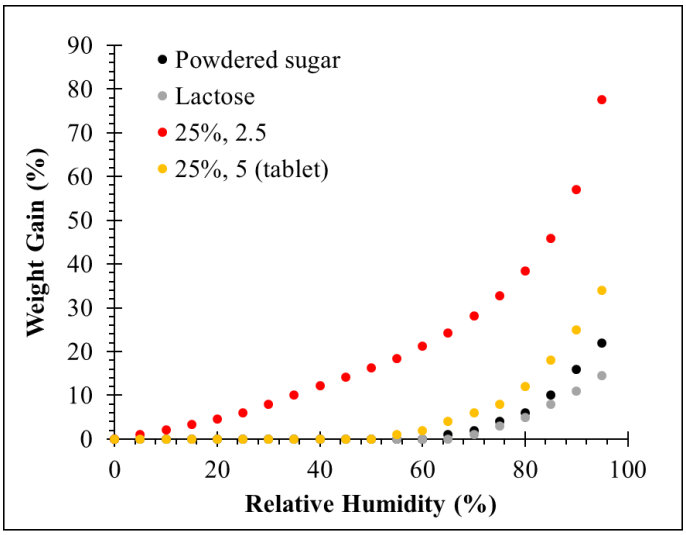

Figure 9.7. TGA-SA results depicting weight gain of water (%) as a function of relative humidity.

Incorporation of an API into the tablet demonstrated the discussed powder and binder combinations as feasible for personalized dosage pharmaceuticals. Inclusion of Acetaminophen into the powder bed at 5, 10, 25, and 50 wt % (**Figure S9.2**) demonstrated the ability to include API into tablets. This wt % range represents a total of 10, 20, 50, and 100 mg of API, which demonstrates the tunability of the tablet making process. ^{1}H NMR spectroscopy with a methyl benzoate standard confirmed the amount of Acetaminophen in the top, bottom, and four quadrants of the tablet to ensure proper mixing occurred and the API was eventually distributed throughout the tablet. At each wt %, the tablet contained the same amount inputted into the powder bed within 1.2% error.

9.5 Conclusions

This manuscript described using graft poly(vinyl pyrrolidone) (PVP) as a polymeric binder for BJ AM to create stronger printed tablets for personalized dosage pharmaceuticals compared to previous examples. The critical overlap concentration (*C**) predicted the maximum jettable concentration of polymers for successful jetting. Solution rheology and pendant drop experiments enabled the calculation of the *Z* parameter, which when printed did not adhere to the acceptable jettable range of 1-10. Determination of *C** enabled the consideration of viscoelastic properties of polymer solutions and accurately predicted the maximum jettable concentrations of each graft copolymer solution. 10%, 2.5 performed better than linear and 4-arm star PVP analogs where the maximum jettable concentrations depended on *C**. 10%, 2.5, 4-arm star and linear PVP experienced *C** values of 14, 10, and 7 wt %, respectively which enabled 10%, 2.5 to jet at 14 wt %. This combination created the strongest tablet compared to linear and 4-arm star analogs at 1.6 MPa. This study further investigated using more compact and low-entanglement polymer architectures compared to linear analogs that possess a lower *C**, jet at higher concentrations, and thus create stronger printed parts.

9.6 Acknowledgements

The authors would like to thank Candace Wall, Dr. Charles Carfagna, Katherine Heifferon, and Ashwath Kumar for conducting surface tension experiments, conducting aqueous SEC experiments, helping with TGA-SA experiments and helpful binder jetting AM discussions, respectively.

9.7 References

(1) Yu, D. G.; Zhu, L.-M.; Branford-White, C. J.; Yang, X. L. Three-Dimensional Printing in Pharmaceutics: Promises and Problems. *J. Pharm. Sci.* **2008**, *97* (9), 3666–3690. https://doi.org/10.1002/jps.21284.

(2) Moulton, S. E.; Wallace, G. G. 3-Dimensional (3D) Fabricated Polymer Based Drug Delivery Systems. *J. Control. Release* **2014**, *193*, 27–34. https://doi.org/10.1016/J.JCONREL.2014.07.005.

(3) Cohen, J. S. Ways to Minimize Adverse Drug Reactions. *Postgrad. Med.* **1999**, *106* (3), 163–172. https://doi.org/10.3810/pgm.1999.09.688.

(4) Alhnan, M. A.; Okwuosa, T. C.; Sadia, M.; Wan, K.-W.; Ahmed, W.; Arafat, B. Emergence of 3D Printed Dosage Forms: Opportunities and Challenges. *Pharm. Res.* **2016**, *33* (8), 1817–1832. https://doi.org/10.1007/s11095-016-1933-1.

(5) Goole, J.; Amighi, K. 3D Printing in Pharmaceutics: A New Tool for Designing Customized Drug Delivery Systems. *Int. J. Pharm.* **2016**, *499* (1–2), 376–394. https://doi.org/10.1016/J.IJPHARM.2015.12.071.

(6) Prasad, L. K.; Smyth, H. 3D Printing Technologies for Drug Delivery: A Review. *Drug Dev. Ind. Pharm.* **2016**, *42* (7), 1019–1031. https://doi.org/10.3109/03639045.2015.1120743.

(7) Norman, J.; Madurawe, R. D.; Moore, C. M. V.; Khan, M. A.; Khairuzzaman, A. A New Chapter in Pharmaceutical Manufacturing: 3D-Printed Drug Products. *Adv. Drug Deliv. Rev.* **2017**, *108*, 39–50. https://doi.org/10.1016/j.addr.2016.03.001.

(8) rebuffs Monsanto, S. First 3D-Printed Pill. *Nature* **2015**, *33*, 1014.

(9) Reis, N.; Ainsley, C.; Derby, B. Ink-Jet Delivery of Particle Suspensions by Piezoelectric Droplet Ejectors. *J. Appl. Phys.* **2005**, *97* (9), 094903. https://doi.org/10.1063/1.1888026.

(10) Özkol, E.; Ebert, J.; Telle, R. An Experimental Analysis of the Influence of the Ink Properties on the Drop Formation for Direct Thermal Inkjet Printing of High Solid Content Aqueous 3Y-TZP Suspensions. *J. Eur. Ceram. Soc.* **2010**, *30* (7), 1669–1678. https://doi.org/10.1016/J.JEURCERAMSOC.2010.01.004.

(11) Fromm, J. E. Numerical Calculation of the Fluid Dynamics of Drop-on-Demand Jets. *IBM J. Res. Dev.* **1984**, *28* (3), 322–333. https://doi.org/10.1147/rd.283.0322.

(12) Derby, B. Inkjet Printing Ceramics: From Drops to Solid. *J. Eur. Ceram. Soc.* **2011**, *31* (14), 2543–2550. https://doi.org/10.1016/J.JEURCERAMSOC.2011.01.016.

(13) Hoath, S. D.; Harlen, O. G.; Hutchings, I. M. Jetting Behavior of Polymer Solutions in Drop-on-Demand Inkjet Printing. *J. Rheol. (N. Y. N. Y).* **2012**, *56* (5), 1109–1127.

https://doi.org/10.1122/1.4724331.

(14) Vadillo, D. C.; Tuladhar, T. R.; Mulji, A. C.; Jung, S.; Hoath, S. D.; Mackley, M. R. Evaluation of the Inkjet Fluid's Performance Using the "Cambridge Trimaster" Filament Stretch and Break-up Device. *J. Rheol. (N. Y. N. Y).* **2010**, *54* (2), 261–282. https://doi.org/10.1122/1.3302451.

(15) Hoath, S. D.; Vadillo, D. C.; Harlen, O. G.; McIlroy, C.; Morrison, N. F.; Hsiao, W.-K.; Tuladhar, T. R.; Jung, S.; Martin, G. D.; Hutchings, I. M. Inkjet Printing of Weakly Elastic Polymer Solutions. *J. Nonnewton. Fluid Mech.* **2014**, *205*, 1–10. https://doi.org/10.1016/J.JNNFM.2014.01.002.

(16) Wilts, E.; Ma, D.; Bai, Y.; Williams, C. B.; Long, T. E. Comparison of Linear and 4-Arm Star Poly(Vinyl Pyrrolidone) for Aqueous Binder Jetting Additive Manufacturing of Personalized Dosage Tablets. *ACS Appl. Mater. Interfaces* **2019**, acsami.9b08116. https://doi.org/10.1021/acsami.9b08116.

(17) Ronda Plummer; David J. T. Hill, and; Whittaker*, A. K. Solution Properties of Star and Linear Poly(N-Isopropylacrylamide). **2006**. https://doi.org/10.1021/MA0614545.

(18) Roovers, J. Dilute Solution Properties of Regular Star Polymers. *Plast. Eng.* **1999**, *53*, 285–341.

(19) Matthew G. McKee, †; Garth L. Wilkes, ‡; Ralph. H. Colby, § and; Timothy E. Long*, †. Correlations of Solution Rheology with Electrospun Fiber Formation of Linear and Branched Polyesters. **2004**. https://doi.org/10.1021/MA035689H.

(20) Wilts, E.M.; Long, T. E. Synthesis and Characterization of Graft Poly(2-Oxazoline) and Poly(Vinyl Pyrrolidone) Copolymers Using Thiol-Ene 'Click' Chemistry. *J. Polym. Sci. Part A Polym. Chem.* **2020**, *submitted*.

(21) Kilb, R. W.; Bueche, A. M. Solution and Fractionation Properties of Graft Polymers. *J. Polym. Sci.* **1958**, *28* (117), 285–294. https://doi.org/10.1002/pol.1958.1202811704.

(22) N. Hadjichristidis, M. P., Hermis Iatrou, P. Driva, M. Chatzichristidi, Georgios Sakellariou, D. J. Lohse. No Title. *Encyclopedia Of Polymer Science and Technology*; Wiley and Sons Inc., 2010.

(23) Roovers, J.; Zhou, L. L.; Toporowski, P. M.; van der Zwan, M.; Iatrou, H.; Hadjichristidis, N. Regular Star Polymers with 64 and 128 Arms. Models for Polymeric Micelles. *Macromolecules* **1993**, *26* (16), 4324–4331. https://doi.org/10.1021/ma00068a039.

(24) Held, D.; Müller, A. H. E. Synthesis and Solution Properties of Star-Shaped Poly(Tert-Butyl Acrylate). *Macromol. Symp.* **2000**, *157* (1), 225–238. https://doi.org/10.1002/1521-3900(200007)157:1<225::aid-masy225>3.0.co;2-1.

(25) Fetters, L. J.; Kiss, A. D.; Pearson, D. S.; Quack, G. F.; Vitus, F. J. Rheological Behavior of Star-Shaped Polymers. *Macromolecules* **1993**, *26* (4), 647–654. https://doi.org/10.1021/ma00056a015.

(26) Richter, D.; Stühn, B.; Ewen, B.; Nerger, D. Collective Relaxation of Star

Polymers-A Neutron Spin-Echo Study. *Phys. Rev. Lett.* **1987**, *58* (23), 2462–2465. https://doi.org/10.1103/PhysRevLett.58.2462.

(27) Friederich, A.; Binder, J. R.; Bauer, W. Rheological Control of the Coffee Stain Effect for Inkjet Printing of Ceramics. *J. Am. Ceram. Soc.* **2013**, *96* (7), 2093–2099. https://doi.org/10.1111/jace.12385.

(28) Jang, D.; Kim, D.; Moon, J. Influence of Fluid Physical Properties on Ink-Jet Printability. *Langmuir* **2009**, *25* (5), 2629–2635. https://doi.org/10.1021/la900059m.

(29) Mckinley, G. H. *Dimensionless Groups For Understanding Free Surface Flows of Complex Fluids*; 2005.

(30) Nallan, H. C.; Sadie, J. A.; Kitsomboonloha, R.; Volkman, S. K.; Subramanian, V. Systematic Design of Jettable Nanoparticle-Based Inkjet Inks: Rheology, Acoustics, and Jettability. *Langmuir* **2014**, *30* (44), 13470–13477. https://doi.org/10.1021/la502903y.

(31) Liu, Y.; Derby, B. Experimental Study of the Parameters for Stable Drop-on-Demand Inkjet Performance. *Phys. Fluids* **2019**, *31* (3), 032004. https://doi.org/10.1063/1.5085868.

(32) Hoath, S. D.; Harlen, O. G.; Hutchings, I. M. Jetting Behavior of Polymer Solutions in Drop-on-Demand Inkjet Printing. *J. Rheol. (N. Y. N. Y).* **2012**, *56* (5), 1109–1127. https://doi.org/10.1122/1.4724331.

(33) Hoath, S. D.; Hutchings, I. M.; Martin, G. D.; Tuladhar, T. R.; Mackley, M. R.; Vadillo, D. Links Between Ink Rheology, Drop-on-Demand Jet Formation, and Printability. *J. Imaging Sci. Technol.* **2009**, *53* (4), 041208. https://doi.org/10.2352/J.ImagingSci.Technol.2009.53.4.041208.

(34) Clasen, C.; Plog, J. P.; Kulicke, W.-M.; Owens, M.; Macosko, C.; Scriven, L. E.; Verani, M.; McKinley, G. H. How Dilute Are Dilute Solutions in Extensional Flows? *J. Rheol. (N. Y. N. Y).* **2006**, *50* (6), 849–881. https://doi.org/10.1122/1.2357595.

(35) Ozkol, E. €. Rheological Characterization of Aqueous 3Y-TZP Inks Optimized for Direct Thermal Ink-Jet Printing of Ceramic Components. **2013**. https://doi.org/10.1111/jace.12285.

(36) Colby, R. H.; Fetters, L. J.; Funk, W. G.; Graessley, W. W. Effects of Concentration and Thermodynamic Interaction on the Viscoelastic Properties of Polymer Solutions. *Macromolecules* **1991**, *24* (13), 3873–3882. https://doi.org/10.1021/ma00013a021.

(37) Wendy E. Krause, †; Enrico G. Bellomo, ‡ and; Ralph H. Colby*, ‡. Rheology of Sodium Hyaluronate under Physiological Conditions. **2001**. https://doi.org/10.1021/BM0055798.

(38) Matthew G. McKee; Matthew T. Hunley; John M. Layman, and; Long*, T. E. Solution Rheological Behavior and Electrospinning of Cationic Polyelectrolytes. **2005**. https://doi.org/10.1021/MA051786U.

(39) Huber, K.; Burchard, W.; Fetters1, L. J. *Dynamic Light Scattering from Regular Star-Branched Molecules1^ Experimental Section*; 1984; Vol. 17.

(40) Bauer, B. J.; Fetters, L. J.; Graesslev, W. W.; Hadjichristidis, N.; Quack, G. F. Chain Dimensions in Dilute Polymer Solutions: A Light-Scattering and Viscometric Study of Multiarmed Polyisoprene Stars in Good and θ Solvents. *Macromolecules* **1989**, *22* (5), 2337–2347. https://doi.org/10.1021/ma00195a058.

(41) Shabana, M. A Review on the Quality Control Analysis of Oral Dosage Form: Tablets. *Res. Rev. J. Pharm. Pharm. Sci.* **2016**, *5* (2), 108–114.

(42) Sammis, C. G.; Ashby, M. F. The Failure of Brittle Porous Solids under Compressive Stress States. *Acta Metall.* **1986**, *34* (3), 511–526. https://doi.org/10.1016/0001-6160(86)90087-8.

(43) Liu, D.-M. Influence of Porosity and Pore Size on the Compressive Strength of Porous Hydroxyapatite Ceramic. *Ceram. Int.* **1997**, *23* (2), 135–139. https://doi.org/10.1016/S0272-8842(96)00009-0.

(44) Patirupanusara, P.; Suwanpreuk, W.; Rubkumintara, T.; Suwanprateeb, J. Effect of Binder Content on the Material Properties of Polymethyl Methacrylate Fabricated by Three Dimensional Printing Technique. *J. Mater. Process. Technol.* **2008**, *207* (1–3), 40–45. https://doi.org/10.1016/J.JMATPROTEC.2007.12.058.

(45) Hancock, B. C.; Colvin, J. T.; Mullarney, M. P.; Zinchuk, A. V. *The Relative Densities of Pharmaceutical Powders, Blends, Dry Granulations, and Immediate-Release Tablets*; 2003.

(46) Garg, G.; Siddiqui, M. N.; Sharma, K. *Fast Dissolving Tablets: Preparation, Characterization and Evaluation: An Overview*; 2010; Vol. 4.

(47) de Gans, B.-J.; Duineveld, P. C.; Schubert, U. S. Inkjet Printing of Polymers: State of the Art and Future Developments. *Adv. Mater.* **2004**, *16* (3), 203–213. https://doi.org/10.1002/adma.200300385.

9.8 Supplemental

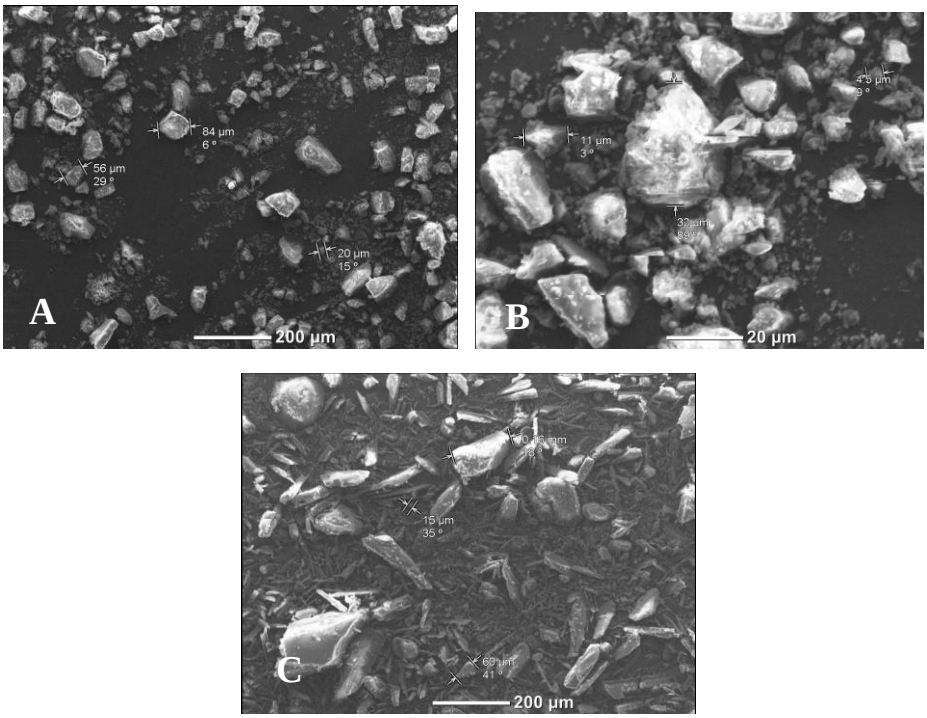

Figure S9.1. SEM images of **(A)** lactose, **(B)** powdered sugar, **(C)** and acetaminophen.

Table S9.1. Physical properties summary of jettable graft copolymer and DI water combinations.

Name	Concentration (wt%)	Compressive strength (MPa)
5%, 2.5	5	0.63 ± 0.05
5%, 2.5	10	1.23 ± 0.04
5%, 5	5	0.57 ± 0.07
5%, 5	10	1.24 ± 0.06
10%, 2.5	5	0.61 ± 0.1
10%, 2.5	8	0.75 ± 0.06
10%, 2.5	10	1.21 ± 0.04
10%, 2.5	12	1.31 ± 0.09
10%, 2.5	14	1.6 ± 0.12
10%, 5	5	0.56 ± 0.02
10%, 5	10	1.22 ± 0.08
25%, 2.5	5	0.63 ± 0.09
25%, 2.5	10	1.3 ± 0.09
25%, 5	5	0.65 ± 0.08
25%, 5	10	1.27 ± 0.1

Table S9.2. Water dissolution summary of jettable tablets with and without API.

Topology/MW (kg mol^{-1})	API in powder (wt%)	Concentration in binder (wt%)	Dissolution Time (s)
5%, 2.5	0	5	22 ± 10
5%, 2.5	0	10	18 ± 10
5%, 5	0	5	13 ± 9
5%, 5	0	10	20 ± 11
10%, 2.5	0	5	14 ± 8
10%, 2.5	0	8	20 ± 11
10%, 2.5	0	10	12 ± 9
10%, 2.5	0	12	16 ± 9
10%, 2.5	0	14	21 ± 10
10%, 5	0	5	16 ± 10
10%, 5	0	10	23 ± 14
25%, 2.5	0	5	18 ± 10
25%, 2.5	0	10	14 ± 12
25%, 5	0	5	13 ± 11
25%, 5	0	10	17 ± 12
10%, 2.5	5	10	15 ± 9
10%, 2.5	10	10	19 ± 11
10%, 2.5	25	10	25 ± 14
10%, 2.5	50	10	25 ± 11

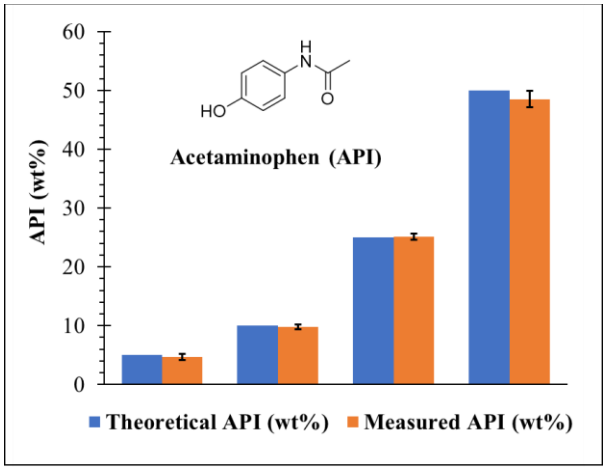

Figure S9.2. API determination of tablets printed with 10 wt% 10%, 2.5.

Chapter 10: Suspension polymerization of Poly(stearyl acrylate) Powders for Powder Bed Fusion of Phase Change Materials

(Formatted for publication in ACS Applied Polymer Materials)

Emily M. Wilts[1], Camden A. Chatham[1,2], Julia Pimentel[3], Jose Sintas[1], Christopher B. Williams[2], and Timothy E. Long[1*]

[1]*Department of Chemistry, Macromolecules Innovation Institute, Virginia Tech, Blacksburg, VA 24061*

[2]*Department of Mechanical Engineering, Macromolecules Innovation Institute, Virginia Tech, Blacksburg, VA 24061*

[3]*Department of Material Science and Engineering, Macromolecules Innovation Institute, Virginia Tech, Blacksburg, VA 24061*

10.1 Abstract

Powder bed fusion (PBF) is a layer-wise additive manufacturing (AM) process producing 3D parts through selectively melting polymer powders with an infrared radiation (IR) laser beam. While this process is extremely successful in printing commercially available polymer powders, most examples require high temperatures, high energy, and large amounts of solvents to not only print the materials, but also produce polymer powders in multiple steps. This manuscript describes using a low-melting (< 80 ^{o}C) novel polymer for PBF, poly(stearyl acrylate) (PSA), and suspension polymerization to produce particles for phase change materials. Suspension polymerization is underutilized in the PBF literature and produces spherical particles with controlled sizes while also only using water, a non-toxic solvent, for the process. Changing stabilizer amounts, poly(vinyl alcohol), in suspension polymerization varied the particle sizes of the PSA and varying temperatures controlled crosslinking percentages. 2 wt % stabilizer produced particles with a 148 µm mean size and 60% gel fraction, which represented the smallest sizes and gel fractions of the series. The high degree of crosslinking may prevent coalescence of particles during

printing and thus solution-made PSA was also added via dry mixing. Static and dynamic powder flowability experiments determined Hausner ratio and avalanche angle of 100% solution-polymerized, 100% suspension-polymerized, and 50:50 mixture powders. All fell within the optimal powder properties for PBF, but 50:50 was chosen to attempt 3D parts based on zero-shear viscosity. The 50:50 mixture produced multi-layered 3D parts thus proving this system's potential for a novel material and particle manufacturing method for PBF. Differential scanning calorimetry also measured latent heat and stability over 50 heat-cool-heat cycles of a printed part to confirm the effectiveness as a phase change material.

10.2 Introduction

Developing new materials for powder bed fusion (PBF)[1], the additive manufacturing (AM) technology first commercialized as Selective Laser Sintering[2], requires material processing into spherical particles within specific size ranges to enable successful printing. Challenges associated with determining powder processing conditions currently limit the materials available for PBF. Specifically for polymers, some example methods for converting bulk materials into spherical particles include grinding, solvent precipitation, and melt emulsion, which also meet flowability and size guidelines for PBF.[3–7] Grinding breaks large particles into small in an uncontrolled fashion that lacks size and shape control.[8,9] Solvent precipitation creates semi-spherical particles but lacks variety of polymers and requires large amounts of solvent.[10,11] Heating polymers above their melting temperature in the presence of a stabilizer will create spherical particles through melt emulsion, but also lacks variety of polymers due to difficulties matching stable solvent/polymer mixtures.[12–14] Most methods are chemical engineering, post-processing/post-polymerization processes that require two or more steps from

polymerization to spherical particles. Alternatively, suspension polymerization produces spherical particles through a one-step, one-pot free radical polymerization and has not been extensively evaluated to manufacture powders for PBF.

Suspension polymerization methods produce polymer particles in a suspension consisting of monomer, polymer, initiator, and stabilizer. In typical systems, the water-insoluble monomer creates monomer droplets under rapid agitation, depicted in **Figure 10.1**.[15] The initiator is also not water soluble and dissolves in the monomer droplets. Free radical polymerization occurs within each droplet following increases in temperature to induce initiator decomposition. The stabilizer prevents the droplets from agglomerating through adsorbing to the droplet surfaces and repelling other droplets.[16,17] Depending on the suspension stability, stabilizer concentration, and monomer concentration, suspension polymerization yields particles ranging from 5 to 500 µm, average conversion of 30-50%, and are spherical in shape.[18] Isolation of the particles through filtration and drying enables use in PBF and other applications requiring polymer powders.

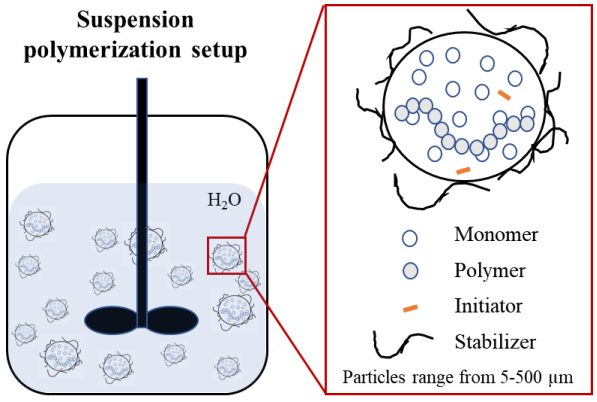

Figure 10.1. Depiction of suspension polymerization.

PBF, like all AM technologies, is a layer-wise manufacturing technique. It consists of the following three sub-functions that are repeated for every layer: (1) powder recoating, (2) energy input, and (3) coalescence and cooling. This manuscript focuses on the impact of synthetic conditions on properties identified as important for successful PBF manufacturing.

At a high level, the powder recoating sub-function involves the automated moving of powder to the build piston, coupled with a descriptor for how the powder will fill and pack the build piston. Properties relevant to powder recoating are primarily a function of powder shape, size, and size distribution with minor contributions from any particular chemical structure. The energy input sub-function is comprised of global heating of all powder inside the print chamber and local heating via a scanning laser beam. Polymer properties relevant to energy input include thermal properties (e.g., specific heat capacity, enthalpy of melting, thermal transition temperatures) and optical properties at the wavelength of the CO_2 laser ($\lambda = 10.6\ \mu m$) commonly used in polymer PBF machines. The coalescence and cooling sub-function is the portion of layer forming involving melt-state polymer flow, consolidation, and solidification. Key properties for this sub-function include rheological properties (e.g., zero-shear viscosity) and crystallization descriptors (e.g., crystallization halftime and enthalpy of fusion). More detailed descriptions of the physics governing each sub-function and relevant polymer properties can be found in the authors' previously published review article.[8]

Semi-crystalline polymers exhibit sharp transitions from solid to molten, which helps create precise shapes without void spaces within layers. However, this transition also renders the shape suspectable to warping and edge curling. Common examples of semi-

crystalline polymers are Nylon 12 and polypropylene printed at bed temperatures of 170 and 130 °C, respectively.[19–21] All polymers currently commercially available for PBF print at or above 120 °C, and literature on low-temperature polymers is lacking. This manuscript explores poly(stearyl acrylate), a crystalline low-melting polymer (T_m = 51 °C) that crystallizes through side chains, which also provides potential for use as PCM.

Poly(stearyl acrylate) (PSA) is a common phase change material (PCM) owing to its highly branched structure, which provides a solid-solid phase change through the melting of crystalline side chains but maintenance of structure until backbone thermal transitions.[22] During melting and freezing, PCM absorb and release thermal energy while maintaining a specific temperature. In an effort to consume less energy for a more sustainable future, PCM facilitate thermal control and storage in construction materials, shipping materials, and refrigerators/freezers. Water is an excellent phase change material due to its high latent heat during melting, but encapsulation of the liquid limits its use.[23,24] The solid-solid phase change of PSA, stability over 50+ heat-cool-heat cycles, and high latent heat render it suitable for PCM.[22,25] Additively manufactured PSA allows the rapid production of a PMC into unique shapes for custom-fit or low volume production, which could save energy, money, and time.[26]

This manuscript describes the synthesis, powder characterization, thermal characterization, and powder bed fusion of PSA made through suspension and solution polymerization. PSA is one of the first examples of printing low melting temperature (T_m = 51 °C) polymers with a room temperature bed temperature. PSA is also a known PCM and benefits from additively manufactured custom shapes to meet demands of complex packaging and storage containers requiring temperature control. Additionally, suspension

polymerization is a facile method of one-step, one-pot polymerization and formation of spherical polymer particles. Particle size analysis, density measurements, and revolution powder analysis characterized the powders and combinations in terms of flowability. Differential scanning calorimetry (DSC) and melt rheology determined melting temperatures and zero-shear viscosities of each combination. Finally, empirical fusion grids helped tune parameters for PBF, which enabled the creation of a 3D part from the 50:50, solution:suspension mixture. The 3D printed parts remained stable over 50 heat-cool-heat cycles and experienced a latent heat of 80.2 J/g, which confirmed potential subsequent use as a PCM.

10.3 Experimental

10.3.1 Materials

Stearyl acrylate was purchased from Sigma Aldrich and ran through a silica column before use to remove inhibitor. Kuraray Poval TM 22-88 was donated from Kuraray and used as received. Azobisisobutyronitrile (AIBN) was recrystallized over methanol and dried in vacuo before use. Toluene and methanol were purchased from Arcos and used as received.

10.3.2 Synthesis of Poly(stearyl acrylate) using Suspension Polymerization

Suspension polymerization of poly(stearyl acrylate) began with a combination of DI water (100 mL) with Poval TM 22-88 (0.2 g) at 50 ^{o}C. Once the Poval TM 22-88 was dissolved, melted stearyl acrylate (20 g, 0.062 mol) and AIBN (0.05 g, $3.0 \cdot 10^{-4}$ mol) were added to the mixture. The combination was sparged with nitrogen for 20 min. A mechanical stirrer enabled the formation of an emulsion at 400 rpm while the mixture was purging. The temperature was raised to 70 ^{o}C and the mixture was allowed to react for 3 h. After 3 h, the

temperature was turned off and the mixture was allowed to stir overnight to come back to room temperature. The mixture was frozen and subsequent lyophilization isolated the particles.

10.3.3 Synthesis of Poly(stearyl acrylate) using Solution Polymerization

Stearyl acrylate (20 g, 0.062 mol), AIBN (0.05 g, $3.0 \cdot 10^{-4}$ mol), and 100 mL of toluene was sparged with nitrogen for 30 min. The mixture stirred at 70 ^{o}C for 24 h. The reaction was exposed to oxygen and cooled to 22 ^{o}C. The solution was next precipitated into 1 L of methanol at 10 mL min^{-1}. The particles were washed with methanol, filtered, and dried at 22 ^{o}C until the methanol evaporated.

10.3.4 Analytical

^{1}H NMR spectroscopy was conducted on a Varian Unity 400 MHz in $CDCl_3$. Differential scanning calorimetry (DSC) with a 50 mL min^{-1} nitrogen flow at a 10 ^{o}C min^{-1} heating rate and 10 ^{o}C min^{-1} cooling rate on a TA instruments Q2000 with indium (mp = 156.60 °C) and zinc (mp = 419.47 °C) standards. Glass transition temperatures (T_g) were determined from the midpoint of the endothermic transition and melting endotherms were identified at the maximum of the peak. The same instrument measured crystallization kinetics as follows. The sample was held at 65 ^{o}C for 10 min and using the "jump" command was held at 50 to 60 ^{o}C one degree at a time for 60 min cycles. TA Instruments Q50 measured for thermogravimetric analysis (TGA) began with a 20 min isotherm at 120 °C and a ramp 10 °C/min from 120 to 800 °C. To prepare for scanning electron microscopy (SEM) a Lecia EM ACE600 sputter coated the particles with 7 nm of iridium. A Leo FESEM imaged the particles under high vacuum at 5 kV accelerating voltage. A Discovery HR-2 rheometer

measured the viscosity through a frequency sweep at 80 °C, 1% strain, and 0.1 to 100 rad s^{-1}. Printed part density was calculated via an adapted ASTM D792[27] method using ethanol as the secondary fluid. This is customary for polymer PBF parts.[28]

10.3.5 Powder Characterization

Bulk and tapped densities of the powder systems were measured according to ASTM D1895[29] and an adapted version of S.3.6 (**Table S10.2**). World Health Organization Pharmacopoeia method[30], respectively. The ratio of tapped to bulk density is known as the Hausner ratio[31], which is often used as an empirical predictor of powder flowability. A powder with a ratio of 1.25 or less is considered freely flowing.[31,32] A Horiba Partica LA-950 light scattering particle size with 500 and 700 nm lasers analyzed measured particles sizes at 25 °C in DI water. A Mercury Scientific Revolution Powder Analyzer (RPA) was used to dynamically evaluate flow behavior in synthesized powders. Standard flowability testing at ambient conditions and 0.3 rpm was used to determine avalanche angle, surface fractal, and dynamic density for all samples. More detailed descriptions of RPA experiments can be found in the following literature.[33–35] Theory and descriptions of powder characterization methods for PBF can be found in the review article by Vock, *et al.*[36]

10.3.6 Powder Bed Fusion

PBF printing[1] was performed using a Prodways ProMaker 2000HT machine. For the small sized batches of experimental powder used in this work, the ProMaker was run in full manual mode with a custom “bed reducer” apparatus (**Figure S10.1**). This enabled printing

of multi-layer structures with a minimum powder batch size of 1 L. Printing occurred under constant nitrogen purge at ambient temperature.

Figure 10.2 depicts the stable sintering region which encompasses the first heat and cool DSC trace (blue) and TGA trace (orange) of PSA made with 2 wt % stabilizer. "T" represents the chosen thermal energy input (i.e., printer chamber temperature) and "O" represents the targeted range of optical energy input. The thermal energy input represents the bed temperature (T_b). Due to the low melting temperature of PSA, T_b was chosen to be ambient temperature (i.e., printer heaters disabled).

The optical energy input range sits above the T_m but below the $T_{d,5\%}$ in the TGA trace to ensure full melting without degradation. Multiple combinations of optical energy input (i.e., laser heating) parameters within this range were empirically evaluated on the basis of coalescence and warping. This empirical evaluation method is known as the "fusion grid" method. Observations regarding out-of-plane warping and mechanical robustness while handling were used to make final selections for laser processing parameters, as seen in **Table 10.1**. Images of fusion grids can be found in supplemental information.

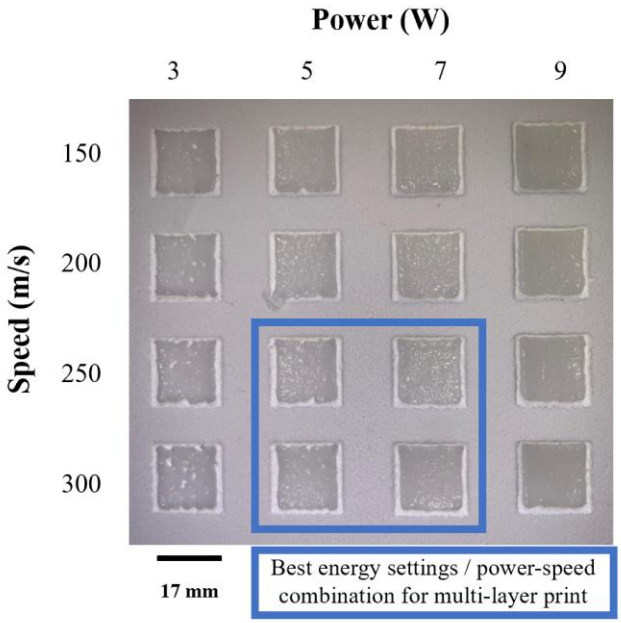

Figure 10.2. Speed as a function of power, also called a fusion grid, where the blue box denotes best printing parameters for 50:50.

The range of suitable optical surface energy densities is theoretically bounded by the energy melt ratio (EMR, Equation 1) and energy melt ratio for degradation ($EMR_{deg,}$ Equation 2) according to literature precedent.[34,37,38] In the equations, P_{min} is theoratical minimum laser power to affect melting, P_{max} is maximum laser power before affecting polymer degradation, h is the distance between laser paths, V_b is the speed of the laser beam, SC is the scan count (i.e., number of laser scans per layer), Cp is specific heat capacity, T_m is the temperature at end of melt behavior, T_b is the chosen bed temperature, h_f is the heat of melting, Q is the density of bulk polymer, and φ is the powder packing fraction. The additional material variables for EMR_{deg} in Equation 2 include the temperature at 5 % weight loss ($T_{d,onset,}$), activation energy for degradation (E_A) (Figure S5), and weight-average molecular weight (M_w).

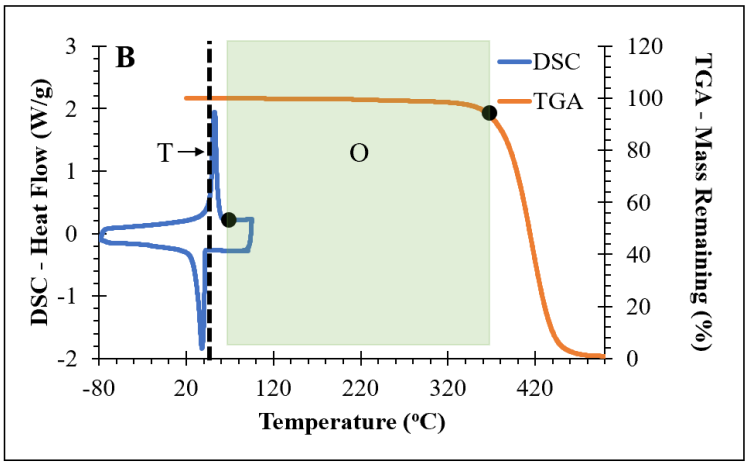

Figure 10.3. Stable sintering region for PSA made through suspension polymerization with 2 wt % stabilizer. The dashed line "T" indicates the chosen bed temperature of 25 °C. The highlighted region "O" indicates the range of optical energy input, i.e., the energy supplied by the laser.

$$P_{min} = \frac{h \times V_b}{SC}\left(\left[C_p(T_m - T_b) + h_f\right] \times (Q)(\Phi)\right) \qquad \text{Equation 1}$$

$$P_{max} = \frac{h \times V_b}{SC}\left(\left[C_p(T_m - T_b) + h_f\right] \times (Q)(\Phi) + \left[C_p\left(T_{d,onset} - T_m\right) + \frac{E_A}{M_w}\right] \times Q\right) \qquad \text{Equation 2}$$

Table 10.2. PBF printing parameter values used in parts specimen fabrication.

PBF Printing Parameter	Value
Laser power (P)	7 W

Beam speed (V_b)	254 mm s^{-1} (10 in. s^{-1})
Hatch spacing (h)	0.152 mm (0.006 in.)
Layer height (z)	0.50 mm (0.019 in.)
Scan count (SC)	1

10.4 Results and Discussion

Suspension polymerization of stearyl acrylate yielded spherical particles with a range of particle sizes and gel fractions. A mixture of stearyl acrylate, poly(vinyl alcohol) (PVA), azobisisobutyronitrile (AIBN), and water stirred at 400 rpm and created dispersed monomer droplets. Increased temperature to 70 ^{o}C enabled initiation of AIBN and subsequent polymerization of the monomer particles. After 3 h, ^{1}H NMR spectroscopy confirmed a plateau conversion and the reaction stopped stirring and brought to room temperature to maintain the polymer particles, as PSA melting temperature is 51 ^{o}C. The majority of the crosslinked particles did not dissolve, therefore the difference in mass of monomer present before and after polymerization determined conversion. Filtering and lyophilization isolated particles and further analysis uncovered whether the powders were suitable for powder bed fusion.

Scheme 10.1. Suspension polymerization of poly(stearyl acrylate).

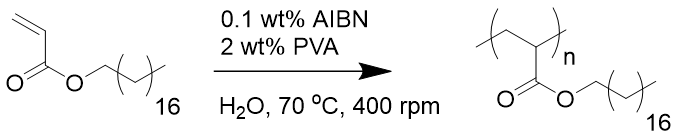

Variation of reaction conditions, such as stabilizer amount, monomer concentration and temperature, uncovered suitable suspension polymerization conditions to produce spherical particles smaller than 150 μm. The stabilizer is soluble in water and adheres to prevents the monomer and polymer particles from coalescing. As the stabilizer amount increases, the more surface area is covered enabling a smaller particle size. Varying monomer concentration will not only change the particles size based on the varying surfactant amount, but also identify which concentration yield the most stable suspension without droplet coalescence. The temperature variation enables a change in gel fraction. As the temperature increases, the more likely acrylates will branch and crosslink, which contribute to a higher gel fraction. Crosslinking occurs within the monomer/polymer droplets when a free radical abstracts an activated, α backbone hydrogen to create branched and crosslinked products. These variations enable a range of particle sizes and gel fractions and, with subsequent thermal analysis and viscosity testing, a suitable reaction condition was determined.

Table 10.2 describes the suspension polymerization reaction conditions to investigate the effects on particle size and gel fractions. Stabilizer amount and monomer concentration effect particle size while reaction temperature will determine the gel fraction. Five reactions ranging from 60 to 90 ^{o}C revealed an increase in gel fraction with increased reaction temperature, summarized in Figure S1. AIBN decomposes at 60 ^{o}C and water boils at 100 ^{o}C, which limited the temperature range. Each reaction contained 1 wt % stabilizer at 0.2 g mL^{-1} of monomer. Ultimately, 70 ^{o}C was chosen for the subsequent stabilizer and monomer concentration studies because it produced one of the lowest gel fractions and the lowest aggregation of particles compared to the 60 ^{o}C reaction. High gel fractions could

lead to high zero-shear viscosities, which may inhibit particle coalescence in PBF. During preliminary melting and coalescence experiments, the crosslinked particles prevented adequate aggregation and thus solution-made PSA particles, without crosslinking, were synthesized to ameliorate this problem.

Table 10.2. Summary of varying suspension polymerization reaction conditions and the resulting gel fractions.

Name	Stabilizer amount (wt %)	Monomer concentration (g mL^{-1})	Temperature (^oC)	Gel fraction (%)
PSS-S3	3	0.2	70	60 ± 1.9
PSS-S2	2	0.2	70	62 ± 2.0
PSS-S1	1	0.2	70	61 ± 1.3
PSS-S0.5	0.5	0.2	70	61 ± 1.5
PSS-S0.25	0.25	0.2	70	60 ± 1.2
PSS-M0.05	1	0.05	70	59 ± 2.2
PSS-M0.1	1	0.1	70	60 ± 1.6
PSS-M0.2	1	0.2	70	59 ± 1.3
PSS-M0.3	1	0.3	70	61 ± 1.0
PSS-M0.4	1	0.4	70	60 ± 2.1
PSS-T60	1	0.2	60	58 ± 2.0
PSS-T70	1	0.2	70	61 ± 1.4
PSS-80	1	0.2	80	72 ± 1.1
PSS-90	1	0.2	90	83 ± 1.2
PSS-100	1	0.2	100	95 ± 2.0

*All surfactant wt %'s were calculated based on the mass of monomer

*All AIBN amounts were kept constant at 1 wt % relative to the mass of monomer

Ease of particle coalescence and degree of fusion during each layer formation determines the final part density, strength, and toughness of PBF created parts.[8] During the particle melting process, timescales related to polymer molecular movement and flow

within the particle and length scales of fusion between particles predict material behavior during printing. PBF applies zero shear to the melted polymer and deforms through biaxial extension. Therefore, particle coalescence can be predicted using the Frenkel model (Equation 3). This equation describes decreasing particle coalescence with increasing zero-shear viscosity where x, r, σ, t, and η_0 represent growing neck radius between two particles, original particle radius, surface tension of the polymer melt, time, and zero-shear viscosity of the polymer melt.[55]

$$\left(\frac{x}{r}\right)^2 = \frac{3\sigma t}{2r\eta_0} \qquad \text{Equation 3}$$

The Frenkel model is an ideal case for particle coalescence assuming the particle maintain their spherical shape and therefore Sun *et al.* expanded on this model using a body-centered-cubic packed until cell. The model incorporates the probability of a sintering neck to form between each particle, called the sintering fraction factor, which is a better representation of the PBF process compared to the Frenkel model alone. Plotting sintering rate at varying sintering fraction factors revealed the rate of change of surface area trended towards zero below sintering fraction factors below 0.3.[55]

Zero-shear viscosity measurements elucidated the potential for particles to coalesce after melting. **Figure 10.4** depicts frequency sweeps at 80 ^{o}C of five combinations of suspension and solution polymerized PSA (solution wt %:suspension wt %). 100% solution-made particles do not contain crosslinking and experienced a zero-shear viscosity of 0.4 Pa·s at 80 ^{o}C, where 100% suspension-made with 60% gel fraction experienced 2000 Pa·s at the same temperature. Crosslinking contributed to the increase in zero-shear

viscosity, which opposes coalescence during the printing process. The zero-shear viscosities reported are relative measurements as the experiments containing crosslinked polymers may hinder the instrument's ability to accurately measure solid flow.

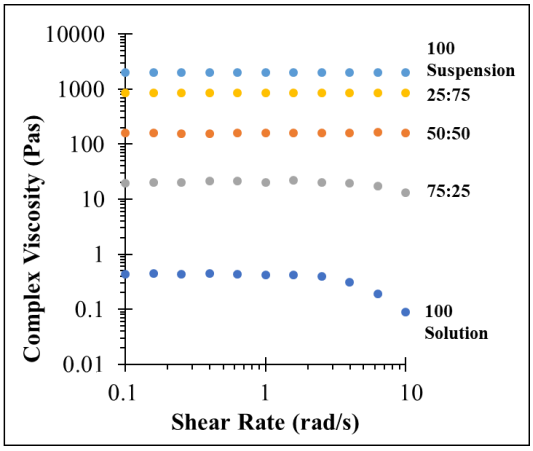

Figure 10.4. Frequency sweeps at 80 °C of suspension- and solution-made powders.

Motivation to utilize 50:50 for multi-layer prints stemmed from a mid-range zero-shear viscosity and qualitative part strength. A mixture of solution-polymerized, and suspension-polymerized particles decreased zero-shear viscosity compared to 100% suspension, which is known to improve coalescence during the PBF process. While polymer melts at unlimited timescales will eventually coalesce, PBF printing rates require complete coalescence before subsequent layer formation.[39,40] The Deborah number (De) represents the relaxation or response to deformation behavior of viscoelastic materials and further elucidates coalescence timescales based on reptation time and surface energy. De number also describes systems with non-constant stretch histories and can describe the rate of released or stored elastic energy.[41,42] In general, higher zero-shear viscosities correspond to longer coalescence timescales.[43]

Solution polymerized particles are not crosslinked and may improve layer coalescence, however, neat solution-made PSA films immediately disintegrated upon handling. Stearyl acrylate, AIBN, and toluene at 70 ^{o}C with subsequent precipitation into methanol created non-crosslinked particles with an average diameter of 102 µm. Although they maintained a smaller particle size compared to suspension-made PSA, only mixtures were utilized because of qualitatively poor strength. The crosslinking in suspension-made particles increased the relative strength where melt pressed filmed were bent and did not crack.

Multiple physical powder properties such as particle size, shape, and density determine optimal powder flowability for PBF. During the powder recoating process, a consistent, homogenous powder layer aids in achieving full coalescence for maximum printed part density. Literature suggests a particle size range from 30-150 µm produces even layers in PBF and binder jetting processes.[44] A distribution of particle sizes within this range also helps to fill in voids and produce layers without gaps or imperfections.[45,46] In this study, light scattering-based particle size analysis determined the resulting particle sizes of suspension polymerization using varying stabilizer amounts and monomer concentrations. **Figure 10.5A** depicts an example particle size distribution of PSA made with 2 wt % stabilizer (blue) and the distribution of solution-made particles (orange). **Figure 10.5B** represents the mean particle size (D50) as a function of stabilizer amount. As the stabilizer increased, the particle size decreased. As stabilizer amount increases, more materials adsorb to the surface of the particles, which enables smaller particle sizes. The table also denotes the D90 of each system, which follows a similar trend compared to D50.

While the solution-made particles have a smaller average particle size, they also exhibit a broader distribution of sizes, which may contribute to increased flowability.

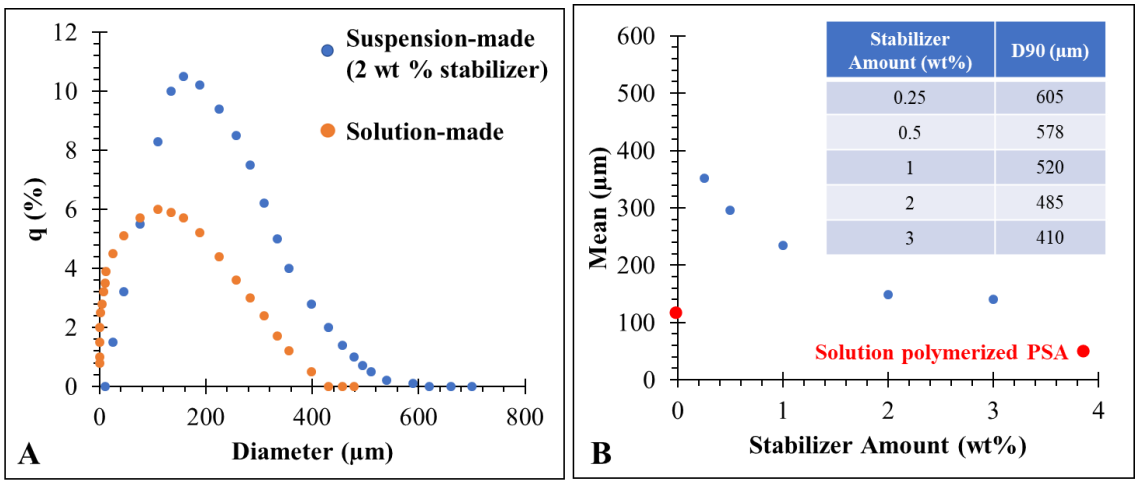

Figure 10.5. (A) Particle size distribution of solution- and suspension-polymerized PSA made with 2 wt % stabilizer and (B) mean particle size (µm) as a function of stabilizer amount (wt %).

Figure 10.6 depicts SEM images of suspension-made, solution-made, and a 50:50 mixture of PSA particles along with their respective Hausner ratios (HR) avalanche angles (AA). The HA is an empirical static flow evaluation commonly used to characterize flowability and is the ratio of tapped to apparent densities of powders. Suspension-made exhibited the largest HA at 1.34 owing to the largest particle sizes and lowest dispersity compared to the other samples. Solution-made particles have a HA of 1.2, the lowest value of the series, because of the smallest particle sizes and largest dispersity. An HA less than 1.25 reportedly indicates a "freely flowing" powder[47]; however, other researchers report successful PBF with polymer powder HA values below 1.4.[34]

As an addition, revolution powder analysis (RPA) represents a dynamic flow evaluation method that compares powder flowability.[33,34] Suspension-made, solution-made, and 50:50 exhibited avalanche angles of 54.4, 45.7, and 47.8 º, respectively. These results fit within the range of avalanche angles reported in literature for commercial PBF polymer powders.[48] Comparatively, the suspension-made PSA was observed to have a high avalanche angle in comparison to the solution-made and the 50:50 exhibited characteristics in between.

Figure 10.6 shows the spherical and semi-spherical particle shapes of each powder. Suspension-made powders, Figure 6A, look spherical and have minimal surface defects, depicted at higher magnifications in Figure S4A. These particles are also hollow, Figure S4B, indicating a core-shell structure commonly observed in suspension polymerization.[49,50] **Figure 10.6B** depicts the 50:50 mixture depicting the larger and smaller particles of both suspension- and solution-made particles. **Figure 10.6C** depicts solution-made particles are that are less uniform compared to the suspension-made. The rough surfaces on the solution-made particles are due to nanoscale particles aggregated to the surface, depicted at higher magnification in Figure S4F.

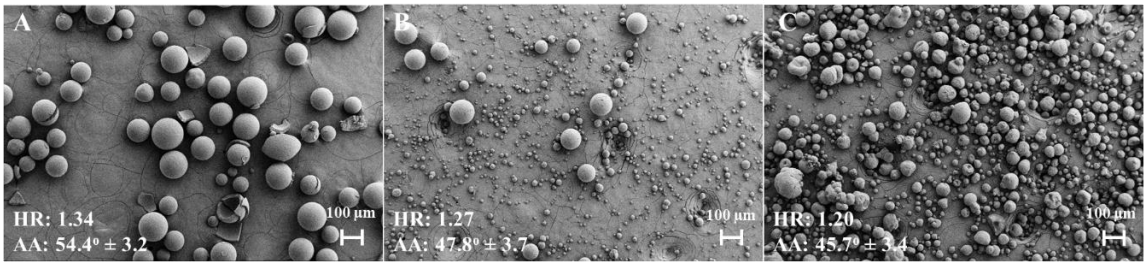

Figure 10.6. SEM images at 500x of (A) suspension-made, (B) 50:50 solution:suspension, (C) solution-made particles.

Crosslinking in PSA produced using suspension polymerization decreases crystallinity percentages (X_c). PSA polymerized using AIBN in toluene does not contain crosslinking and was thus used to compare X_c of PSA polymerized through both methods. **Figure 10.7** depicts first heat DSC traces of PSS synthesized in toluene (solution) and a suspension polymerization-produced PSA with 2 wt % stabilizer containing 29 and 41% crystallinity. Crosslinking suppresses crystallinity through preventing chain alignment, which also increased zero-shear viscosity.

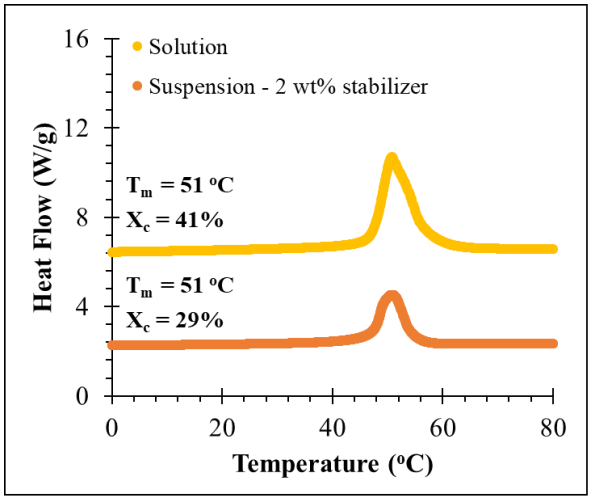

Figure 10.7. DSC first heat traces of poly(stearyl acrylate) synthesized through suspension and solution polymerization.

The different powder and thermal properties of suspension- and solution-made PSA also influenced the decision to combine them. Suspension-polymerized particles exhibited a uniform, spherical shape suitable for flowability. However, large particle sizes (D50 = 148 µm, D90 = 485 µm) and cohesive tendencies resulted in a Hausner ratio above 1.25 and avalanche angle of 54.4°, which may negatively affect the powder recoating process. Additionally, 60% gel fractions and decreased crystallinity and increased zero-shear

viscosity compared to non-crosslinked PSA hindered the potential coalescence of particles. One major downfall of the solution-made particles was the lack of mechanical strength, where touching a melt-pressed film cracked the surface. Such behavior would result in an unhandlable printed part, likely resulting in an inability to remove from the printer without destruction. Combining the powders created a composite where the crosslinked particles increased the strength and the solution-made particles helped with coalescence within each printed layer.

Through a 50:50 dry mixture of solution and suspension polymerized PSA, parts with varying cross-sectional area were fabricated. **Figure 10.8** depicts printed complex shapes from the 50:50 powder. Part resolution was limited by the large PSA particles (i.e., d90 > 485) forcing the 0.5 mm layer height. Even still, part shapes and proportions are recognizable and able to be depowdered and removed from the printer. Selected images of printed shapes are presented in Figure 8. Density of printed parts was found to be 0.970 ± 0.008 g cm^{-3}.

Figure 10.8. PBF printed Spiral Rook[51] (left), ship[52] (right), and part collection (center) using 50:50 powder.

Figure 10.9 depicts DSC traces of heat-cool-heat cycles 1 and 50 and images of 3D rook before and after melting to demonstrate potential for PCM. Thermal cycling at 1 ^{o}C/min 30 ^{o}C above and 25 ^{o}C below T_m over 50 cycles with < 1 % change in latent heat absorbed and released revealed the stability and longevity of additively manufactured PSA.[53] The latent heat storage during melting and freezing averaged 80.1 and 82.4 J/g, respectively. Interestingly, cycling at 1 ^{o}C/min revealed a kinetically-controlled, second crystallization exotherm, due to phase separation between crosslinked and non-crosslinked sections.[54] The best PCM experience solid-solid phase changes through melting transitions, which prevents the need to seal and contain liquids.[25] The images depict the 3D rook above and below T_m, which revealed a solid-solid phase change and thus another advantageous quality for PCM. At 57 ^{o}C, the top began to turn translucent, indicating melting of PSA side chains. The part became soft, but ultimately maintained shape and supported its weight, even after 30 min above T_m.

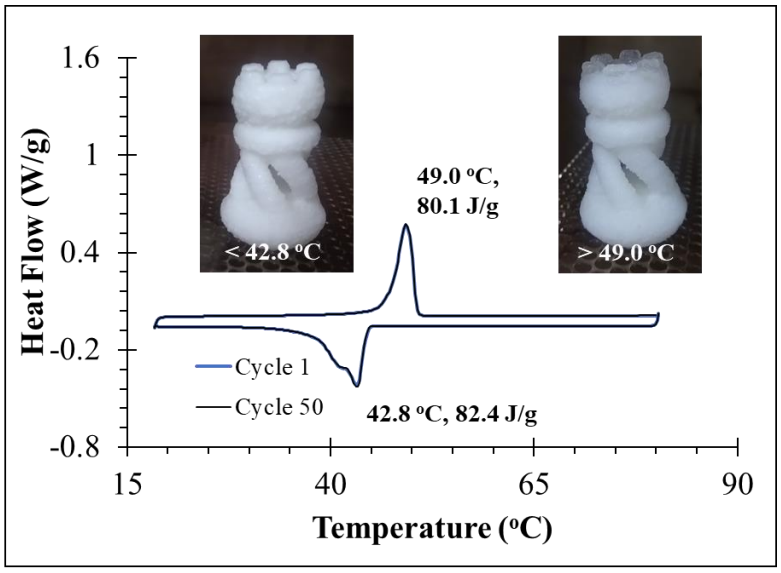

Figure 10.9. DSC traces of heat-cool-heat cycles 1 and 50 and pictures of a 3D rook below and above T_m.

10.5 Conclusions and Future Work

Suspension and solution polymerization produced poly(stearyl acrylate) average sized particles slightly above the conventional powder bed fusion (PBF) powder requirements. Particle sizes below 150 μm, Hausner ratios of below 1.25, and spherical particles produced powders with suitable flowability to create an even, homogenous layer during the recoating process in PBF. Not only is PSA a new material for PBF, but it is also one of the only examples of a low-melting polymer (< 80 ^oC) compared to other materials used for PBF. Incorporation of crosslinked particles provided a range of zero-shear viscosities for the suspension- and solution-polymerized mixtures. 3D parts of varying cross-sectional area demonstrated the potential for PSA as a new material for PBF, but some qualities, such as micron-scale resolution, require improvement.

Suspension polymerization is a versatile method allowing the production of controlled particle sizes using free-radical polymerization with and without crosslinking. Another approach to create particles without crosslinking is using methacrylate-based monomers, which prevents α-hydrogen abstraction and thus branching and crosslinking. Emulsion polymerization is a similar method of creating spherical polymer particles, but requires additional stabilizers and surfactants and also creates smaller particles (10-1000 nm). Using these alternative methods may expand the types of polymers used for PBF using a facile polymerization method without the need for post-processing.

PBF printing work presented in this manuscript should be viewed as a first success, but not as an exhaustive investigation into the printability of PSA. Future work will include investigations into balancing the low zero-shear viscosity of the linear, non-crosslinked architecture with the mechanical robustness of the partially crosslinked networks, thereby finding properties for optimal coalescence behavior without rendering the printed part too brittle to handle. The tunable viscosity and crosslink density of the demonstrated PSA system is ideal for investigating particle coalescence of partially crosslinked materials.

10.6 Acknowledgements

Funding for this work has been provided by the Department of Energy's Kansas City National Security Campus, operated by Honeywell Federal Manufacturing & Technologies, LLC under contract number DE-NA0002839. The authors would like to thank Stephen McCartney for SEM imaging assistance and Jeff Nolte (Virginia Tech Department of Mechanical Engineering) for design and fabrication of ProMaker 2000HT bed reducer. In addition, the authors acknowledge the Macromolecules Innovation Institute (MII) at Virginia Tech for providing a collaborative infrastructure focused across the spectrum of topics in cutting edge polymer science and engineering research.

10.7 References

(1) ISO - ISO/ASTM 52900:2015 - Additive manufacturing — General principles — Terminology https://www.iso.org/standard/69669.html (accessed Feb 24, 2020).

(2) Gibson, I.; Rosen, D.; Stucker, B. *Additive Manufacturing Technologies*; Springer New York: New York, NY, 2015. https://doi.org/10.1007/978-1-4939-2113-3.

(3) Schmid, M.; Amado, A.; Wegener, K. Polymer Powders for Selective Laser Sintering (SLS). In *AIP Conference Proceedings*; American Institute of Physics Inc., 2015; Vol. 1664. https://doi.org/10.1063/1.4918516.

(4) Amado, A.; Schmid, M.; Levy, G.; Wegener, K. *ADVANCES IN SLS POWDER CHARACTERIZATION*.

(5) Laumer, T.; Stichel, T.; … P. A.-H. V.; 2013, undefined. Qualification and Modification of New Polymer Powders for Laser Beam Melting Using Ulbricht Spheres. *books.google.com*.

(6) Schmidt, J.; Sachs, M.; Fanselow, S.; Zhao, M.; Romeis, S.; Drummer, D.; Wirth, K.-E.; Peukert, W. Optimized Polybutylene Terephthalate Powders for Selective Laser Beam Melting. *Chem. Eng. Sci.* **2016**, *156*, 1–10. https://doi.org/10.1016/j.ces.2016.09.009.

(7) Dechet, M. A.; Kloos, S.; Peukert, W.; Schmidt, J. Production of Spherical Micron-Sized Polymer Particles for Additive Manufacturing by Liquid Phase Processes. In *AIP Conference Proceedings*; American Institute of Physics Inc., 2019; Vol. 2055, p 140002. https://doi.org/10.1063/1.5084905.

(8) Chatham, C. A.; Long, T. E.; Williams, C. B. A Review of the Process Physics and Material Screening Methods for Polymer Powder Bed Fusion Additive Manufacturing. *Progress in Polymer Science*. Elsevier Ltd June 1, 2019, pp 68–95. https://doi.org/10.1016/j.progpolymsci.2019.03.003.

(9) Liang, S. B.; Hu, D. P.; Zhu, C.; Yu, A. B. Production of Fine Polymer Powder under Cryogenic Conditions. *Chem. Eng. Technol.* **2002**, *25* (4), 401–405. https://doi.org/10.1002/1521-4125(200204)25:4<401::AID-CEAT401>3.0.CO;2-S.

(10) *United States Patent (19) McAlea et Al*.

(11) Wang, G.; Wang, P.; Zhen, Z.; Zhang, W.; Ji, J. Preparation of PA12 Microspheres with Tunable Morphology and Size for Use in SLS Processing. *Mater. Des.* **2015**, *87*, 656–662. https://doi.org/10.1016/j.matdes.2015.08.083.

(12) Fanselow, S.; Emamjomeh, S. E.; Wirth, K. E.; Schmidt, J.; Peukert, W. Production of Spherical Wax and Polyolefin Microparticles by Melt Emulsification for Additive Manufacturing. *Chem. Eng. Sci.* **2016**, *141*, 282–292. https://doi.org/10.1016/j.ces.2015.11.019.

(13) Schmidt, J.; Sachs, M.; Fanselow, S.; Wirth, K.-E.; Peukert, W. *NOVEL APPROACHES FOR THE PRODUCTION OF POLYMER POWDERS FOR SELECTIVE LASER BEAM MELTING OF POLYMERS*.

(14) Kleijnen, R. G.; Schmid, M.; Wegener, K. Production and Processing of a Spherical Polybutylene Terephthalate Powder for Laser Sintering. https://doi.org/10.3390/app9071308.

(15) Abu-Thabit, N. Y.; Makhlouf, A. S. H. Recent Advances in Nanocomposite Coatings for Corrosion Protection Applications. In *Handbook of Nanoceramic and Nanocomposite Coatings and Materials*; Elsevier Inc., 2015; pp 515–549. https://doi.org/10.1016/B978-0-12-799947-0.00024-9.

(16) Dowding, P. J.; Vincent, B. Suspension Polymerisation to Form Polymer Beads. *Colloids Surfaces A Physicochem. Eng. Asp.* **2000**, *161* (2), 259–269. https://doi.org/10.1016/S0927-7757(99)00375-1.

(17) Vivaldo-Lima, E.; Wood, P. E.; Hamielec, A. E.; Penlidis, A. An Updated Review on Suspension Polymerization. *Ind. Eng. Chem. Res.* **1997**, *36* (4), 939–965. https://doi.org/10.1021/ie960361g.

(18) Pladis, P.; Kiparissides, C. Polymerization Reactors. In *Reference Module in Chemistry, Molecular Sciences and Chemical Engineering*; Elsevier, 2014. https://doi.org/10.1016/b978-0-12-409547-2.10908-4.

(19) Slotwinski, J.; LaBarre, E.; Forrest, R.; Crane, E. Analysis of Glass-Filled Nylon in Laser Powder Bed Fusion Additive Manufacturing. *JOM* **2016**, *68* (3), 811–821. https://doi.org/10.1007/s11837-015-1792-y.

(20) Flores Ituarte, I.; Wiikinkoski, O.; Jansson, A. Additive Manufacturing of Polypropylene: A Screening Design of Experiment Using Laser-Based Powder Bed Fusion. *Polymers (Basel).* **2018**, *10* (12), 1293. https://doi.org/10.3390/polym10121293.

(21) Goodridge, R.; Ziegelmeier, S. Powder Bed Fusion of Polymers. In *Laser Additive Manufacturing: Materials, Design, Technologies, and Applications*; Elsevier Inc., 2017; pp 181–204. https://doi.org/10.1016/B978-0-08-100433-3.00007-5.

(22) *Synthesis of High Molecular Weight Polystearylacrylate and Polystearylmethacrylate Polymers via ATRP Method as Thermal Energy Storage Materials*.

(23) Characterization of microencapsulated PCMs using DSC and TGA https://www.puretemp.com/stories/characterization-of-microencapsulated-pcms-using-dsc-and-tga (accessed Feb 22, 2020).

(24) DSC and T-history: Complementary methods for measuring the melting and freezing ranges of PCMs https://www.puretemp.com/stories/dsc-t-history-method-farid (accessed Feb 22, 2020).

(25) Heifferon, K. V.; Long, T. E. Advanced Polymers for Reduced Energy Consumption in Architecture. *Macromolecular Rapid Communications*. Wiley-VCH Verlag February 1, 2019, p 1800597. https://doi.org/10.1002/marc.201800597.

(26) Nofal, M.; Pan, Y.; Al-Hallaj, S. Selective Laser Sintering of Phase Change Materials for Thermal Energy Storage Applications. *Procedia Manuf.* **2017**, *10*, 851–865. https://doi.org/10.1016/j.promfg.2017.07.071.

(27) Density and Specific Gravity ASTM D792, ISO 1183 https://www.intertek.com/polymers/testlopedia/density-and-specific-gravity-astm-d792/ (accessed Mar 10, 2020).

(28) Drexler, M.; Lexow, M.; Drummer, D. ScienceDirect Selective Laser Melting of Polymer Powder-Part Mechanics as Function of Exposure Speed. *Phys. Procedia* **2015**, *78*, 328–336. https://doi.org/10.1016/j.phpro.2015.11.047.

(29) ASTM D1895 - 17 Standard Test Methods for Apparent Density, Bulk Factor, and Pourability of Plastic Materials https://www.astm.org/Standards/D1895.htm

(accessed Mar 10, 2020). https://doi.org/10.1520/D1895-17.

(30) *S.3.6. BULK DENSITY AND TAPPED DENSITY OF POWDERS Final Text for Addition to The International Pharmacopoeia S.3.6. BULK DENSITY AND TAPPED DENSITY OF POWDERS BULK DENSITY*.

(31) Van den Eynde, M.; Verbelen, L.; Van Puyvelde, P. Assessing Polymer Powder Flow for the Application of Laser Sintering. *Powder Technol.* **2015**, *286*, 151–155. https://doi.org/10.1016/j.powtec.2015.08.004.

(32) Technique, G. Standard Test Methods for Apparent Density , Bulk Factor , and Pourability of Plastic. *Methods* **1996**, *08*, 1–5. https://doi.org/10.1520/D1895-96R10E01.

(33) Ziegelmeier, S.; Christou, P.; Wöllecke, F.; Tuck, C.; Goodridge, R.; Hague, R.; Krampe, E.; Wintermantel, E. An Experimental Study into the Effects of Bulk and Flow Behaviour of Laser Sintering Polymer Powders on Resulting Part Properties. *J. Mater. Process. Technol.* **2015**, *215*, 239–250. https://doi.org/10.1016/J.JMATPROTEC.2014.07.029.

(34) Chatham, C. A.; Long, T. E.; Williams, C. B. Powder Bed Fusion of Poly(Phenylene Sulfide)at Bed Temperatures Significantly below Melting. *Addit. Manuf.* **2019**, *28*, 506–516. https://doi.org/10.1016/j.addma.2019.05.025.

(35) Mercury Scientific Revolution ASTM Paper - Meritics https://www.meritics.com/mercury-scientific-revolution-astm-paper/ (accessed Feb 22, 2020).

(36) Vock, S.; Klöden, B.; Kirchner, · Alexander; Weißgärber, T.; Kieback, · Bernd. Powders for Powder Bed Fusion: A Review. **2019**, *4*, 383–397. https://doi.org/10.1007/s40964-019-00078-6.

(37) Berretta, S.; Evans, K. E.; Ghita, O. R. Predicting Processing Parameters in High Temperature Laser Sintering (HT-LS) from Powder Properties. *Mater. Des.* **2016**, *105*, 301–314. https://doi.org/10.1016/j.matdes.2016.04.097.

(38) Vasquez, M.; Haworth, B.; Hopkinson, N. Methods for Quantifying the Stable Sintering Region in Laser Sintered Polyamide-12. *Polym. Eng. Sci.* **2013**, *53* (6), 1230–1240. https://doi.org/10.1002/pen.23386.

(39) Benedetti, L.; Brulé, B.; Decraemer, N.; Evans, K. E.; Ghita, O. Evaluation of Particle Coalescence and Its Implications in Laser Sintering. *Powder Technol.* **2019**, *342*, 917–928. https://doi.org/10.1016/j.powtec.2018.10.053.

(40) Hejmady, P.; Lambè, A.; Van Breemen, C. A.; Anderson, P. D.; Cardinaels, R. Laser Sintering of Polymer Particle Pairs Studied by in Situ Visualization †. *pubs.rsc.org* **2019**. https://doi.org/10.1039/c8sm02081g.

(41) Huilgol, R. R. On the Concept of the Deborah Number. *Trans. Soc. Rheol.* **1975**, *19* (2), 297–306. https://doi.org/10.1122/1.549372.

(42) Hoath, S. D.; Harlen, O. G.; Hutchings, I. M. Jetting Behavior of Polymer Solutions

in Drop-on-Demand Inkjet Printing. *J. Rheol. (N. Y. N. Y).* **2012**, *56* (5), 1109–1127. https://doi.org/10.1122/1.4724331.

(43) Scribben, E.; Eberle, A. P. R.; Baird, D. G. Viscoelastic Coalescence of Thermotropic Liquid Crystalline Polymers: The Role of Transient Rheology. *J. Rheol. (N. Y. N. Y).* **2005**, *49* (6), 1159–1175. https://doi.org/10.1122/1.2039827.

(44) Prasad, L. K.; Smyth, H. 3D Printing Technologies for Drug Delivery: A Review. *Drug Dev. Ind. Pharm.* **2016**, *42* (7), 1019–1031. https://doi.org/10.3109/03639045.2015.1120743.

(45) Ziegelmeier, S.; Christou, P.; Wöllecke, F.; Tuck, C.; Goodridge, R.; Hague, R.; Krampe, E.; Wintermantel, E. An Experimental Study into the Effects of Bulk and Flow Behaviour of Laser Sintering Polymer Powders on Resulting Part Properties. *J. Mater. Process. Technol.* **2015**, *215* (1), 239–250. https://doi.org/10.1016/j.jmatprotec.2014.07.029.

(46) Wilts, E.; Ma, D.; Bai, Y.; Williams, C. B.; Long, T. E. Comparison of Linear and 4-Arm Star Poly(Vinyl Pyrrolidone) for Aqueous Binder Jetting Additive Manufacturing of Personalized Dosage Tablets. *ACS Appl. Mater. Interfaces* **2019**, acsami.9b08116. https://doi.org/10.1021/acsami.9b08116.

(47) Schmid, M.; Amado, A.; Wegener, K. Polymer Powders for Selective Laser Sintering (SLS). In *AIP Conference Proceedings*; American Institute of Physics Inc., 2015; Vol. 1664, p 160009. https://doi.org/10.1063/1.4918516.

(48) Ziegelmeier, S.; Wöllecke, F.; Tuck, C.; Goodridge, R.; Hague, R. *Characterizing the Bulk & Flow Behaviour of LS Polymer Powders*.

(49) Okubo, M.; Konishi, Y.; Minami, H. *SHORT COMMUNICATION Production of Hollow Polymer Particles by Suspension Polymerization Part CLXXX of the Series "'Studies on Suspension and Emulsion';"* Steinkopff Verlag, 1998; Vol. 276.

(50) Okubo, M.; Minami, H.; Yamashita, T. Production of Micron-Sized Monodispersed Cross-Linked Polymer Particles Having Hollow Structure. *Macromol. Symp.* **1996**, *101* (1), 509–516. https://doi.org/10.1002/masy.19961010157.

(51) Another Spiral Chess Set by JaaYoo - Thingiverse https://www.thingiverse.com/thing:1094870 (accessed Mar 10, 2020).

(52) Catan Pirate Ship by JulyForToday - Thingiverse https://www.thingiverse.com/thing:861658 (accessed Mar 10, 2020).

(53) *Phase Change Materials (Phasenwechselmaterial) Gütesicherung Quality Assurance RAL-GZ 896*.

(54) Kolesov, I.; Dolynchuk, O.; Letters, H. R.-E. P.; 2015, undefined. Shape-Memory Behavior of Cross-Linked Semi-Crystalline Polymers and Their Blends. *researchgate.net*.

(55) Sun, Ming-shen; Nelson, Christian; Beaman, Joseph J.; Barlow, Joel J. 1991 International Solid Freeform Fabrication Symposium, http://hdl.handle.net/2152/64279.

10.8 Supplemental

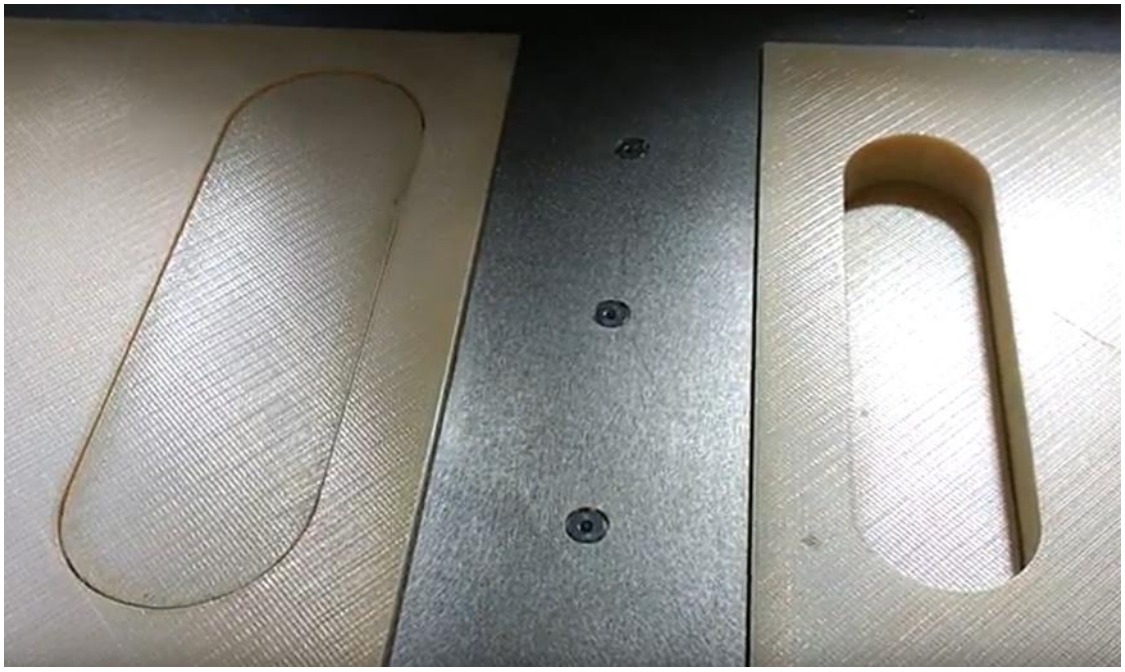

Figure S101. Image of custom “bed reducer” apparatus enabling multi-layer printing with a 1 L powder batch size.

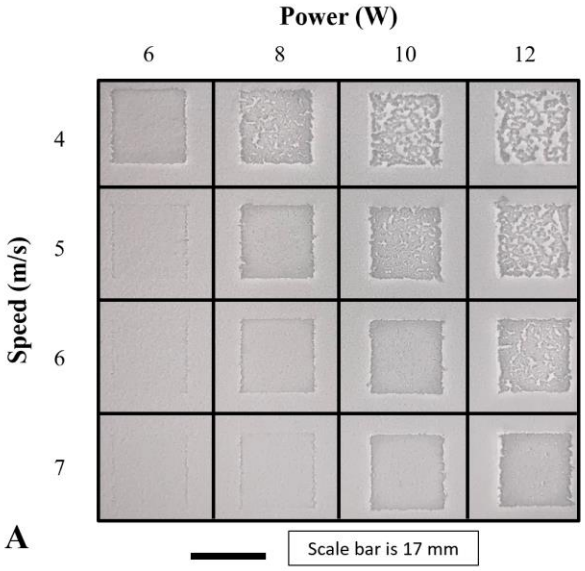

Thickness (in)

0.0392	0.0379	0.0470	0.0546
N/A	N/A	0.0395	0.0444
N/A	N/A	0.0378	0.0386
N/A	N/A	N/A	0.0307

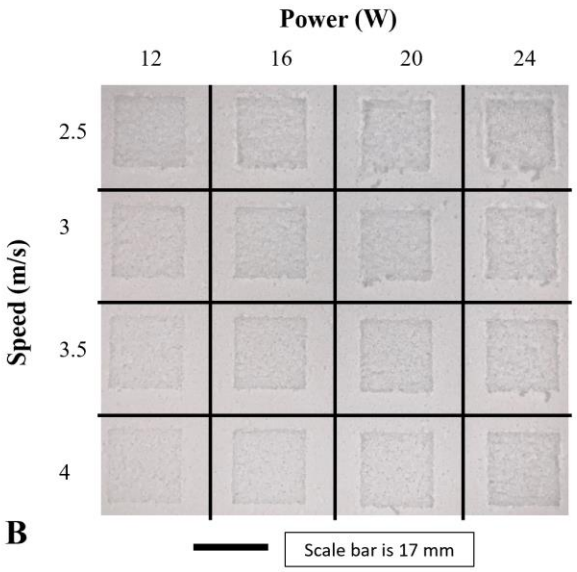

Thickness (in)

0.0421	0.0480	0.0488	0.0478
0.0384	0.0386	0.0471	0.0403
0.0406	0.0335	0.044	0.0422
N/A	0.0436	0.0381	0.0425

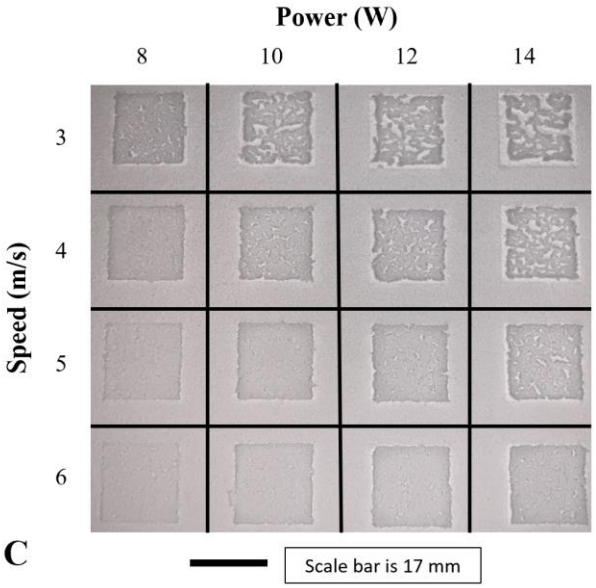

Thickness (in)

0.0285	0.0382	0.0458	0.0427
0.0264	0.0287	0.0414	0.0270
N/A	0.0260	0.0303	0.0299
N/A	0.0279	0.0206	0.0339

Figure S10.2. Additional fusion grids of **(A)** solution-made, **(B)** 50:50, and **(C)** suspension-made PSA.

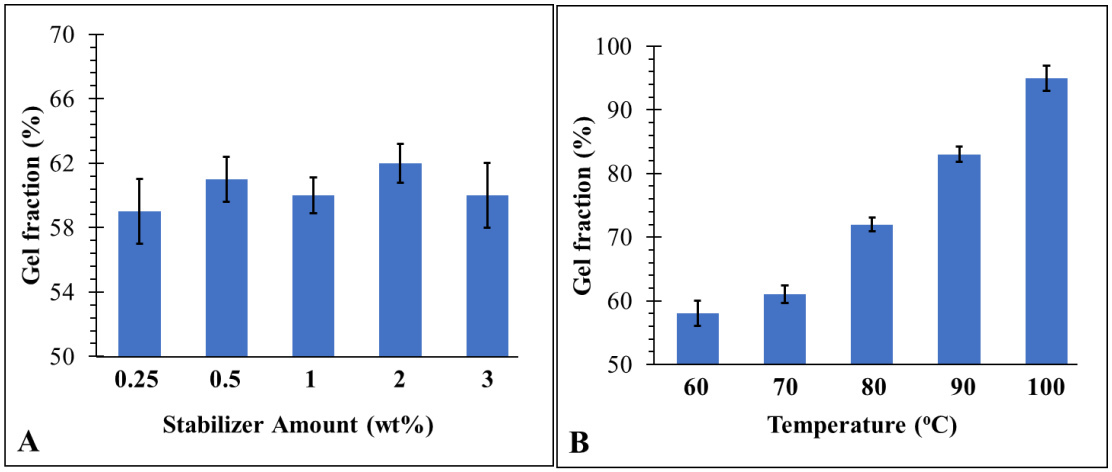

Figure S10.3. (A) Gel fractions as a functional of stabilizer amount and **(B)** as a function of reaction temperature.

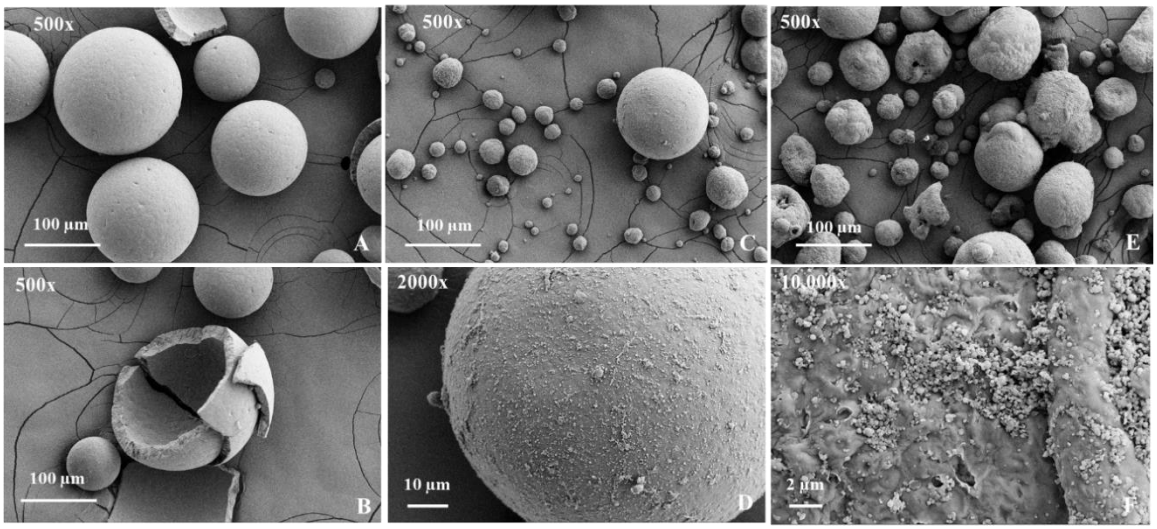

Figure S10.4. (A, B) Suspension-made PSA at 500x, **(C, D)** 50:50 at 500x and 2000x, and **(E, F)** solution-made PSA at 500x and 10,000x.

Table S10.1. Summary of apparent and tapped density data.

	Solution		Suspension		50:50	
	Apparent (g/cm³)	Tapped (g/cm³)	Apparent (g/cm³)	Tapped (g/cm³)	Apparent (g/cm³)	Tapped (g/cm³)
n=1	0.509836711	0.6165	0.430847924	0.596170213	0.492327366	0.627317073
n=2	0.511115483	0.614117647	0.441471572	0.589268293	0.491442062	0.622264151
n=3	0.508557938	0.603111111	0.454849498	0.589787234	0.490753492	0.619574468
Average	0.509836711	0.611242919	0.442389665	0.591741913	0.49150764	0.623051897
Standard deviation	0.001044113	0.005831731	0.009820083	0.003138439	0.000644202	0.00320961
Hausner ratio (HR)	1.20		1.34		1.27	

Table S10.2. Summary of RPA data.

	Solution	**50:50**	**Suspension**
Surface fractal	1.860	2.050	3.240
Avalanche angle (º)	45.7 ± 3.4	47.8 ± 3.7	54.4 ± 3.2
After vibration density (g mL^{-1})	0.6044	0.5617	0.5658

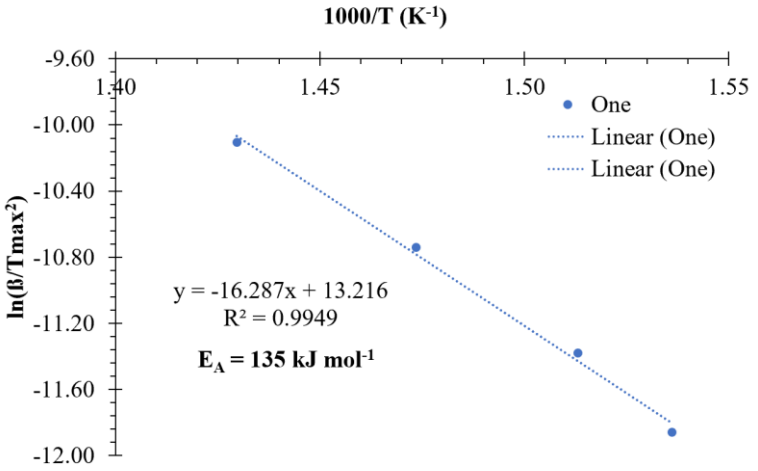

Figure S10.5. Kissinger analysis for activation energy of decomposition (E_A).

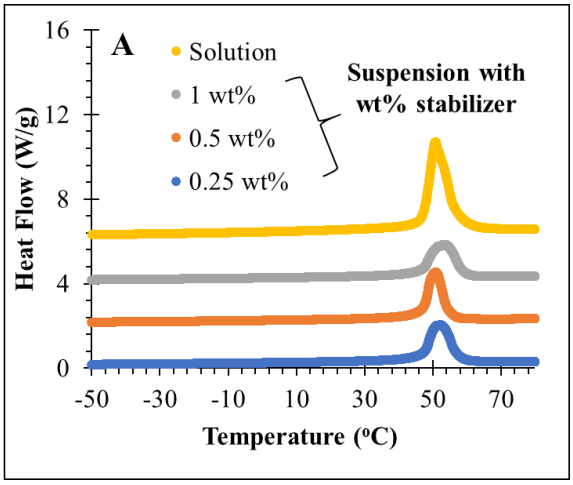

Figure S10.6. (A) DSC first heat traces of poly(stearyl acrylate) synthesized through suspension and solution polymerization.

Figure S10.7. Depiction of additively manufactured rook below and above T_m= 51 °C

Chapter 11: Solution Viscosity Scaling Relationships in Water of Linear, 4-Arm Star, and Graft Poly(vinyl pyrrolidone)

Emily M. Wilts and Timothy E. Long

(Research Chapter)

Department of Chemistry, Macromolecules Innovation Institute, Virginia Tech, Blacksburg, VA 24061

11.1 Abstract

Polymers in solution possess multiple applications such as suspensions in paint, drug delivery systems, additive manufacturing, and coatings. Processing conditions of polymeric solutions depend on four viscoelastic regimes, namely dilute, semi-dilute unentangled, semi-dilute entangled, and concentrated when studying zero-shear viscosity as a function of concentration. This research chapter describes the thermal analysis, discovery of linear, 4-arm star, and graft poly(vinyl pyrrolidone) (PVP) viscosity regimes, and comparisons between each system. The varying architectures impart varying polymer coil sizes in solution, which produce a wide variety of regime transitions. The critical overlap concentration (C^*) and entanglement concentration (C_e) represent the transitions from dilute to semi-dilute unentangled and semi-dilute unentangled to semi-dilute entangled and are the main transitions examined in the manuscript. Chapters 6 and 8 described binder jetting additive manufacturing of linear, 4-arm star, and graft and how C^* predicts jettability for thermal printheads. Building on those chapters, the current study aims to expand on the solution properties of the three polymers architectures and describe relationships and differences between them.

11.2 Introduction

When plotting specific viscosity (η_{sp}) as a function of concentration for a linear polymer in a good solvent, four main viscosity regimes exist. **Figure 9.1.** depicts a physical representation of the first three regimes beginning with dilute, and with increasing concentration to semi-dilute unentangled, and semi-dilute entangled.[1,2] Single, non-overlapping polymer chains contribute the viscosity in a dilute solution. When polymers begin to interact and overlap, the regime crosses over the critical overlap concentration (C^*) and enters the semi-dilute unentangled regime.[3–5] As the fraction of solvent decreases, proximity of the chains enables backbone entanglements, which transitions the system into the semi-dilute entangled regime. The entanglement concentration (C_e) denotes the transition into this regime.[6,7] The last regime, called concentrated, occurs when the chain entanglements govern the viscosity profile opposed to the solvent.

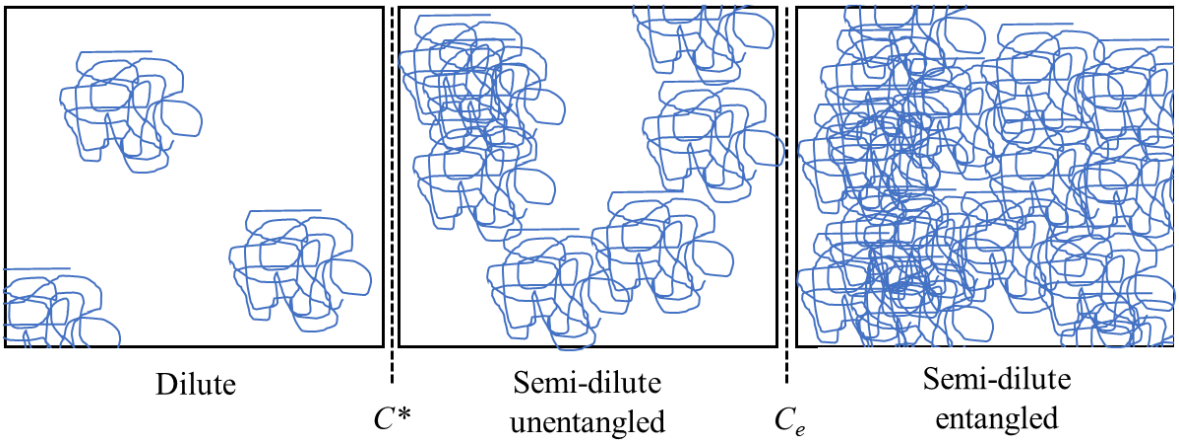

Figure 11.1. Physical representation of solution viscosity regimes as a function of concentration depicting three sections, dilute, semi-dilute unentangled, and semi-dilute entangles, where C^* and C_e denote the transitions between each state.

Using processing windows within specific viscoelastic regimes of polymeric solutions dictate the success and quality of manufactured parts in electrospinning and binder jetting additive manufacturing. Mckee *et al.* observed the formation of polymer beads and fibers during the electrospinning process as related to viscosity regimes. The authors found in the dilute regime only polymer droplets formed due to the lack of chain entanglement in the dilute regime. Beads and fibers formed in the semi-dilute unentangled and semi-dilute entangled regimes. Consistent fibers formed for successful electrospun products from M_w of 12,470–205,800 g mol^{-1} in the semi-dilute entangled regimes even with broad molecular weight distributions.[1,8] Wilts *et al.* identified the maximum jettable concentration for thermal printheads of PVP in solution is related to C^* in water. Linear and 4-arm star PVP experienced varying *C** values but solutions were unable to jet higher than these concentrations. They hypothesized the viscoelastic properties of polymeric solutions in the semi-dilute unentangled regimes prevented the liquid from jetting out of the nozzle. These two examples of how viscoelastic regimes influence processing greatly contributed to successful electrospinning and binder jetting additive manufacturing.[9]

11.3 Background Theory

For a linear polymer in a good solvent in the dilute regime, the Huggins Equation (**Eqn. 1**) describes solution viscosity where $\eta_{sp}(c)$, $[\eta]$, and k_H represent the specific viscosity, intrinsic viscosity, and Huggins coefficient. The initial slope in **Eqn. 1** is the intrinsic viscosity and is related to the root-mean-square end-to-end distance ($\langle R^2 \rangle^{1/2}$) according to the Flory-Fox relationship of a linear polymer with N monomers (**Eqn. 2**).

$$\eta_{sp}(c) = [\eta]c + k_H([\eta]c)^2 + \cdots \qquad \textbf{Eqn. 1}$$

$$[\eta] \sim \frac{< R^2 >^{3/2}}{N} \qquad \textbf{Eqn. 2}$$

Eqn. 3 describes the critical overlap concentration (*C**), which represents the transition from dilute to semi-dilute unentangled regime, and how it related to intrinsic viscosity ([η]). Based on the calculation below, *C**[η] ~ 1 in the dilute regime therefore *C** = 1/[η] represents an experimental method to estimate *C**. **Eqn. 4** represents another method to estimate *C** based on chain dimensions where N_{av} and M represent Avogadro's number and molecular weight respectively.

$$C^* \sim \frac{N}{< R^2 >^{3/2}} \sim \frac{1}{[\eta]} \qquad \textbf{Eqn. 3}$$

$$C^* \sim \frac{3M}{4\pi < R^2 >^{3/2} N_{av}} \sim \frac{1}{[\eta]} \qquad \textbf{Eqn. 4}$$

In general, radius of gyration (R_g) is a more reliable measure of size than $<R^2>^{1/2}$ because it takes into consideration the interactions between the solvent and swollen chains. **Eqn. 6** describes calculating R_g from hydrodynamic radius (R_h) from the Kirkwood-Riseman theory.[10] Dynamic light scattering also measures R_g through plotting light scattering and molecular weight data on a Zimm plot.[11]

$$R_g \sim \frac{R_h}{0.875} \qquad \textbf{Eqn. 6}$$

Eqn. 7 describes the power law dependency of concentrations above *C** where η_s, and v represent the solvent viscosity and the Flory exponent (0.5 or 0.6, theta or good solvent, respectively). Reptation theory predicts an exponent of 3.75 for the semi-dilute

unentangled regime, but experimental data suggests a larger molecular weight effect where $\eta \sim M^{3.4}$. This suggests other modes of relaxation aside from reptation such as contour length fluctuations.[12] Further experimental of linear polymers in good solvents confirmed the power law scaling relationship to be 1.25 in the semi-dilute unentangled regime, and 4.25-4.5 in the semi-dilute entangled regime.[1,2]

$$\eta = \eta_s \left(\frac{c}{c^*}\right)^{\left(\frac{3}{3\nu}-1\right)} \qquad \textbf{Eqn. 7}$$

While most non-associating, linear polymers in a good solvent adhere to the accepted power law dependencies on viscosity as a function of concentration, electrostatic interactions, hydrogen bonding effects, and varying architectures lead to deviations from the norm. For example, polyelectrolytes experience a decrease in relaxation times in the semi-dilute regions compared to an increase in neutral polymers. They also exhibit greater shear thinning effects, which contribute to a different power law dependence ($C^* < C < C_e \sim C^{0.5}$).[13,14] Polymers in aqueous solutions capable of hydrogen bonding also revealed slightly different scaling relationships compared to known literature values.[9,15]

11.4 Experimental

11.4.1. Materials

(1-Bromoethyl)benzene, 1,2,4,5-tetrakis(bromomethyl)benzene, Tween 20®, silica, acetaminophen, methyl benzoate (99%), and 40k PVP were purchased from Sigma Aldrich and used without further purification. *N*-Vinyl pyrrolidone (NVP) was filtered through a basic aluminum column to remove inhibitor before use. Azobisisobutyronitrile (AIBN) was purchased from Sigma Aldrich and recrystallized from methanol before use. O-ethyl

xanthic acid potassium salt was dried at 40 °C under high vacuum (0.1 mbar) for 24 h before use. Diethyl ether, deionized (DI) water, extra dry acetone (99.9%) and methanol were purchased from Acros and used without further purification. Lactose 315 was purchased from Foremost Farms USA and Kroger Inc. powdered confectioners' sugar (5-30 μm particle size) was purchased from the local store, and both were dried at 60 °C under vacuum for 24 h and sifted to break up aggregates before use. Diisopropylamine and methyl oxazoline were purchased from Sigma Aldrich and distilled over calcium hydride before use. *N*-butyl-lithium, allyl bromide, methyl triflate, piperidine, vinyl pyrrolidone, *O*-ethyl xanthic acid potassium salt, silver nitrate, sodium hydroxide, and 1-bromo ethyl benzene were purchased from Sigma Aldrich and used without further purification. Saturated bromine water was purchased from ITW Reagents and diluted with DI water to 0.1 M before use. Azobisisobutyronitrile (AIBN) was purchased from Sigma Aldrich and recrystallized over methanol before use. Extra dry acetonitrile, chloroform, tetrahydrofuran, dichloromethane, methanol, pyridine and acetone were purchased from Acros and used without further purification.

11.4.2. Synthetic Methods

RAFT polymerization kinetics of N-vinyl pyrrolidone

Previously reported from Wilts *et. al.*[9] As an example procedure for linear PVP, a stock batch of NVP (35 g, 0.315 mol), *O*-ethyl-*S*-(1-ethylphenyl) dithiocarbonate (0.16 g, $7 \cdot 10^{-4}$ mol), and AIBN (11.4 mg, $7 \cdot 10^{-5}$ mol) were mixed and split into six 50-mL round-bottomed flasks and purged with nitrogen for 30 min. The molar ratio of NVP:CTA:AIBN was 450:1:0.1. The mixtures were allowed to react at 60 °C for 2, 4, 8, 12, 16, and 24 h. ^{1}H

NMR spectroscopy of the crude product determined conversion. The reaction mixture was precipitated twice into diethyl ether and stirred for 20 min. Aqueous SEC determined absolute molecular weight of each system.

Graft copolymer synthesis (PMeOx-g-PVP)

Previously reported from Wilts *et. al.*[16] PMeEneOx (1 g, $1 \cdot 10^{-4}$ mol, 1 eq.) and diphenyl(2,4,6-trimethylbenzoyl)phosphine oxide (TPO) (9.7 mg, 0.3 eq.) were dissolved in chloroform (15 wt % solids) and added to the PVP-SH reaction mixture. The mixture was purged with nitrogen for 30 min and exposed to a broad spectrum (320-500 nm) UV light for 10 min and stirred for an additional 24 h. Chloroform was removed under reduced pressure and the product was dissolved in methanol. The solution was put into dialysis for five days against methanol with 3.5 kg mol^{-1} pores. After five days the methanol was removed, and the product was precipitated into diethyl ether and dried under high vacuum at 80 ^{o}C.

11.4.3. Solution Mixing

As an example of a 2 wt % solution, 2.05 g of PVP was dissolved in 100 mL of DI water and stirred with a magnetic stirrer for 15 min. Immediately before testing, the solutions were stirred again for 10 min with a magnetic stirrer and placed in a water bath at 20 ^{o}C.

11.4.4. Analytical

Aqueous SEC-LS in 54/23/23 v/v/v mixture of DI water, methanol, and glacial acetic acid with 0.1 M sodium acetate at a pH=4 determined M_n, M_w, and Đ. A Waters Breeze Aqueous SEC with Wyatt miniDAWN treos light scattering and Waters 2414 RI detector with poly(ethylene oxide) (PEO) standards determined absolute molecular weight of each

system. Solution viscosity experiments were performed on a DHR Discovery Rheometer in steady state mode with a concentric cylinder geometry at 20 ^{o}C where n=3. Differential scanning calorimetry (DSC) was ran at 50 mL min^{-1} nitrogen flow at a 10 ^{o}C per min heating rate and 100 ^{o}C per min cooling rate on a TA instruments Q2000 with indium (mp = 156.60 °C) and zinc (mp = 419.47 °C) standards. Glass transition temperatures (T_g) were determined from the midpoint of the endothermic transition. TA Instruments Q50 measured for thermogravimetric analysis (TGA) started with a 30 min isotherm at 120 °C and a ramp 10 °C/min from 120 to 800 °C.

11.4.5. Nomenclature

The six polymers in the discussed graft copolymer series follow the naming sequence "xx%, yy" where "xx" represents the mol % grafting sites and "yy" represents the PVP graft molecular weight, displayed in **Table 11.1**. The six polymers contain 5, 10, and 25 mol % grafting sites and 2.5 and 5 kg mol^{-1} PVP grafts.

Table 11.1. Summary of graft copolymer nomenclature.

Name	M_n PVP (kg mol^{-1})	Me:Ene mol %
5%, 2.5	2.5	95:5
5%, 5	5	95:5
10%, 2.5	2.5	90:10
10%, 5	5	90:10
25%, 2.5	2.5	75:25
25%, 5	5	75:25

11.5 Results and Discussion

11.5.1. Chemical and thermal analysis

Figure 11.2. depicts the three PVP architectures tested in this study, linear, 4-arm star, and graft. Reversible addition-fragmentation chain-transfer (RAFT) polymerization yielded linear and 4-arm star at 5, 25, and 50 kg mol^{-1}. RAFT polymerization enabled the production of controlled molecular weight polymers through maintaining a constant and small number of radicals throughout the reaction and reduction of termination events. Ring-opening cationic polymerization of oxazolines and subsequent thiol-ene click chemistry yielded graft PVP from 35 to 91 kg mol^{-1} total molecular weight and 5 to 25 mol % grafting sites on the backbone. RAFT polymerization of linear and 4-arm star PVP yielded polymers with Đ values from 1.1 – 1.2. The graft PVP combinations exhibit Đ values from 1.5 – 1.8 because of the two-step process beginning with poly(2-oxaozline) backbones with Đ values of 1.3. All polymer systems were readily water soluble, therefore all subsequent solution property experiments were performed in DI water.

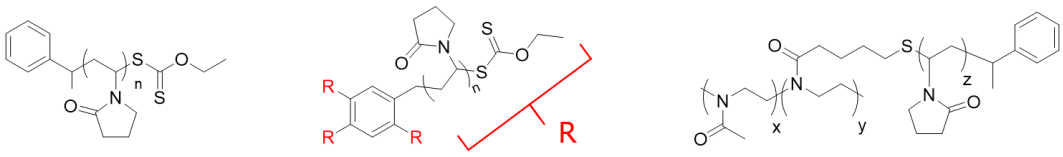

Figure 11.2. Chemical structures of linear, 4-arm star, and graft poly(vinyl pyrrolidone).

Aqueous SEC-LS confirmed M_n, M_w, and Đ and linear, 4-arm star, and graft PVP. **Figure 11.3.** depicts the light scattering traces of 25 kg mol^{-1} linear and 4-arm star PVP and 25 kg mol^{-1} graft PVP. Light scattering traces coupled with dn/dc values of each polymer systems enabled the most accurate reading of molecular weight. Branched and star polymers exhibit anchoring effects in SEC columns, which could skew RI detector

data. As discussed above, linear and 4-arm star PVP maintains a lower Đ compared to graft PVP due to the method of polymerization.

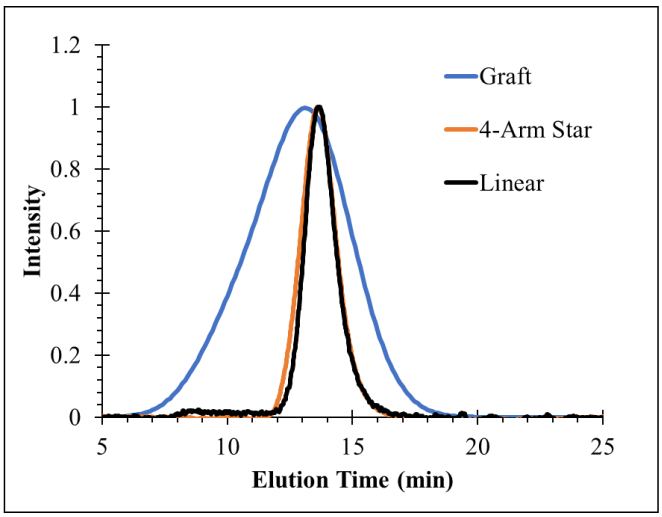

Figure 11.3. Aqueous SEC-LS of one example of each architecture at similar molecular weights.

Figure 11.4. A and **B** depict selected DSC and TGA traces of linear, 4-arm star, and graft PVP at 25, 25, and 35 kg mol^{-1}. Linear, 4-arm star, and graft PVP experienced T_g's of 162, 155, and 96 ^{o}C. Linear PVP exhibits the largest T_g compared to the other architectures due to the lowest number of end-groups and the highest likelihood to entangle. 4-arm star PVP experienced a slightly lower T_g because of increased chain ends in the system possibly producing more free volume in the system.[17,18] Graft PVP exhibited a large decrease in T_g compared to the other architectures because of the contribution from the poly(2-oxazoline) backbone, with a T_g of 67 ^{o}C, and an increase in chain ends.[19,20] **Figure 11.4 B** depicts TGA traces of each architecture where each polymer experienced a $T_{d,5\%}$ of 368 to 370 ^{o}C. This is expected because PVP exhibits a $T_{d,5\%}$ of 370 ^{o}C above 3 kg mol^{-1}. **Table S11.1** summarizes the remaining T_g and $T_{d,5\%}$ values for all architectures.

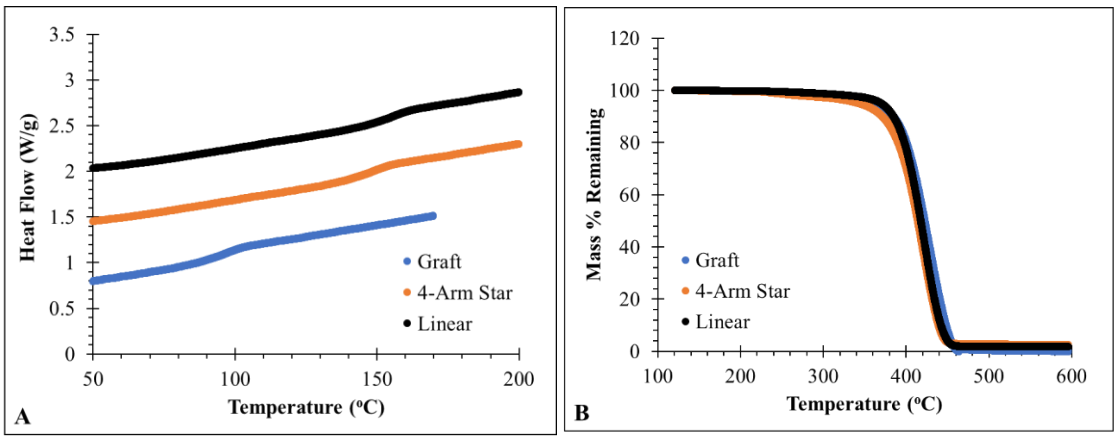

Figure 11.4. (A) DSC and **(B)** TGA of one example of each architecture at similar molecular weights.

9.5.2. Solution properties

Table 11.2. summaries C^* and C_e values for all compositions of linear, 4-arm star, and graft PVP. As a general trend, C^* and C_e both increase with decreasing size of polymer architecture. At the same M_n, linear, 4-arm star, and graft PVP decrease in size or R_g because of branching. Linear polymers do not contain branching and therefore rescind into a random coil in solution. 4-Arm star contained one core and arms equivalent to one fourth the M_n of its linear analog, therefore decreasing its size in solution. Graft PVP 10, 2.5 contained a linear backbone and 10 arms, which created the smallest and most compact polymer.

Table 11.2. Summary of C^* and C_e transitions for linear, 4-arm star, and graft PVP.

Name	C^* (wt %)	C_e (wt %)
Linear, 5k	14.4 ± 0.2	26.6 ± 0.3
Linear, 25k	7.2 ± 0.7	17.8 ± 0.5
Linear, 50k	3.1 ± 0.5	13.9 ± 0.1
4-Arm Star, 5k	16.6 ± 0.7	29.6 ± 0.6

4-Arm Star, 25k	11.0 ± 0.6	25.4 ± 0.6
4-Arm Star, 50k	6.0 ± 0.1	17.8 ± 0.8
5%, 2.5	18.8 ± 0.6	32.2 ± 0.7
5%, 5	17.4 ± 0.5	30.5 ± 0.5
10%, 2.5	14.2 ± 0.3	22.1 ± 0.4
10%, 5	12.2 ± 0.2	19.8 ± 0.4
25%, 2.5	10.3 ± 0.5	18.4 ± 0.1
25%, 5	9.8 ± 0.5	17.1 ± 0.5

Figure 11.5 depicts specific viscosity (η_{sp}) as a function of concentration to determine the critical overlap concentration (*C**). The transition from the dilute to semi-dilute unentangled regime denotes *C**, where polymer chains begin to overlap and interact. The power law slope from the dilute to semi-dilute unentangled regime changes from 1.0 to 1.25 in homogenous solutions of linear, non-associating polymers. **Figure 11.5** reveals the *C** values increase from linear, 4-arm star, and graft PVP. This trend is related to the radii of gyration (R_g) of each polymer architecture. Linear compared to 4-arm star polymers at the same molecular weight exhibit a larger R_g because of the less compact orientation. 4-arm star polymers at 25 kg mol^{-1} contain approximately 6 kg mol^{-1} arms tethered at a single point, rendering the shape in solution more compact. Aqueous SEC-LS attempted to measure R_g of the example linear, 4-arm star, and graft PVP discussed above, but the sizes were out of the range of detection, therefore calculations of each R_g were performed.

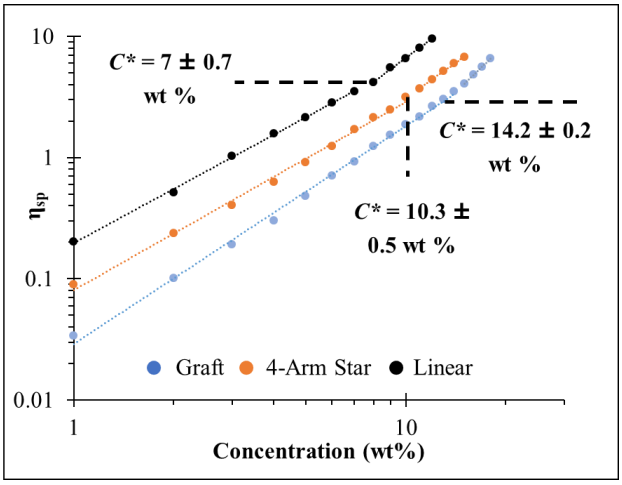

Figure 11.5. η_{sp} as a function of concentration, where power law slope changes denoted *C** of linear, 4-arm star, and graft PVP.

R_g is the average distance from a polymer chain center of gravity to the outer-most edge of the system. A common method of expressing this metric is through the root-mean square radius of gyration. For linear, star, and graft polymers, the Rg^2 can be estimated via **Eqn. 8, 9,** and **10**, respectively. N, b, and f represent number of segments, Kuhn length, and number of arms in **Eqn. 8** and **9**.[21] **Eqn. 10** is for graft polymers where p, M_A, M_B, N_A, b_A, N_B, b_B, and M represent number of side chains, molecular weight of the backbone, molecular weight of the side chains, number of backbone segments, Kuhn length of the backbone, number of side chain segments, Kuhn length of the side chains, and total molecular weight.[22] The Kuhn length for PVP is 3.0 nm and used for the calculations below.[15]

$$R_g^2 = \frac{Nb^2}{6} \quad \textbf{Eqn. 8}$$

$$R_g^2 = [\frac{3f-2}{f^2}](\frac{Nb^2}{6}) \quad \textbf{Eqn. 9}$$

$$R_g^2 = \{[(p+1)^3 M_A^2 + p(p+1) * (2p+1) M_A M_B + p(p-1)(p+1) M_B^2] N_A b_A^2 + [3p(p+1) M_A M_B + p(3p-2) M_B^2] N_B b_B^2\} / 6M^2 \quad \textbf{Eqn. 10}$$

For linear, 4-arm star, and graft PVP at 25, 25, and 35 kg mol^{-1}, respectively, the calculated R_gs are 10.6, 8.4, and 6.6 nm, respectively. As R_g decreases for varying polymers architectures at the same molecular weight and dissolved at the same concentration in solution, the solution viscosity decreases. For example, comparing the PVP samples discussed above, moving from linear to star to graft polymers, the R_g decreases.[23] If these polymers were dissolved in water, a good solvent for PVP, at 5 wt %, the solution viscosity of the linear would be the highest, followed by the star and then graft. This is because with increasing R_g, the move volume the polymer chains will occupy in solution, which will not only increase frictional forces in solution, but the chains will be more likely to entangle and overlap.[2] This relationship is also depicted in the measurement of *C**, where decreasing R_g results in increasing *C**. Polymers with the smallest R_g values need more polymer in solution to begin to overlap.[1,2,13]

Figure 11.6 depicts η_{sp} as a function of concentration above *C** which determined C_e for 25 kg mol^{-1} architectures. C_e depends on the ability to entangle and R_g. As R_g increases, C_e decreases because chains must reach a higher concentration to not only overlap, but also entangle. C_e for linear, 4-arm star, and graft PVP, was 17.8 ± 0.5 wt %, 25.4 ± 0.6 wt %, and 22.1 ± 0.4 wt %, respectively. The slope of the line also elucidated the concentration dependency on viscosity and suggested if the chains were entangled in solution. Linear, 4-arm star, and graft PVP exhibited $C^{4.86}$, $C^{3.91}$, and $C^{3.98}$, respectively.

Linear PVP exhibited the steepest slope because it entangles in solution. 4-Arm star and graft PVP do not entangle, and therefore experienced swallower slopes.

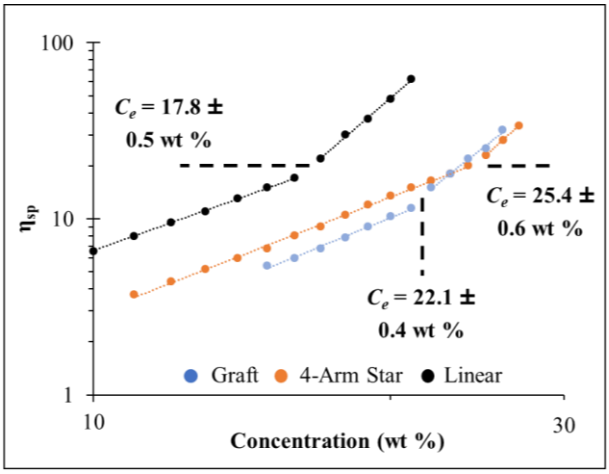

Figure 11.6. η_{sp} as a function of concentration, where power law slope changes denoted C_e of linear, 4-arm star, and graft PVP.

11.6. Conclusions

Optimal processing conditions of polymeric solutions depend on solution viscosity regimes, especially in electrospinning and binder jetting additive manufacturing. This research chapter describes the thermal analysis and solution viscosity regimes of linear, 4-arm star, and graft PVP at varying molecular weights. DSC revealed T_gs decreased from linear, 4-arm star, to graft PVP possibly due to a decrease in chain entanglement and an increase in chain ends. Next, solution viscosity as a function of concentration experiments revealed graft PVP experienced the highest C^* values and linear the lowest. Calculations of R_g, which is related to C^*, revealed graft PVP experienced the smallest and linear the largest because of the different sizes and conformations in solution.

11.7. Acknowledgements

The authors would like to thank Katherine Heifferon and Ryan Mondschein for conversations leading to the development of this work.

11.8. References

(1) Gupta, P.; Elkins, C.; Long, T. E.; Wilkes, G. L. Electrospinning of Linear Homopolymers of Poly(Methyl Methacrylate): Exploring Relationships between Fiber Formation, Viscosity, Molecular Weight and Concentration in a Good Solvent. *Polymer (Guildf).* **2005**, *46* (13), 4799–4810. https://doi.org/10.1016/J.POLYMER.2005.04.021.

(2) Colby, R. H.; Fetters, L. J.; Funk, W. G.; Graessley, W. W. Effects of Concentration and Thermodynamic Interaction on the Viscoelastic Properties of Polymer Solutions. *Macromolecules* **1991**, *24* (13), 3873–3882. https://doi.org/10.1021/ma00013a021.

(3) Faraz, M. I. Rheology of Organoclay Dispersions and Modeling of Gelation Behavior and Finding Overlap Concentration. *Arab. J. Sci. Eng.* **2019**, *44* (12), 10117–10126. https://doi.org/10.1007/s13369-019-03960-1.

(4) Wehrman, M. D.; Leduc, A.; Callahan, H. E.; Mazzeo, M. S.; Schumm, M.; Schultz, K. M. Rheological Properties and Structure of Step- and Chain-Growth Gels Concentrated above the Overlap Concentration. *AIChE J.* **2018**, *64* (8), 3168–3176. https://doi.org/10.1002/aic.16062.

(5) Wang, Y.; Fu, J.; Liu, M.; Fu, Q.; Polymer, J. Z.-; 2019, undefined. The Effect of Chain Entanglement State on Melt Crystallization of the Polymer Freeze-Extracted from Solution: The Role of Critical Overlap Concentration. *Elsevier*.

(6) Milner, S. T. Unified Entanglement Scaling for Flexible, Semiflexible, and Stiff Polymer Melts and Solutions. *Macromolecules* **2020**. https://doi.org/10.1021/acs.macromol.9b02684.

(7) Keshavarz, M.; Engelkamp, H.; Xu, J.; Van Den Boomen, O. I.; Maan, J. C.; Christianen, P. C. M.; Rowan, A. E. Confining Potential as a Function of Polymer Stiffness and Concentration in Entangled Polymer Solutions. *J. Phys. Chem. B* **2017**, *121* (22), 5613–5620. https://doi.org/10.1021/acs.jpcb.6b12667.

(8) Matthew G. McKee, †; Garth L. Wilkes, ‡; Ralph. H. Colby, § and; Timothy E. Long*, †. Correlations of Solution Rheology with Electrospun Fiber Formation of Linear and Branched Polyesters. **2004**. https://doi.org/10.1021/MA035689H.

(9) Wilts, E.; Ma, D.; Bai, Y.; Williams, C. B.; Long, T. E. Comparison of Linear and 4-Arm Star Poly(Vinyl Pyrrolidone) for Aqueous Binder Jetting Additive Manufacturing of Personalized Dosage Tablets. *ACS Appl. Mater. Interfaces* **2019**, acsami.9b08116. https://doi.org/10.1021/acsami.9b08116.

(10) Wilemski, G.; Tanakat, G. *Polymer 1981, 22, 783. (12) Horta, A.; Fernández-Piérola, I. Macromolecules, Preceding Paper in This Issue*; 1981; Vol. 14.

(11) Menasveta, M. J.; Hoagland, D. A. *Light Scattering from Dilute Poly(Styrene) Solutions in Uniaxial Elongational Flow*; 1991; Vol. 24.

(12) Pearson, D. S. RECENT ADVANCES IN THE MOLECULAR ASPECTS OF POLYMER VISCOELASTICITY. *Rubber Chem. Technol.* **1987**, *60* (3), 439–496. https://doi.org/10.5254/1.3536138.

(13) Matthew G. McKee; Matthew T. Hunley; John M. Layman, and; Long*, T. E. Solution Rheological Behavior and Electrospinning of Cationic Polyelectrolytes. **2005**. https://doi.org/10.1021/MA051786U.

(14) Wendy E. Krause, †; Enrico G. Bellomo, ‡ and; Ralph H. Colby*, ‡. Rheology of Sodium Hyaluronate under Physiological Conditions. **2001**. https://doi.org/10.1021/BM0055798.

(15) Knappe, P.; Bienert, R.; Weidner, S.; Thünemann, A. F. Characterization of Poly(N-Vinyl-2-Pyrrolidone)s with Broad Size Distributions. *Polymer (Guildf).* **2010**, *51* (8), 1723–1727. https://doi.org/10.1016/j.polymer.2010.02.039.

(16) Wilts, E.M.; Long, T. E. Synthesis and Characterization of Graft Poly(2-Oxazoline) and Poly(Vinyl Pyrrolidone) Copolymers Using Thiol-Ene 'Click' Chemistry. *J. Polym. Sci. Part A Polym. Chem.* **2020**, *submitted*.

(17) Kauzmann, W. The Nature of the Glassy State and the Behavior of Liquids at Low Temperatures. *Chem. Rev.* **1948**, *43* (2), 219–256. https://doi.org/10.1021/cr60135a002.

(18) Hess, M.; Allegra, G.; He, J.; Horie, K.; Kim, J. S.; Meille, S. V.; Metanomski, V.; Moad, G.; Stepto, R. F. T.; Vert, M.; et al. Glossary of Terms Relating to Thermal and Thermo Mechanical Properties of Polymers (IUPAC Recommendations 2013). *Pure Appl. Chem.* **2013**, *85* (5), 1017–1046. https://doi.org/10.1351/PAC-REC-12-03-02.

(19) Hong, S. C.; Jia, S.; Teodorescu, M.; Kowalewski, T.; Matyjaszewski, K.; Gottfried, A. C.; Brookhart, M. Polyolefin Graft Copolymers via Living Polymerization Techniques: Preparation of Poly(n-Butyl Acrylate)-Graft-Polyethylene through the Combination of Pd-Mediated Living Olefin Polymerization and Atom Transfer Radical Polymerization. *J. Polym. Sci. Part A Polym. Chem.* **2002**, *40* (16), 2736–2749. https://doi.org/10.1002/pola.10348.

(20) Yamashita, K.; Ito, K.; Tsuboi, H.; Takahama, S.; Tsuda, K.; Otsu, T. Graft Copolymerization by Iniferter Method; Structural Analyses of Graft Copolymer by Glass Transition Temperature. *J. Appl. Polym. Sci.* **1990**, *40* (910), 1445–1452. https://doi.org/10.1002/app.1990.070400903.

(21) Polymer Solutions: An Introduction to Physical Properties - Iwao Teraoka - Google Books https://books.google.com/books?hl=en&lr=&id=XB_y4o1IDb4C&oi=fnd&pg=PR7&dq=Teraoka,+A.+A.%3B+Teraoka,+I.,+Polymer+solutions:+an+introduction+to+physical+properties.+John+Wiley+%26+Sons:+2002.&ots=pt-sfOHVRN&sig=rknokfgKbtRRm1CJlzQJkq74_6I#v=onepage&q=Teraoka%2C A. A.%3B Teraoka%2C I.%2C Polymer solutions%3A an introduction to physical properties.

John Wiley %26 Sons%3A 2002.&f=false (accessed Oct 24, 2019).

(22) Scholte, T. G. Unperturbed Dimensions of Copolymer Molecules. *J. Polym. Sci. Part A-2 Polym. Phys.* **1967**, *5* (3), 461–470. https://doi.org/10.1002/pol.1967.160050306.

(23) Colby, R. H.; Fetters, L. J.; Funk, W. G.; Graessley, W. W. *Effects of Concentration and Thermodynamic Interaction on the Viscoelastic Properties of Polymer Solutions*; 1991; Vol. 24.

11.9 Supplemental

Table S11.1. Summary of T_g and $T_{d,5\%}$ of all architectures from DSC and TGA experiments.

Name	T_g (ºC)	$T_{d,5\%}$ (ºC)
Linear, 5k	123	365
Linear, 25k	162	369
Linear, 50k	176	370
4-Arm Star, 5k	116	366
4-Arm Star, 25k	155	371
4-Arm Star, 50k	172	368
5%, 2.5	88	345
5%, 5	95	352
10%, 2.5	96	370
10%, 5	111	370
25%, 2.5	112	366
25%, 5	119	372

Chapter 12: Synthesis and characterization of photoactive polyisobutylene for additive manufacturing of heart valves

Emily M. Wilts[1], Danny Rau[2], Christopher B. Williams[2], and Timothy E. Long[1*]

(Research Chapter)

[1]*Department of Chemistry, Macromolecules Innovation Institute, Virginia Tech, Blacksburg, VA 24061*

[2]*Department of Mechanical Engineering, Macromolecules Innovation Institute, Virginia Tech, Blacksburg, VA 24061*

12.1 Abstract

Additive manufacturing (AM) for tissue replacement presents a unique opportunity to manufacture personalized therapies for patients. Patients in need of heart valves, skin grafts, or other hard or soft tissue replacements require very precise sizes, functionalities, and therapeutics depending on current health. AM provides the ability to tailor a myriad of functional materials with different strengths and sizes to the patient in a short time frame, which could save lives. This chapter describes the functionalization of polyisobutylene (PIB) to use in direct ink write (DIW) printing of heart valves. Acryloyl chloride functionalized PIB-diol into a photoactive, liquid precursor where thermogravimetric analysis and differential scanning calorimetry measured thermal transitions. Size exclusion chromatography and ^{1}H nuclear magnetic resonance spectroscopy confirmed absolute molecular weight and chemical structure. Rheological experiments confirmed zero-shear viscosities of PIB-diol and PIB-diacrylate of 830 and 640 Pa·s, respectively. Subsequent DIW and DIW/vat photopolymerization hybrid printing enable thed production of a model heart valve.

12.2 Introduction

In the past 15 years, additive manufacturing (AM) became one of the most attractive manufacturing methods for tissue replacement and personalized medical devices because of its inherit tunability.[1–5] Tissue replacement requires collaboration across chemistry, biology, and engineering to create non-degradable or degradable implants that are biocompatible, do not illicit immune responses, and function as native tissue.[6] Non-degradable implants remain in the body to replace missing tissue, for example heart valves, and function as a tissue replacement. Common polymeric materials for this application in include poly(ethylene terephthalate), (PET), polyurethanes (PU), poly(tetrafluoroethylene) (PTFE), polyisobutylene (PIB) and polypropylene (PP) where these materials remain inert in the body.[7] All materials listed are now additively manufactured to form precise shapes and functionalities to meet patient needs in tissue replacement. While all platforms of AM manufacture forms for tissue engineering, this chapter focuses on vat photopolymerization (VP) and direct ink write (DIW) because they maintain the highest resolution parts of common AM methods.[8,9]

VP and DIW represent two AM platforms that often utilize UV light to transform photoactive precursors to solid 3D parts. VP begins with a liquid vat, a transparent stage, and a rising build platform. Projected, broad spectrum UV light or lasers project light through the stage to cure the first layer onto the platform.[10–13] The platform then moves upwards and another layer of photoactive precursor fills the void for the next layer. To ensure the liquid flows onto the transparent stage for the subsequent layer, the viscosity must remain below 10 Pa·s.[9] DIW also often utilizes UV light to cure photoactive liquids, however, this method uses an extrusion process. A high viscosity photoactive liquid,

usually above 100 Pa·s, is extruded onto a build stage that is solidified with UV light.[8,14,15] VP contains high resolution parts and DIW allows for high viscosity precursors. This chapter also discusses the combination of these two technologies to utilize both advantages.

Cationic polymerization with strong acids of isobutylene yields highly controlled polyisobutylene (PIB). Low permeability, high chemical resistance, high thermal and oxidative stability render PIB optimal for applications from adhesives to biomaterials. PIB is commonly used with combinations of other known biomaterials, polyacrylates, polymethacrylates, polysiloxanes, polylactones, polyurethanes, poly(ethylene oxide), and poly(vinyl alcohol) (PVA), to produce unique properties.[16] Bone cements made with poly(methyl methacrylate)s are often brittle, which leads to decreased longevity. To ameliorate this problem, researches combined tri-telechelic PIB with poly(methyl methacrylate)s to create an effective bone cement with more durability.[17] Other examples include PIB-based amphiphilic networks where PIB and hydrophilic polymers covalently combine to achieve unique properties. Kennedy *et al.* combined PIB with poly(ethylene glycol) and water-soluble acrylates to achieve pH sensitively, controlled swelling based on compositions, and controlled release of pharmaceuticals.[17–20] These examples elucidate the potential for PIB in other biomedical applications.

This manuscript reports the functionalization of polyisobutylene-diol and subsequent DIW printing of a model heart valve. Polyisobutylene-diol (PIB-diol) was functionalized with acryloyl chloride to create PIB-diacrylate. SEC, ^{1}H NMR spectroscopy, and thermal analysis revealed absolute molecular weight, chemical structure confirmation, and thermal transitions. Rheology experiments revealed zero-shear viscosities of PIB-diol and PIB-acrylate, reported as 830 and 640 Pa·s, respectively. DIW

and a hybrid DIW and VP printing systems manufactured a model heart valve with an expandable inner valve. RSA revealed storage moduli of printed, crosslinked, extracted, PIB-diacrylate of $4.1 \cdot 10^6$ Pa at 37 ^oC.

12.3 Experimental

12.3.1 Materials

Polyisobutylene-diol (PIB-diol) was provided from Boston Scientific and used without further purification. Potassium carbonate (Sigma Aldrich) was dried at 80 ^oC under high vacuum before use. Acryloyl chloride (Sigma Aldrich), aluminum oxide (Sigma Aldrich), and Chloroform ($CHCl_3$) (Acros Organics) was used without further purification.

12.3.2 Synthesis of polyisobutylene-diacrylate (PIB-diacrylate)

A mixture of PIB-diol (5 g, $2.6 \cdot 10^{-3}$ mol, 1 eq.), potassium carbonate (27.6 g, 0.20 mol, 8 eq.), and 100 mL of chloroform was stirred until PIB-diol dissolved. Acryloyl chloride (0.94 g, 0.10 mol, 4 eq.) was added dropwise over 10 min at 0 ^oC. The mixture stirred for 24 and 4 mL of water quenched the reaction. The mixture was stirred with and filtered through aluminum oxide three times. The solvent was removed *in vacuo* and the isolated product (92% yield) was left at 20 ^oC under high vacuum for 24 h to dry.

12.3.3 Analytical

^1H NMR was conducted on a Varian Unity 400 MHz in $CDCl_3$ at a 3 s relaxation delay. A Waters ACQUITY Advanced Permeation Chromatograph (APC) equip with a column set of one 125 Å x 150 mm and two 45 Å x 150 mm XT, an OMNISEC quad detector in chloroform at 40 °C and 1.0 mL min^{-1} flow rate measured absolute molecular weight. Waters Empower software calculated absolute molecular weight. Thermogravimetric analysis (TGA) was performed on a TGA Q500 with a 20 min isotherm at 110 ^oC and a

ramp at 10 ^{o}C min^{-1} to 600 ^{o}C. $T_{d,5\%}$ values were calculated where 5 wt % of the mass was lost and the data was normalized after the isothermal step. Differential scanning calorimetry (DSC) was performed on a TA Instruments Q2000 with heat/cool/heat cycles of 10 °C min^{-1}, 100 °C min^{-1}, and 10 °C min^{-1}, respectively. Samples were dried at 60 °C under vacuum prior to analysis. Glass transition temperatures (T_gs) were calculated from the second heat inflection point. Photorheology occurred on a TA Instruments Discovery HR-2 Rheometer with photo attachment and 20 mm PDMS bottom plate with 20 mm disposable upper geometry. Samples were equilibrated at 25 °C for 30 s to provide baselines for all samples. Samples were oscillated at 1 Hz, providing sampling rates relevant for the second timescale. Following 30 s, samples were irradiated at 20 mW/cm^2 and modulus was monitored. The crossover point was determined as the first instance the storage modulus (G') exceeded loss modulus (G").

12.3.4 Ultraviolet-Assisted Direct Ink Write Printing

The first of two additive manufacturing technologies that demonstrated printing with the PIB-diacrylate ink was Ultraviolet-Assisted Direct Ink Write (UV-DIW) on a custom built Mulimodal AM platform. The custom built printer (**Figure 12.1**) consists of two Zaber A-LST500 linear slides that provide the extruder 500mm of in the XY direction and a Zaber A-LST250 linear slide that provides the build plate 250mm of travel in the Z direction. The printer is controlled with a custom-built LabVIEW control software that uses standard GCODE to control the printer's movements and turn the extrusion on and off. A Nordson EFD Ultimus V DIW System is responsible for extruding the viscous ink. A Keynote Photonics LC4500-UV Digital Light Processing (DLP) projector provided UV-

irradiation at 405 nm with a measured intensity of 14 mW cm^{-2} on the build plate which was responsible for curing the printed photosensitive ink.

The projector providing UV irradiation is mounted adjacent to the extruder, which allows the entire layer to be extruded and then be cured homogeneously at once following printing. This *ex-situ* curing method has multiple benefits. First it eliminates nozzle clogging due to unwanted photocuring of the material at the nozzle exit. By exposing each layer to UV irradiation for a fixed period after deposition ensures the ink is not over cured and enough photocurable groups remain to form a strong interlayer adhesion with the next layer. Additionally, a homogenous cure of each layer contributes to more isotropic material properties. Use of *ex-situ* curing was enabled by the highly viscous ink that retained its as-deposited shape in the time between deposition and cure.

The ink was printed using a stainless-steel nozzle with an inner diameter of 0.25 mm and 12.7 mm length supplied by Nordson EFD. Parts were printed onto glass substrates with a deposition speed of 8 mm/s and each layer was exposed to UV irradiation for 5s. The ink was extruded at a 689.5 kPa (100 psi). Tensile dogbones (ASTM D-638 IV, scaled proportionally to a 55 mm length) were printed from three 200-µm thick layers. Rectangular bars used in Dynamic Mechanical Analysis were also printed from three 200-µm thick layers. Honeycomb structures (**Figure 12.9**) were printed from twenty-five 250-µm thick layers.

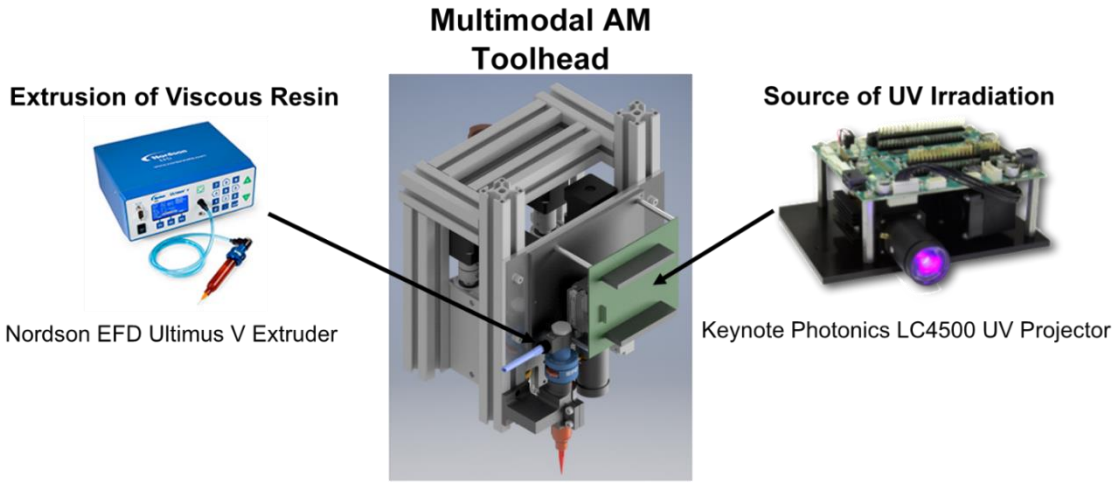

Figure 12.1. Ultraviolet-Assisted Direct Ink Writing (UV-DIW) setup integrating a Nordson EFD Ultimus V DIW system and a Keynote Photonics LC4500-UV Digital Light Processing (DLP) projector.

12.3.5 Vat Photopolymerization and Direct Ink Write Hybrid Printing

Using the same Multimodal AM platform described in Section 12.3.4, the ink is printed using a hybrid Vat Photopolymerization (VP) and Direct Ink Write (DIW) process described in detail by Rau et. al (2020, In Preparation).

Vat Photopolymerization (VP) is an AM process that enables due to its selective patterning of UV irradiation the fabrication of parts with high-resolution features and sharp edges. Currently, due to the recoating required to provide a fresh layer of uncured photoresin, VP is capable of only processing low viscosity photoresins, which limits both the available materials and the mechanical properties of the final parts. Conversely, Direct Ink Write (DIW), a material extrusion process, is capable of processing high viscosity photoresins but patterns feature directly via a nozzle, limiting both feature resolution and shape. Therefore, to enable the layered processing of this highly viscous photocurable inks and produce high-resolution features with sharp edges a DIW and a VP system were

integrated into one platform (described in section 12.3.4) to create a hybrid process. The hybrid process uses the DIW system to extrude an unpatterned layer of photoresin that is then selectively cured into the desired layer shape via the Mask-Projection VP system (**Figure 12.2**). This hybrid process is fundamentally different from UV-DIW as features are patterned be selective curing instead of directly by the DIW extruder, increasing feature resolution.

The hybrid process is cyclical, repeating in a layer-by-layer fashion characteristic of additive manufacturing processes. To ensure each layer is level and homogenous, the printing of each layer is split into two steps (**Figure 12.2Error! Reference source not found.**):

(1) Extruding and curing of the "vat" outline: First, the rectangular bounding box of the layer called the "outline" is extruded with the DIW extruder. The outline is then subsequently selectively cured with a rectangular image the same size as the perimeter using the UV projector. The bounding box is sized just larger than the part, reducing the material needed for printing.

(2) Extruding and selective curing of the "vat" infill: Second, the area contained by the outline rectangle, called the "infill", is extruded. After infill deposition, the build process is paused to allow the uncured extruded photoresin to spread and the layer height become even, reducing the non-homogeneity of the discrete beads that result from extrusion. Last, the infill is selectively photocured by projecting a UV pattern of the image of the layer .

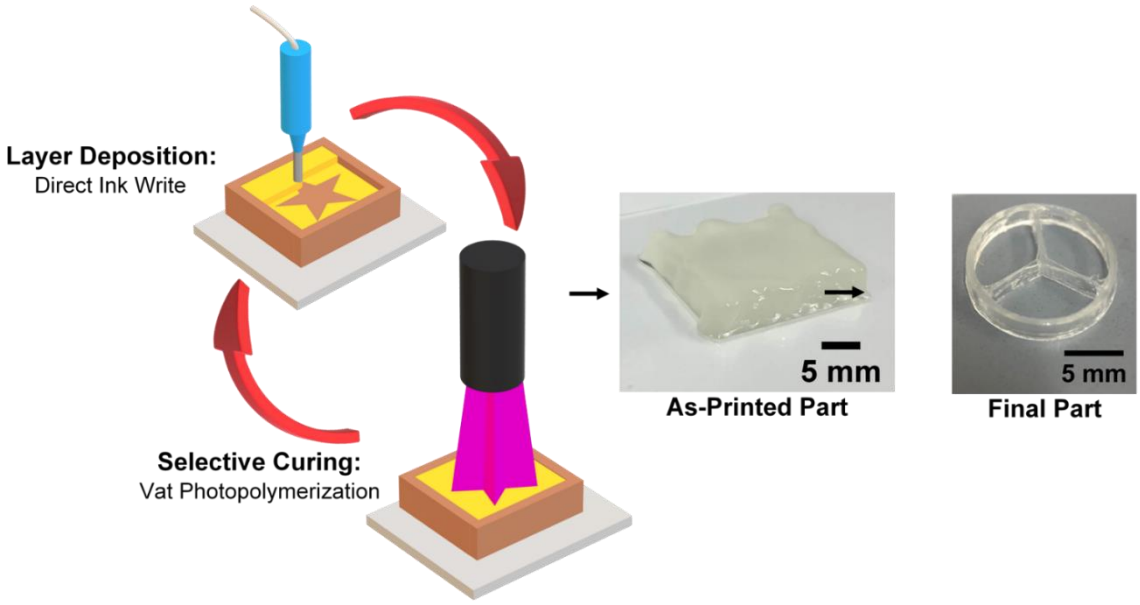

Figure 12.2. Summary of the hybrid DIW and VP process. First, a bounding box of a new layer of high viscosity photopolymer is extruded using the DIW extruder and then the outline is selectively photocured with the VP UV projector. Next, the infill is extruded and then the layer is selectively photocured in the desired layer pattern using the VP UV projector. This process is repeated in a layer-by-layer fashion, producing a 3D part.

In experimental printing, the ink was deposited using a stainless-steel nozzle with an inner diameter of 0.25 mm and 12.7 mm length supplied by Nordson EFD. Parts were printed onto glass substrates with a deposition speed of 4 mm/s and an extrusion pressure of 496.4 kPa (72 psi). Each layer was exposed to UV irradiation for 3s, the time cured the ink to the full depth of the 250 µm layers, forming adequate interlayer adhesion without resulting in overcuring. The cross-section heart valve demonstrated consisted of 25 x 250 µm layers.

12.4 Results and Discussion

End-group functionalization of PIB-diol yielded a viscous, translucent product of PIB-diacrylate. Dropwise incorporation of acryloyl chloride into a mixture of PIB-diol, K_2CO_3, and $CHCl_3$ at 0 ^oC ensured temperature control and gradual addition of acrylate moieties. An eight times excess of K_2CO_3 reacted with forming acid and limited water production. Filtration through aluminum oxide removed excess acrylic acid and water and subsequent removal of $CHCl_3$ *in vacuo* isolated the viscous product.

Scheme 12.1. End-group functionalization of PIB-diol yielded PIB-diacrylate.

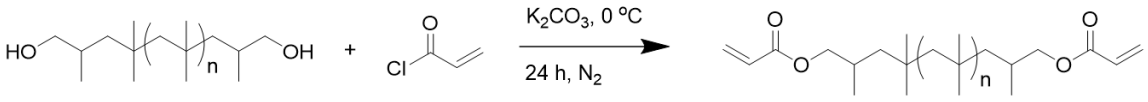

Figure 12.3 depicts the ^1H NMR spectroscopies of PIB-diol (top) and PIB-diacrylate (bottom), which confirms both chemical structures. Peak a and b in PIB-diol represent the two protons adjacent to the hydroxyl groups and two protons adjacent to the backbone, respectively. Peak c corresponds to the backbone protons where the integration in relation to peak a measured a number-average molecular weight (M_n) of 1980 g mol^{-1}. Peaks a, b, and c in the bottom spectrum confirmed end-group functionalization of PIB-diol to PIB-diacrylate. Each peak integrated to 2.04 protons, indicating 100% acrylate substitution on both ends. Peak d represents the two protons adjacent to the acrylate moiety, which also confirms end-group functionalization.

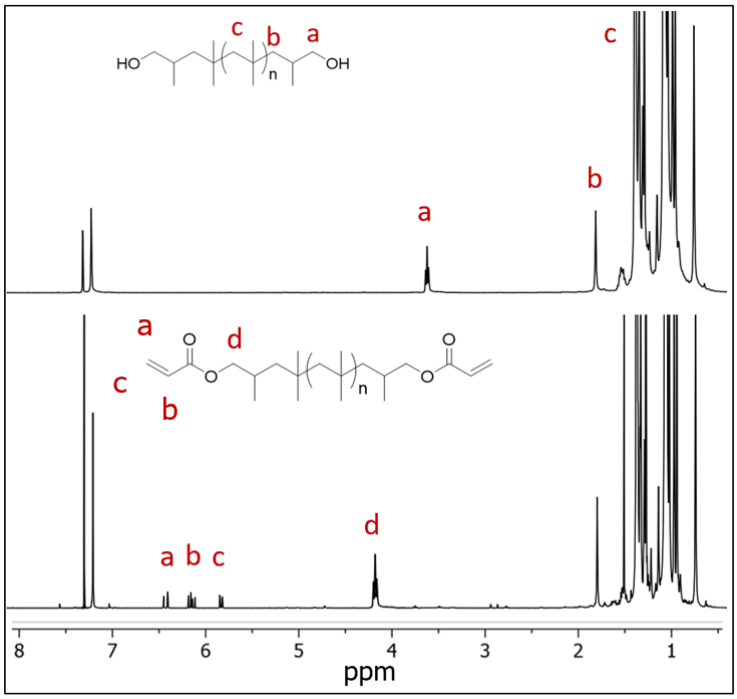

Figure 12.3. ^{1}H NMR spectroscopy of PIB-diol (top) and PIB-diacrylate (bottom).

Advanced permeation chromatography (APC) equip with RI and LS measured the absolute molecular weight of PIB-diol. APC measured M_n, M_w, and Đ as 1800 g mol^{-1}, 2400 g mol^{-1}, and 1.33 respectively. **Figure 12.4** depicts the RI trace, which emphasizes the narrow, monomodal peak. Additive manufacturing using VP or DIW both require a liquid, photoactive precursor, which drove the decision to maintain low molecular weights for PIB-diol.

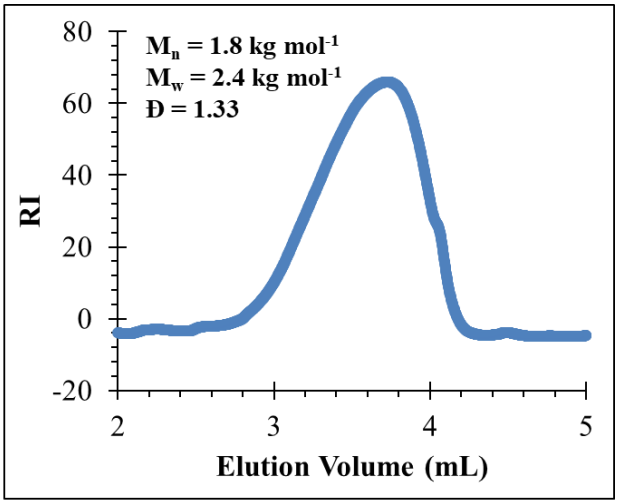

Figure 12.4. SEC-LS of PIB-diol.

Figure 12.5 depicts modulus as a function of time during a photorheology experiment. Rheological experiments with a UV light attachment elucidated crossover point of storage and loss moduli and the plateau storage modulus (G_N^o). Storage and loss modulus represent the elastic and viscous response, respectively. Crossover of storage and loss moduli exemplified solid-like properties overtaking liquid-like properties. Exposure to UV light crosslinked the viscous PIB-diacrylate into a crosslinked solid. PIB-diacrylate exhibited a crossover point of 0.8 s, which helped predict layer irradiation time per layer during printing. Crosslinked PIB-diacrylates experienced a G_N^o of $3.4 \cdot 10^6$ Pa. Even though this is a relative measure of modulus dependent on adhesion to each plate, studies showed values above $1 \cdot 10^5$ Pa provide adequate strength to maintain shape and survive recoating processes during printing.[1,10]

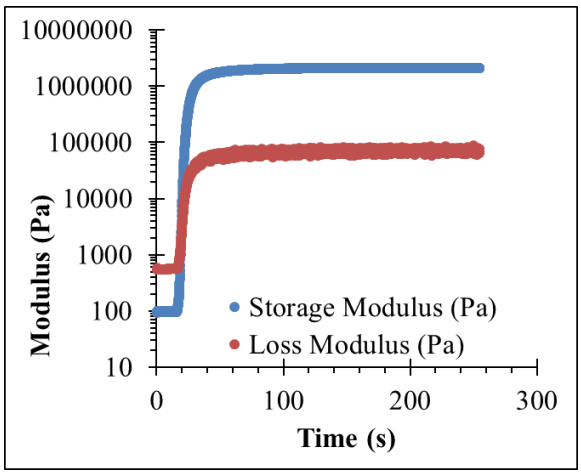

Figure 12.5. Modulus as a function of time during photorheology experiments.

After crosslinking, gel fraction elucidated amount of PIB-diacrylate incorporated into the network. Extraction in toluene for 5 days dissolved remaining PIB-diacrylate and revealed 85% gel percent. High viscosity (630 Pa·s) may contribute to low gel percent, where previous studies showed zero-shear viscosities above 10 Pa·s experienced a drop in gel percent due to decreased chain mobility.[1] All further thermal or mechanical testing were performed on extracted, crosslinked PIB-diacrylate.

Thermal analysis of PIB-diol and PIB-acrylate revealed thermal transitions and decomposition insights. **Figure 12.6A** depicts TGA analysis of both samples where both $T_{d,5\%}$s remained from 365-368 ^{o}C. **Figure 12.6B** depicts DSC traces of PIB-diol and extracted, crosslinked PIB-diacrylate. PIB is an amorphous, low T_g polymer and at high molecular weights, usually exhibits T_gs from -73 to -60 ^{o}C. PIB-diol experienced a T_g of -65 ^{o}C, which is consistent with previous literature. Crosslinked, extracted PIB-acrylate exhibited a T_g of -1 ^{o}C. When a low molecular weight polymer is crosslinked, the backbone is very restricted, which increased the T_g significantly. This temperature is still appropriate for biomedical applications as it will remain flexible in the body at 37 ^{o}C.

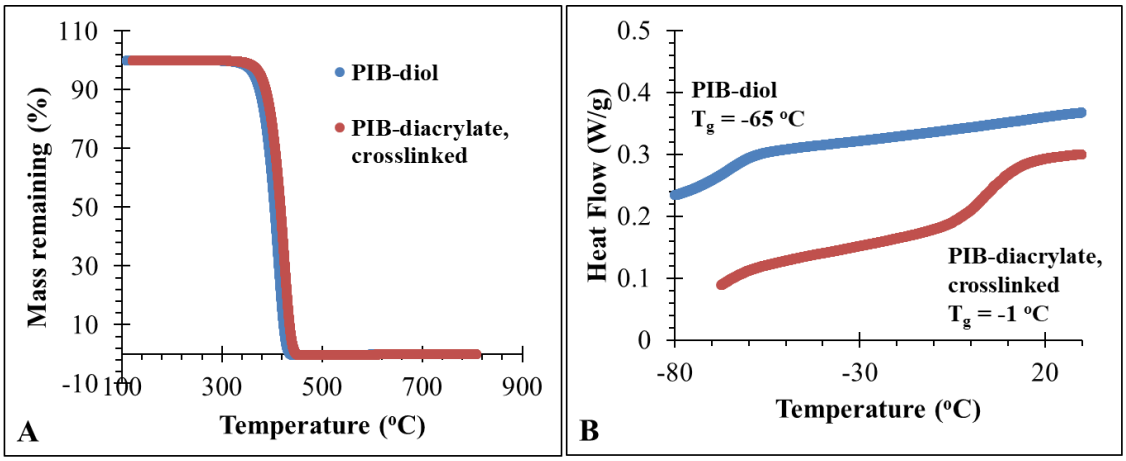

Figure 12.6. Thermal analysis of PIB-diol and crosslinked, extracted PIB-diacrylate depicting **(A)** TGA and **(B)** DSC.

AM requires varying viscosities depending on type of printing method. VP commonly requires 1 to 10 Pa·s to ensure adequate layer recoating. DIW requires viscosities of above 50 Pa·s as higher viscosities help printed layer maintain shape. **Figure 12.7** depicts complex viscosity of PIB-diol and PIB-diacrylate. PIB-diol and PIB-diacrylate experienced zero-shear viscosities of 830 and 640 Pa·s, respectively. PIB-diol maintained a higher zero-shear viscosity compared to PIB-diacrylate because it contained hydrogen bonding through hydroxyls end-groups. The end-groups aligned creating non-covalent bonds, thus increasing zero-shear viscosity. After end-group functionalization, hydrogen bonding no longer exists and zero-shear viscosity decreased. Interestingly, neither PIB-diol or PIB-diacrylate showed a significant degree of shear thinning behavior. Shear thinning behavior, the decrease of a materials viscosity at increasing oscillation frequency/shear rate, is often required to enable deposition through small diameter nozzles at moderate pressures.[21] Experimentally, this was not an issue as successfully printing was conducted through nozzles with a diameter of only 250 µm.

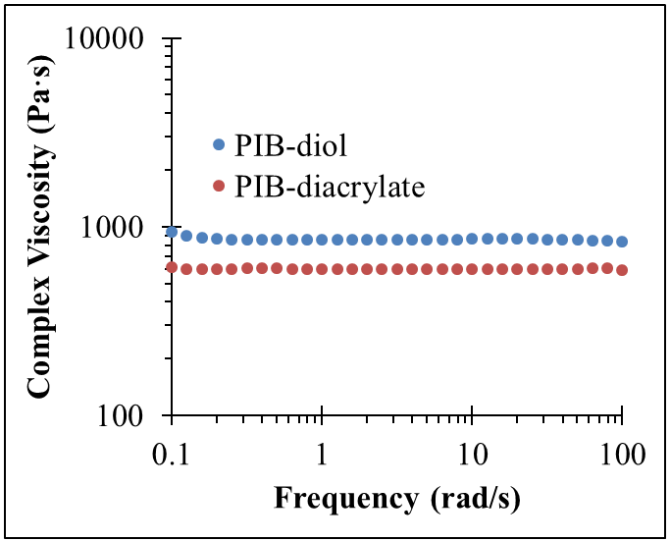

Figure 12.7. Complex viscosity as a function of frequency for PIB-diol and PIB-diacrylate.

Figure 12.8 depicts a hexagon structure of crosslinked PIB-diacrylate fabricated through DIW. PIB-diacrylate maintained high viscosity, which helped in the extrusion and maintenance of shape after extrusion.

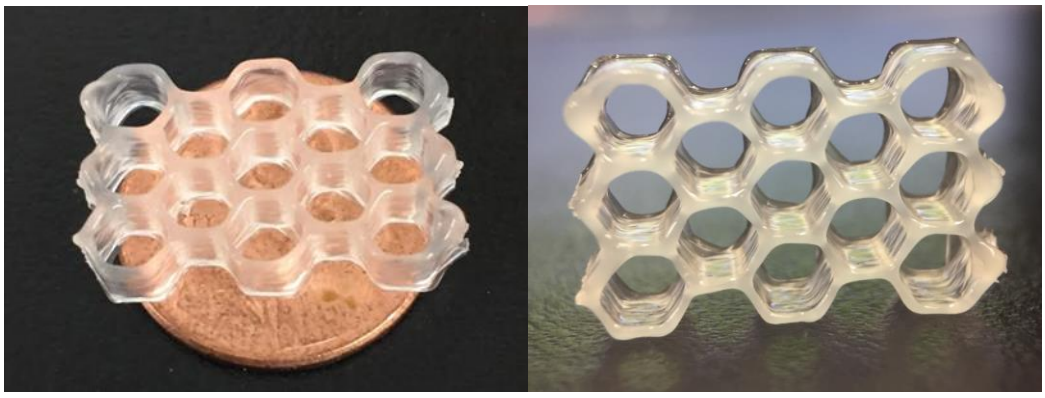

Figure 12.8. DIW printing enabled the production of a proof-of-concept hexagon structure.

Figure 12.9 depicts a model of a heart valve printed using a hybrid DIW and VP printing method. The flexibility of crosslinked PIB-diacrylate enabled the valve to open and close without loss of shape or strength.

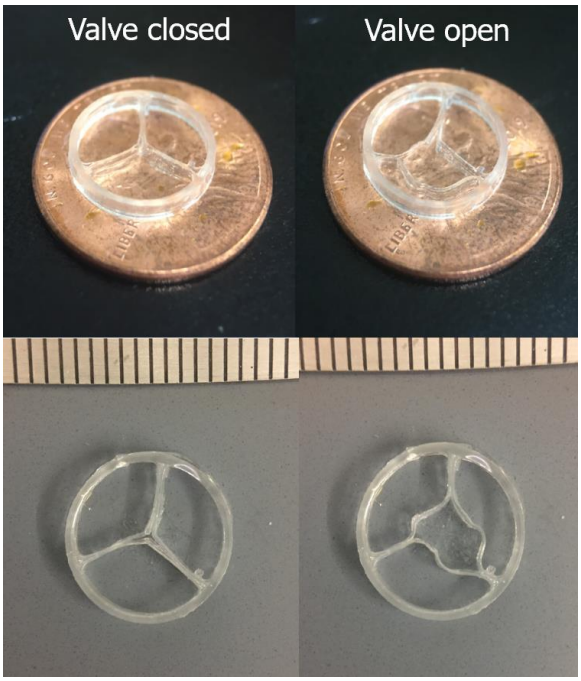

Figure 12.9. A hybrid DIW and vat photopolymerization printer produced heart valves.

RSA measured mechanical strength of printed, crosslinked, extracted, PIB-diacrylate. **Figure 12.10A** depicts a temperature sweep from 25 to 37 ^{o}C. While the storage modulus remained constant, the loss modulus steadily decreased, which suggested the material decreased strength as temperature increased. **Figure 12.10B** depicts frequency sweeps at 25 and 37 ^{o}C. As frequency increased, storage modulus increased slightly. The sample at 37 ^{o}C experienced a lower modulus compared to 25 ^{o}C, $4.1 \cdot 10^{6}$ and $4.7 \cdot 10^{6}$ Pa, respectively. Human aortic heart valves maintain dynamic moduli of $1 \cdot 10^{5}$ Pa.[22] Even though PIB-diacrylate is one order of magnitude off, plasticizers could be added to reduce the modulus.

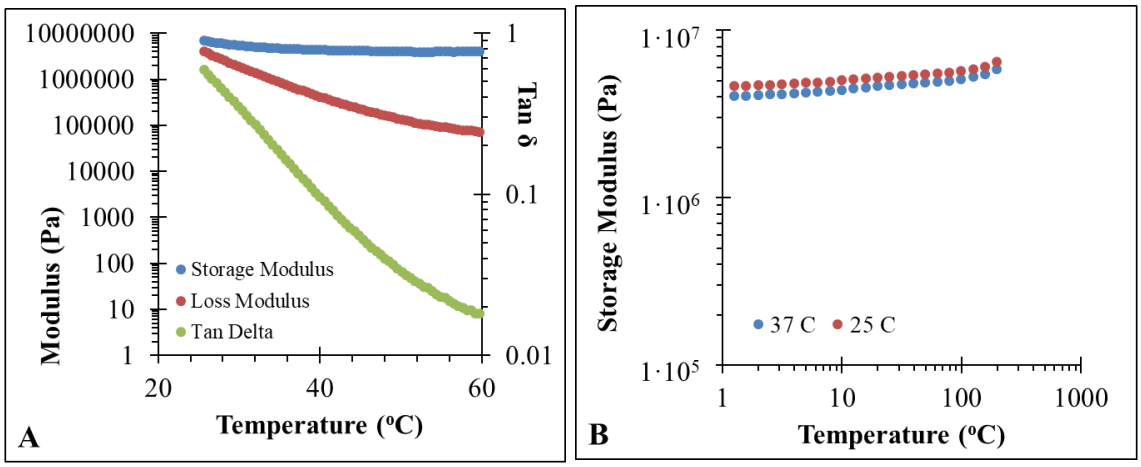

Figure 12.10. RSA experiments of printed, crosslinked, extracted PIB-acrylate where **(A)** depicts a temperature sweep and **(B)** shows frequency sweeps at 25 °C and 37 °C.

12.5 Conclusion

This manuscript reports end-group functionalization of polyisobutylene-diol (PIB-diol) with acryloyl chloride to create photoactive PIB-diacrylate for direct ink write (DIW) additive manufacturing. SEC and ^{1}H NMR spectroscopy confirmed an M_n of 1800 g mol^{-1} and chemical structure. DSC and TGA measured thermal transitions of PIB-diol and crosslinked PIB-diacrylate. Photorheology confirmed quick crosslinking times (below 1 s), which was adequate for quick printing using DIW. The high zero-shear viscosity of PIB-diacrylate (830 Pa·s) enable high-resolution DIW printing of a model heart valve. This manuscript describes preliminary data for the potential of PIB-diacrylate to be used as an artificial heart valve. Future studies include cytotoxicity in vitro and in vivo along with fine-tuning the printing process for tunable shapes based on patients' needs.

12.6 Acknowledgements

The authors would like to thank Boston Scientific for providing motivation and PIB-diol for the discussed experiments.

12.7 References

(1) Wilts, E. M.; Gula, A.; Davis, C.; Chartrain, N.; Williams, C. B.; Long, T. E. Vat Photopolymerization of Liquid, Biodegradable PLGA-Based Oligomers as Tissue Scaffolds. *Eur. Polym. J.* **2020**, *130*, 109693. https://doi.org/10.1016/j.eurpolymj.2020.109693.

(2) Camarero-Espinosa, S.; Calore, A.; Wilbers, A.; Harings, J.; Moroni, L. Additive Manufacturing of an Elastic Poly(Ester)Urethane for Cartilage Tissue Engineering. *Acta Biomater.* **2020**, *102*, 192–204. https://doi.org/10.1016/j.actbio.2019.11.041.

(3) Tytgat, L.; Van Damme, L.; Van Hoorick, J.; Declercq, H.; Thienpont, H.; Ottevaere, H.; Blondeel, P.; Dubruel, P.; Van Vlierberghe, S. Additive Manufacturing of Photo-Crosslinked Gelatin Scaffolds for Adipose Tissue Engineering. *Acta Biomater.* **2019**, *94*, 340–350. https://doi.org/10.1016/j.actbio.2019.05.062.

(4) Moreno Madrid, A. P.; Vrech, S. M.; Sanchez, M. A.; Rodriguez, A. P. Advances in Additive Manufacturing for Bone Tissue Engineering Scaffolds. *Materials Science and Engineering C*. Elsevier Ltd July 1, 2019, pp 631–644. https://doi.org/10.1016/j.msec.2019.03.037.

(5) Alhnan, M. A.; Okwuosa, T. C.; Sadia, M.; Wan, K.-W.; Ahmed, W.; Arafat, B. Emergence of 3D Printed Dosage Forms: Opportunities and Challenges. *Pharm. Res.* **2016**, *33* (8), 1817–1832. https://doi.org/10.1007/s11095-016-1933-1.

(6) Mondschein, R. J.; Kanitkar, A.; Williams, C. B.; Verbridge, S. S.; Long, T. E. Polymer Structure-Property Requirements for Stereolithographic 3D Printing of Soft Tissue Engineering Scaffolds. *Biomaterials* **2017**, *140*, 170–188. https://doi.org/10.1016/J.BIOMATERIALS.2017.06.005.

(7) Puskas, J. E.; Chen, Y. Biomedical Application of Commercial Polymyers and Novel Polyisobutylene-Based Thermoplastic Elastomers for Soft Tissue Replacement. *Biomacromolecules*. July 2004, pp 1141–1154. https://doi.org/10.1021/bm034513k.

(8) Rau, D. A.; Herzberger, J.; Long, T. E.; Williams, C. B. Ultraviolet-Assisted Direct Ink Write to Additively Manufacture All-Aromatic Polyimides. *ACS Appl. Mater. Interfaces* **2018**, *10* (41), 34828–34833. https://doi.org/10.1021/acsami.8b14584.

(9) Appuhamillage, G. A.; Chartrain, N.; Meenakshisundaram, V.; Feller, K. D.; Williams, C. B.; Long, T. E. 10th Anniversary: Vat Photopolymerization-Based Additive Manufacturing: Current Trends and Future Directions in Materials Design. **2019**. https://doi.org/10.1021/acs.iecr.9b02679.

(10) Wilts, E. M.; Pekkanen, A. M.; White, B. T.; Meenakshisundaram, V.; Aduba, D. C.; Williams, C. B.; Long, T. E. Vat Photopolymerization of Charged Monomers: 3D Printing with Supramolecular Interactions. *Polym. Chem.* **2019**, *10* (12). https://doi.org/10.1039/c8py01792a.

(11) Sirrine, J. M.; Meenakshisundaram, V.; Moon, N. G.; Scott, P. J.; Mondschein, R. J.; Weiseman, T. F.; Williams, C. B.; Long, T. E. Functional Siloxanes with Photo-

Activated, Simultaneous Chain Extension and Crosslinking for Lithography-Based 3D Printing. *Polymer (Guildf).* **2018**, *152*, 25–34. https://doi.org/10.1016/j.polymer.2018.02.056.

(12) Herzberger, J.; Sirrine, J. M.; Williams, C. B.; Long, T. E. Polymer Design for 3D Printing Elastomers: Recent Advances in Structure, Properties, and Printing. *Prog. Polym. Sci.* **2019**, *97*, 101144. https://doi.org/10.1016/j.progpolymsci.2019.101144.

(13) Herzberger, J.; Meenakshisundaram, V.; Williams, C. B.; Long, T. E. 3D Printing All-Aromatic Polyimides Using Stereolithographic 3D Printing of Polyamic Acid Salts. *ACS Macro Lett.* **2018**, *7* (4), 493–497. https://doi.org/10.1021/acsmacrolett.8b00126.

(14) Manning, K. B.; Wyatt, N.; Hughes, L.; Cook, A.; Giron, N. H.; Martinez, E.; Campbell, C. G.; Celina, M. C. Self Assembly–Assisted Additive Manufacturing: Direct Ink Write 3D Printing of Epoxy–Amine Thermosets. *Macromol. Mater. Eng.* **2019**, *304* (3), 1800511. https://doi.org/10.1002/mame.201800511.

(15) Lewis, J. A. Direct Ink Writing of 3D Functional Materials. *Adv. Funct. Mater.* **2006**, *16* (17), 2193–2204. https://doi.org/10.1002/adfm.200600434.

(16) Puskas, J. E.; Chen, Y.; Dahman, Y.; Padavan, D. Polyisobutylene-Based Biomaterials. *J. Polym. Sci. Part A Polym. Chem.* **2004**, *42* (13), 3091–3109. https://doi.org/10.1002/pola.20114.

(17) Kennedy, J. P.; Richard, G. C. Polyisobutylene-Toughened Poly(Methyl Methacrylate). 1. Synthesis, Characterization, and Tensile Properties of PMMA-l-PIB Networks. *Macromolecules* **1993**, *26* (4), 567–571. https://doi.org/10.1021/ma00056a002.

(18) Isayeva, I. S.; Kasibhatla, B. T.; Rosenthal, K. S.; Kennedy, J. P. Characterization and Performance of Membranes Designed for Macroencapsulation/Implantation of Pancreatic Islet Cells. *Biomaterials* **2003**, *24* (20), 3483–3491. https://doi.org/10.1016/S0142-9612(03)00172-8.

(19) Shamlou, S.; Kennedy, J. P.; Levy, R. P. Amphiphilic Networks. X. Diffusion of Glucose and Insulin (and Nondiffusion of Albumin) through Amphiphilic Membranes. *J. Biomed. Mater. Res.* **1997**, *35* (2), 157–163. https://doi.org/10.1002/(SICI)1097-4636(199705)35:2<157::AID-JBM3>3.0.CO;2-M.

(20) Kennedy, J. P.; Fenyvesi, G.; Levy, R. P.; Rosenthal, K. S. Amphiphilic Membranes with Controlled Mesh Dimensions for Insulin Delivery+. *Macromol. Symp.* **2001**, *172* (1), 56–66. https://doi.org/10.1002/1521-3900(200107)172:1<56::AID-MASY56>3.0.CO;2-D.

(21) Udofia, E. N.; Zhou, W. A Guiding Framework for Microextrusion Additive Manufacturing. *J. Manuf. Sci. Eng. Trans. ASME* **2019**, *141* (5). https://doi.org/10.1115/1.4042607.

(22) Jiao, T.; Clifton, R. J.; Converse, G. L.; Hopkins, R. A. Measurements of the Effects of Decellularization on Viscoelastic Properties of Tissues in Ovine, Baboon, and Human Heart Valves. *Tissue Eng. Part A* **2012**, *18* (3–4), 423–431. https://doi.org/10.1089/ten.tea.2010.0677.

Chapter 12: Overall Conclusions

Additive manufacturing has the most potential in personalized products, but due to the lack of materials available, few products are commercially available. Popular materials include ABS, PET, PLA, and polyurethanes, but these materials lack functionality. This dissertation aims to add new materials to the additive manufacturing toolbox that have the potential for large-scale production. To achieve large-scale production with today's infrastructure, variations of polymers already made at large scales are optimal. For example, instead of synthesizing completely novel monomers and polymers, modifying commercially available polymers with specific functionalities to impose strength, biodegradable, or stability provide the largest potential to achieve large scale incorporation into the additive manufacturing paradigm.

Vat photopolymerization (VP) is the fastest additive manufacturing type with the invention of CLIP (Continuous Liquid Interface Production), which uses an oxygen-permeable membrane to hinder crosslinking at the UV light accessible window. Because of its speed, CLIP and other types of VP provide rapid and local production of personalized products. For example, Chapter 4 and 5 provide dissolvable and degradable additively manufactured products that have the potential for personalized biomedical applications. Chapter 4 describes polymerizing electrolyte-containing monomers in a VP process to create soluble parts. TMAEA and NVP photopolymerized copolymers provided a range of dissolution rates from 27 to 41 min. A range of strengths, up to 0.47 MPa Young's modulus, enable applications from drug delivery implants to oral medications. Chapter 5 discusses PLGA-based oligomers for VP where the Photokinetics, degradation rates of the

crosslinked films, and final cytotoxicity were investigated for tissue scaffold applications. This study elucidated these systems maintained between 0.03 to 0.05 MPa in Young's modulus, which is suitable for soft tissue scaffolds. Low toxicity and a range of degradable rates, 4 to 16 weeks, enabled the potential for soft tissue scaffolds. Chapter 5 also revealed a dependence of precursor viscosity on photokinetics, which provided the motivation for Chapter 6. Chapters 4 and 5 were also based on commercially available polymers systems, which provides hope for large-scale production in the future.

Chapter 6 describes using PEGDA and H-bonding PEGDA in solution to investigate the dependency of viscosity on photokinetics in VP processes. Thousands of reports describe novel materials containing varying amounts of precursor, reactive diluents, and solvents, but the literature lacks the investigate of viscosity and printability. This study revealed a higher viscosity, larger concentrations of the precursors in water, enabled faster crosslinking times but lower conversions. Larger molecular weights produced slower crosslinking times and lower conversions in some samples. The largest molecular weights tested, 35 kg mol^{-1}, only produced solid films after crosslinking in 55 and 60 wt% in water of the H-bonding PEGDA samples. 35 kg mol^{-1} PEGDA without H-bonding did not produce solid films at 60 wt%. This study revealed the lowest molecular weights, 2 kg mol^{-1}, and concentrations above the critical overlap concentration (C^*) produced the highest conversions. As the viscosity increased, ranging from 12 to 23 wt% depending on the sample, produced lower conversions. Depending on the application, this data is helpful to determine which conversions are needed to help strength or the conversion of toxic moieties.

Within the vat photopolymerization field, research is lacking on dissolvable or recyclable materials and the relationships between viscosity and photokinetics. 3D parts made through vat photopolymerization are usually covalently crosslinked with no pathway of dissolving or recycling. Chapter 4 discusses using a physically crosslinked network after printing to enable dissolution in water and recyclability. As scientists strive to create a more sustainable and circular economy, materials discussed in Chapter 4 opened a new field of materials for vat photopolymerization. Viscosity of photoactive precursors is discussed in the literature to predict printability and to determine optimal recoating mechanisms. Chapter 5 described a relationship between viscosity and acrylate conversion, where lower conversions led to more cytotoxicity in vitro. Chapter 6 expanded on the concept of viscosity controlling acrylate conversion and explored varying molecular weight and concentrations in water. These studied revealed a lower conversion with increasing molecular weight and concentration, which will serve as a guide for future researchers to achieve the highest conversions possible and thus reduce cytotoxicity in vitro.

Chapters 7, 8, and 9 elucidated the use of linear, 4-arm star, and graft PVP as polymeric adhesives for binder jetting additive manufacturing (BJ AM). Literature describes PVP as an excellent binder for oral personalized dosage pharmaceuticals made through BJ AM, but the tablets report low strengths. This dissertation reports using 4-arm star and graft PVP lowers the solution viscosity of the binder, enabling a higher polymer concentration of polymer in the binder, resulting in stronger tablets. The strongest tablet exhibited 1.6 MPa of compressive strength made with 14 wt% graft PVP. Not only can these varying architectures of PVP can be used for personalized dosage pharmaceuticals, but researchers can also use the theory of varying architectures to achieve stronger parts

for other applications. These chapters also investigated the relationship of C^* and jettability in thermal inkjet printheads where the maximum jettable concentration aligned with C^*.

Literature surrounding jetting polymeric solutions currently focuses on linear, non-associating polymers and lacks research into physical properties that predict jettability. Chapter 7 and 9 explored jetting 4-arm star and graft copolymers for the first time reported in literature and demonstrated these solutions did not fall into the traditional jettable range of Z = 1-10. These chapters also elucidated a physical solution property, C^*, that predicted the maximum jettable concentrations of linear, 4-arm star, and graft copolymers using thermal printheads. Researchers can now utilize this parameter to predict maximum concentrations of polymeric solutions, which will lead to more cost and time efficient material development.

To investigate powder development for powder-bed additive manufacturing processes, Chapter 10 discusses creating PSA powders for powder bed fusion (PBF). Suspension polymerization methods produced crosslinked powders (average 60% gel fraction) which met the specifications for PBF printing. The crosslinked powders experienced a 2000 Pa·s zero-shear viscosity, which may have prevented particles from coalescing efficiently after melting. To ameliorate this problem, the suspension-made powders were mixed with solution-made powder, which was not crosslinked. This combination created coalescing particles, which also contained small amounts of crosslinking to increase strength. 50:50 mixtures of suspension- and solution-made PSA enabled printing of multiple parts and 50 heat-cool-heat cycles proved potential for phase change materials.

PBF literature lacks studies printing low temperature materials (> 80 ^{o}C), using suspension polymerization to create spherical particles, and printing crosslinked materials. Common materials printed using PBF include Nylon and polypropylene, which both print above 120 ^{o}C. To explore novel, low temperature printing, Chapter 10 investigates printing poly(stearyl acrylate) (PSA), which melts at 51 ^{o}C. This process used less energy and achieved printing at a room temperature bed temperature, which has not been reported. Researchers also use cryogrinding, melt emulsification, and precipitation to create spherical particles, which leads to inconsistent powder shapes and use of large amounts of solvents. Creating spherical powders using suspension polymerization has also not been reported, and it represents a method to create spherical powders in one step instead of multiple steps for conventional powder manufacturing. Finally, Chapter 10 described printing crosslinked powders where the addition of solution-made, non-crosslinked PSA modified zero-shear viscosity to achieve homogeneous layer coalescence.

This dissertation aims to create and characterization new materials for additive manufacturing that have potential for large-scale production. Another underlying theme aims to predict the printability of polymers in solution for VP and BJ AM. Polyelectrolytes, PVP, PLGA, and PSA are all commercially available polymers and with the modifications described in this document, they have potential to expand the materials toolbox for additive manufacturing. Studies of viscosity dependency on photokinetics in VP, viscosity of binders dependence on jettability, and gel fraction effects on PBF, provided vital information for printability in the additive manufacturing field.

Chapter 13. Suggested Future Work

13.1 Comprehensive study of polymers used in binder jetting additive manufacturing to examine solution properties and how *C** relates to jettability

Chapters 7, 8, and 9 discuss using water-soluble polymers of varying architectures to not only increase binder jetted part strength, but also utilize *C** as a method to predict printability using thermal printheads. These chapters only discuss poly(vinyl pyrrolidone) therefore this theory of *C** governing maximum jettable wt %'s should be expanded to other polymers and solvents. **Figure 13.1** depicts all of the polymers used for binder jetting previously, which also used either water, ethanol, acetone, or chloroform as solvents.

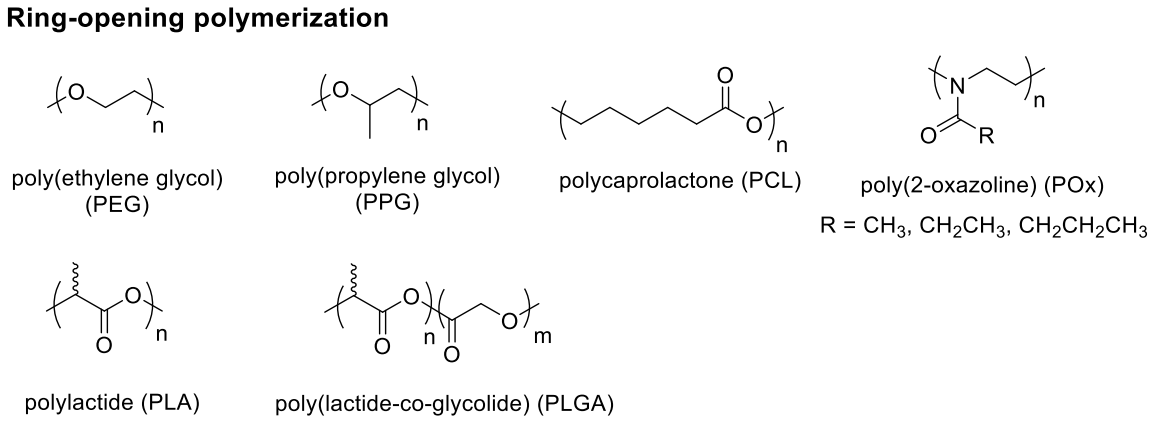

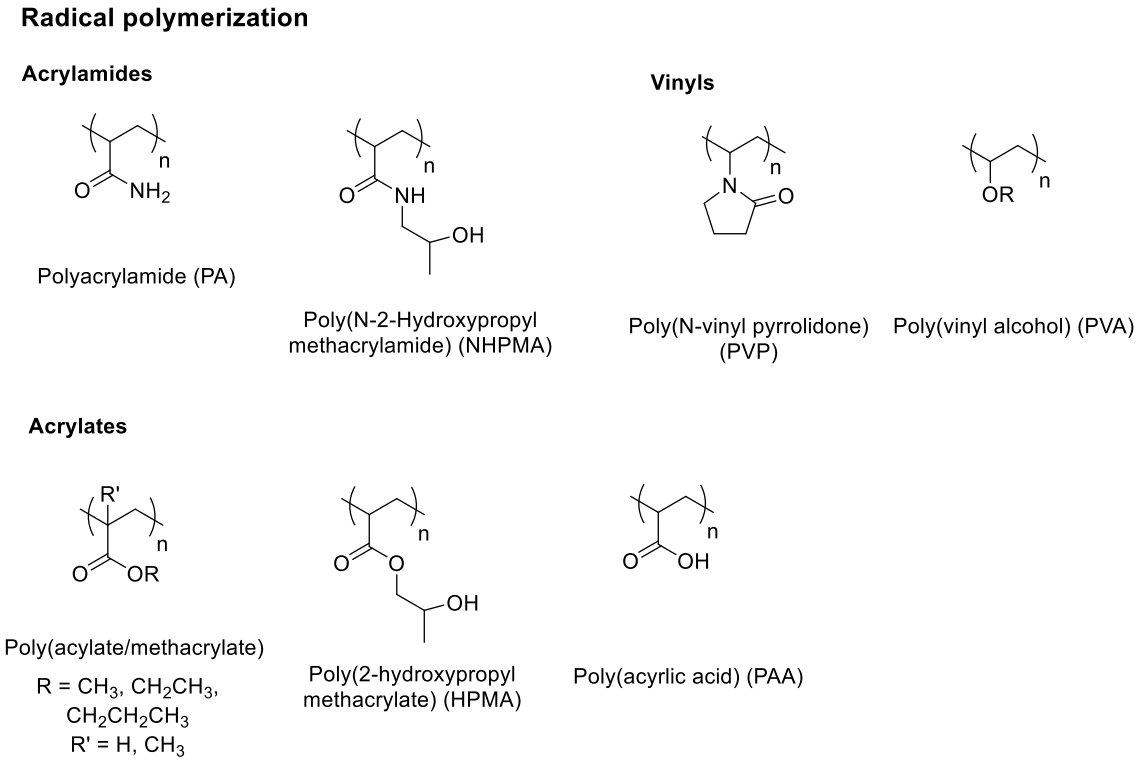

Figure 13.1. Types of polymers divided into polymerization methods of all polymers previously used for binder jetting of personalized dosage pharmaceuticals.

Thermal printheads eject drops of binder using a combination of electric pulses and explosive evaporation of a solvent.[1] An electric pulse is sent to the resistor element, which locally heats the binder to the superheat limit temperature (TSL). The TSL is defined as 90% of the critical fluid temperature, which is 312 ^{o}C for water at atmospheric pressure. These temperatures induce the liquid-vapor phase changes to occur through explosive evaporation. The formation of a vapor bubble through this process forces a drop to eject from the nozzle.[1] Depending on the solvent and varying TSL values, the solvents may jet differently out of the nozzle. Using acetone, ethanol, and chloroform as solvents to investigate whether *C** values still govern maximum jettable concentrations will further elucidate the validity of this screening technique. Conducting similar studies with different

solvents other than water as Chapters 6 and 8, testing a range of concentrations above and below *C** on jettability, will provide enough experiments to test this theory.

Each polymer will possess a unique solution viscosity profile depending on solvent choice, R_g, and architecture.[2] Depending on whether polymers are dissolved in a good, bad, or theta solvent will determine how they orient in solution.[3,4] Chapters 7 and 9 describe linear, 4-arm star, and graft PVP in a good solvent, water. To investigate solvent effects, the same experiments with a water/salt solution, considered a theta solvent for PVP, will elucidate different viscosity transitions and if the different transitions effect jettability. A jettability study of poly(ethylene glycol) solutions in water at varying molecular weights will elucidate if chemical structure and solution properties affect jetting behavior. This experiment will only vary the polymer structure, not the solvent, to solely investigate structure effects. Experiments changing one variable at the time, either solvent, solvent-type, architecture, or structure will reveal whether using *C** as a concentration limit for thermal printheads holds.

Polymers containing non-covalent interactions, such as hydrogen bonding and electrostatic interactions, also will experience unique solution properties and could aid to the mechanical strength of printed parts. Depending on the solvent, associating polymers will increase quicker in viscosity as a function of concentration. Even though this may cause the maximum jettablility concentration to decrease, the mechanical properties of the final part may improve. After the associating polymer solution is jetted and the part is dried, the non-covalent interactions may cause an increase in mechanical strength compared to a non-associating polymer system.

13.2 Binder jetting additive manufacturing of multi-drug oral tablets

Multi-drug oral tablets improve the quality of patient's lives through taking one pill for all medication needs, the capability of personalized dosage, and tailored release rates to prevent drug-drug interactions.[5,6] Instead of taking multiple pills throughout the day, a multi-drug single pill will deliver all needed medication in one dose. The versatility of additive manufacturing oral tablets enables precise placement of active ingredients and a range of release rates. Multi-drug tablets and personalized dosage in concert could potentially reduce side-effects and prevent drug-drug interactions. Zero-order and delayed release rates of multiple medications in one oral tablet renders the medication more effective.[5,7,8] Through additive manufacturing, a multi-drug oral tablet will improve treatments and improve patient quality of life. **Figure 13.2** depicts a design of a multi-drug oral tablet made through binder jetting additive manufacturing.

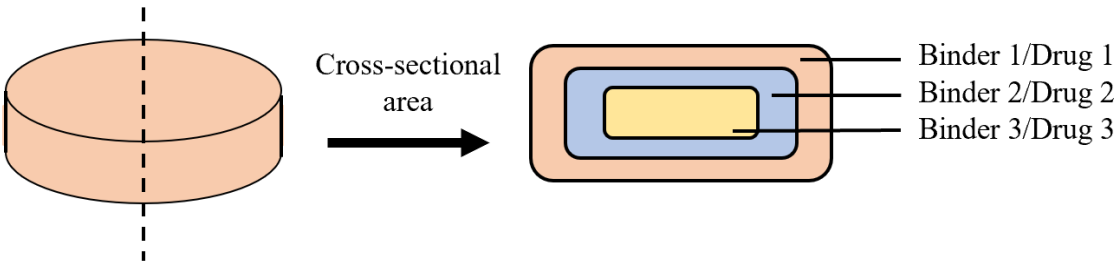

Figure 13.2. Design of multi-drug oral tablet where each layer represents a different active ingredient.

Each layer depicted in **Figure 13.2** represents a different active ingredient. In this example, the active ingredient is dissolved in the binder solution where three printheads

deposit different binders in a circle pattern. The order of the active ingredients can be changed according to specific drug interactions. For example, if drug 1 and drug 3 interact, drug 1 will release first and dissolve before the release of drug 3. There is also an option to incorporate another active ingredient in the powder if there are no interactions with any of the other drugs. The medication will release steadily over the lifetime of the tablet. The same or different binders with varying dissolution rates can create varying delays. For example, if all of the active ingredients interact, the binder for layers 2 and 3 will have a longer dissolution rate to create a delay between each medication. This system will tailor active ingredient delivery to the specific patient while reducing side-effects and streamlining the tablet taking process.

13.3. Influence of solution properties on photokinetics of VP AM: Optimizing mechanical and biocompatible properties of printed objects

Chapter 6 discusses a comprehensive study on PEG and hydrogen bond-containing PEG to elucidate solution viscosity effects on photo-kinetics, conversion of acrylates, and mechanical properties. To expand upon this study, different polymers with different associating moieties will elucidate whether the trends seen in Chapter 6 translate to other systems. Chapter 6 elucidated the highest conversions emerged between C^* and C_e, but some of those combinations were not strong enough for vat photopolymerization. The studies also found non-associating PEG at 35 kg mol^{-1} did not form a solid at any of the tested concentration. Hydrogen-bonding PEG at 35 kg mol^{-1} formed solids at higher concentrations (40 wt % and above).

To further build on this study, conducting similar experiments with different polymer structures and varying associating moieties will elucidate this a trend arises between viscosity transitions and photokinetics, conversion, and mechanical properties. **Figure 13.3** depicts sulfonated PEG that would be a natural transition and complement to the work described in Chapter 6. Electrostatic interactions in sulfonated PEG may decrease solution viscosity transitions but also provide enough mechanical strength to print and form solid parts at higher molecular weights, 35 kg mol^{-1} for example.

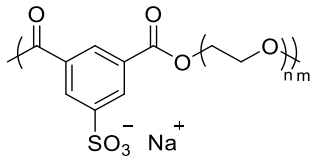

Figure 13.3. Structure of sulfonated PEG.

13.4. Vat photopolymerization of water-soluble poly(vinyl pyrrolidone) and poly(acrylic acid) complexes

Chapter 4 describing using charged monomers for vat photopolymerization to achieve a water-soluble and swellable part. Usually in vat photopolymerization, chemical crosslinking is necessary to form a solid part. Covalent crosslinking produces an insoluble part, which cannot be reformed. The Long group currently uses this method to 3D print high performance polymers, but did not utilize the potential dissolution of the printed organogels.[9,10] Utilizing electrostatic interactions to produce water-soluble parts enable recycling of starting materials and potential for biomedical applications. **Scheme 13.4** depicts the synthesis scheme of using PVP and acrylic acid to form an electrostatic interaction, crosslink, and possess the ability to dissolve post-printing.

This project will involve the comprehensive study of varying molecular weight PVP mixed with varying equivalents of acrylic acid. When PVP and acrylic acid are mixed in an organic solvent such as methanol, an electrostatic interaction between a tertiary amine and carboxylic acid.[11,12] To monitor this interaction, ^{1}H NMR spectroscopy will measure the shift in adjacent protons to the tertiary amine and carboxylic acid proton. After the non-covalent bond is formed, exposure to UV light in the presence of a photoinitiator will crosslink through the acrylate moieties. The labile electrostatic interactions will allow solvation after printing when exposed to water or other protic solvents.

Scheme 13.4 Synthesis of covalently and non-covalently crosslinked PVP-*co*-acrylic acid.

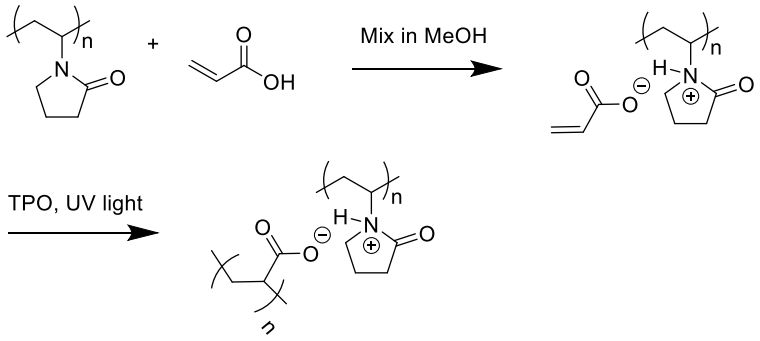

To examine this system further, three molecular weights of PVP and five different equivalents of acrylic acid should be tested. ^{1}H NMR spectroscopy will monitor the amount of interactions made depending on the equivalent of acrylic acid added. Photocalorimetry will reveal conversion, progression of crosslinking, and provide photokinetic details that could potentially dictate printing parameters. Photorheology will also reveal photokinetic habits of the system and also the relative modulus of the crosslinked part. TGA, DSC, and DMA of crosslinked part will reveal thermomechanical properties. Swelling and

dissolution studies in water will reveal if the parts are completely dissolvable and potentially recyclable.

13.5. Poly(2-oxazoline)-ureas with tailored water dissolution for ammonia-releasing fertilizers

Poly(2-oxazoline)s are a diverse group of highly tunable polymers with many applications in drug delivery and biomaterials. To date, examples of urea-containing poly(2-oxazoline)s do not exist and provide an opportunity to improve the mechanical strength and functionality of conventional poly(2-oxazoline) examples.[13,14] **Figure 13.5** depicts the chemical structure of a urea-containing poly(2-oxazoline) where depending on the R group, becomes more or less hydrophilic thus tuning the water dissolution. Extrusion 3D printing of these materials may also provide another avenue of tuned dissolution based on shape.[15]

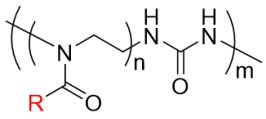

R = methyl, ethyl, propyl

Figure 13.5. Chemical structure of a urea-containing poly(2-oxazoline).

Previous work in the Long group showed polyureas become biodegradable in the presence of the enzyme urease, where the degradation speed depends on the hydrophilicity of the polymer or compound.[16,17] Substituting a poly(2-oxazoline) backbone with methyl, ethyl, and propyl side-groups provide a range of hydrophilicity.[18] When this urea-containing poly(2-oxazoline) comes into contact with urease, the backbone will degrade according to the range of hydrophilicities of the poly(2-oxazoline)s. **Scheme 13.5** depicts

a facile pathway to synthesis urea-containing poly(2-oxazoline)s beginning with a difunctional initiator yielding a poly(2-oxazoline)-diamine. Reacting the diamine with isophorone diisocyanate yields a urea-containing poly(2-oxazoline).

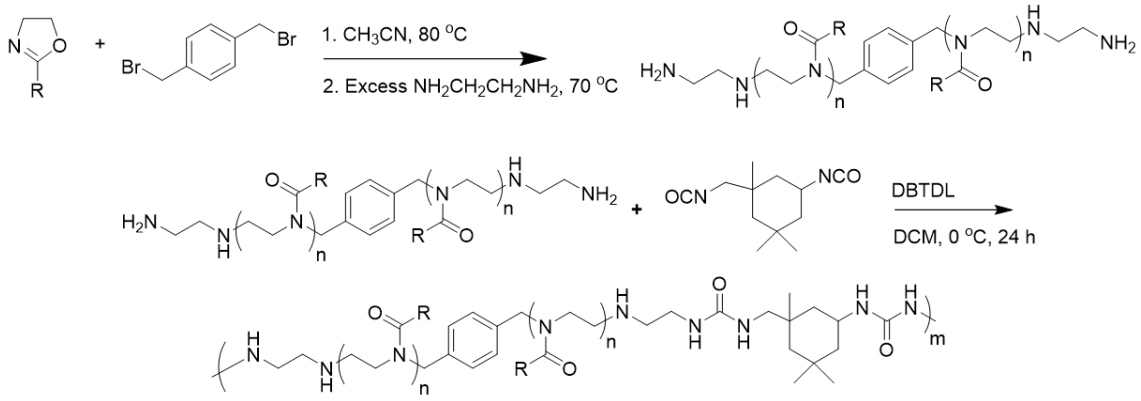

Scheme 13.5 Synthesis of a urea-containing poly(2-oxazoline) utilizing isophorne diisocyanate.

Figure 13.5 A and **B** depict TGA and DSC traces of the poly(2-oxazoline)-diamines containing methyl, ethyl, propyl, and 50:50 molar ratios of each monomer. Aqueous SEC and ^{1}H NMR spectroscopy confirmed an average molecular weight of 2000 g mol^{-1} of each diamine. **Figure 13.5 A** depicts the TGA traces where each diamine exhibited a $T_{d,5\%}$ between 290 and 310 ^{o}C. **Figure 13.5 B** depicts the DSC traces where each diamine exhibited T_g between 35 and 49 ^{o}C. The methyl oxazoline-containing diamine showed the highest T_g (49 ^{o}C) and the propyl-containing diamine showed the highest (35 ^{o}C) due to the increase in mobility of the propyl side-group.[13] To expands upon this work, higher molecular weight (5000, 10,000 g mol^{-1}) diamines and subsequent use in synthesizing poly(2-oxazoline)-ureas will elucidate thermal and mechanical properties based on varying amounts of hydrogen bonding. The dissolution rates in water of each

diamine combination will also elucidate the differences in dissolution times of each diamine combination. Previous reports in literature show poly(2-methyl oxazoline) is soluble within seconds in water, where ethyl and propyl species take longer times or need heat to dissolution.[14,18]

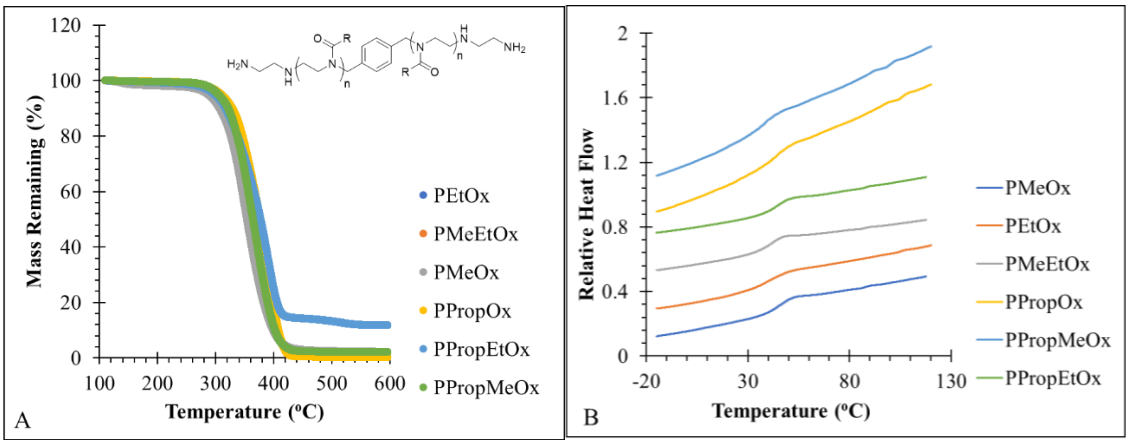

Figure 13.5. (A) TGA and **(B)** DSC traces of six poly(2-oxazoline)-diamines elucidating $T_{d,5\%}$ and T_g.

The next step in this project is to synthesize poly(2-oxazoline)-ureas with the discussed diamines and isophorone diisocyanate, depicted in **Scheme 13.5. Figure 13.6** depicts the ^{1}H NMR spectrum of poly(2-ethyl oxazoline)-urea using a 1:1 equivalence to achieve the highest molecular weight possible. Aqueous SEC revealed a M_n of 43,000 g mol^{-1} and Đ of 1.95. Synthesizing the previously discussed diamines with isophorone diisocyanate will produce a range of poly(2-oxazoline)-ureas with varying dissolution rates. Subsequent dissolution and degradation studies will determine how quickly each polymer will degrade and which agricultural application they can be applied to.

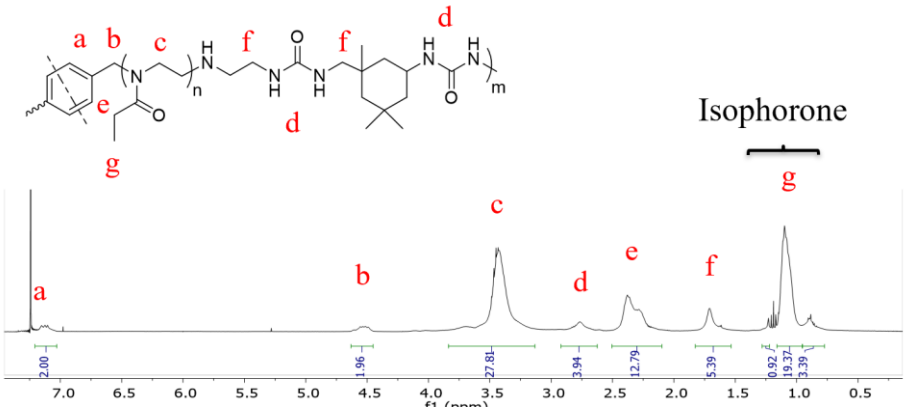

Figure 13.6. ^{1}H NMR spectrum of poly(2-ethyl oxazoline)-urea.

Other experiments to probe thermal, mechanical, and viscosity profiles will further elucidate the feasibilily for these polymers to be used for fertilizer-release and 3D printing. Use DSC and TGA to measure thermal transitions to uncover the nature of the polymers through an application temperature range. Poly(2-ethyl oxazoline) homopolymers experience T_g's ranging from 20 to 30 ^{o}C. The application range of fertilizers range from 10 to 120 ^{o}C depending on the geographical location. Probing thermal transitions will assess where these polymers can be used. DMA and tensile will evaluate the mechanical properties over the application temperature range. Determining the mechanical strength of each polymer will determine how it is packaged and applied to farms. Finally, melt rheology will assess whether the polymer maintains the optimal viscosity to print using extrusion. Subsequent extrusion 3D printing in varying shapes will also tune dissolution times.

13.6 Structure-property relationships between varying amounts of hydrogen bonding in poly(2-oxazoline)s

Poly(2-oxazoline)s are a diverse group of highly tunable polymers with many applications in drug delivery and biomaterials. Poly(2-oxazoline) homopolymers lack mechanical strength due to low molecular weight and lack of crystallinity.[13,14] Implementation of hydrogen bonding may improve mechanical strength and enable applications that require better mechanical strength. Literature cites examples of urethane-containing poly(2-oxazoline)s, but does not provide examples of urea-, amide-, or oxamide-containing poly(2-oxazoline)s, which may further improve mechanical strength.[19] **Scheme 13.7, 13.8,** and **13.9** represent synthetic pathways towards urea-, amide-, or oxamide-containing poly(2-oxazoline)s. All pathways begin with a difunctional initiators to yield poly(2-oxazoline)-diamines. Subsequent reactions with diisocyanates and diacid chlorides yield the described polymers.

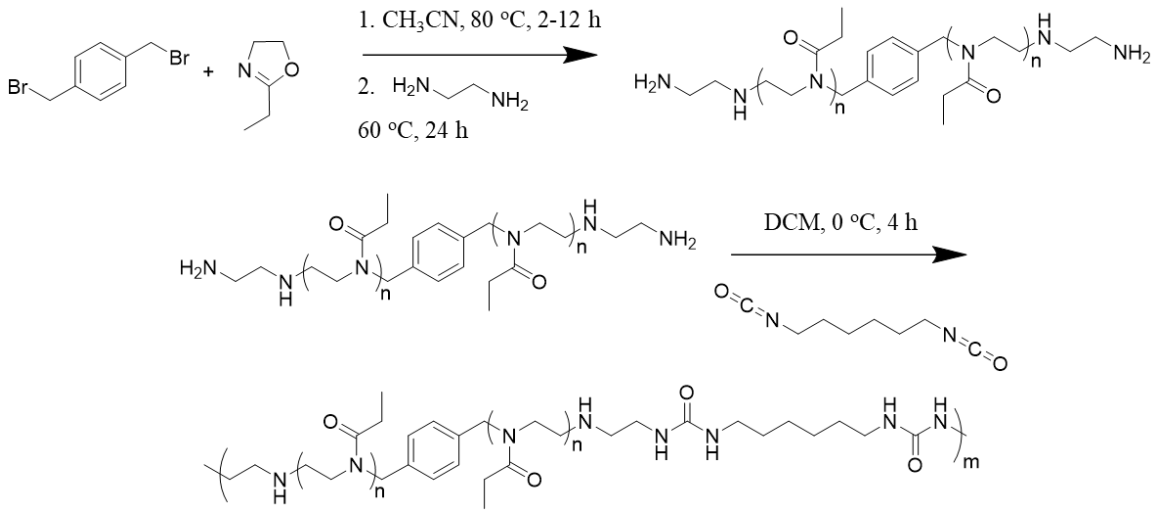

Scheme 13.7. Synthesis of a urea-containing poly(2-oxazoline) utilizing hexamethylene diisocyanate.

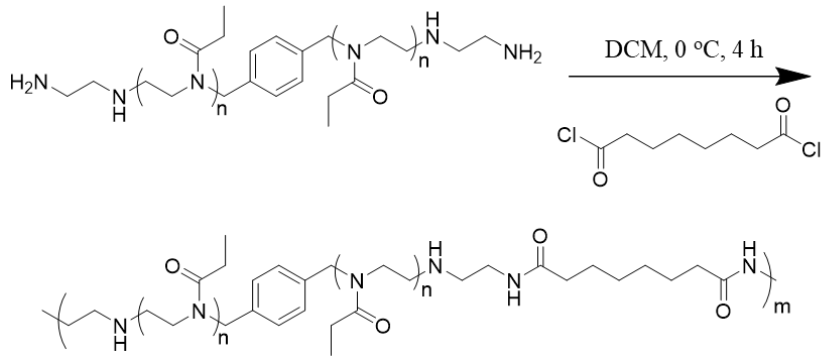

Scheme 13.8. Synthesis of a amide-containing poly(2-oxazoline).

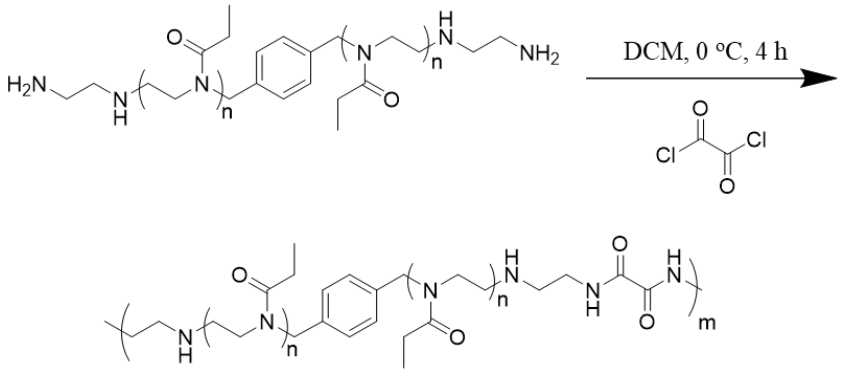

Scheme 13.9. Synthesis of a oxamide-containing poly(2-oxazoline).

To further investigate this system, synthesis of urea-, amide-, or oxamide-containing poly(2-oxazoline)s at the same molecular weight and same degree of polymerization will elucidate structure-property relationships. To explore varying amounts of hydrogen bonding within the same functional group, synthesize three different molecular weight poly(2-oxazoline)-diamines. Using SEC may be difficult due to hydrogen bonding groups. ^{1}H NMR spectroscopy and ^{13}C NMR spectroscopy will reveal the molecular weight of each polymer.

Thermal and thermomechanical analysis will reveal the dependence of the different hydrogen bonding groups on thermal transitions and their relationships to mechanical

properties. DSC will determine if any crystallinity exists and the T_g of each polymer. TGA will reveal the $T_{d,5\%}$ of each system. TGA and ^1H NMR spectroscopy experiments in conjunction should also be conducted to reveal whether amine end-groups are degrading before the $T_{d,5\%}$. If this is the case, acetic anhydride can end-cap the polymers to ensure amines are not degrading at high temperatures and causing color changes. DMA will reveal the thermomechanical properties of each system and reveal trends on how the different hydrogen bonding groups change the thermomechanical profile. Tensile analysis against a poly(2-oxazoline) homopolymer will also reveal whether the hydrogen bonding groups helped mechanical strength. Finally, variable temperature FTIR will reveal which temperatures hydrogen bond dissociation occurs. The different hydrogen bonding groups may experience different temperature of hydrogen bonding dissociation and thus enable different applications.

13.7 References

(1) Özkol, E.; Ebert, J.; Telle, R. An Experimental Analysis of the Influence of the Ink Properties on the Drop Formation for Direct Thermal Inkjet Printing of High Solid Content Aqueous 3Y-TZP Suspensions. *J. Eur. Ceram. Soc.* **2010**, *30* (7), 1669–1678. https://doi.org/10.1016/J.JEURCERAMSOC.2010.01.004.

(2) Wilts, E.; Ma, D.; Bai, Y.; Williams, C. B.; Long, T. E. Comparison of Linear and 4-Arm Star Poly(Vinyl Pyrrolidone) for Aqueous Binder Jetting Additive Manufacturing of Personalized Dosage Tablets. *ACS Appl. Mater. Interfaces* **2019**, acsami.9b08116. https://doi.org/10.1021/acsami.9b08116.

(3) Luzzati, S.; Adam, M.; Delsanti, M. Size Determination of a Chain in a Bad Solvent by Intensity Light Scattering Comparison with a Good Solvent State. *Polymer (Guildf).* **1986**, *27* (6), 834–838. https://doi.org/10.1016/0032-3861(86)90290-9.

(4) Batista, M. M.; Guirardello, R.; Krähenbühl, M. A. Determination of the Hansen Solubility Parameters of Vegetable Oils, Biodiesel, Diesel, and Biodiesel–Diesel Blends. *J. Am. Oil Chem. Soc.* **2015**, *92* (1), 95–109. https://doi.org/10.1007/s11746-014-2575-2.

(5) Prasad, L. K.; Smyth, H. 3D Printing Technologies for Drug Delivery: A Review. *Drug Dev. Ind. Pharm.* **2016**, *42* (7), 1019–1031.

https://doi.org/10.3109/03639045.2015.1120743.

(6) Goole, J.; Amighi, K. 3D Printing in Pharmaceutics: A New Tool for Designing Customized Drug Delivery Systems. *Int. J. Pharm.* **2016**, *499* (1–2), 376–394. https://doi.org/10.1016/J.IJPHARM.2015.12.071.

(7) Rowe, C. .; Katstra, W. .; Palazzolo, R. .; Giritlioglu, B.; Teung, P.; Cima, M. . Multimechanism Oral Dosage Forms Fabricated by Three Dimensional Printing™. *J. Control. Release* **2000**, *66* (1), 11–17. https://doi.org/10.1016/S0168-3659(99)00224-2.

(8) Katstra, W. .; Palazzolo, R. .; Rowe, C. .; Giritlioglu, B.; Teung, P.; Cima, M. . Oral Dosage Forms Fabricated by Three Dimensional Printing™. *J. Control. Release* **2000**, *66* (1), 1–9. https://doi.org/10.1016/S0168-3659(99)00225-4.

(9) Rau, D. A.; Herzberger, J.; Long, T. E.; Williams, C. B. Ultraviolet-Assisted Direct Ink Write to Additively Manufacture All-Aromatic Polyimides. *ACS Appl. Mater. Interfaces* **2018**, *10* (41), 34828–34833. https://doi.org/10.1021/acsami.8b14584.

(10) Herzberger, J.; Meenakshisundaram, V.; Williams, C. B.; Long, T. E. 3D Printing All-Aromatic Polyimides Using Stereolithographic 3D Printing of Polyamic Acid Salts. *ACS Macro Lett.* **2018**, *7* (4), 493–497. https://doi.org/10.1021/acsmacrolett.8b00126.

(11) Henke, A.; Kadlubowski, S.; Ulanski, P.; Rosiak, J. M.; Arndt, K.-F. Radiation-Induced Cross-Linking of Polyvinylpyrrolidone-Poly(Acrylic Acid) Complexes. *Nucl. Instruments Methods Phys. Res. Sect. B Beam Interact. with Mater. Atoms* **2005**, *236* (1–4), 391–398. https://doi.org/10.1016/J.NIMB.2005.04.003.

(12) Moharram, M. A.; Khafagi, M. G. Application of FTIR Spectroscopy for Structural Characterization of Ternary Poly(Acrylic Acid)–Metal–Poly(Vinyl Pyrrolidone) Complexes. *J. Appl. Polym. Sci.* **2007**, *105* (4), 1888–1893. https://doi.org/10.1002/app.25703.

(13) Glassner, M.; Vergaelen, M.; Hoogenboom, R. Poly(2-Oxazoline)s: A Comprehensive Overview of Polymer Structures and Their Physical Properties. *Polym. Int.* **2018**, *67* (1), 32–45. https://doi.org/10.1002/pi.5457.

(14) Lava, K.; Verbraeken, B.; Hoogenboom, R. Poly(2-Oxazoline)s and Click Chemistry: A Versatile Toolbox toward Multi-Functional Polymers. *Eur. Polym. J.* **2015**, *65*, 98–111. https://doi.org/10.1016/j.eurpolymj.2015.01.014.

(15) Chia, H. N.; Wu, B. M. Recent Advances in 3D Printing of Biomaterials. *J. Biol. Eng.* **2015**, *9* (1), 4. https://doi.org/10.1186/s13036-015-0001-4.

(16) Sirrine, J. M.; Schexnayder, S. A.; Dennis, J. M.; Long, T. E. Urea as a Monomer for Isocyanate-Free Synthesis of Segmented Poly(Dimethyl Siloxane) Polyureas. *Polymer (Guildf).* **2018**, *154*, 225–232. https://doi.org/10.1016/J.POLYMER.2018.09.003.

(17) Dennis, J. M.; Steinberg, L. I.; Pekkanen, A. M.; Maiz, J.; Hegde, M.; Müller, A. J.;

Long, T. E. Synthesis and Characterization of Isocyanate-Free Polyureas. *Green Chem.* **2018**, *20* (1), 243–249. https://doi.org/10.1039/C7GC02996A.

(18) Hoogenboom, R. Poly(2-Oxazoline)s: A Polymer Class with Numerous Potential Applications. *Angew. Chemie Int. Ed.* **2009**, *48* (43), 7978–7994. https://doi.org/10.1002/anie.200901607.

(19) Del Rio, E.; Lligadas, G.; Ronda, J. C.; Galià, M.; Cádiz, V. Poly-2-Oxazoline-Derived Polyurethanes: A Versatile Synthetic Approach to Renewable Polyurethane Thermosets. *J. Polym. Sci. Part A Polym. Chem.* **2011**, *49* (14), 3069–3079. https://doi.org/10.1002/pola.24744.